Organic-inorganic interactions in siliciclastic oil reservoirs, North Sea

vorgelegt von
M. Sc. Geologin
Nana Mu
aus Luoyang, China

Von der Fakultät VI - Planen Bauen Umwelt
der Technischen Universität Berlin
zur Erlangung des akademischen Grades
Doktor der Naturwissenschaften
Dr. rer. nat.

genehmigte Dissertation

Promotionsausschuss:
Vorsitzender: Prof. Dr. Wilhelm Dominik
Berichter: Prof. Dr. Brian Horsfield
Berichter: Prof. Dr. Jan Schwarzbauer
Berichter: Priv. Doz. Dr. Hans-Martin Schulz
Tag der wissenschaftlichen Aussprache: 21. Februar 2017

Berlin 2017

Dedicated to my parents

Statement of Original Authorship

I, Nana Mu, hereby state that the work contained in this thesis or any parts thereof has not previously been submitted to the Fakultät VI - Planen, Bauen, Umwelt at the Technical University of Berlin or any other institution except where explicitly acknowledged.

To the best of my knowledge and belief, the thesis does not contain any previously published material or any material which has been written by another person except where due reference is made.

Hiermit erkläre ich, Nana Mu, dass diese Arbeit bisher von mir weder an der Fakultät VI -Planen, Bauen, Umwelt der Technischen Universität Berlin noch einer anderen wissenschaftlichen Einrichtung zum Zwecke der Promotion eingereicht wurde. Ferner erkläre ich, dass ich diese Arbeit selbständig verfasst und keine weiteren als die darin angegebenen Quellen und Hilfsmittel benutzt habe.

Nana Mu

30-10-2016

Acknowledgements

This dissertation would not have been possible without the support of a number of people.

Frist of all I would like to thank my supervisor Priv. Doz. Dr. Hans-Martin Schulz for his great support and tremendous help throughout my four-year PhD study. Without his dedication and his encouragement, I could not have finished my study and this dissertation.

I am also very grateful to Prof. Dr. Wolfgang van Berk and Dr. Yunjiao Fu from Clausthal University of Technology for their many inspiring ideas and invaluable scientific discussions. Dr. Yunjiao Fu is specially thanked for helping me to conduct hydrogeological modelling using Phreeqc.

I would also like to acknowledge Prof. Dr. Brian Horsfield for letting me join the Organic Geochemistry group of GFZ and study with many brilliant scientists and PhD students.

My supervisor in China, Prof. Huang, Wen Hui from China University of Geosciences, is acknowledged for recommending GFZ to me.

Dong Energy, the British Geological Survey and the Norwegian Petroleum Directorate are acknowledged for providing core samples for this dissertation. My special appreciation goes to the China Scholarship Council (CSC). Without the financial support from CSC, it would have been impossible for me to study four years in Germany.

Many thanks also go to all technical staff of the Organic Geochemistry section at GFZ. Anika Zabel is thanked for helping me to do lab works at the first beginning. Anke Kaminsky, Cornelia Karger, Kristin Günther, Ferdinand Perssen, and Mirco Rahn are thanked for their assistance in analyzing samples and solving IT problems. I also owe many thanks to several persons of the Inorganic and Isotope Geochemistry section at GFZ for their help in sample analyses: Ilona Schäpan, Dr. Dieter Rhede, Dr. Rudolf Naumann, Andrea Gottsche, and Dr. Anja Maria Schleicher. Dr. Richard Wirth of the Chemistry and Physics of Earth Materials section at GFZ is also thanked for TEM analysis.

Further thanks are directed to my colleagues at GFZ. The big Chinese group (Shouzi Hu, Yuanjia Han, Songqi, Pan, Yaling Zhu, Shengyu Yang, Shuangbiao Han, Jingqiang Tan, and Liangliang Wu) of our section are very thanked for their accompany and sharing many pleasant times during my four-year PhD study. The small "mushroom team" (Rene Jarling, Andrea Gruner and Bastian Kasek) are thanked for sharing knowledge about mushrooms, exchanging foods and cultures, and organizing many enjoyable mushroom-searching trips in woods. Tobias Nickschick and Lukas Belz, my officemates, are appreciated for creating humorous working environment. Rene Jarling, Tobias Nickschick and Volker Ziegs are also specially thanked for improving the language of my dissertation. Dr. Stefanie Pötz and Dr. Mareike Noah are appreciated for instructing FT-ICR-MS analysis and valuable discussions. My thanks also go to Sascha Kuske, Seyed Hossein Hosseini Baghsangani, Janina Stapel, Dr. Andreas Hübner, Dr. Julia Nickel, Dr. Alexandra Vetter, Dr. Victoria Sachse, Dr. Zahie Anka, Jacqueline Mireya Calzada-Mendoza, Prof. Dr. Rolando di Primio, Dr. Robert Ondrak, Dr. Volker Lüders, Dr. Horst Kämpf, and Dr. Kai Mangelsdorf.

My final gratitude goes to my dear parents and my boyfriend Li, Pan for their love and support.

Nana Mu

30-10-2016

List of Publications

Articles in peer-reviewed journals

1) **Mu, N.**, Schulz, H.-M., Fu, Y., van Berk, W., and Poetz, S., 2016. Testing meteoric water flushing as a factor for oil degradation and mineral alteration in deep-marine sandstones - Case study: Frigg and Grane field, northern North Sea. Sedimentary Geology, under review.

2) **Mu, N.**, Fu, Y., Schulz, H.-M., van Berk, W., 2016. Authigenic albite formation due to water-rock interactions – Case study: Magnus oilfield (UK, Northern North Sea). Sedimentary Geology, 331, 30-41. http://dx.doi.org/10.1016/j.sedgeo.2015.11.002

3) **Mu, N.**, Schulz, H.-M., Fu, Y., Schovsbo, N. H., Wirth, R., Rhede, D., van Berk, W., 2015. Berthierine formation in reservoir rocks from the Siri oilfield (Danish North Sea) as result of fluid-rock interactions: Part I. Characterization. Marine and Petroleum Geology, 65, 302-316. http://dx.doi.org/10.1016/j.marpetgeo.2015.04.010

4) Fu, Y., van Berk, W., Schulz, H.-M. and **Mu, N.**, 2015. Berthierine formation in reservoir rocks from the Siri oilfield (Danish North Sea) as result of fluid-rock interactions: Part II. Deciphering organic-inorganic processes by hydrogeochemical modeling. Marine and Petroleum Geology, 65, 317-326. http://dx.doi.org/10.1016/j.marpetgeo.2015.01.007

5) Fu, Y., van Berk, W., Schulz, H.-M. and **Mu, N.**, 2015. Berthierine formation in reservoir rocks from the Siri oilfield (Danish North Sea) as result of fluid-rock interactions: Part III. Determining mineral stability and CO_2-sequestering capacity of glauconitic sandstones. Marine and Petroleum Geology, 65, 327-333. http://dx.doi.org/10.1016/j.marpetgeo.2015.01.008

Presentations at international symposia

1) **Mu, N.**, Schulz, H.-M., Poetz, S.. Organic-inorganic interactions at oil-water transition zones in Tertiary siliciclastic reservoirs (Norwegian continental margin): baseline data

for studies along an API gravity gradient". IMOG 2015 Meeting. Prague, Czechia, 2015. POSTER

2) **Mu, N.**, Schulz, H.-M., Fu, Y., van Berk, W.. Organic-inorganic interactions in a petroleum reservoir: An example from the Heimdal Member, Siri field, North Sea. Reservoir quality of clastic and carbonate rocks: Analysis, Modelling, and Prediction. London, UK, 2014. POSTER

3) **Mu, N.**. Organic-inorganic interaction in petroleum reservoir- an example of the Palaeocene Heimdal sandstones, Siri field. The Second International Youth Scholars Forum, Sun Yat-sen University, Zhuhai, China, 2016. ORAL

Presentations at internal seminar

1) **Mu, N.**, Schulz, H.-M., Fu, Y., Schovsbo, N. H., van Berk, W.. Organic-inorganic interactions in petroleum reservoirs. GeoForschungZentrum Potsdam, Germany, 2014. ORAL

2) **Mu, N.**, Schulz, H.-M.. Quartz cements distribution and quartz morphologies in sandstone reservoirs: An example from the Heimdal sandstones, Siri field. The 8th annual Ph.D day at GeoForschungZentrum Potsdam, Potsdam, Germany, 2013. POSTER

3) **Mu, N.**, Schulz, H.-M., Fu, Y., van Berk, W.. Organic-inorganic interactions in a petroleum reservoir: An example from the Heimdal sandstone, Siri field. The 9th annual Ph.D day at GeoForschungZentrum Potsdam, Potsdam, Germany, 2014. POSTER

4) **Mu, N.**, Schulz, H.-M., Poetz, S.. Gas-rock-fluids interactions at oil-water contacts in petroleum reservoirs. The 10th annual Ph.D day at GeoForschungZentrum Potsdam, Potsdam, Germany, 2015. POSTER

Abstract

Sandstones are important reservoir rocks for a variety of fluids. Their properties, such as porosity and permeability, which are crucial factors for petroleum production, primarily depend on depositional environments. Additionally, subsequent geochemical alterations by depth-related reactions ("classic diagenesis"), organic-inorganic interactions, and mixing of basin fluids can also significantly alter reservoir properties via mineral dissolution and (re-)precipitation. However, the impact of organic-inorganic interactions on mineral alteration is still poorly understood and the controlling factors for meteoric water intrusions are unknown. It is the aim of this dissertation to investigate the diagenesis of sandstones in order to figure out how organic-inorganic interactions affected mineral assemblages depending on oil degradation of different intensity, on mineralogical composition and on pore water composition. Furthermore, the controlling factors for meteoric waters intruding into deep marine turbidites and their consequence on organic-inorganic interactions were studied.

To achieve these objectives, more than one hundred core samples were taken from four oil fields (Siri field, Magnus field, Frigg field and Grane field) in the North Sea. These samples vary in lithology (glauconite sandstone, arkose sandstone, and subarkose sandstone), and cover an age range of Jurassic, Palaeocene and Eocene, and a depth interval from shallow (1,734-1,798 m) to deep (3,200-3,240 m). An interdisciplinary approach including imaging techniques (thin section, SEM, TEM), inorganic geochemical techniques (XRD and XRF) and organic geochemical methodologies (GC-FID, GC-MS, FT-ICR-MS) was used for analyzing the inorganic and organic constituents of the samples, and their genetic relationships.

In the glauconite-bearing Heimdal sandstone reservoir of the Siri field (2,096-2,137 m depth), authigenic berthierine is one of the most significant diagenetic phases. Berthierine mainly appears as pore-lining or pore-filling crystals, and is most abundant at the oil-water contact (OWC) where glauconite is relatively depleted and where extracted bitumens show the highest extent of biodegradation. Berthierine commonly occurs in semi-dissolved glauconite and its formation postdates oil filling. Based on these two observations, it can be inferred that the formation of berthierine was result of glauconite dissolution, and that this process was probably driven by organic-inorganic interactions due to oil degradation at the OWC. Due to these interconnected processes, other diagenetic alterations, such as feldspar

dissolution and quartz overgrowth, also take place in the Heimdal glauconite-bearing sandstone.

In the Magnus field, the Jurassic Magnus sandstone is the main reservoir which is at present deeply buried at depths of ca. 3,200-3,240 m. The Magnus sandstone is an arkose sandstone with a high feldspar content. This sandstone reservoir has experienced various intensive post-depositional alterations, including quartz overgrowth, formation of ankerite, siderite, albite, and kaolinite, as well as K-feldspar dissolution. Petrographic and geochemical analyses indicate that part of albite was formed within the reservoir at temperatures of around 80-100°C after oil emplacement. Three potential mechanisms for albite formation were proposed and tested by hydrogeochemical modelling approaches. The results indicate that (1) dissolution of unstable minerals (such as kaolinite and chalcedony) coupled to reduction of ferric iron minerals, but also (2) dissolution of non-end member feldspar coupled to illite formation can account for albite formation.

The Eocene Frigg sandstones of the Frigg field and the Palaeocene Heimdal sandstones of the Grane field are both sub-arkose sandstones and are buried at 2,045-2,075 m and 1,734-1,798 m, respectively. However, the Eocene Frigg sandstones display intensive feldspar dissolution and kaolinite formation, and stronger oil degradation compared to the Palaeocene Heimdal sandstones of the Grane field. Most likely, meteoric water intrusion into the Frigg sandstones due to its adjacency of the East Shetland Platform could have led to both alterations. Furthermore, organic-inorganic interactions triggered by oil degradation could also be a reason for feldspar dissolution and kaolinite formation accompanied by siderite formation.

Keywords: Organic-inorganic interaction, sandstone, glauconite, berthierine, albite, meteoric water, FT-ICR-MS, North Sea.

Zusammenfassung

Sandstein ist ein wichtigstes Reservoirgestein für Fluide. Seine Eigenschaften, wie zum Beispiel Porosität und Permeabilität, die entscheidend für die Erdöl- und Erdgasproduktion sind, hängen stark vom Ablagerungsmilieu ab. Zusätzlich können nachfolgende geochemische Prozesse wie z.B. tiefenabhängige Reaktionen ("Klassische Diagenese"), organisch-anorganische Wechselwirkungen, und Vermischungen von unterschiedlichen Beckenfluiden die Reservoir-Eigenschaften durch Lösung und Ausfällung von Mineralen erheblich verändern. Trotzdem ist der Einfluss organisch-anorganischer Wechselwirkungen auf Mineralveränderungen immer noch wenig erforscht und die kontrollierenden Faktoren von Intrusionen meteorischen Wassers weitestgehend unbekannt. Das Ziel der vorliegenden Dissertation ist die Untersuchung der Sandsteindiagenese in Bezug auf den Einfluss organisch-anorganischer Wechselwirkungen auf Mineralvergesell-schaftungen und deren Abhängigkeit von der Intensität des Erdölabbaus, der primären mineralogischen Zusammensetzung, und von der Porenwasser-Zusammensetzung. Weiterhin wurden die Einflussfaktoren von Intrusionen meteorischen Wassers in tiefmarine Turbidite und deren Folgen auf organisch-anorganischen Wechselwirkungen untersucht.

Hierzu wurden mehr als 100 Kernproben aus vier Ölfeldern in der Nordsee genommen (Siri Feld, Magnus Feld, Frigg Feld und Grane Feld). Diese Proben variieren im Hinblick auf Lithologie (glaukonitscher Sandstein, Arkose-Sandstein, subarkosischer Sandstein), Alter (von Jura, Paläozän, bis Eozän), und Tiefe, wo sie sich von flachen (1,734-1,798 m) bis zu tiefen (3,200-3,240 m) Bereichen erstrecken. Um organische und anorganische Bestandteile der Proben und deren genetische Zusammenhänge zu analysieren, wurde ein interdisziplinärer Ansatz mit bildgegebenden Verfahren (Dünnschliff, SEM, TEM), anorganisch-geochemischen (XRD und XRF), und organisch-geochemischen Methoden (GC-FID, GC-MS, FT-ICR-MS) angewendet.

Im Glaukonit-haltigen Heimdal-Sandstein des Siri-Reservoirs (2,096-2,137 m) ist authigener Berthierin eine der bedeutendsten diagenetischen Mineralphasen. Berthierin kommt hauptsächlich als Porensaum oder Porenfüllung vor und tritt zumeist am Öl-Wasser-Kontakt (OWC) auf. Hier ist Glaukonit relativ verarmt und extrahierte Bitumina zeigen das

höchste Biodegradationsstadium. Berthierin tritt normalerweise in angelöstem Glaukonit auf und seine Bildung eröffnet die Möglichkeit, die Füllungsgeschichte des Reservoirs zu datieren. Aus beiden Beobachtungen lässt sich schließen, dass der Übergang von Glaukonit zu Berthierin durch organisch-inorganische Wechselwirkungen verursacht wird und im Umkehrschluss durch die Öldegradation am OWC angetrieben wird. Aufgrund dieser miteinander verbundenen Prozesse finden zudem andere diagenetische Prozesse in den Glaukonit-haltigen Heimdal-Sandsteinen statt, zum Beispiel Auflösung von Feldspäten und Quarz-Überwachsung.

Jurassische Magnus Sandsteine sind das Hauptreservoir im Magnus-Feld und bis in 3,200-3,240 m Tiefe versenkt. Diese bestehen aus Arkosesandsteinen mit hohem Feldspat-Anteil. Das Reservoir hat verschiedene, intensive Prozesse nach der Ablagerung erlebt, wie Quarz-Überwachsung, Neubildung von Ankerit, Siderit, Albit, sowie Auflösung vom Kalifeldspat. Petrographische und geochemische Untersuchungen weisen darauf hin, dass ein Teil des Albits bei Temperaturen von ca. 80-100°C im Reservoir gebildet wurde, nachdem das Öl eingedrungen ist. Drei mögliche Mechanismen für die Albit-Bildung wurden mit Hilfe von hydrogeochemischen Modellierungen überprüft. Die modellierten Ergebnisse deuten darauf hin, dass (1) die Auflösung von instabilen Mineralen (wie Kaolinit und Chalzedonit) mit der Reduktion Eisen(III)-haltiger Minerale verbunden sind, und (2) dass die Neubildung vom Albit auch durch Auflösung von Feldspatmischkristallen und gleichzeitiger Illit-Bildung verantwortlich sein kann.

Die eozänen Sandsteine des Frigg Feldes und die paläozänen Sandsteine des Grane Felds sind beide Subarkosesandsteine und treten in Tiefen von jeweils 2,045-2,075 m und 1,734-1,798 m auf. Jedoch zeigen die Frigg Sandsteine eine intensivere Feldspatauflösung, eine stärkere Kaolinitbildung, sowie eine stärkere Erdöldegradation im Vergleich zu den paläozänen Heimdal-Sandsteinen des Grane Feldes. Es wird vermutet, dass die Intrusion meteorischen Wassers in die Frigg-Sandsteine aufgrund seiner Nähe zur East Shetland Plattform stattfand, und dies zu beiden genannten Alterationsprozessen geführt hat. Weiterhin könnten die vom Ölabbau ausgelösten organisch-anorganischen Interaktionen eine Ursache für Feldspatauflösungen und Bildung von Kaolinit sowie Siderit sein.

Schlüsselwörter: Organisch-anorganische Wechselwirkung, Sandstein, Glaukonit, Berthierin, Albit, meteorische Wässer, FT-ICR-MS, Nordsee.

Table of Contents

List of Figures

Figure 3.5 BSE images of berthierine types. (a) Type 3: berthierine (bright area) growing in strongly dissolved glauconite, Well Siri-2, oil leg; (b) Growth of berthierine crystals (bright areas) together with muscovite in transforming glauconite, Well Siri-2, OWC. (c) Type 2: pore filling berthierine (the upper left corner) cemented by calcite. The glauconite grain in the lower right corner is covered by berthierine type 1 (white arrow), Well Siri-2, OWC. (d) Type 4: as elongated crystals together with newly formed siderite between lamellae of mica transformed from glauconite. High resolution image of the rectangle area in c, Siri-2, OWC. (e) Type 5: berthierine in siderite concretions, Well Siri-2, Oil leg. (f) Type 1, Subtype II: berthierine growing in dissolved feldspar, Well Siri-2, oil leg. B: berthierine; G: glauconite; Q: quartz; M: mica; C: calcite cement; S: siderite; O: residual oil; F: feldspar.

Figure 3.6 TEM investigations of berthierine type 1 and 4. Type 1 berthierine (a-e) coating glauconite grains in direct contact with residual oil. (a) High-magnification scanning transmission electron microscopy (STEM) image (high-angle annular dark-field [HAADF] mode) of a focused ion beam (FIB) foil. (b) EDS spectrum of berthierine in c. (c) High resolution image of the left white rectangle in a. (d) Bright-field image of berthierine in c. (e) High-resolution transmission electron microscopy (HRTEM) image of berthierine in d showing lattice fringes with 0.7 nm periodicity. The insert shows a selected area electron diffraction (SAED) pattern with a pronounced 0.7 nm periodicity. Type 3 berthierine (e-f) in transforming glauconite close to a mineralized oil water emulsion. (f) High resolution image of the right rectangle in a. Berthierine co-occurs with small Mn-oxide particles close to a mineralized oil-water emulsion (white dotted circle) in a glauconite pore. (g) High resolution image of the white circle in f shows small organic matter particles with carbon, calcium and nitrogen contents (illustrated in the inserted electron energy loss spectroscopy (EELS) spectrum). G: glauconite; B: berthierine; C: calcite; O: oil; M: Mn-Ti oxide. Well Siri-2, OWC.

Figure 3.7 TEM investigations of berthierine type 5 (a-d) and type 2 (e-g). Type 5 berthierine (a-d) as blade-like particles in a siderite concretion. (a, b) High-magnification scanning transmission electron microscopy (STEM) images (high-angle annular dark-field [HAADF] mode) of a focused ion beam (FIB) foil extracted from the red rectangle in Figure 3.2b. (a) Growth of 1 μm large fibre-shaped berthierine in oil-filled pore. (b) High resolution image of the white rectangle area in a. Berthierine bridges siderite crystals. Additional berthierine (white arrow) is growing on a siderite surface. (c) EDS analysis of the berthierine bridge marked by the black arrow in b. (d) High-resolution transmission electron microscopy (HRTEM) image of the berthierine bridge in b with the insert displaying its calculated diffraction (fast Fourier Transform FFT) pattern of 0.7 nm periodicity. Type 2 berthierine (e-g) in open pore space filled by residual oil. (e) Several fibrous berthierine crystals in oil near an authigenic microquartz grain. (f) High-resolution transmission electron microscopy (HRTEM) image of one fibrous berthierine crystal in e with well-defined 0.7 nm lattice fringes and selected area electron diffraction (SAED) pattern of 0.7 nm periodicity (insert). (g) High-resolution transmission electron microscopy (HRTEM) image and selected area electron diffraction (SAED pattern (insert) of the

List of Tables

List of Abbreviations

µm	Micrometer
Ab	Albite
An	Anorthite.
API	American Petroleum Institute
aq	Aqueous
atm	Atmosphere
BP	Before present
BSE	Backscattered scanning electron
ca.	Circa
cm	Centimeter
CPI	Carbon Preference Index
CSC	Chinese Scholarship Council
DBE	Double bond equivalents
DCM	Dichloromethane
EDS	Energy-dispersive X-ray spectroscopy
EELS	Electron energy loss spectroscopy
EMPA	Electron microprobe analysis
ESI	Electrospray ionization
FeR	Bacterial iron reduction
FFT	Fast Fourier Transform
FIB	Focused Ar-ion beam

FIB	Focused ion beam
FID	Flame Ionization Detector
FT-ICR-MS	Fourier Transform Ion Cyclotron Resonance Mass Spectrometry
GC	Gas chromatography
GC-FID	Gas chromatography-flame ionization detection
GC-MS	Gas chromatography-mass spectrometry
GOC	Gas-oil contact
HAADF	High-angle annular dark-field
HDOM	Hydrolytic disproportionation of organic matter
HFO	Hydrous ferric oxide
HRTEM	High-resolution transmission electron microscopy
IS	Internal standard
kgw	Kilo gram water
kV	Kilovolt
L	Liter
LHCPI	Light hydrocarbon carbon preference index
Ma	Million years
mA	Milliampere (milliamps)
mD	Millidarcy
Me	Methanogenesis
min.	Minute
ml	Milliliter
MnR	Manganese reduction
MPLC	Medium Pressure Liquid Chromatography

MSM	Magnus Sandstone Member
nA	Nanoampere (nanoamps)
nm	Nanometer
NR	Nitrate reduction
NSO	Nitrogen, sulfur, oxygen compounds
OWC	Oil-water contact
OWTZ	Oil-water transition zone
P	Pressure
PDB	Pee Dee Belemnite
Ph	Phytane
Pr	Pristane
s	Second
SAED	Selected area electron diffraction
SARA	Saturates, Aromatics, Resins, Asphaltenes
SEM	Scanning electron microscopy
SR	Sulphate reduction
STEM	Scanning transmission electron microscopy
TEM	Transmission electron microscopy
UCM	Unresolved complex mixture
v	Volum
vol.-%	Volum-%
wt.-%	Weight-%
XRD	X-ray powder diffraction
XRF	X-ray fluorescence

Chapter 1 Introduction

1.1. General introduction

1.1.1. Organic matter diagenesis

Preservation of organic matter

Organic matter, mainly consisting of phytoplankton, higher plants, bacteria, and zooplankton, is an important component in sediments (Killops and Killops, 2005). The contents of organic matter in sedimentary deposits vary significantly, ranging from 0% in certain sandstones to nearly 100% in coals, but are commonly below 2% in present marine sediments. The enrichment of organic matter in sediments is favored by various factors, including high primary productivity, low-energy depositional environment, low rates of dilution by inorganic minerals and anoxic environments for preservation (Killops and Killops, 2005). Accordingly, environments with a restricted circulation of water favor the deposition of organic-rich sediments. On the continental shelves and slopes, organic matter is rich in depositional environments, such as lagoons, estuaries, and deep basins (Tissot and Welte, 1984).

Evolution of organic matter

Organic matter undergoes four stages of evolution under increasing temperature and pressure conditions, namely: diagenesis, catagenesis, metagenesis and finally metamorphism (Tissot and Welte, 1984, Fig. 1.1).

Diagenesis refers to the alteration processes of organic matter both prior to deposition and during the early stage of burial. After organic matter deposits on the seafloor and is further buried within the sediment-water interface zone, it starts to be decomposed by microbial and chemical actions. As a result, individual monomers, such as amino-acids, sugars, etc. are formed. With increasing time and burial depth, the residue unassimilable monomers become progressively insoluble due to increasing polycondensation and form brown materials, which resemble humic acids (Tissot and Welte, 1984). Under mild temperature and pressure condition, these humin-like materials proceed to continue condensation and insolubilization to from new polycondensed structures, called “geopolymers” (Tissot and Welte, 1984, Fig. 1.1). These geopolymers combine with selectively preserved

biopolymers to form kerogen (Killops and Killops, 2005). In this stage, hydrocarbons, mainly methane due to methanogenesis, are produced in addition to CO_2, H_2O and some heavy heteroatomic compounds (Tissot and Welte, 1984).

With increasing burial, the deposited organic matter enters the catagenic stage, which covers a geological condition with a temperature range of 50-150°C and a pressure range of 300 up to 1500 bars. As temperature and pressure increase with depth, the kerogen structure evolves towards a thermodynamic equilibrium during burial. In this process, liquid petroleum is firstly generated and subsequently condensate and "wet gas" are produced (Tissot and Welte, 1984). During these two evolution stages, a significant amount of methane is released as well (Tissot and Welte, 1984). At the end of catagenesis, aliphatic carbon chains in the kerogen structures are nearly depleted and no petroleum can be generated anymore.

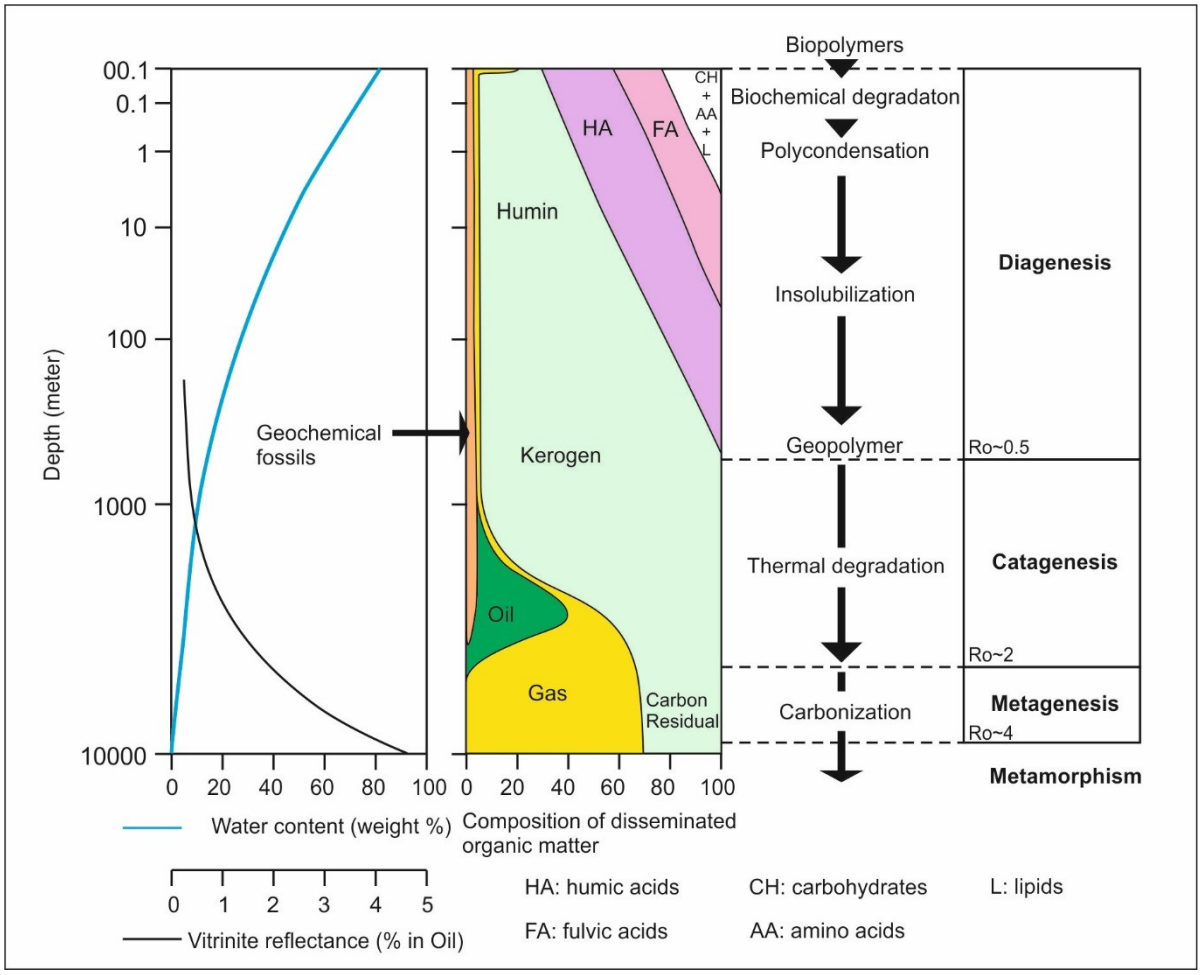

Figure 1.1 Evolution of organic matter from freshly deposited sediment to the metamorphic zone (modified after Tissot and Welte, 1984).

At the stage of metagenesis, where temperature and pressure become even higher, methane, referred as dry gas, is the only hydrocarbon released from kerogen or from thermal cracking of previously evolved hydrocarbons (Killops and Killops, 2005). Thereby, the residual kerogen transforms into graphitic carbon, finally reaching metamorphism.

1.1.2. Biodegradation in oil reservoirs

Since oil is generated in source rocks, it starts to migrate into reservoirs rocks where it may also experience various alteration processes, such as oil degradation, water washing, phase separation, gravity segregation, etc. (Wenger et al., 2002; Killops and Killops, 2005). Among them, oil degradation is one of the most important alteration processes. Oil biodegradation defines the alteration processes of crude oil by living microorganisms (Connan, 1984; Palmer, 1993). During this process, living microorganisms, primarily bacteria (Connan, 1984), preferentially consume saturated and aromatic hydrocarbons. CO_2 and oxidized species, such as acyclic and cyclic, saturated and aromatic carboxylic acids and phenols are formed as metabolic products (Peters et al., 2005; Meredith et al., 2000; Taylor et al., 2001; Mackenzie et al., 1983). Thereby, the residual biodegraded oils become preferentially depleted in paraffin contents, enriched in NSO compounds and trace metals. Such oils are more viscous and acidic, and exhibit lower API values. Biodegradation causes a decline of oil quality and, therefore, greatly impacts the economic values of oil production and refining.

For a long time, it has been considered that degradation of oil in subsurface reservoirs is connected to aerobic microbial activities related to oxygen-bearing meteoric waters (Connan, 1984; Palmer, 1993). This hypothesis was established based on two arguments: (1) the common occurrence of oil degradation in shallow reservoirs, (2) and the observable aerobic degradation rate of oil within human life time scale (Larter et al., 2003; Aitken et al., 2004). However, mass balance calculations pose problems on the large volume of water needed to transport enough oxygen into subsurface reservoirs (Horstad et al., 1992). Moreover, even in meteoric water flushed basin, maintaining sufficient oxygen into deep reservoirs seems to be difficult as oxygen could be already consumed by minerals and microorganisms at shallow depths (Head et al., 2003; Larter et al., 2003). Furthermore, formation waters in deep reservoirs of marine basins are commonly high in salinity which may also indicate limited flushing of fresh water into deep reservoirs (Larter et al., 2003). Accordingly, anaerobic biodegradation is proposed to dominate in subsurface oil reservoirs. Besides electron

accepting processes, like sulphate or iron reduction, methanogenesis is thought to be very important and widespread in subsurface reservoirs (Larter et al., 1999; Jones et al., 2008).

Prerequisites for in-reservoir biodegradation of oil

The prerequisites for the occurrence of oil biodegradation in subsurface reservoirs include (1) the existence of living microorganisms, (2) access to petroleum, (3) the presence of water, (4) the sufficient availability of electron acceptors (e.g., oxygen, sulfates, ferric iron), and (5) inorganic nutrients (Peters et al., 2005). In subsurface petroleum reservoirs, the oil-water contact (OWC), in most cases the oil-water transition zone, is the site where most biodegradation takes place (Head et al., 2003; Peters et al., 2005). This is because at the OWC organisms can get access to both hydrocarbons from the overlying oil leg by diffusion and inorganic nutrients that are derived from dissolution of minerals in the water zone (Fig. 1.2, Head et al., 2003).

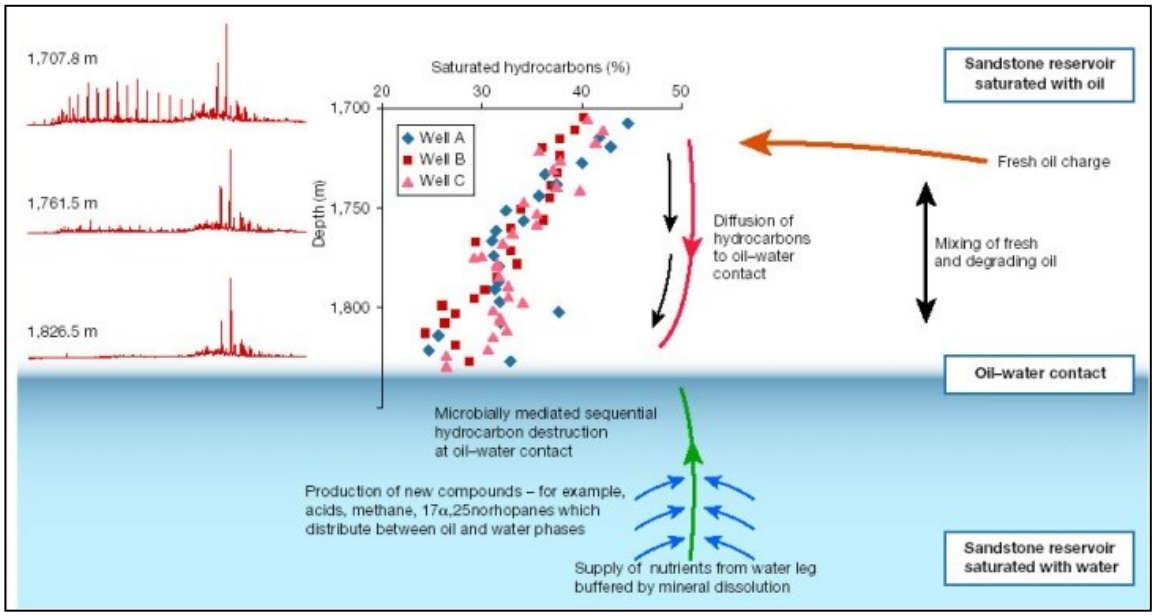

Figure 1.2 Oil degradation at an OWC and oil chemical composition (Head et al., 2003).

Controls for oil biodegradation

Upon the controls for the degree of biodegradation, reservoir temperature is the primary impacting factor. Oil biodegradation is prevalent in shallower reservoirs and is rarely found in

deep reservoirs with a temperature above 80°C. In addition, the level of biodegradation decreases with increasing reservoir temperature below 80°C (Connan, 1984; Bernard and Connan, 1992; Wilhelms et al., 2001). For example, heavy to severe degraded oil commonly occurs in low temperature reservoirs (< 50°C) (Wilhelms et al., 2001; Wenger et al., 2002) while it is nearly absent in the reservoirs around 80°C (Wilhelms et al., 2001; Peters et al., 2005). The reason for this could be that bacterial activity is significantly inhibited with increasing temperature and that microbial life is absent at temperatures above approximately 80°C (Bernard and Connan, 1992). However, not all oils in low temperature (< 80°C) reservoirs are biodegraded. There exist some oil fields where the reservoirs have low reservoir temperature but contain non-biodegraded oils (Wilhelms et al., 2001). This could be due to either that a recent charge of oil took place or that a paleopasteurization of the reservoir has occurred before oil charge. According to Wilhelms et al. (2001), the reservoirs which were once deeply buried to a depth with the temperature > 80°C go through "paleopasteurization", in which hydrocarbon degrading bacteria are destructed. Therefore, biodegradation is not likely to take place in these pasteurised reservoirs even though they were subsequently uplifted again to a shallow depth with temperature < 80°C.

Impact and scale assessment of oil biodegradation

The impact of biodegradation on the alteration of oil compositions has been well documented. Due to different components have different susceptibilities against biodegradation, an order of preference of removal compounds exists (Wenger et al., 2002). The most susceptible compounds are straight-chain *n*-alkanes, followed by less degradable branched alkanes and monocyclic alkanes while the most resistant compounds are polycyclic alkanes and aromatic hydrocarbons (Aitken et al., 2004; Wenger et al., 2002). The preference of removal of *n*-alkanes leads to the presence of a broad hump representing the unresolved complex mixture (UCM) in the gas chromatograms of saturates (Killops and Killops, 2005). In addition, due to the compounds with light isotopes are preferentially utilized by microorganisms during biodegradation, the residual oils become isotopically heavier for the $\delta^{13}C$ values (Connan, 1984; Wilkes et al., 2000).

Based on the sequential removal of compounds due to their different resistance to biodegradation, scales to assess the level of biodegradation have been established (Wenger et al., 2002; Larter et al., 2012; Peters et al., 2005). Wenger et al. (2002) developed a five-level biodegradation scale (very slight-slight-moderate-heavy-severe) based on the sequence of

removal of selected compounds. However, this scale was modified by Peters et al. (2005). In the biodegradation scale of Peters et al. (2005), a systematic classification scheme of ranking biodegradation level with a scale of 0 (least altered) to 10 (most altered) is given.

Products of oil biodegradation

Petroleum biodegradation is assumed to be an anaerobic hydrocarbon oxidation process, most likely methanogenesis, which leads to the formation of carbon dioxide, methane and partially oxidized residues such as organic acids (Peters et al., 2005; Larter et al., 2012). Methane associated with biodegraded oil in marine petroleum systems has light $\delta^{13}C$ values ranging from -45‰ to -55‰ PDB (Larter et al., 2005; Jones et al., 2008). In contrast, the accompanied carbon dioxide often has isotopically heavier values of $\delta^{13}C$ spanning from -25‰ to +20‰ (Larter et al., 2005; Pallaser, 2000; Jones et al., 2008). In addition to methane and carbon dioxide, organic acids (naphthenic acids) are also produced during oil biodegradation. The aerobic biodegradation of crude oil in laboratory experiments by Watson et al. (2002) indicate that a significant amount of carboxylic acids are produced coupled with the removal of *n*-alkanes. Due to different solubilities, C1-C5 acids are often present in formation water (Zengler et al., 1999) while organic acids with high molecular weight are enriched in the oil phase (Wenger et al., 2002).

Impact of oil emplacement on diagenesis

Oil emplacement was thought to inhibit diagenesis based on the less extent of diagenesis in the oil-filling zone compared to the underlying aqueous zone in oil filling reservoirs (Saigal et al., 1992). However, the impact of oil charge on diagenesis seems to depend greatly on the wettability of reservoirs rocks. In water-wet reservoirs, oil charge seems to have a significant impact on diagenesis as a thin film of water coating usually forms on the surface of minerals after oil emplacement. Whereas in oil-wet reservoirs oil filling could greatly halt chemical alterations due to an absence of water film coating.

Moreover, oil filling into sandstones can have more subtle effects on diagenesis. Oil degradation taking place after emplacement was thought to promote the alterations of reservoirs. Formation of minerals, such as calcite or pyrite, was related to oil degradation by microbiological reactions (Fig. 1.3, Wolicka and Borlowski, 2012). Oil field studies provide further geological evidence. For example, Ehrenberg and Jakobsen (2001) attributed the enhancement of plagioclase dissolution and kaolinite formation in the southern wells of the

Gullfaks Field to the acidity produced by oil biodegradation. Furthermore, Watson et al. (1995) related the carbonate cemented horizons in the Forth and Balmoral fields (northern North Sea) to the oil biodegradation at the oil-water contact.

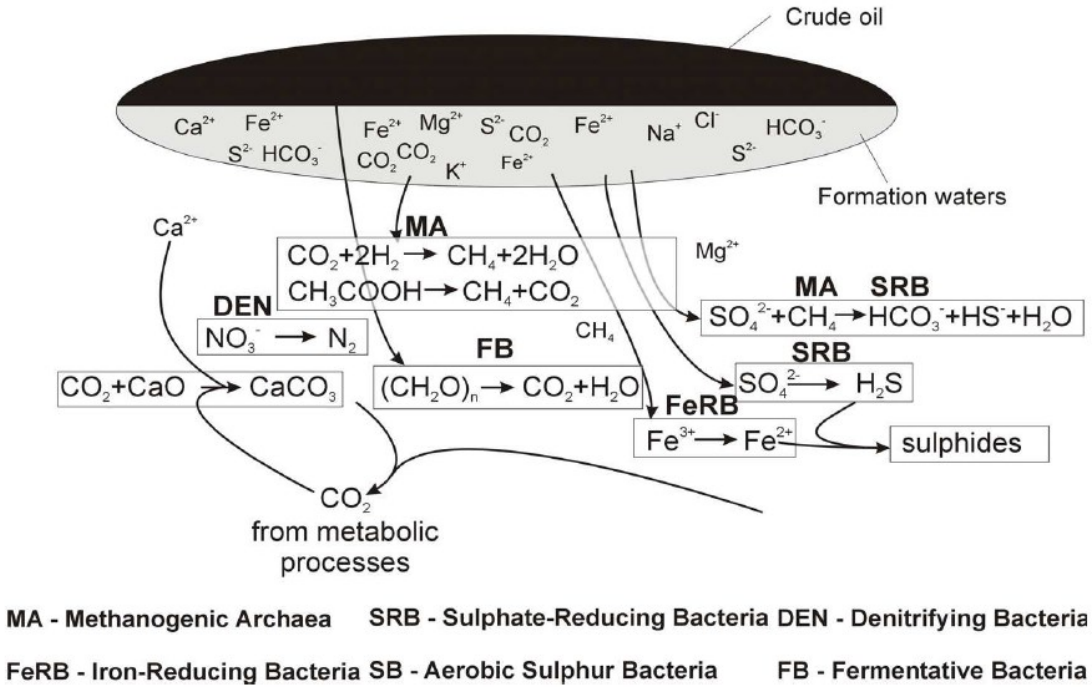

Figure 1.3 Possible mineral formations related to oil degradation by microbiological reactions at OWC (Wolicka and Borlowski, 2012).

1.1.3. Sandstone and sandstone diagenesis

Sandstone reservoirs are important reservoir types for oil and gas all over the world. In addition to the distribution of sand bodies, the important properties (porosity and permeability) are critical for petroleum production and recovery. Depositional environments are the first order of control determining not only the geometry of sandstones but also the porosity and permeability of sandstone.

Depositional environments

Depositional environments determine sand body geometry, sedimentary textures, and the shale/sand ratio which are the first order of parameters on evaluating reservoirs. In addition, the depositional environment has a significant impact on the diagenesis of sandstones. Given the same source area, the detrital mineralogy (mineral composition and

grain size), the starting point of diagenesis, is determined by the energy level of depositional environments. In high energetic environments, sediments are mechanically and chemically more stable due to their higher degree of reworking and therefore they are less susceptible to alteration processes. In contrast, sediments in low energetic environments are quite susceptible to alteration due to their low mechanical and chemical maturities. In addition, the chemistry of fluids in different deposition environments varies greatly, which thus could lead to different pathways of diagenetic evolution. In marine depositional environments, such as deep-sea turbidites, the initial pore water is marine water. Under this marine water condition, the main eogenetic alteration of deep-sea turbidites sandstones is the formation of carbonate and pyrite (Morad et al., 2010).

Diagenesis

Diagenesis refers to alterations or changes of sediments since deposition and is another factor impacting the porosity and permeability of sandstone reservoirs. It comprises a broad spectrum of modification processes, including weathering in subaerial environments, oxidation in water columns, compaction and lithification during burial (Worden and Burley, 2003). The main diagenetic processes include:

(1) Mechanical compaction. It is an important process that is induced by net stress (geostatic pressure - pore pressure). It results in pore volume reduction and pore fluids expulsion. The volume of mechanical compaction on porosity loss varies greatly depending significantly on texture and primary composition of sediments. For example, the sandstones consisting of mainly competent grains (quartz, feldspar) are likely to lose less porosity than mudstones during the compaction process. In contrast, sandstones rich in ductile grains (e.g., mud intraclasts, volcanic fragments) seem to lose more porosity due to the great potential of deformation of these grains (Worden and Burley, 2003).

Furthermore, the development of overpressure in sandstones is another important factor determining the volume of reduced pores. Overpressure exists if the fluid pressure is greater than hydrostatic pressure. In this case, the effective stress, referring to the difference between lithostatic pressure and fluid pressure, is reduced compared with that in normal pressure (fluid pressure = hydrostatic pressure). Therefore, the effects of compaction in overpressured sandstones are relatively reduced in comparison with normally pressured sandstones, which consequently lead to less porosity loss.

(2) Chemical reaction (diagenesis). It involves the dissolution of unstable primary minerals and precipitation of stable secondary minerals. The primary mineral assemblages of sandstones comprise of various minerals that are formed at different temperature and pressure conditions. Therefore, this primary assemblage is not in equilibrium, which then drives chemical alteration of primary minerals towards thermodynamically more stable minerals assemblage (Bjørlykke and Jahren, 2010). During this thermodynamic evolution of primary mineral assemblages, multiple diagenetic processes (e.g. dissolution, precipitation as well as replacement) take place. For example, the most common diagenetic alteration in sandstones is that unstable feldspar dissolves resulting in more stable kaolinite formation.

According to Morad et al. (2000), diagenesis can be subdivided into eodiagenesis, mesodiagenesis and telodiagenesis.

(1) Eodiagenesis refers to the overall physical, chemical and biogenic processes dominated by surface or modified surface water (Worden and Burley, 2003; Morad et al., 2000). It covers depths < 2 km and temperature < 70°C (Morad et al., 2000). As depositional environments for sands are associated with aerated conditions, therefore, sandstones, in general, have extremely low content of organic matter due to oxidation processes. In these organic matter-poor sandstones, compaction is the main feature during eodiagenesis. However, in organic matter-rich sandstones, such as graywackes which may contain up to several percent organic matters, the formation of pyrite and carbonate, in addition to compaction, is featured during eodiagenesis. This is because oxidation of organic matter takes place in these organic matter-rich sandstones. Coupling with oxidation processes, carbonate (calcite) could precipitate by combining Ca^{2+} sourced from biogenetic carbonate with produced CO_2. In addition, as the marine interstitial water is SO_4^{2-}-rich seawater, sulphate reduction leads to pyrite formation.

(2) Mesogenesis defines all diagenetic processes that are beyond the depositional environment and are manipulated by evolved formation water (Worden and Burley, 2003; Morad et al., 2000). It covers a geological regime of depths > 2 km and temperature > 70°C (Morad et al., 2000). The initial mineral assemblage for mesogenesis consists of both deposited phases and authigenic phases that have achieved stability (metastability) with interstitial waters during eodiagenesis. However, due to the increase of temperature and pressure during burial, the previously stable mineral assemblages formed during eogenesis

become unstable both in physical and chemical aspects. Therefore, both physical and chemical processes take place in response to increasing temperature and pressure.

The sediments firstly experience physical compaction resulting in reorientation of detrital grains, expulsion of pore water and then reduction of intergranular pores. With increasing burial depths, chemical compaction operates which leads to pressure dissolution of detrital grains and further reduction of pores. Paralleling, a range of depth-related chemical reactions involving both organic and inorganic constituents within takes place. Due to increased temperature during burial, thermally induced reactions such as maturation of source rock, transformation of smectite to illite, gypsum dehydration, replacement of kaolinite by dickite become dominant. It is suggested that, under compactional pressure drive, compaction fluids with dissolved Na^+, K^+, Ca^{2+},Mg^{2+}, Fe^{2+}, HCO_3^-, SO_4^{2-} and Cl^-, known as "mass solute transfer", migrate from low permeability, low porosity mudstones towards high permeability, high porosity sandstones (Burley et al., 1985; Curtis, 1978; Fig. 1.4). Such migrated fluids influence the cementation and mineralization of sandstones, such as quartz overgrowth and calcite cementation.

(3) Telodiagenesis represents a regime near/at earth surface due to rocks uplift. It covers a wide range of diagenetic modification, such as weathering and erosion. The reason for these alterations of uplifted rock is that minerals within formed during burial have achieved a chemical stable state-equilibrium at elevated temperature and pressure but are unstable in oxidizing conditions at near surface. During uplift, organic matter and minerals go through oxidization. For example, in Westphalian Carboniferous sediments of the Lake District, removal of organic matter, iron carbonates being oxidized into hematite, oxidization of sulphides to gypsum were attributed to telodiagenesis during exposure in early Permian (Taylor, 1978). Besides oxidization, alterations related to freshwater flushing, such as kaolinization of feldspar, are common during telodiagenesis. The replacement of detrital feldspar by pore-filling kaolinite in the Middle Jurassic Brent sandstones of the northern North Sea was ascribed to the exposure to acidic freshwater during uplift in the Late Jurassic to Early Cretaceous (Burley et al., 1985).

Mechanisms of diagenesis

The overall consequence of diagenesis is that the unstable sedimentary mineral assemblage evolves towards a more stable (chemically and physically) mineral assemblage in

pore waters under increasing changes of temperature and pressure. Therefore, the changes of pore-fluid chemistry, temperature and pressure are the fundamental driving mechanisms for diagenetic reactions. Diagenetically active species, such as CO_2 and organic acids, which could influence the pH and Eh of formation water, also play key roles in diagenetic pathways of reservoir rocks. The following section will discuss the interactions of organic and inorganic reactions that could account for diagenetic alterations of reservoir rocks.

1.1.4. Organic-inorganic interactions

Organic-inorganic interactions, which refer to the reactions that organic alteration products participate in alteration processes in sandstone reservoirs, have been studied in sedimentary basin for many years (Schmidt and McDonald, 1979; Surdam et al., 1985; 1989; Ehrenberg and Jakobsen, 2001; Seewald, 2003; Onstott et al., 2012; Furmann et al., 2014; Schulz et al., 2015; Fu et al., 2015). These organic-inorganic interactions create or destroy the porosity and permeability of sandstone reservoirs.

Organic-inorganic interactions relating to processes in source rocks

Previous studies related the alterations in sandstone reservoirs to the organic products, such as CO_2 and organic acids, in source rocks (Schmidt and McDonald, 1979; Surdam et al., 1985; 1989).

Thermal maturation of source rocks

During thermal maturation of source rocks, large amounts of CO_2 can be released in addition to oil and nature gas CH_4 (Killops and Killops, 2005). This source rock originated CO_2 was proposed as the driving force for the formation of secondary porosity resulted from mineral dissolution (Schmidt and McDonald, 1979; Franks and Forester, 1984). However, some doubts were cast on this mechanism as mass balance calculation results indicated that the amount of CO_2 produced from this process are not sufficient to lead to the observed secondary porosity in sandstones (Bjørlykke, 1984, Lundergard et al., 1984, Giles and Marshall, 1986).

An alternative mechanism advocated by Surdam and coworkers (Surdam et al., 1989; Surdam and Crossey, 1985) is that carboxylic acids can be cleaved from kerogen before, during and after liquid hydrocarbon generation and that these organic acids account for the dissolution of aluminosilicate minerals and secondary porosity in sandstones by the means of

transporting aluminium as organic complex. In addition, based on oil-field formation water analyses they proposed an optimum temperature zone of 80-100°C for enhancement of porosity in sandstones, as the concentrations of carboxylic acids peaks over this temperature interval. However, some doubts on this proposed mechanism also have been raised:

(1) Mass-balance calculations indicate that the amount of organic acids generated from maturation of source rocks is insufficient to lead to the observed secondary porosity in sandstones (Giles and Marshall, 1986; Lundegrad et al., 1984).

(2) Transportation of this source rock derived acidic fluid into reservoirs and maintaining its corrosion capacity is problematic. As source rocks and adjacent organic depleted shale frequently contain carbonates and feldspars which could react with acidic fluids, these organic acids generated from source rocks, therefore, could have been neutralized and lost their corrosion potentials with source rocks and/or migration pathways before reaching reservoirs (Bjørlykke, et al., 1989; Bjørlykke, 1984; Lundergard et al., 1984).

(3) Detailed formation water analyses revealed that in most cases organic acids in formation water have very low concentration so that they cannot significantly affect rock-water equilibria (Barth and Bjørlykke, 1993; Lundegard and Kharaka, 1994).

(4) Published experiment data failed to support that organic acids have significant impacts on feldspar dissolution by influencing Al mobility in the form of Al-complexes (Manning et al., 1991; Bevan and Savage, 1989; Stoessell and Pittman, 1990).

Hydrogenation of kerogen

The aforementioned two mechanisms were based on the traditional wisdom that oil and gas generation was a thermal cracking process of kerogen releasing low-molecular hydrocarbons and, therefore, the oxygen incorporating in produced CO_2 exclusively originates from kerogen. However, aqueous-pyrolysis hydrocarbon experiments by Price (1989), Wenger and Price (1991), and Price and Wenger (1992) show that excessive CO_2 can be generated by hydrogenation of kerogen by water. During this process, water reacts with kerogen and the oxygen from water combines to CO_2 (Price and DeWitt, 2001).

Oxidation of organic matter

Besides the thermal maturation-related mechanisms, CO_2, and organic acids can also be generated in source rock by other processes. Organic acids have been advocated to be generated by oxidation of organic matter in source rocks by minerals oxidants and/or Fe^{3+} released from clay minerals transformation (Surdam et al., 1984, 1993).

In summary, CO_2 and organic acids which are generated in source rocks by a range of processes: thermal maturation of source rocks (Schmidt and McDonald, 1979; Franks and Forester, 1984; Surdam et al., 1989; Surdam and Crossey, 1985), hydrogenation of kerogen (Price and DeWitt, 2001), and oxidation of organic matter by mineral oxidants (Surdam et al., 1984; 1993). Due to the transportation problem, the source rock derived acidic fluids are expected to preferentially leach sandstones in the vicinity of source rocks.

Organic-inorganic interactions relating to processes in reservoir rocks

Organic products (CO_2 and organic acids) that take part in the alteration processes in sandstone reservoirs can also be generated in reservoir rocks via various alteration processes of organic matter (oil).

Oil degradation

In oil reservoirs, the oil-water contact, actually an oil-water transition zone, expands from the bottom of the overlying oil leg to the underlying water leg. In addition to these "macro" OWC or OWTZ, "micro" OWCs develop at water-coated mineral surfaces (irreducible, immobile water) within the oilfield parts of water-wet reservoirs. In subsurface reservoirs, the OWC or OWTZ is a hot spot where oil degradation takes place (Fig. 1.2). Many microbiological reactions could occur at this site in which organic matter (hydrocarbon) is consumed on one hand and carbon dioxide, methane, etc. are produced on the other hand (Fig. 1.3). These products could participate in the formation of multiple mineral reactions leading to the precipitation of calcite and pyrite (Fig. 1.3, Wolicka and Borlowski, 2012).

Hydrolytic disproportionation of hydrocarbons

In petroleum reservoirs water and reservoir oil at the oil-water contacts are thought to maintain a metastable equilibrium (Helgeson et al., 1993). The process was termed "hydrolytic disproportionation of organic matter" (HDOM) in which irreversible reactions of hydrocarbons with water at the oil-water interface form lighter paraffins and $CO_{2(aq)}$, $CH_3COOH_{(aq)}$, and other oxidized carbon-bearing aqueous species (Helgeson et al., 1993).

These reactions are strongly favored by their chemical affinities and are regarded as characteristic processes at oil-water contacts in petroleum reservoirs (Helgeson et al., 1993). Irreversibly produced carbonic acid during HDOM at the oil-water interface may be a driving mechanism for much of the diagenetic processes in basins by lowering the pH of oil field waters (Helgeson et al., 1993).

Similarly, Seewald (2003) also put forward "hydrolytic disproportionation of hydrocarbons" which involves the reaction of hydrocarbons with water to produce shorter chain carbon compounds at elevated temperature and pressure. The process can be represented by the reaction:

$$C_{20}H_{42} + 2H_2O = C_{16}H_{34} + 2CH_4 + CH_3COOH$$

Considering acetic acid is decomposed by decarboxylation, the above process can be written as:

$$C_{20}H_{42} + 4H_2O = C_{16}H_{34} + 2CH_4 + 2CO_2 + 4H_2$$

The net effect of these types of reactions is the conversion of long-chain alkanes in oils to short-chain hydrocarbons in gas (Seewald, 2003).

Redox reactions of hydrocarbons and minerals oxidants

Bleaching of red sandstones by hydrocarbon invasion is a common geological phenomenon worldwide, for example in the Sespe Formation of California, in the Rotliegendes sandstone of the North Sea, and in the Layons sandstones of Colorado (Surdam et al., 1993). In these red sandstones, the bleaching zone is more porous compared to the tight red unbleached zone. The bleaching of red sandstones is due to the redox reaction of hydrocarbons and red hematite leading to ferrous iron without red colour. Moreover, organic acids can also be generated in this process, which can dissolve carbonate cement leading to secondary porosity enhancement. This type of redox reaction is favoured to occur in red sandstones but also can take place in other reservoir lithologies which contain oxidants (hematite, sulfates, amorphous iron oxides, Fe^{3+}-bearing clay, etc.). Thermodynamically, redox reactions are regarded to predominate in the 80-100°C thermal window (Surdam et al., 1993).

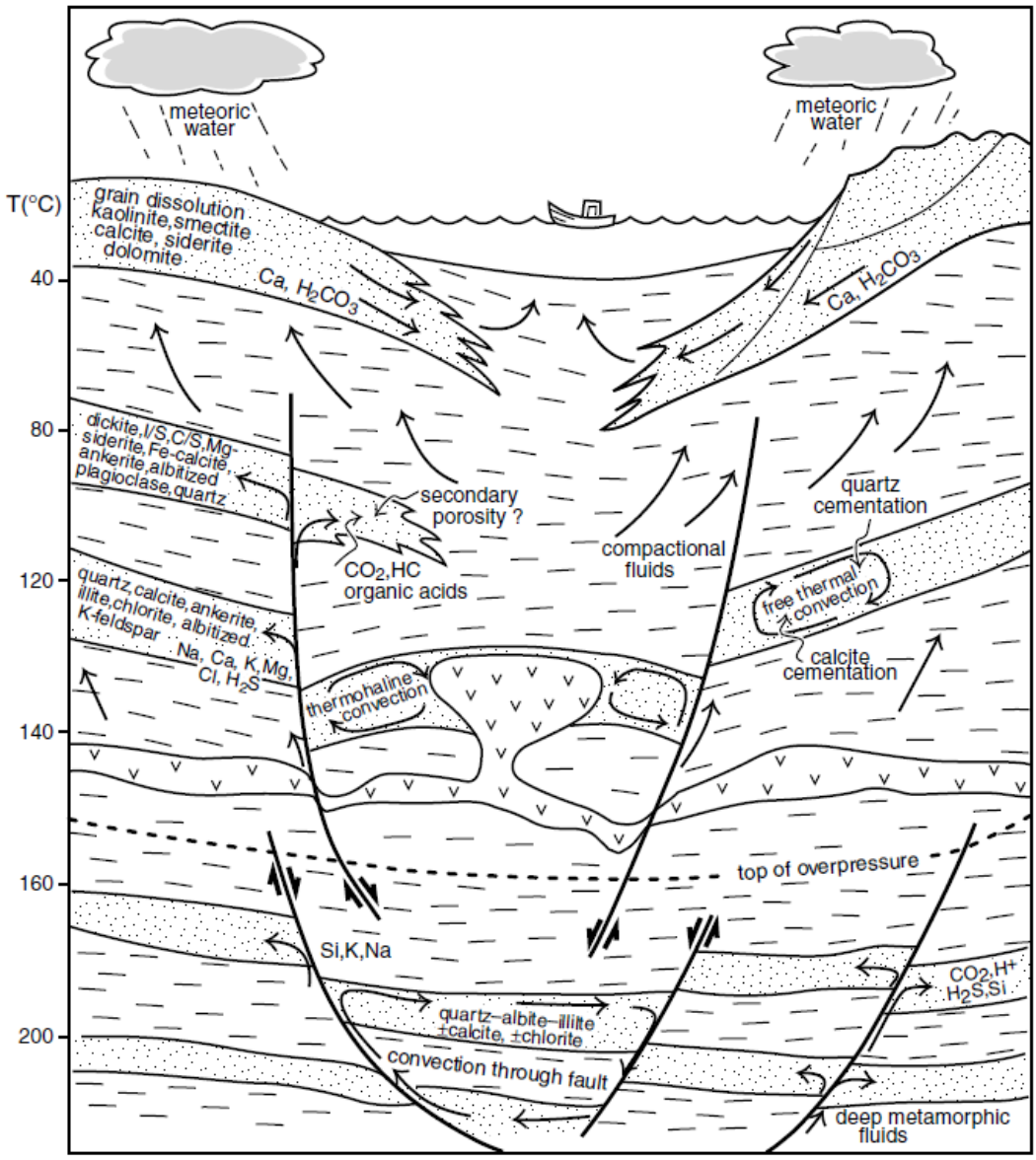

Figure 1.4 Diagenetic alterations and patterns of fluid flow in a hypothetical basin (Morad et al., 2000).

1.1.5. Water-rock interactions

Formation waters are the media for transporting ions needed for mineral dissolution/ precipitation. In reservoirs, due to low porosities, formation water only represents a small volume of rocks, which suggests that formation water cannot lead to significant amount of mineral dissolution and/or precipitation unless other sourced fluids, such as meteoric water, are involved.

Meteoric water

Meteoric water, the precipitation (snow/rain) derived water, is one of the most important fluids in sedimentary basins, which can influence mineral alterations in both sandstone and carbonate reservoirs at shallow burial depths or during uplifting. It is commonly oxidizing, has low pH and is undersaturated with feldspar and carbonate. Therefore, by contacting with meteoric water, not only the minerals but also the organic matter within the reservoirs can be altered. For example, oil biodegradation, which is prevalent in shallow depths, was previously thought to be subjected to aerobic degradation processes related to meteoric water intrusions as meteoric water transporting the oxygen and bacteria required for aerobic degradation of oil (Connan, 1984; Palmer, 1993).

In addition, meteoric water is also often regarded as a driving mechanism for feldspar dissolution and accompanying kaolinite formation in sandstones (Longstaffe, 1993; Bjørlykke and Aagaard, 1992; Morad et al., 2000). For example, unlike the previous hypotheses that the observed secondary porosities at great depths resulting from dissolution of feldspar were attributed to acids derived from source rock (Schmidt and McDonald, 1979; Franks and Forester, 1984; Surdam et al., 1989; Surdam and Crossey, 1985), Bjørlykke et al. (1989) suggested that the secondary porosity could have been formed at relatively shallow depths due to meteoric water flushing and then have been buried and preserved to current depths. Furthermore, Giles and Marshall (1986), based on mass-balances, also proposed that meteoric water could serve as an additional cause for these observed secondary porosities due to feldspar dissolution besides source rock generated acids.

The occurrence of meteoric water flushing is thought to prevail in shallow deposits, such as in fluvial systems, beach sands, and shoreline deposits. The intrusion of meteoric water into deep marine turbidites was thought to be less likely due to turbidite deposits often being located far away from the shoreline (Bjørlykke and Aagaard, 1992). However, meteoric water has been reported to penetrate into a considerable depth in sedimentary basins. For example, in the Great Artesian Basin of Australia where meteoric water was reported to penetrate a depth of 2000 m (Habermehl, 1980). Similarly, it can also migrate a considerable distance into the shelf, for example, freshwater aquifers were reported to discharge on the seafloor as far as 120 km off the coast of Florida (Manheim, 1967). Furthermore, an increasing number of reports based on oil field studies also indicate that meteoric water can influence turbidites deposits. The deep-sea turbidite sandstones of Shetland-Faroes Basin, UK (Mansurbeg et al., 2006; 2008) and the turbidite reservoirs of Campos Basin, Brazil

(Prochnow et al., 2006; Carvalho et al., 1995) can be taken as examples. The flushing of meteoric water into deep-water sandstones is usually linked to a major sea-level fall and/or tectonic uplifts (Bjørlykke and Jahren, 2010; Morad et al., 2000; Worden and Morad, 2003).

Compaction water and deep basin brine

Besides meteoric water, mass transfer between mudstones and sandstones, which refers to transportation of ions such as K^+, Ca^{2+}, Fe^{2+}, Mg^{2+}, was thought to account for diagenetic phases in sandstones (Burley et al., 1985; Curtis, 1978). However, Bjørlykke and Jahren (2012) questioned that such mass transport between shales and sandstones is limited due to the low concentration gradients existing between shales and sandstones as the pore water is buffered by the same minerals as in shale.

Deep basin brine is another type of fluid in sedimentary basin which can affect minerals alteration. Migration of deep brines into sandstone reservoirs can cause mineral alterations. For example, dissolution of pore-filling and detrital carbonate in the Middle Miocene sandstone reservoirs of the Pircaroon field, offshore Texas was observed and attributed to the highly saline Na-Ca-Cl formation water within (Taylor and Land, 1996). Based on the similarities of this formation water with deep brines in terms of major element and isotope composition, it was suggested that the highly saline formation water in the Middle Miocene sandstone reservoirs of the Pircaroon field was derived from deep brines which could migrate via faults (Taylor and Land, 1996).

1.2. Objectives

Mineral alterations (dissolution and precipitation) in sandstone reservoir rocks can be caused by various mechanisms as mentioned above. Besides “classical” diagenetic models, organic-inorganic interactions driven by maturation and alteration processes of organic matter (such as kerogen, oil) play a significant role in the diagenetic history of sedimentary basins. Feldspar dissolution resulting in abnormally enlarged secondary porosity in sandstones was previously attributed to organic compounds, CO_2, and organic acids, produced by source rock maturation (Schmidt and McDonald, 1979; Franks and Forester, 1984; Surdam et al., 1989; Surdam and Crossey, 1985). However, there are some debates on the efficiency of these source rock generated products due to transportation efficiencies (Bjørlykke et al., 1989; Bjørlykke, 1984; Lundergard et al., 1984; Giles and Marshall, 1986).

Oil biodegradation in situ has recently been proposed to trigger organic-inorganic interactions which influence mineral alterations within reservoirs (Watson et al., 1995; Ehrenberg and Jakobsen, 2001; Prochnow et al., 2006; Wolicka and Borlowski, 2012). A threshold of around 80°C is suggested for such "degradation" processes (Wilhelms et al., 2001). However, hydrolytic disproportionation can lead to further degradation of petroleum compounds also at higher temperature conditions (Helgeson et al., 1993; Seewald, 2003). The conversion process of petroleum compounds takes place at oil-water contacts which mainly occur at the bottom of the oil leg but also in the oil filling zone of water-wet reservoirs. This is because in the oil filling zone of water-wet reservoirs "micro OWCs" can be formed as irreducible water films are maintained on the surface of mineral grains. These in situ conversion processes may not only alter the original composition of petroleum fluids trapped in petroleum reservoirs, but also consequently modify the aqueous phase and the mineral matrix.

In addition to organic-inorganic interactions, meteoric water, one of the most common basin fluids, also plays an important role not only in oil degradation (Connan, 1984; Palmer, 1993), but also in mineral alterations (Mansurbeg et al., 2006; 2008; Prochnow et al., 2006; Carvalho et al., 1995). Moreover, production of organic compounds during oil degradation induced by meteoric water flushing could further facilitate alteration of minerals via organic-inorganic interactions.

However, some research gaps still exist. For example, the parameters that control the likelihood and extent of meteoric water intrusion into deep marine turbidite reservoirs are still poorly understood. Moreover, the significance of organic-inorganic interactions is underestimated. Furthermore, quantitative approaches about the overall consequences of complex organic-inorganic interactions are still rare.

The aims of this thesis are (1) to investigate inorganic-organic interactions in sandstone reservoirs varying at burial depths and lithologies, (2) to evaluate their consequences on reservoir alterations, and (3) to reveal the controls influencing meteoric water flushing and their consequences. A quantitative evaluation of the effect of organic-inorganic interactions on mineral alteration by means of hydrogeochemical modelling is also a part of the work presented in this thesis. Reproduction of diagenetic features is performed to figure out the geochemical conditions for observed mineral dissolution/formation based on diagenetic

studies: (1) what kind of alterations took place in the studied sandstones, (2) when did these alterations take place, and (3) where do they prevail.

Conducting this study has far-reaching implications for successful reservoir prediction and engineering. Formation of pore-filling minerals, such as kaolinite and calcite, could significantly deteriorate reservoir quality by both reducing porosity and permeability of rocks and oil recovery. In contrast, dissolution of feldspar and carbonate producing secondary porosity could greatly improve reservoir quality and thus enhance oil production. Understanding “when”, “where” and “how” of such processes by using hydrogeochemical modelling could, therefore, provide valuable information for an improved reservoir engineering.

1.3. Structure of the dissertation

In this first chapter, an introduction to this study, research problems and main objectives of this dissertation are described. Additionally, an outline of the structure of this dissertation is given.

Chapter 2 describes the geology of the North Sea and the geological settings of the study areas. In addition, the investigated samples and applied methods are also described in detail in the second chapter. For this thesis, samples from four oil fields of the North Sea Basin were investigated: Siri field, Magnus field, Frigg field, and Grane field. The applied organic geochemical methods include gas chromatography-flame ionization detector, gas chromatography- mass spectrometry and Fourier transform ion cyclotron resonance mass spectrometry. The methods for inorganic assessment comprise light microscopy, scanning electron microscopy, focused ion beam-transmission electron microscopy, X-ray powder diffraction, and X-ray powder fluorescence.

In Chapter 3, an investigation of the Palaeocene Heimdal glauconite-bearing sandstone reservoir (2,096-2,137 m) of the Siri field (Danish North Sea) is presented as a case study of organic-inorganic interactions in a shallow sandstone reservoir. 42 core samples of Well Siri-2 have been used for investigation. In the Heimdal sandstone, berthierine, as the dominant diagenetic phase besides carbonate comment, is mainly in the forms of pore-filling and grain-coating. Its formation postdates oil filling and is related to glauconite dissolution. Berthierine is most intensive at OWC where oil shows the strongest degradation. Based on these results, a

concept is established, which is that the oil degradation occurring at the OWC and "micro OWC" in the oil-filled reservoir triggered glauconite dissolution and associated feldspar dissolution leading to berthierine formation. The content of Chapter 3 has been published in Marine and Petroleum Geology (Mu et al., 2015).

Chapter 4 represents a study of organic-inorganic interactions in a deep sandstone reservoir: the Jurassic Magnus sandstones of the Magnus field. Unlike the Siri case, the Magnus sandstones are buried at present at a depth of 3,200-3,240 m and have a reservoir temperature of 116°C. The Magnus sandstones have been extensively altered by multiple diagenetic processes: quartz overgrowth, feldspar dissolution, carbonate cementation, etc. Among them, authigenic albite is one of the most common diagenetic phases, which has been paid less attention to. Authigenic albite which formed after oil generation and charge could result from the dissolution of K-feldspar. Organic-inorganic interactions related to oil generation, migration and degradation processes could serve the main driving force for the formation of authigenic albite and associated siderite. Hydrogeochemical modellings were conducted to test this hypothesis. The material of Chapter 4 has been published in Sedimentary Geology (Mu et al., 2016).

As mentioned in section 1.1.5, besides organic-inorganic interactions, water-rock interaction is also a driving force for mineral alterations in reservoirs. Chapter 5 presents a study of the impact of meteoric water influx and associated oil degradation on sandstone reservoir alterations by comparing the Frigg field with the Grane field. This chapter has submitted to Sedimentary Geology for reviewing.

In Chapter 6, the results of the preceding chapters of the thesis are summarized and a research outlook for future work is discussed.

Chapter 2 Geological setting, data, and methodology

2.1. Geological setting of study areas

The North Sea Basin, a prolific hydrocarbon province in west Europe, has been intensively studied for more than 50 years. As such, a good understanding of the geology of this basin has been established. Accordingly, various types of data including drilling cores from reservoirs of various lithologies and depositional settings are accessible. The North Sea Basin is thus an ideal site to study the diagenetic evolution of sandstones and has been chosen for investigation of organic-inorganic interactions in siliciclastic reservoirs.

Samples for this study were collected from four oil fields located in three different regions of the North Sea Basin (Fig. 2.1): (1) the Siri field in the Danish North Sea; (2) the Magnus field in the East Shetland Basin; and (3) the Frigg and Grane Fields in the Central Viking Graben. A synthesis of the geological setting of the North Sea and details about the study areas are outlined below.

2.1.1. The North Sea basin

The North Sea basin is located between Norway and Denmark to the east, Scotland and England towards the west, and it lies between Germany and Netherlands in the South (Fig. 2.1). It covers an area of ca. 625,000 km^2.

Geological setting of the North Sea basin

The North Sea basin is a rift basin which is flanked to the northeast by the Precambrian Fennoscandian shield, to the east by the Russian Platform, to the south by the late Palaeozoic Variscan massifs and to the west by the Caledonides of Scotland. The North Sea basin comprises two grabens: the Viking Graben and the Central Graben. In the central and southern North Sea, the Central Graben is the main structure with an NW-SE orientation, extending from the north of the Dutch coast to the east region of Scotland. In the northern North Sea, the Viking Graben is the dominant structure, which extends about 500 km from the triple junction with the Central Graben and Moray Firth Basin in the south to the Sogn

Graben in the north. This NE-SW trending structure consists of three main individual segments known as the North, Central and South Viking Graben (Fig. 2.1).

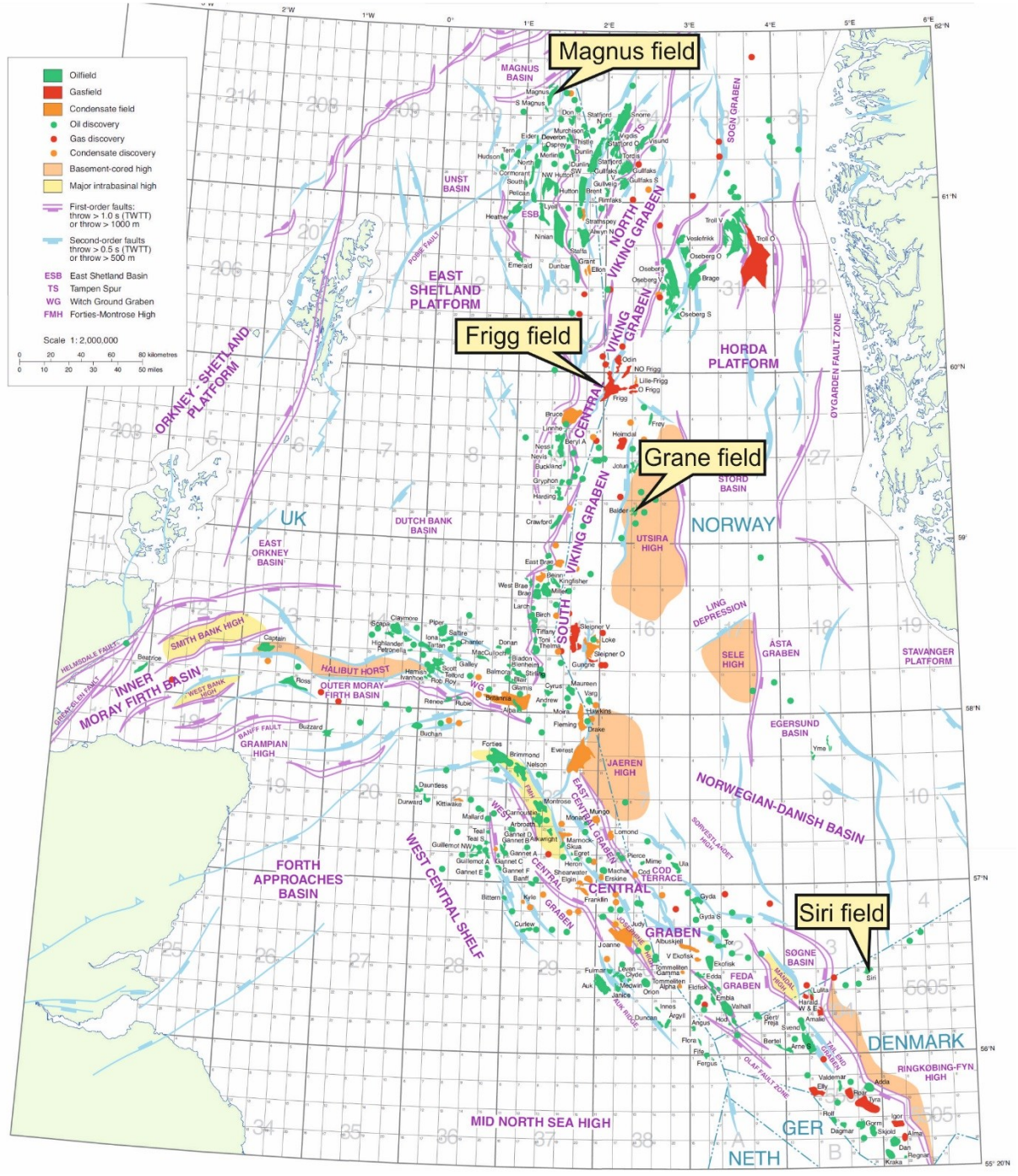

Figure 2.1 Map showing the structural elements of the North Sea basin and study areas (adapted from Brzozowska et al., 2003).

Tectonic evolution of the North Sea basin

The North Sea Basin is filled with up to 9,000 m thick sediments ranging in age from late Palaeozoic to Quaternary (Fig. 2.2). It has undergone a long and complex tectonic history (Glennie and Underhill, 1998). The main tectonic events that controlled the structural development of the North Sea Basin compromise two main phases: (1) the pre-Mesozoic original tectonic organization, and (2) the Mesozoic-Cenozoic tectonic reworking (Glennie and Underhill, 1998).

Pre-Mesozoic tectonic events

The original structural framework of the North Sea developed in two tectonic episodes: The Caledonian and Variscan orogeny (Coward et al., 2003).

(1) The Caledonian plate cycle (late Cambrian-late Silurian). Metamorphic and intrusive rocks of the Caledonian orogeny formed the floor or basement for much of the North Sea area (Ziegler, 1975; Ziegler and Haag, 1977). Prior to these events, the North Sea area comprises separated continental fragments (Glennie and Underhill, 1998).

(2) The Variscan plate cycle (Devonian-late Carboniferous). From the Devonian to Carboniferous, the North Sea area went through rifting followed by the late Carboniferous Variscan orogeny (Glennie and Underhill, 1998). During this stage, a thick essentially clastic wedge was deposited in the southern North Sea from the south over the eroded Caledonides and reached northwards into the central North Sea. Thick Carboniferous peat (today coal seams) deposited in the southern and west-central North Sea during the late Carboniferous (Ziegler and Haag, 1977).

Mesozoic-Cenozoic tectonic events

From the Permian to present day the North Sea has been largely in an intraplate setting (Glennie and Underhill, 1998). The original structural framework of the North Sea formed in pre-Mesozoic was modified by the Mesozoic-Cenozoic tectonic events.

(1) The Permian-Triassic rifting and thermal subsidence. During the Permian-Triassic, extensional stresses related to the rifting of the northern North Atlantic predominated in the North Sea leading to the subsidence of Northern and Southern Permian basins and formed half graben structures (Glennie and Underhill, 1998). During this stage, sedimentary deposition started with the middle Permian Rotliegend red sandstones followed by up to 1,000 m thick Zechstein evaporites and a continental deposition sourced from the highlands.

(2) Middle Jurassic domal uplift. The development of the Mid-Jurassic mantle-plume led to widespread erosion of the central North Sea (Glennie and Underhill, 1998). Sediments derived from the eroded area formed the Brent Group reservoirs in the northern North Sea.

(3) Late Jurassic to earliest Cretaceous rifting. During this stage, the North Sea was subjected to extensional stress due to the continuous widening of the Arctic North Atlantic. As a result, a triple junction of three joined grabens (Moray Firth Basin in the west, the Viking Graben in the north and Central Graben in the south) were formed (Coeward et al., 2003). Sediments deposited during this rifting stage form the main source rocks (Kimmeridgian shale) and excellent reservoirs (the Rhaetic to Lower Statfjord sandstones and the Dogger Brent sandstone) in the North Sea basin (Ziegler, 1975; Ziegler and Haag, 1977).

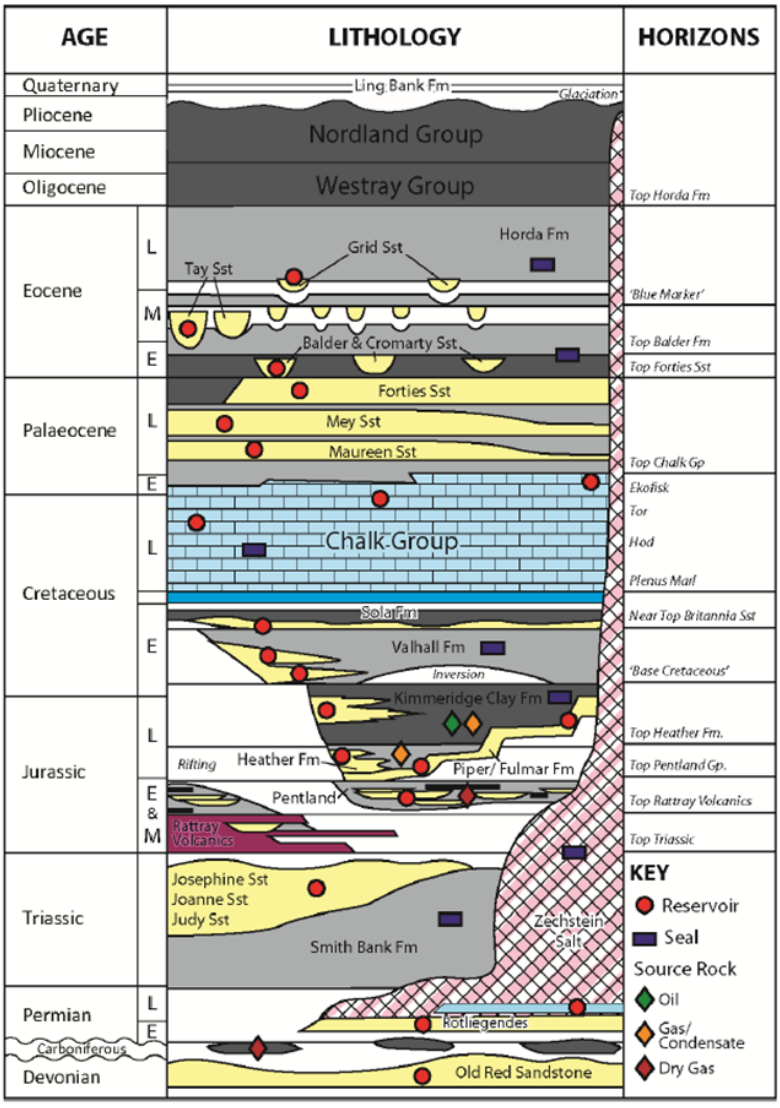

Figure 2.2 Generalized stratigraphic column of the Central North Sea indicating basin development, main source rocks, reservoirs and seals (adapted from Robertson, 2013).

(4) Late Cretaceous to Cenozoic post-rifting. The rifting stage in the North Sea basin ceased and was followed by a thermal subsidence of graben systems and an uplifting and erosion of the rift flanks due to the creation of the Atlantic Ocean (Glennie and Underhill, 1998). Sedimentary depositions are characterized by up to 1,200 m thick Cretaceous chalk and a thick unit of siliciclastic sediments. The siliciclastic sediments were shed from the Orkney-Shetland Platform to the west (Johnson et al., 1993), forming a series of submarine fan sandstones which are the major hydrocarbon reservoirs in the Central and Viking Graben (Ziegler, 1975; Ziegler and Haag, 1977).

2.1.2. The Siri field, Siri Canyon

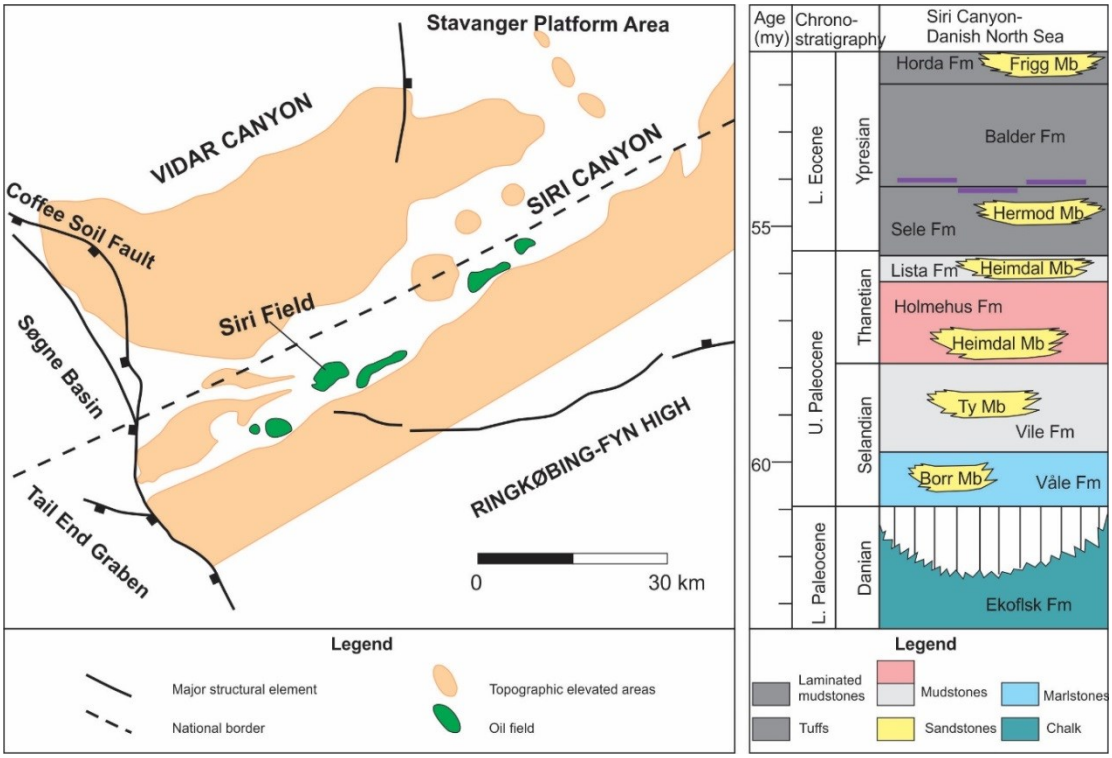

Figure 2.3 Location of the Siri field and structural elements of Siri Canyon-Danish North Sea basin (left) and stratigraphic column of Siri Canyon-Danish North Sea (right) (modified after Hamberg et al., 2005).

The Siri field is located in the Norwegian-Danish Basin at the Danish–Norwegian North Sea border. It sits at the Siri Canyon which is a large Palaeogene submarine canyon extending in NE-SW direction from the Stavanger Platform to the Søgne Basin and Tail End Graben (Fig. 2.3; Ahmadi et al., 2003, Hamberg et al., 2005). The Siri Canyon formed in the Early Palaeocene when a major submarine erosion of the uppermost Ekofisk chalk deposits occurred due to tectonic instability and uplift of the Scandinavian hinterlands (Hamberg et al.,

2005). The margin of the Siri canyon is controlled by salt structure growth (Hamberg et al., 2005).

The lithostratigraphy of the Siri Canyon is shown in Figure 2.3. The canyon fill consists of hemipelagic marlstones and mudstones interbedded with sandstones deposited from sandy mass-flows and sandy turbidites (Hamberg et al., 2005). These sandy turbidites are well-sorted, fine-grained glauconitic sandstones and are presumed to originate from the Stavanger Platform (Ahmadi et al., 2003; Hamberg et al., 2005).

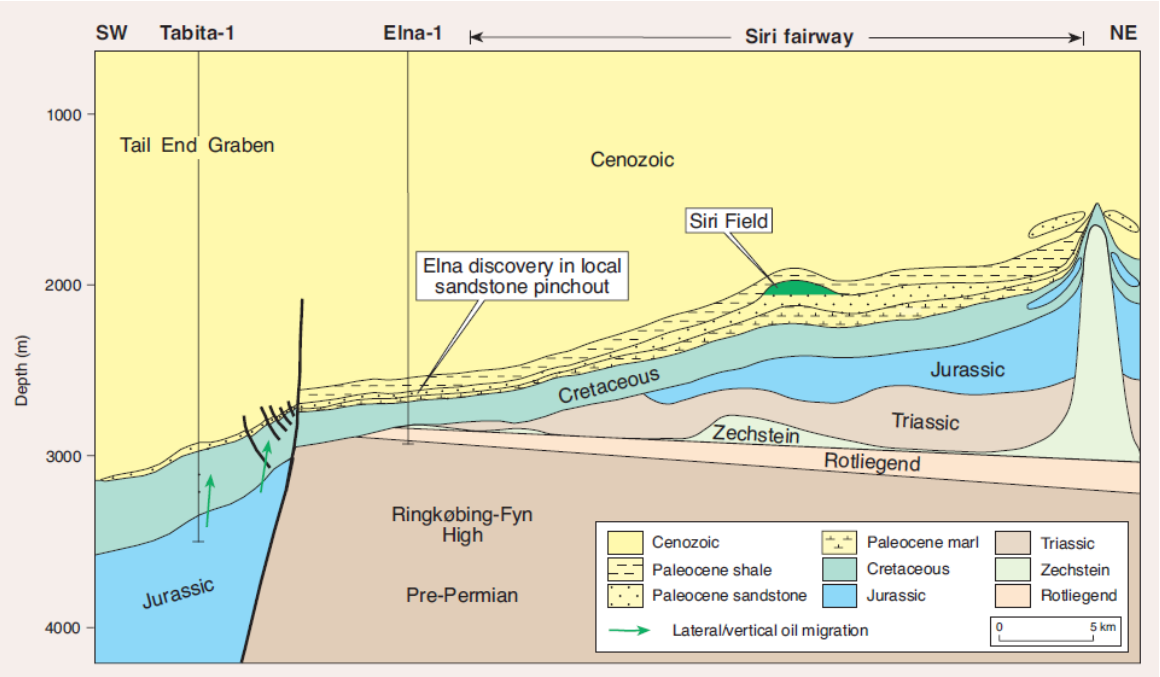

Figure 2.4 SW-NW cross section of the Siri Canyon-Danish North Sea showing the migration pathway of oil generated in Jurassic source rock of the Tail End Graben to the Palaeocene reservoirs of Siri field (adapted from Ahmadi et al., 2003).

The Siri field is a significant hydrocarbon discovery in the Danish sector. It covers an area of 15 km^2 and contains a 25 m hydrocarbon accumulation. This field is a structural/stratigraphic trap that is established by differential compaction of the sand-rich Heimdal sandstone member and laterally equivalent shales (Ahmadi et al., 2003). The Heimdal sandstone Member, which comprises the main reservoir of the Siri field, is made of very fine- to fine-grained sandstone with grains dominated by quartz and a relatively high percentage of glauconite (15-25%). Pyrite and mica account are few. It was deposited from high-concentrate gravity flows with sediments sourced from the Norwegian Shield. The

Heimdal reservoir has an average porosity of 31% and a permeability range of 15 to 250 mD (Ahmadi et al., 2003). The oil extracts of the Siri-2 have an API gravity of 42° (Ohm et al., 2006). The source rocks for the hydrocarbons of the Siri field are the mature Upper Jurassic Mandal Formation shales in the Søgne Basin and the Tail End Graben (Fig. 2.4; Ahmadi et al., 2003). The expulsion of hydrocarbons from the source rocks in the Tail End Graben took place during Later Palaeogene to Early Neogene (Hamberg et al., 2005). The generated hydrocarbons probably migrated vertically along the boundary fault of the Ringkøbing-Fyn High into the Palaeocene section, and then migrated laterally about 25-30 km within the Palaeocene into the Siri structure (Fig. 2.4; Ahmadi et al., 2003).

2.1.3. The Magnus field, East Shetland Basin

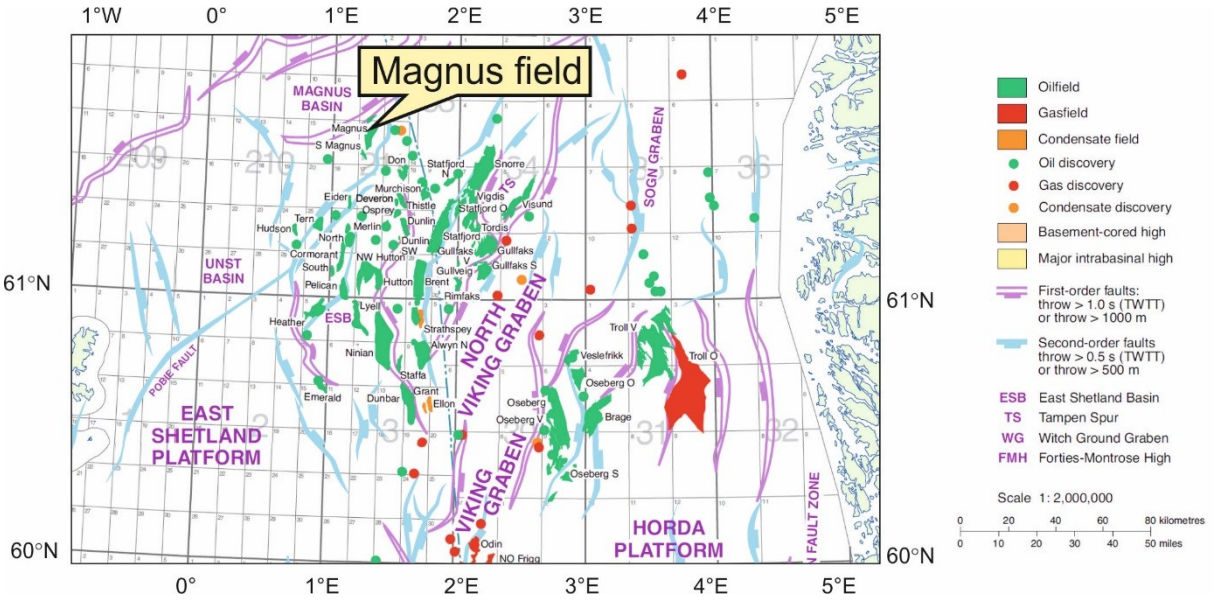

Figure 2.5 Structural elements of the Northern North Sea and the location of the Magnus field (adapted from Brzozowska et al., 2003).

The Magnus field is situated on the northern margin of the East Shetland Basin (ESB) (Fig. 2.5). The ESB is a rhombic-shaped intermediate terrace region between the East Shetland Platform and the deep North Viking Graben. It is characterized by tilted fault blocks.

The Magnus field, as a northmost field in the North Sea, covers an area of 33 km^2. It sits on a south-eastward dipping, tilted fault block. This field is a mixed stratigraphic pinch out/ truncation unconformity trap. The areal extent of the field is defined to the east by the oil-water contact (3,150 m subsea), to the west, north and south by a depositional pinch-out, and

by a sub-Cretaceous unconformity in the crest region (Macaulay et al., 1992). The Magnus Sandstone Member is the main reservoir of the Magnus field, which comprises up 180 m of good-quality reservoir (Fig. 1B). The reservoir is currently buried at approximately 3,000 m with a reservoir temperature at around 116° C.

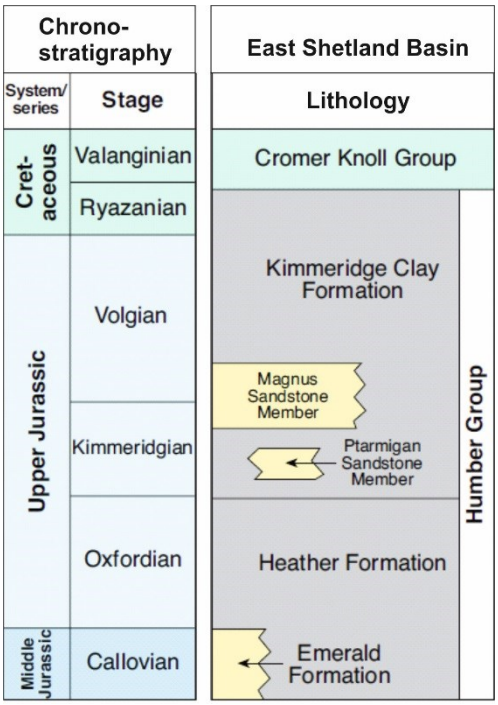

Figure 2.6 Stratigraphic column of the East Shetland Basin indicating the Magnus Sandstones Member (adapted from Brzozowska et al., 2003).

The Magnus Sandstone, intercalated with the carbonaceous Kimmeridge Clay Formation, was deposited as a deep-water, submarine-fan system during late Jurassic (Fig. 2.6; De'Ath and Schuyleman, 1981; Shepherd, 1991). Following the deposition of the Magnus sandstone and Upper Kimmeridge Clay Formation, a depositional hiatus occurred during the early Cretaceous (late Cimmerian). During this period, the Jurassic deposition (Magnus field and Upper Kimmeridge) was faulted, uplifted, and exposed to erosion. The overlying Cretaceous deposition was punctuated by a second break during the mid-Cretaceous (Cenomanian-Turonian) with erosion removing the Lower Cretaceous and Jurassic sediments locally from the northern area of the field. Rapid subsidence and deposition occurred during the Tertiary and Quaternary, with the tilting of the reservoir towards the northeast during the early Tertiary (De'Ath and Schuyleman, 1981).

The crude oil in the Magnus Field is a light, low sulphur (0.28%), and medium wax (4-6% by weight) oil with an API gravity of 39° (Shepherd, 1991). The oil in the Magnus field was sourced from both the overlying and underlying Kimmeridge Clay Formation (De'Ath and Schuyleman, 1981; Barclay and Worden, 1998). The main kitchen area lies to the east of the field although some oil was probably also sourced from the north (Shepherd, 1991). Oil generation is thought to have commenced approximately 75 Ma BP (Maastrichtian-Campanian) (Shepherd, 1991), and migration probably took place during the early Tertiary (De'Ath and Schuyleman, 1981). Formation waters in the Magnus field are very fresh with salinities averaging about 20,000 ppm total dissolved solids (Shepherd, 1991).

2.1.4. The Frigg and Grane fields, Central Viking Graben

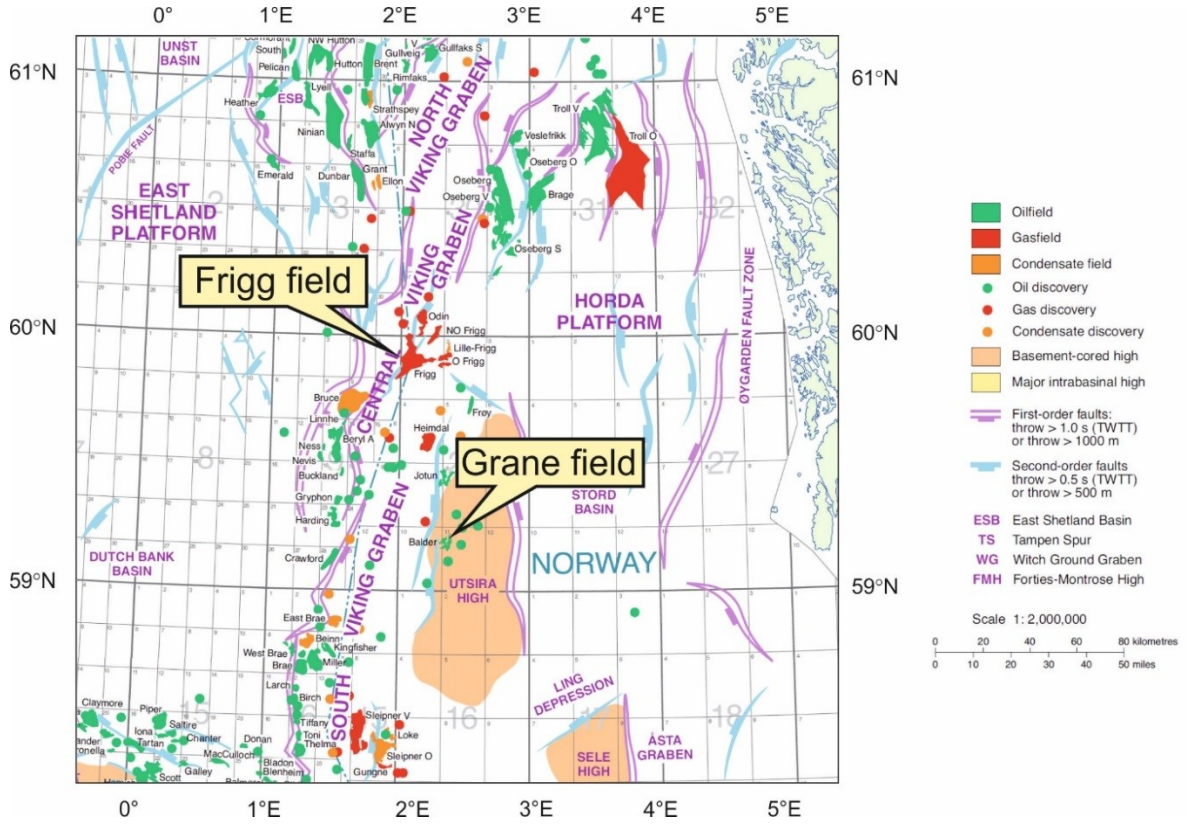

Figure 2.7 Structural elements of the Central North Sea and the locations of the Frigg field and Grane field (adapted from Brzozowska et al., 2003).

The Frigg and Grane fields are located in the northern North Sea along the Norwegian and United Kingdom border (Fig. 2.7). They are situated at the South-Central Viking Graben systems which are parts of the Viking Graben-the major tectonic structures in the northern North Sea (Fig. 2.7). The grabens are offsets along strike by transfer zones and are deformed

by normal faults which have been active during the latest Jurassic to earliest Cretaceous extension.

The western side of the Viking Graben is bound by the East Shetland Platform, while the Horda Platform and Utsira High constitute the eastern boundary of the Viking Graben. The western margin of the South Viking Graben is marked by a major east dipping set of faults whereas the eastern margin of the South Viking Graben is defined by smaller, west dipping faults (Corver et al., 2011).

The large gas field-Frigg field situates at the Norwegian-UK border in the northern North Sea (Fig. 2.7). The Frigg field consists of a thick gas pool (up to 163 m) and an underlying oil disc (up to 10 m thick) (Brewster, 1991). The oil disc shows features of biodegradation with the absence of normal alkanes and has a gravity of 23-24° API (tested in well 25/1-3) (Brewster, 1991; Heritier et al., 1980). The main reservoir is the Lower Eocene Frigg sandstones which were deposited as a submarine fan complex in the South Viking Graben during the early Eocene (Heritier et al., 1980). The Frigg sediments were sourced from canyons that cut into the East Shetland Platform (Heritier et al., 1980). The reservoir has a high porosity of 27-32% and a permeability of 900-4,000 mD (Brewster, 1991). It is sealed by overlying Middle Eocene marine shales. The oil of the Frigg field is thought to be derived from locally deeply buried Lower and Middle Jurassic source rocks (Brewster, 1991; Heritier et al., 1980). Oil generation from the Jurassic source rocks of drainage area began during the later Cretaceous and peaked during the Palaeocene (Goff, 1983). The gas in the Frigg field is dry and has a thermogenic origin indicated by the $\delta^{13}C$ value of CH_4 (-43.3‰; Heritier et al., 1980). It shares the same source rocks with the Frigg oil but was generated during the late burial phase (Brewster, 1991; Heritier et al., 1980). Migration of gas into the Frigg reservoirs probably took place during the Oligocene and Miocene via “gas chimneys” in fractured shales (Brewster, 1991).

The Grane oil field is located in the Norwegian North Sea, sitting on the western flank of the Utsira High (Fig. 2.7). It contains degraded (19°API), highly viscous oil with no initial gas cap. The main reservoir is the Palaeocene Heimdal Formation which is made up of homogeneous unconsolidated marine turbidite sandstones sourced from the East Shetland Platform (Ross et al., 2010). It forms the distal, east toe of the large Heimdal/Andrew deep-water system (Jones and Milton 1994; Martinsen et al., 2005). The reservoir with a high porosity of 31.5-37% and a permeability of 1,510-12,640 mD has been affected

insignificantly by diagenetic processes (Ross et al., 2010). The source rock is the Upper Jurassic Draupne Formation in the South Viking Graben (Justwan et al., 2006a). Hydrocarbon generation from the source rocks in the Viking Graben is thought to proceed from the Cretaceous until today (Isaksen and Ledje, 2001) or from the early Palaeocene to the present (Justwan et al., 2006b).

2.2. Data

There are three sample sets used in this thesis and they were collected during three sampling trips from three different study areas including the Norwegian-Danish Basin, the East Shetland Basin and the Central Viking Graben (Table 2.1).

2.1.1. Sample set 1 from the Siri field

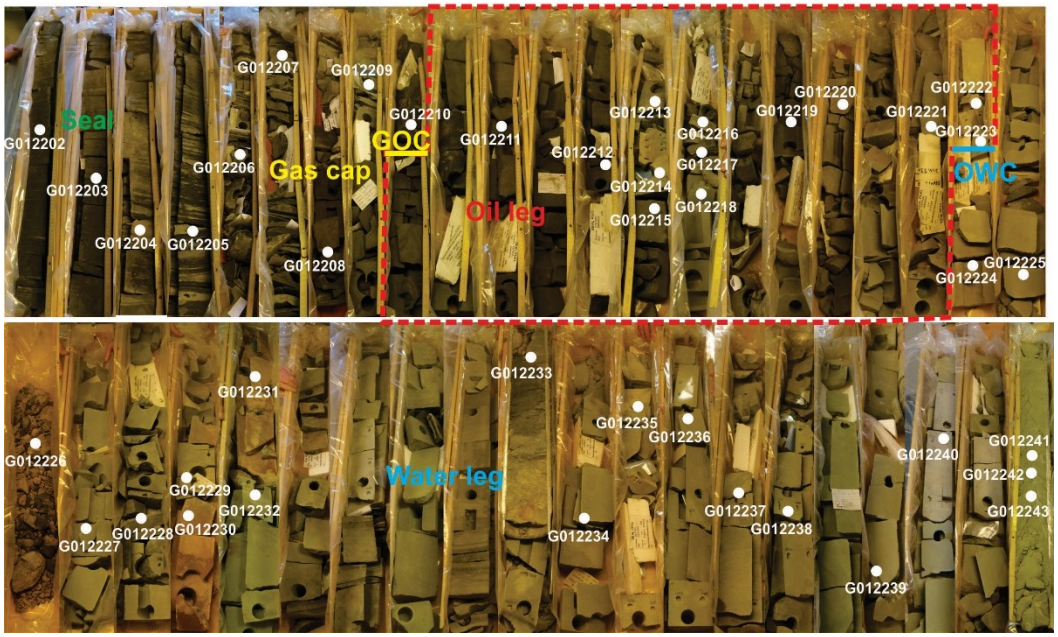

Figure 2.8 Core photos of Well Siri-2 and locations of collected samples.

Forty-two core samples from the well Siri-2 in the Siri field, offshore Denmark were collected from the core repository of Dong Energy. The sample list is present in Table A1 in the Appendix. All samples are from the Palaeocene Heimdal Member sandstones which are glauconite-bearing sandstones (Fig. 2.8). The OWC in the Siri-2 is identified at 2,116.9 m in core by considering the color of cores: the oil legs are dark brown while the water legs are white grey, green-grey.

Table 2.1 Details concerning the three sample sets used in this study.

		Sample sets		
		1	**2**	**3**
Sampling trip	Date	October 2012	March 2013	February 2014
	Institute	Dong Energy	British Geological Survey	Norwegian Petroleum Directorate
	Sample location	Offshore Denmark	Offshore UK	Offshore Norway
	Collected samples	42 from one well	100 samples from four wells	75 samples from five wells
Samples information	Oil field	Siri field	Magnus field	Frigg and Grane field
	Well name	Siri 2	211/12a-9	25/1-9; 25/11-15
	API	42° (Ohm et al., 2006)	39° (Shepherd, 1991)	23-24° (Brewster, 1991); 19° (Ross et al., 2010)
	Sample number	42	24	15; 15
	Age	Palaeocene	Jurassic	Eocene; Palaeocene
	Depths	2,096-2,137 m	3,200-3,240 m	2,045-2,075 m; 1,734- 1,798 m
	Temperature	78°C	116°C	60; 70°C
	Formation /Member	Palaeocene Lista Formation/ Heimdal sandstone Member	Jurassic Kimmeridge Clay Formation/ Magnus sandstone Member	Eocene Frigg sandstone Formation; Palaeocene Lista Formation /Heimdal sandstone Member
	Lithology	Glauconite bearing sandstone	Arkose	Subarkose
	Facies	Turbidite	Submarine fan	Submarine fan
	Source rock	Upper Jurassic Farsund and Mandal Formations in the Central Graben	Overlying and underlying Kimmeridge Clay Formation to the east	Lower and Middle Jurassic (Brewster, 1991); Upper Jurassic Draupne Formation in the South Viking Graben (Justwan et al., 2006a)
	Oil generation	Later Palaeogene to Early Neogene (Hamberg et al., 2005)	Later Cretaceous (Maastrichtian-Campanian) 75 Ma BP, (Shepherd, 1991)	Palaeocene until the present day (Goff, 1983); Early Palaeocene to the present (Justwan et al., 2006b)

The sampling interval extends from the uppermost gas cap through the oil leg to the underlying water leg of this well (from 2,096 m to 2,137 m in depth) (Fig. 2.8). All of these samples were undertaken detailed investigation using multiple approaches outlined in Section 2.4. The results have been published (Mu et al., 2015) and constitute the Chapter 3 of this thesis.

2.1.2. Sample set 2 from the Magnus field

Figure 2.9 Core photos of Well 211/12a-9 and locations of collected samples.

A second sample set was collected from Magnus field, offshore UK. It was taken from the Jurassic Magnus sandstones Member of Well 211/12a-9. The sample list is present in Table A2 in the Appendix. Unlike the obvious OWC of Well Siri-2, the OWC of Well

211/12a-9 is obscure in cores due to low oil saturation. Prior to sampling, OWC was identified at around the depth of 3,212.90 m in well 211/12a-9 by using well logs. Afterwards, a total of twenty-four samples were collected from the Well 211/12a-9 cores between the depths of 3,200 m and 3,240 m, an interval extending from the seal through the oil leg to the water leg (Fig. 2.9). These samples are subarkosic sandstones with high contents of feldspar. These study results are presented in Chapter 4.

2.1.3. Sample set 3 from the Frigg and Grane fields

The third sample set was collected from the Frigg field and the Grane field, offshore Norway. The sample lists of these two oil fields are present in Table A3 and A4 in the Appendix, respectively. In the Frigg field, the collected samples are from Well 25/11-15 and they belong to the Palaeocene Heimdal Member. In Well 25/11-15, a sharp OWC can be readily recognized in cores at depth of 1,785.6 m according to the dark-brown color of the oil leg compared to the white colour of the water leg (Fig. 2.10). Fifteen samples were then collected from Well 25/11-15 extending from the oil leg to the water leg (Fig. 2.10).

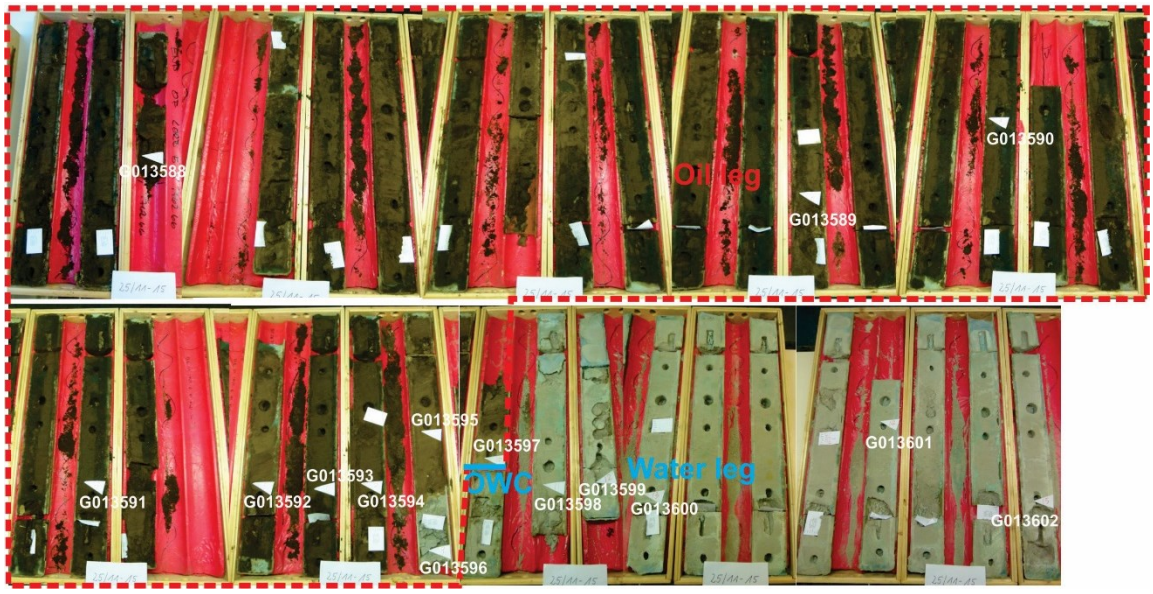

Figure 2.10 Core photos of Well 211/11-15 and locations of collected samples.

In the Grane field, collected samples are from Well 25/1-9 and they belong to the Eocene Frigg sandstone Formation. In well 25/1-9, an OWC is also recognized, although the contact is not as sharp as the one in Well 25/11-15 due to its low oil saturation. Fifteen

samples were also collected from Well 25/1-9 covering both the oil leg and the water leg (Fig. 2.11). All samples from Well 25/11-15 and Well 25/1-9 were analyzed using multiple methods listed in Section 2.4. The results are presented in Chapter 5.

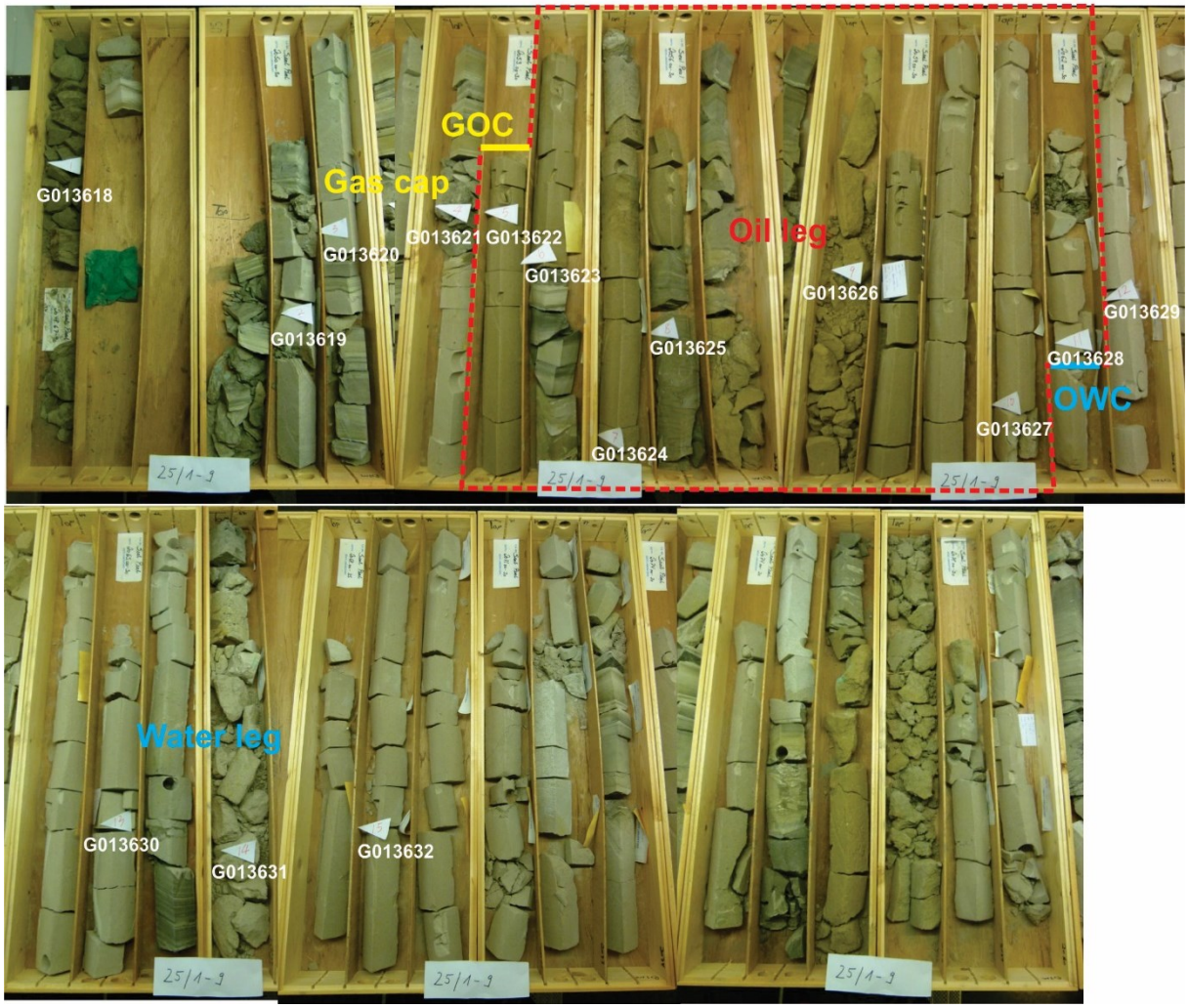

Figure 2.11 Core photos of Well 211/1-9 and locations of collected samples.

2.3. Sample Preparation

All collected samples were split into two parts, with one part of each stored as “safe samples” and another half used for analysis. For preparation of thin sections, small rectangular strips (2 cm wide, 4cm long, and 0.5 cm thick) which are perpendicular to beddings were cut from samples using a water-cooled saw. These small rock chips were then impregnated with blue-dyed epoxy before they were further grinded to prepare thin sections

for light microscopy investigation. In addition, smaller rectangular strips (0.3-0.5 cm thick, 0.5-1.0 cm wide, and >1 cm long) for SEM analysis were further cut. The remaining sample fragments were grounded into powders which were then used for Soxhlet extraction and inorganic geochemistry study (XRD and XRF).

2.3.1. Soxhlet extraction

Prior to preparation of thin sections and SEM, Soxhlet extraction with 99:1 (v: v) dichloromethane/ethanol mixture in 24 h was performed in order to remove bitumen. In this study, 20-30 g sample materials including chips and powders were used for Soxhlet extraction. A schematic diagram of a Soxhlet extractor is presented in Fig. 2.12.

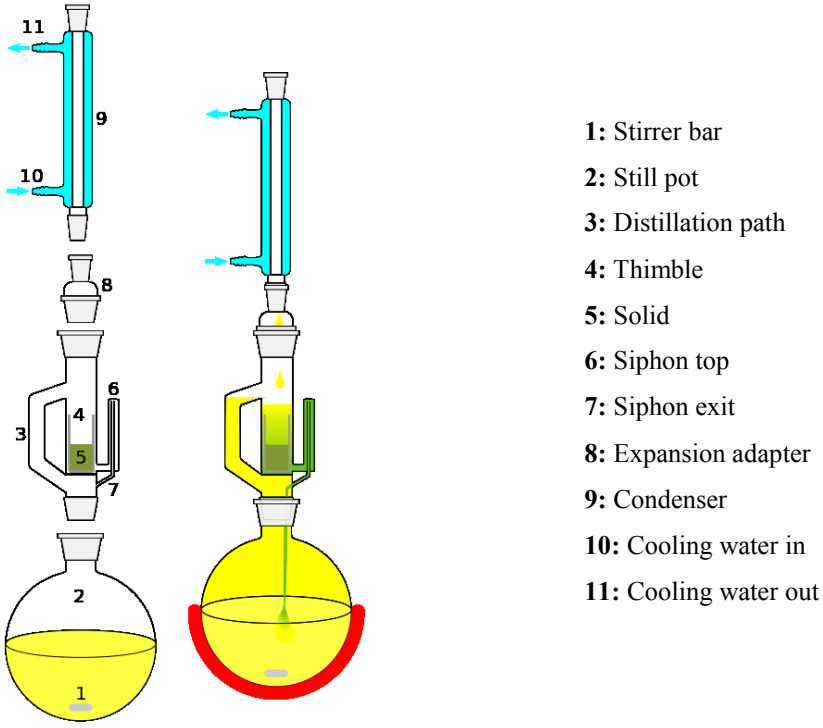

Figure 2.12 Schematic illustration of a Soxhlet extractor (Quantockgoblin, 2006).

The samples were weighted in a solvent pre-cleaned extraction thimble which was placed into the main chamber of the Soxhlet extractor. The extraction pot was filled with 150 ml of 99:1 (v: v) dichloromethane/ethanol mixture and was heated at a constant temperature of 42°C. During heating, the solvent vaporized and travelled up via the distillation arm to the chamber housing where the solvent vapour cooled and dropped down into the thimble of rock powder in the chamber housing due to the cooling system. Once the Soxhlet chamber was full

of solvent, the chamber was automatically emptied by a siphon side arm, with the solvent and dissolved bitumen running back down to the distillation flask. This cycle was allowed to repeat over 24 hours. After extraction, the solvent was removed by turbo vaporization, and the reservoir rock extracted bitumen was dried under nitrogen gas in 10 ml brown vail, and then was weighed and stored in a fridge at around -20°C. Extracted bitumen was subsequently subjected to asphaltene precipitation and fraction separation by MPLC.

2.3.2. Asphaltene precipitation

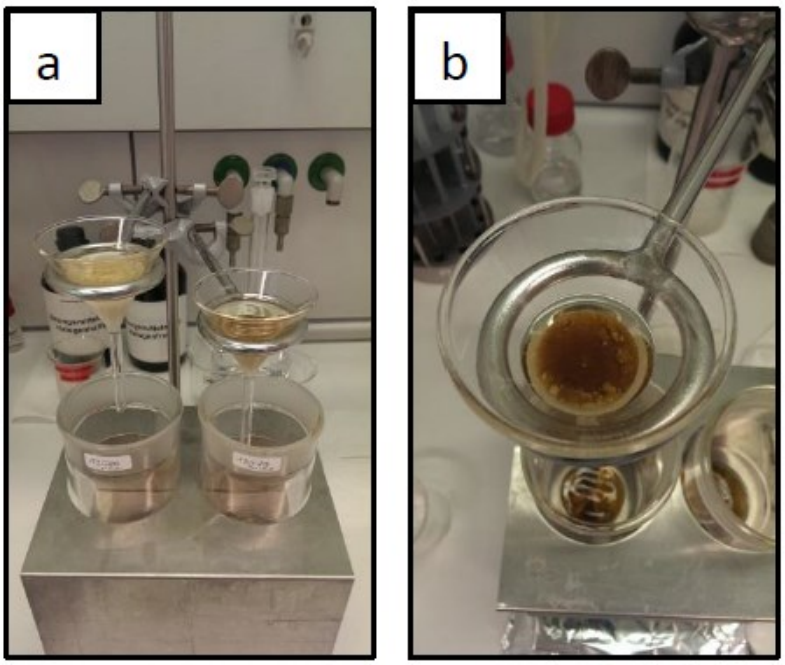

Figure 2.13 Instrument installation for asphaltene precipitation: (a) solving maltenes by flushing enough volume of n-hexane, (b) precipitated asphaltenes above sodium sulfate layer (modified after Steinmann, 2015).

For asphaltene precipitation, a simple instrument was installed by using a funnel sealed with previously extracted cotton and 1cm think of sodium sulfate (Fig. 2.13). 5 ml *n*-hexane was added in the funnel for cleaning. 250 µl of a mixture of dichloromethane and ethanol (99:1, v: v) and 10 ml *n*-hexane were added into the dried extracts. Afterwards, this mixture was then homogenized in an ultrasonic bath for 10 minutes and was then transferred to the funnel. Following this, the funnel was gradually flushed with enough volume of fresh *n*-hexane until outflow was clean (Fig. 2.13a), which indicated the maltenes were completely removed. The residual asphaltenes were filtered and precipitated at the surface of sodium

sulfate layer (Fig. 2.13b). To get asphaltenes, dichloromethane was added to the funnel for resolving and washing asphaltenes. The maltene solution and asphaltenes solution were subsequently concentrated by removing the solvent using turbo vaporization and then dried under a continuous nitrogen gas flow. The dried maltenes and asphaltenes were weighed and stored in a fridge at around -20°C. The maltenes were subjected to following fraction separation by MPLC.

2.3.3. Medium pressure liquid chromatography (MPLC)

After asphaltene precipitation, the maltenes were then separated into saturated hydrocarbon, aromatics and NSO compounds by MPLC (Radke et al., 1980). The MPLC system was equipped with a thermally deactivated silica 100 pre-column (63–200μm) and a LiChroPrep Si60 main column with *n*-hexane as the mobile phase (Radke et al., 1980). The main columns were filled different size silica gel: fine-grained silica gel (Margot: 200-500 μm) at the bottom and coarse-grained samples diluted (Margot: 100-200 μm) at the top. All maltenes were performed column chromatography using a K-501 MPLC system. With this system, up to 15 samples can be loaded at a time.

For sample injection, 500μl *n*-hexane was added into the maltenes. The 5α- Androstane and 1-Ethylpyrene were also added into the maltenes fraction as internal standards for saturates and aromatics, respectively. The rate of *n*-hexane flow was set up as initial 8 ml/min for distributing sample material within the column, followed by 8 ml/min for separating aliphatic fraction and 12 ml/min for separating aromatic fraction. For the whole column chromatography program, pressure was set at 2 bars. The NSO compounds trapped on the precolumns were released by using a dichloromethane/methanol (95:5) solvent mixture in a nitrogen pressure condition (2 bars). Separated fractions were dried and weighted.

2.4. Methodology

2.4.1. Organic Geochemical Measurements

Gas Chromatography-Flame Ionization Detector (GC-FID)

The separated aliphatic fractions by MPLC were diluted in *n*-hexane and examined on a GC-FID system (6890A, Agilent Technologies, USA) equipped with an HP Ultra 1 capillary column (film thickness = 0.33 μm, 50 m x 0.2 mm i.d.). A schematic diagram of a GC-FID

system is illustrated in Fig. 2.14. The injector was set an initial temperature of 30°C and then was heated up to 300°C within 23 seconds, held for 3 minutes. The GC oven was heated from 40°C (2 min isothermal) to a final temperature 300°C (65 min isothermal) at a heating rate of 5°C/min. The helium gas was used as the carrier gas with a constant flow rate of 1 ml/min. The operation temperature for the FID was 310°C.

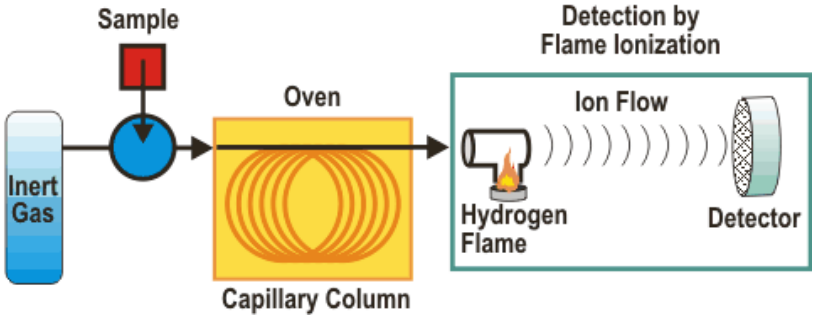

Figure 2.14 Schematic illustration of GC-FID (Blogreu, 2015).

Gas Chromatography- Mass Spectrometry (GC-MS)

The aliphatic and the aromatic hydrocarbon fractions were analyzed for biomarker using a gas chromatographic system coupled with a mass spectrometer. Compound separation was performed on an Agilent 6890 Series GC-instrument equipped with a PTV injection system and a fused silica capillary column (SGE BPX5; 50 m length, inner diameter = 0.22 mm, film thickness = 0.25 μm). A schematic diagram of a GC-MS system is illustrated in Fig. 2.15. Helium was used as carrier gas, and the temperature of the GC oven was programmed from 50°C (1 min) to 310°C at a rate of 3°C/min, followed by an isothermal phase of 10 min. The injector temperature was programmed from 52°C to 300°C at a rate of 12°C/s. For compound identification, the gas chromatographic system was linked to a Finnigan MAT 95 XL mass spectrometer operating in the electron impact mode (70 eV). Full scan mass spectra were recorded from m/z 50 to 650 at a scan rate of 1 s per decade and an interscan delay of 0.2 s, resulting in a scan cycle time of 1.3 s.

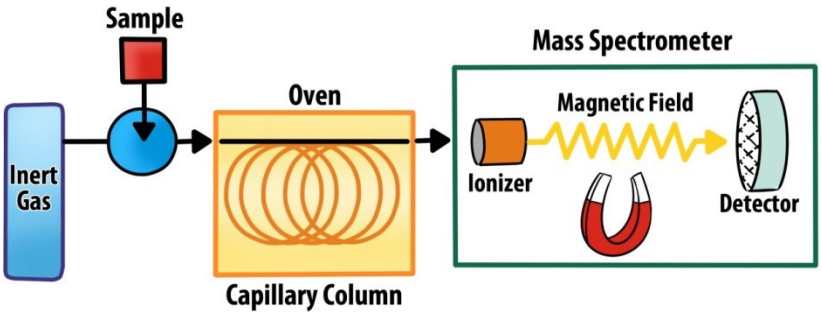

Figure 2.15 Schematic illustration of GC-MS.

Fourier Transform Ion Cyclotron Resonance Mass Spectrometry (FT-ICR-MS)

For Fourier Transform Ion Cyclotron Resonance Mass Spectrometry (FT-ICR-MS) analysis, 5 mg extracted bitumen of ten selected samples from well 25/1-9 and well 25/11-15 were dissolved in dichloromethane and diluted with a methanol-toluene mixture (1:1; v: v) to produce a concentration of 100 µg/mL. Prior to the measurement, 10 µL of a concentrated aqueous NH3 solution was added to each sample solution. Mass analyses were performed in negative electrospray ionization (ESI) mode with a Bruker Solarix FT-ICR-MS. The procedure of measuring, data evaluation and sorting have been described previously in detail (Poetz et al., 2014). In addition to the compound class depicting the sort and number of abundant heteroatoms in a molecule, the double bond equivalents (DBE) as a measure for unsaturation and the carbon number distributions have been evaluated. The DBE has been calculated for each assigned molecular according to the formula: DBE = C - H/2 + N/2 + 1 (C: the number of carbon; H: the number of hydrogen; N: the number of nitrogen).

2.4.2. Mineralogical Examinations

Light Microscopy

Thin sections were prepared for analysis of mineralogical compositions and structural fabrics. Prepared thin sections were investigated at various magnifications under plane-polarized and cross-polarized light using a Zeiss Axiophot Electronic Microscope System. This system was equipped with a Carl Zeiss Axiocam digital camera and a Carl Zeiss Axiovision 2.0 software and is capable of taking high resolution photomicrographs with

magnifying lenses of 10×, 20×, 30×, and 40×. Thin section microscopy was carried out at GFZ Potsdam.

Point counting

The point counting technique was used to determine sandstone composition and sandstone classification. Photomicrographs were taken under cross-polarized light for point counting. Three hundred equally spaced points of each photomicrograph were counted based on mineral identification.

Scanning Electron Microscopy (SEM)

SEM is an analytical tool that provides high-resolution images of sample surfaces. Rectangular strips of 0.3-0.5 cm thick, 0.5-1.0 cm width, and >1 cm length were prepared for SEM analysis. A fresh surface was created by breaking the strip. Afterwards, the broken strip was mounted on specimen holders with fresh surface upside using resin and was stored in the lab overnight to dry. Subsequently, the dried sample was coated with a gold-palladium alloy for SEM investigation. Selected thin sections were also coated with carbon for further investigations by SEM using scanning (SE) and backscattered scanning electron (BSE) modes. Investigations were carried out at GFZ Potsdam using an Ultra 55 plus Carl Zeiss SMT field emission scanning electron microscope (FE-SEM), and images were obtained under high vacuum at 20 kV acceleration voltages using the SE, Inlens-SE, and BSE detectors.

Focused Ion Beam - Transmission Electron Microscopy (FIB-TEM)

FIB is similar to the scanning electron microscope (SEM) but it is an ion beam rather than an electron beam. It is used to directly modify or "mill" the specimen surface with nanometer precision. TEM is an analytic tool that allows visualization and analysis of samples at μm to nm scale. It enables analysis of crystal structures, specimen orientations and chemical compositions of phases. In order to identify clay minerals and analyze their composition, fabric, and texture at nm scale, thin sections of five samples of Well Srir-2 were selected for TEM study.

FIB thin foils of 15-20 μm wide, 10-15 μm high, and 100-150 nm thick for TEM were cut from pre-defined areas in the polished thin sections by focused Ar-ion beam (FIB) milling in an ultrahigh vacuum using an FEI FIB200 instrument (for more details see Wirth, 2004, 2009). These ultrathin samples were investigated at GFZ Potsdam, using a FEI Tecnai G2 F20

X-Twin TEM, equipped with a field-emission electron source (operated at 200 kV), a Fishione high-angle annular dark-field detector (HAADF), a Gatan Tridiem imaging filter for acquisition of energy-filtered images, and an EDAX Genesis X-ray analyzer with an ultrathin window. The characterization of samples included bright-field/dark-field imaging, high-resolution imaging, electron diffraction, and EDX analyses (in scanning-TEM mode).

Electron Microprobe Analysis (EMPA)

Electron microprobe analysis is an analytical technique that is used to accurately obtain the in-situ non-destructive elemental composition of a small area on specimens, with high sensitivity at the level of ppm. To quantify the chemical composition of berthierine, selected thin sections from Siri field were coated with carbon for EMPA at GFZ Potsdam. The major element chemistry was determined using wavelength-dispersive analysis by a JEOL field emission gun JXA-8500F electron microprobe operating at 20 kV, with a beam current of 10 nA and a beam diameter of 1−5 μm or focus beam depending on minerals grain sizes. The peak counting times were 20−30 s and the background counting times were always set to half of the respective peak counting times.

X-ray Powder Diffraction (XRD)

XRD is a rapid analytical method used for phases identification and characterization of unknown crystallines material. XRD was performed at GFZ Potsdam using a Siemens D5000 powder diffractometer equipped with Cu Ka radiation, automatic divergent and antiscatter slits and a secondary graphite monochromator with scintillation counter to determine proportions of matrix minerals. The diffraction data were recorded from 4° to 75° 2 θ with a step width of 0.02° and a counting time of 4 s per step. The generator settings were 40 kV and 30 mA. Measured data were then analyzed qualitatively using the EVA (Bruker) software and quantitatively using the AutoQuant software.

X-ray Powder Fluorescence Spectrometry (XRF)

XRF is a routine method that is used for non-destructive chemical analysis of rocks, minerals, sediments and fluids. The working theory is that secondary X-rays fluorescence that has characteristic wavelengths produced by elements of sample materials can be excited when the sample material is irradiated with X-rays. Separation of individual wavelengths of each element can yield proportions of elements in the samples. To obtain major and trace elements

of core samples, powder samples of the Magnus field were analyzed at GFZ Potsdam by X-ray fluorescence (XRF, Siemens SRS 303) equipped with a Rh X-ray tube SST-mAX, scintillation detectors, sealed Xe detector.

Chapter 3 Berthierine formation in reservoir rocks from the Siri oil field (Danish North Sea) as result of fluid-rock interactions

3.1. Abstract

Berthierine as the only authigenic Fe-rich clay mineral occurs in an oil-bearing, glauconite-rich sandstone (Palaeocene Heimdal Member of the Lista Formation, Danish North Sea). Based on the results of thin section, transmission and scanning electron microscopy, five different morphological types of berthierine were identified: (1) mainly as grain-coatings partly together with authigenic quartz covering detrital grains, (2) as pore-filling clay in open pores, (3) small crystals in transformed glauconite grains; (4) small crystals associated with siderite in layers of mica/micaceous glauconite; and (5) as elongated crystals in siderite concretions. Although different in occurrence, all berthierine types investigated by microprobe analysis are of similar chemical composition, suggesting similar precipitation conditions. Investigations by transmission electron microscopy reveal that fine berthierine crystals display straight parallel layers with a typical lattice fringe spacing of 0.7 nm and that their occurrence is intimately connected to oil phases in pore space. Partly, berthierine textures resemble mineralized oil-water emulsions. Berthierine is more abundant in the oil leg than in the water leg but occurs especially abundant at the oil-water contact. The coexistence of berthierine together with quartz overgrowth, but also its appearance in glauconite indicates that berthierine formed in situ and that it is a product of glauconite dissolution.

This chapter has been published as: Mu, N., Schulz, H.-M., Fu, Y., Schovsbo, N. H., Wirth, R., Rhede, D., van Berk, W., 2015. Berthierine formation in reservoir rocks from the Siri oilfield (Danish North Sea) as result of fluid-rock interactions: Part I. Characterization. Marine and Petroleum Geology, 65, p. 302-316. DOI: http://doi.org/10.1016/j.marpetgeo.2015.04.010

Berthierine formation is coupled to the reduction of aqueous Fe^{3+} into Fe^{2+} derived from glauconite dissolution and is related to fluid-rock interactions triggered by oil degradation which occurred in the oil-filled zone and at the oil-water contact. The biomarker parameters pristane/*n*-C_{17} and phytane/*n*-C_{18} indicate an increased extent of oil degradation at the oil-water contact. On the one hand, soluble oil degradation products (methane, carbon dioxide, and hydrogen) changed the hydrogeochemical conditions (such as pH, pe, alkalinity, etc.), and controlled dissolution of glauconite (and feldspar). On the other hand, the changed hydrogeochemical conditions led to berthierine and quartz precipitation in water-wet reservoir intervals.

Keywords

Berthierine; Glauconite; Sandstone; Fluid-rock interactions; Oil degradation

3.2. Introduction

Berthierine is an aluminous Fe^{2+}-rich 1:1-type layer silicate with a basal spacing of 0.7 nm, belonging to the kaolinite-serpentine group (Kodama and Foscolos, 1981; Damyanov and Vassileva, 2001; Worden and Morad, 2003; Wise, 2007). Alternative or ancient names for this mineral are septechlorite, septechamosite, chamosite, 0.7 nm-chamosite, and/or 0.7 nm-chlorite (Hornibrook and Longstaffe, 1996).

Berthierine is composed of Al_2O_3 (28−12 wt.-%), SiO_2 (19−27 wt.-%), FeO (32−37 wt.-%), and minor portions of Fe_2O_3 and MgO, and chemically and crystallographically resembles iron-rich chlorite (chamosite; Brindley, 1982; Hornibrook and Longstaffe, 1996). Conventional XRD methods are limited to unequivocally detect berthierine in mixtures with chlorite or whether exclusively chlorite prevails. However, heating samples cause the disappearance of the 1.4 nm basal reflection on XRD patterns that is characteristic of chlorite (Brindley, 1982; Rivas-Sanchez et al., 2006). Heating, furthermore, leads to an increase of the 0.73 nm peak of chlorite, whereas this peak weakens in berthierine because of sheet breakdown (Deer et al., 1992). In addition, transmission electron microscopy (TEM) can also be applied to distinguish berthierine from chlorite by the absence of 1.4 nm and the presence of 0.7 nm, dhkl [001] basal spacing in lattice fringes (Coombs et al., 2000; Rivard et al., 2013; Rivas-Sanchez et al., 2006).

Berthierine is chemically and structurally also similar to the 1:1-layer silicate odinite. Similarities are the basal spacing of 0.7 nm, and many identical XRD lines (Bailey, 1988; Huggett and Gale, 2002; Odin, 1990). In contrast to odinite, berthierine may have higher alumina contents, but less Mg and Si contents (Hornibrook and Longstaffe, 1996). In addition, berthierine is rich in ferrous iron (Fe^{2+}) whereas odinite contains dominantly ferric iron (Fe^{3+}). Therefore, berthierine is less likely to be misidentified as odinite in ancient sedimentary rocks.

Berthierine frequently occurs in marine-oolitic ironstone formations. Prominent examples are berthierine ooids in the marine Lower Miocene strata of the Tenggol Arch area, offshore Peninsular Malaysia (Madon, 1992), or ooids and fine berthierine crystals together with siderite in the marine Jurassic ironstone-mudstone succession, UK (Taylor and Curtis, 1995), to name but two. However, berthierine may also occur in non-marine sedimentary strata such as arctic desert soil (Kodama and Foscolos, 1981), laterite (Toth and Fritz, 1997), coal measures (Iijima and Matsumoto, 1982), and sediments deposited in brackish water (Rohrlich et al., 1969; Taylor, 1990). Apart from sedimentary environments, inferred hydrothermal berthierine has been observed in altered mafic rocks (Ruotsala et al., 1964), sedimentary exhalative siderite iron formations (Damyanov and Vassileva, 2001), volcanogenic massive sulfide deposits (Slack et al., 1992), and in granitic pegmatites (Wise, 2007). A detailed compilation of berthierine occurrences was presented by Toth and Fritz (1997).

In contrast, the occurrence of berthierine in sandstone reservoirs was rarely reported, e.g., in oil sands of the Lower Cretaceous Clearwater Formation in Alberta, Canada (Hornibrook and Longstaffe, 1996), in the Greensand Formation of the Late Cretaceous Sherbrook Group, Otway Basin, Australia (Boyd et al., 2004), and in the Palaeocene Hermod sandstone of the Stine segment in the Siri field (Stokkendal et al., 2009). Interestingly berthierine formation in the Upper Jurassic Georgiev Formation was probably controlled by products of organic matter diagenesis in the overlying Lower Cretaceous Bazhenov Formation (Sánchez-Navas et al., 2008) which is the main source rock for oil and gas fields in the Western Siberian Basin. In addition, berthierine has been documented in the Burgess Shale as a coating on organic remains, which are assumed to be diagenetic oxidation products of organic matter in the iron-reducing pathway (Petrovich, 2001).

The present contribution builds on existing findings and assumptions for the Palaeocene siliciclastic oil (and gas) reservoirs in the Danish North Sea (e.g., Stokkendal et al., 2009). In

the glauconite-rich sandstone reservoirs of the Palaeocene Heimdal and Hermod members in the Siri field, berthierine mainly occurs as grain coating in close association with siderite, glauconite, and –importantly– also with oil and gas fillings (details in section 5). This specific mineral assemblage in oil-filled reservoirs offers a window of opportunity to study intimately interconnected organic-inorganic processes that may lead to berthierine formation due to oil degradation and related petroleum-water-rock-gas interactions.

It is the conceptual approach of this first part of three companion manuscripts (Part II by Fu et al., 2015a; Part III by Fu et al., 2015b) to characterize berthierine in terms of shape (morphology, structure), crystallographic structure and chemical composition together with the mineralogical framework of the hosting oil-stained sandstone reservoir. It is the aim to elaborate a first qualitative pathway about fluid-rock interactions leading to berthierine formation based on the applied methodology including light microscopy, scanning electron microscopy (SEM), transmission electron microscopy (TEM), X-ray diffraction (XRD) and electron microprobe analysis (EMPA). The descriptive results will raise overall questions about the genetic pathways and on quantitative aspects of berthierine formation due to organic-inorganic interactions in an oil reservoir.

3.3. Physicochemical conditions of berthierine formation– a brief review

The different genetic pathways leading to berthierine precipitation are still a matter of debate. The generally favored concept is that berthierine forms in a reducing environment during early diagenesis by replacement or modification of a precursor (Hornibrook and Longstaffe, 1996). Odinite is regarded as the most frequent precursor because it is chemically similar to berthierine (Odin, 1990) and could evolve to berthierine during early diagenesis by a loss of Mg and reduction of Fe^{3+} to Fe^{2+} (Huggett and Hesselbo, 2003). Moreover, kaolinite was proposed to be another precursor for berthierine in ironstones (Bhattacharyya, 1983) and in Triassic soils (Sheldon and Retallack, 2002). Under laboratory conditions diagenetic transformation of Fe(III) oxyhydroxides to berthierine has also been achieved (Harder, 1978, 1989). However, Maynard (1986) suggested that the process of precursor replacement relies on a complete dissolution followed by re-precipitation rather than a simple addition of divalent cations to kaolinite and its structural reformation. In contrast to rather general

concepts, Van Houten and Purucker (1984) proposed that berthierine formation was caused by neoformation, with the evidence of grain-coating, pore- and void-filling berthierine.

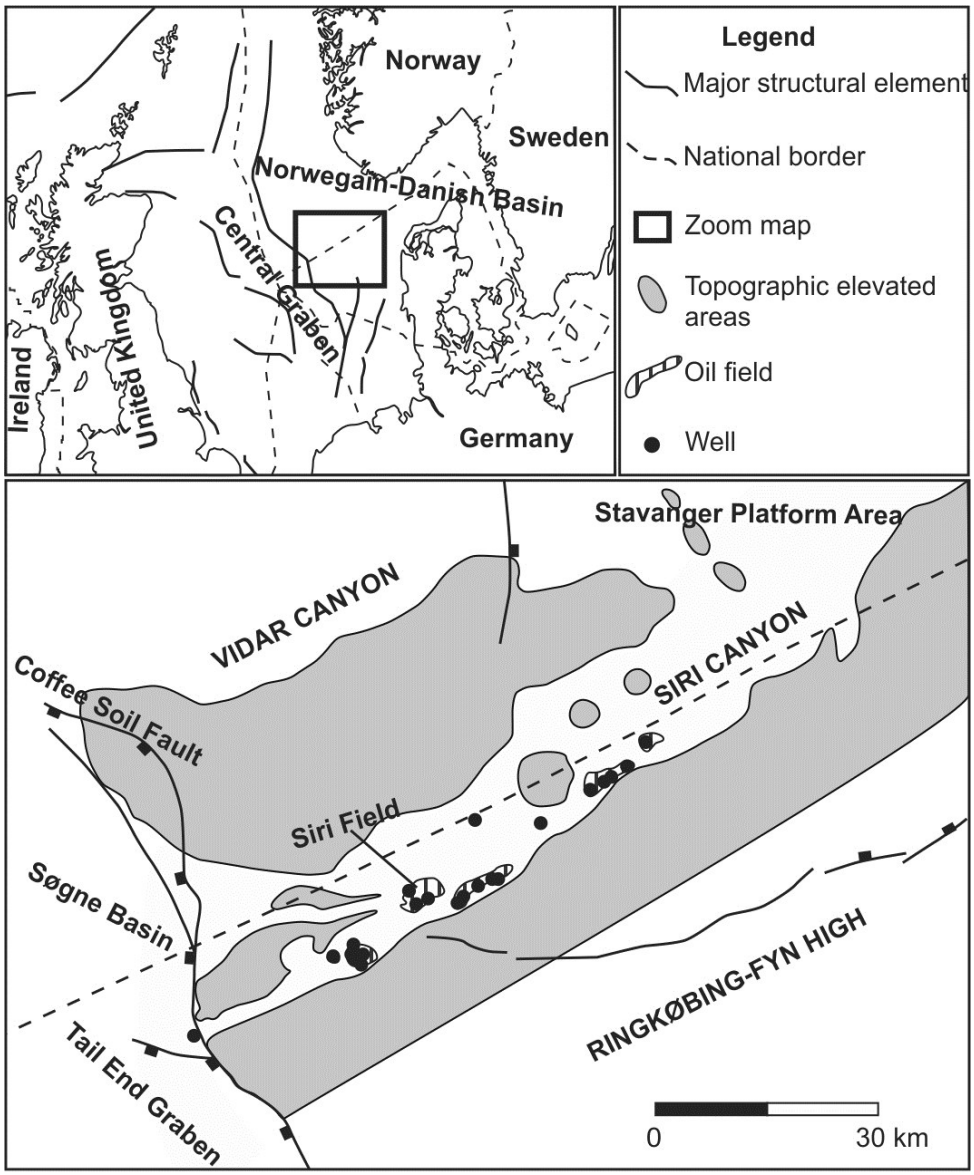

Figure 3.1 Location map of the study area in the Danish North Sea sector and depositional environment during the Palaeocene (modified after Hamberg et al., 2005).

Even though berthierine may form under different conditions and in different geological settings, its manifold occurrence reveals similar physicochemical conditions during formation. The most important controlling factor for berthierine formation is a reducing environment. For example, Taylor and Macquaker (2011) stated that iron reduction predominated in marine shelf systems with consequently changed pore water composition, leading to the precipitation of iron-bearing clay minerals such as berthierine in the absence of sulfide. Another example is

the formation of pore-filling Fe-berthierine in a Cretaceous laterite under reducing conditions which were established by downward percolation of organic-rich waters derived from swamps (Toth and Fritz, 1997). Moreover, it is important to note that pore-lining berthierine formed in oil sands of the Clearwater formation. The reducing environment for berthierine formation in the oil sands is argued to be due to intense microbial activity (Hornibrook and Longstaffe, 1996). In summary, thermodynamic calculations based on a study of a Cretaceous Fe-berthierine-bearing laterite (Fritz and Toth, 1997) further revealed that berthierine precipitation is favored by solutions having: (1) low Mg^{2+}/Fe^{2+} ratios; (2) extremely low sulfate contents in formation water before reduction takes place; and (3) moderately reducing conditions.

3.4. Geological setting and mineralogical framework

The Siri oil field is located in the Siri Canyon, which was part of a larger system of submarine canyons. The canyons developed during the Palaeocene in the Norwegian-Danish Basin and today extend towards the North Sea Central Graben (Fig. 3.1; Huuse, 1999; Hamberg et al., 2005). The Siri Canyon sedimentary rocks consist of deep marine pelagic to hemipelagic marlstones and shales that contain a series of back stepping sandstones. The youngest sandstones are represented by the Bor and Tyr members in the Våle Formation. The youngest are the Heimdal and Hermod members embedding in the Lista and Sele Mudstone formations (Hamberg et al., 2005; Stokkendahl et al., 2009). These sediments were deposited on eroded Late Cretaceous chalk rock and are –in turn– conformably overlain by marine shales of the Sele Formation (Poulsen et al., 2007). Sourced from the Stavanger Platform, the glauconite-bearing sands were transported by gravity flows through the submarine canyon to their present-day location (Danielsen et al., 1995; Hamberg et al., 2005). The source rocks for the hydrocarbons in the Siri field are the Middle Jurassic coaly Bryne Formation, and the Upper Jurassic Farsund and Mandal Formations in the Central Graben. Petroleum migration from Jurassic source rocks in the Central Graben into Palaeocene sandstones took place along the Coffee Soil Fault and vertically through the Late Cretaceous chalk. The first oil charge took place during the Late Paleogene-Early Neogene when the Heimdal sandstone was buried to approximately 1,000m depth (Hamberg at al., 2005; Ohm et al., 2006). A regional Fennonscandian uplift resulted in leakage and remigration of oil in the Siri field due to the tilted palaeo oil-water contact (OWC). Petroleum from the shallow Søgne Basin is believed to enter the Siri field quite recently. In the Siri field, the present burial depths of the Heimdal

sandstone are around 2,150m and the bottom temperature is approximately 79°C. Burial history reconstructions suggest that the maximum depth and temperature did not exceed the current burial depth and temperature. The produced oil in the Siri field has API gravities of more than 35-42° (Ohm et al., 2006), and the water saturation of the Heimdal Member is as high as 30−40% in the oil leg (data from Siri field).

3.5. Methods

Prior to preparations, all core samples were extracted for 24 hours using 99 *n*-hexane: 1 dichloromethane in a Dionex ASE 200 soxhlet at 50°C in order to remove freely accessible hydrocarbons. However, the treated core samples still contained residual oil in small, isolated pores (e.g., Figs. 3.2c, 3.2e). 24 extracted samples taken from the gas cap, the oil leg, the OWC and the underlying water leg were selected for preparation of thin sections. All these sections were stained with blue-dyed epoxy and later microscopically studied under white and UV light. Six thin sections selected each from the gas cap, the oil leg, the oil-water contact and the water leg were coated with carbon for further investigations by SEM using scanning (SE) and backscattered scanning electron (BSE) modes. 600 points counted data were obtained from nine thin sections using transmitted light microscope images. Using freshly broken chips, the micromorphology of berthierine was determined under a Philips SEM-515 with an Edax PV 9100 energy-dispersive X-ray spectroscopy (EDS) system, operated at 30 kV. To further identify berthierine, the clay fraction of sample powders was analyzed by XRD. Clay fractions were prepared by mechanical separation, followed by adding distilled water into sample powder, ultrasonic treatment, piping the upper part of the liquid into glass containers after 1-2 minutes of settling, and lastly air-drying at room temperature. XRD analyses of the clay fractions were conducted applying a PHILIPS PW 1820 device, using Cu Kα radiation (35 kV, 35 mA). Scans were run between 2 and 36°, 2ϴ with a step size of 0.013° in the air-dry state.

Berthierine and its mineral matrix filled by residual oil were further investigated by TEM. Samples for TEM were cut from pre-defined areas in the polished thin sections by focused Ar-ion beam (FIB) milling in an ultrahigh vacuum using an FEI FIB200 instrument (for more details see Wirth, 2004, 2009). These ultrathin samples were analyzed using an FEI Tecnai G2 F20 X-Twin TEM, equipped with a field-emission electron source (operated at 200 kV), a Fishione high-angle annular dark-field detector (HAADF), a Gatan Tridiem imaging

filter for acquisition of energy-filtered images, and an EDAX Genesis X-ray analyzer with an ultrathin window. The characterization of samples included bright-field/dark-field imaging, high-resolution imaging, electron diffraction, and EDX analyses (in scanning-TEM mode).

For determining the qualitative chemical composition of berthierine, two selected thin sections from the oil leg and the water leg were coated with carbon for EMPA. The major element chemistry of berthierine was determined using wavelength-dispersive analysis by a JEOL field emission gun JXA-8500F electron microprobe operating at 20 kV, with a beam current of 10 nA and a beam diameter of 1−5 μm or focus beam depending on berthierine grain sizes. The peak counting times were 20−30 s and the background counting times were always set to half of the respective peak counting times. The structural formula for berthierine was calculated on the basis of 7 oxygens.

For biomarker analysis, a total of twelve core extracts were selected from the gas cap, the oil leg, and the OWC. All extracts were separated into maltenes (*n*-hexane-soluble fraction) and asphaltenes by asphaltene precipitation using a hexane-dichloromethane solution. The *n*-hexane-soluble fractions were furthermore separated into saturated hydrocarbons, aromatic hydrocarbons and resins using medium-pressure liquid chromatography (MPLC). The aliphatic fractions were analyzed using GC-FID (flame ionization detection) to obtain distribution patterns in the *n*-C_{15} to *n*-C_{30} range. The GC-FID instrument was equipped with an HP Ultra 1 capillary column, using He as a carrier gas. The oven temperature was programmed from 40°C (2 min isothermal) to 300°C (65 min isothermal) at 5°C/min heating rate. The identification of individual compounds was accomplished on the basis of retention times.

3.6. Results

3.6.1. Petrography of Heimdal sandstone

The Palaeocene Heimdal Member is characterized by 30−100m thick beds of olive-green to greenish-gray, fine to very fine-grained, well-sorted glauconitic sandstones. The glauconitic sandstones are of uniform grain size, sorting and mineralogical composition, containing 40 vol.-% of glauconite, 30 vol.-% of quartz and 15 vol.-% of feldspar (Table 3.1, Fig. 3.2). Glauconite mainly occurs as rounded grains (Fig. 3.2e), but also as micaceous glauconite which has mica cleavages (Fig. 3.2g). Mica (mainly muscovite) is a minor

component. Pyrite, zircon, rutile and Fe-Ti oxides occur as accessory minerals. Authigenic minerals include quartz overgrowth, kaolinite, siderite, berthierine and calcite (Table 3.1, Fig. 3.2).

Main diagenetic phenomena in the Heimdal sandstone are quartz overgrowth, feldspar and glauconite dissolution, berthierine precipitation, and calcite cementation (all illustrated in Fig. 3.2). Authigenic quartz commonly occurs in form of an overgrowth rim on detrital quartz grains (Fig. 3.2a) and also as microcrystalline quartz on the surface of detrital grains, such as glauconite and feldspar. The interfaces between quartz overgrowth and detrital quartz always contain dark margins (Figs. 3.2a, 3.2d), which were proven to be residual oil or small petroleum inclusions by their yellow fluorescence under UV illumination. Obviously, quartz overgrowth often co-exists with berthierine (Figs. 3.2d, 3.4c and 3.4d). Detrital feldspar grains including K-feldspar and albite display different stages of dissolution from slight to nearly complete dissolution (Figs. 3.2a, 3.4b, 3.5f). Calcite as pore-filling cement may account for up to 36 vol.-% at the OWCs (Table 3.1) and may completely occlude pores (Figs. 3.2b, 3.2e), which significantly reduces porosity and permeability. Calcite cement is a late stage diagenetic phase, postdating oil filling and other diagenetic processes. This cement precipitated on quartz overgrowth, after the dissolution of feldspar and glauconite with bitumen rims, and after precipitation of authigenic berthierine and glauconite with bitumen rim (Figs. 3.2b, 3.2e). Siderite in the Heimdal sandstone occurs as large concretions (Fig. 3.2b) or as small subhedral crystals in pores (Fig. 3.2b), but also in mica together with berthierine and residual oil (Figs. 3.2c, 3.4d) and in micaceous glauconite (Figs. 3.2g, 3.2h).

Berthierine, the most important diagenetic phase, is present in all samples and has the highest amount (7 vol.-%) at the OWC (Table 3.1). Even though berthierine is quite similar to chlorite in terms of texture and chemical composition, only berthierine (no chlorite) in the Heimdal sandstone was determined by the exclusive presence of a 0.7 nm peak and the absence of a 1.4 nm peak in XRD diagrams (Fig. 3). Berthierine was further proven based on its 0.7 nm lattice reflection by TEM (Figs 3.6e, 3.7d and 3.7f) and its chemical composition by EMPA (Fig. 3.8). In thin sections, berthierine was identified by its brown (Figs. 3.2d, 3.2f) to brown-green color (Figs. 3.2e, 3.2g).

Berthierine also shows close proximity to dissolved glauconite, mica and residual oil/bitumen. Glauconite grains may be surrounded by black residual solid bitumen, showing an obviously lighter green fabric structure in-between (Fig. 3.2e), which is –at higher

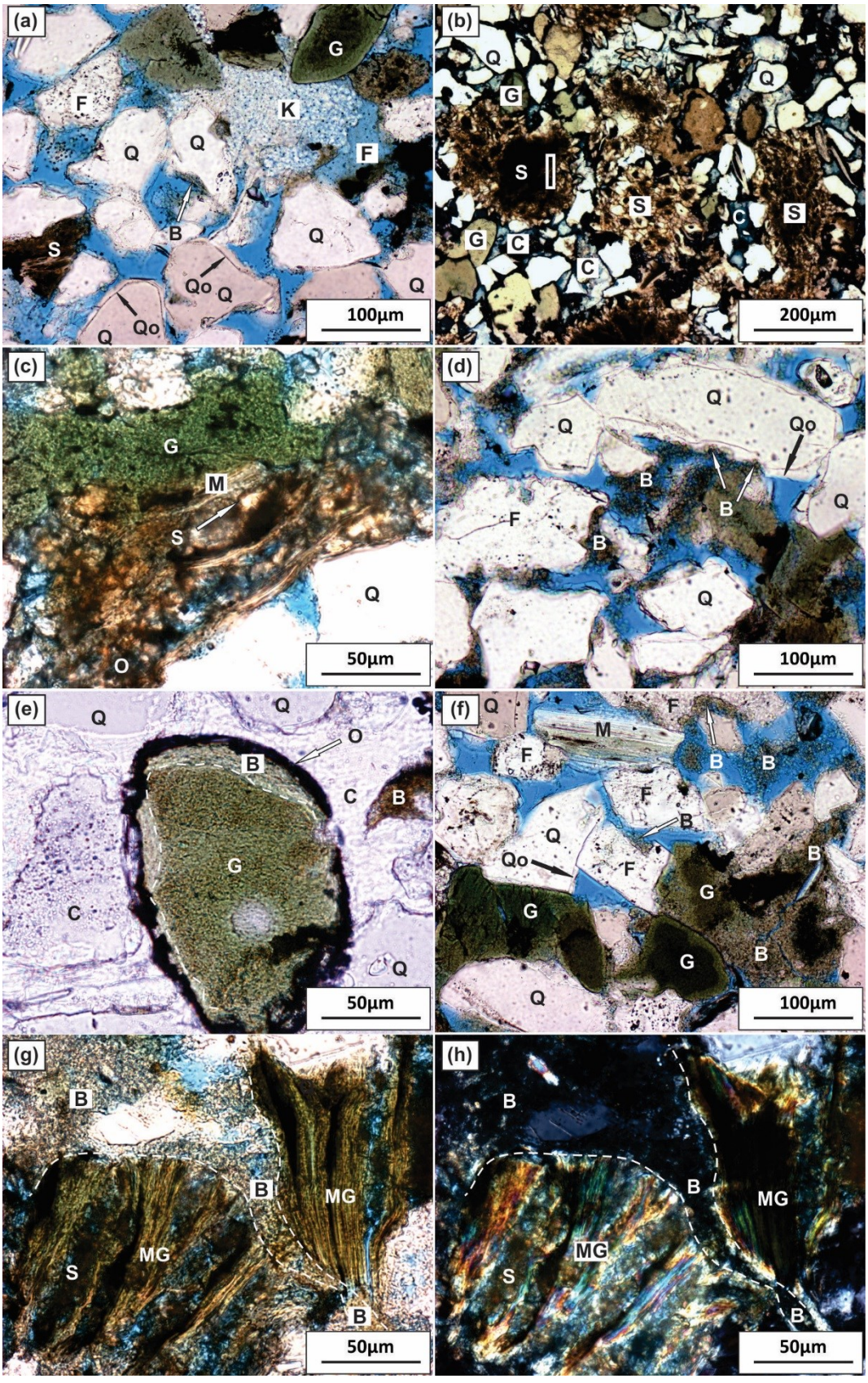
(a)
G
F
K
Q
Q
F
B
S
Q
Qo
Q
Q
Qo
Q
100µm
(b)
Q
G
Q
S
S
C
S
G
C
C
200µm
(c)
G
M
S
Q
O
50µm
(d)
Q
Q
Qo
B
B
Q
F
B
Q
100µm
(e)
Q
Q
O
B
C
B
G
C
Q
50µm
(f)
Q
F
M
F
B
B
F
B
Q
Qo
F
B
G
G
B
G
B
Q
100µm
(g)
B
B
MG
MG
S
B
50µm
(h)
B
B
MG
MG
S
B
50µm

magnification– a berthierine belt (Figs. 3.4a, 3.5c). In addition, berthierine was also observed in dissolved glauconite (Figs. 3.2f, 3.5a) and close to dissolved micaceous glauconite which has micaceous layers and siderite in between (Figs. 3.2g, 3.2h).

3.6.2. Berthierine typing in the Heimdal sandstone

Five different types of berthierine were distinguished based on morphology and their relation to other minerals: (1) as grain coatings partly with or without quartz overgrowth covering detrital grains (Figs. 3.4, 3.5f); (2) as pore fillings (Figs. 3.2d, 3.2f and 3.5c); (3) as blade-like crystals in detrital glauconite grains (Figs. 3.5a, 3.5b); (4) in layers of mica or micaceous glauconite associated with siderite (Figs. 3.5c, 3.5d); and (5) in siderite concretions (Figs. 3.5e, 3.7a). Although different in occurrence, they all are of 1−2 μm size and have a similar chemical composition (Fig. 3.8).

Type 1 berthierine appears in the form of grain coating and is the most frequent type. It can be subdivided into four different (I-IV) morphological subtypes. Subtype I berthierine coating exclusively covers glauconite grains except for grain-grain contacts (Fig. 3.4a), which indicates that berthierine coating formed after burial compaction. This berthierine subtype occurs throughout the reservoir but is more abundant in the oil leg and at the OWC (Table 3.2). Subtype II berthierine occurs in or on dissolved feldspar (Figs. 3.4b, 3.5f). Subtype III berthierine coats detrital quartz together with quartz overgrowth (Figs. 3.4c, 3.4d), showing a genetic relationship with quartz overgrowth. This subtype is the most common one, and -as for subtype I- predominates in the oil leg and at the oil-water contact. Subtype IV berthierine

Figure 3.2 Thin section microphotographs (// nicols) of core samples from the Palaeocene Heimdal Member of the Lista Formation in the Siri field. (a) General mineralogical composition of the Heimdal sandstone, Well Siri-2, oil leg. (b) Siderite clusters and calcite cements filling the pore space; the area marked by a red rectangle was investigated by TEM (results in Figure 3.8a), Well Siri-2, oil leg. (c) Siderite growing between lamella of bitumen stained mica, Well Siri-2, oil leg. (d) Pore-filling berthierine in pores. Berthierine also occurs as grain coating together with quartz overgrowth and also partly on quartz overgrowth indicated by red arrows, Well Siri-1, water leg. (e) Glauconite grain with lighter green berthierine coating surrounded by a black ribbon of residual bitumen, Well Siri-1, OWC (Fu, 2014). (f) Brownish berthierine as pore-filling clay in open pore space and also as grain-coating on dissolved feldspar indicated by red arrows. Note that brownish berthierine in the lower right corner replaces dissolved green glauconite, Well Siri-1, water leg. (g) Brown-green berthierine filling in pore space close to micaceous glauconite which contains siderite in lamellas. Note that the interface of berthierine and micaceous glauconite is transitional, Well Siri-1, oil leg. (h) g under crossed nicols. Q: quartz; Qo: quartz overgrowth; G: glauconite; MG: micaceous glauconite; M: mica; K: kaolinite; F: feldspar; S: siderite; C: calcite; B: berthierine; O: residual oil; pores in blue.

forms as network coatings together with pyrite framboids (Fig. 3.4e) or occurs together with quartz overgrowth (Fig. 3.4f). The berthierine net coating on microquartz overgrowth in Figure 3.4f indicates that berthierine formation may postdate quartz growth. This berthierine type is less common and restricted to few samples from both the oil and the water leg (Table 3.2).

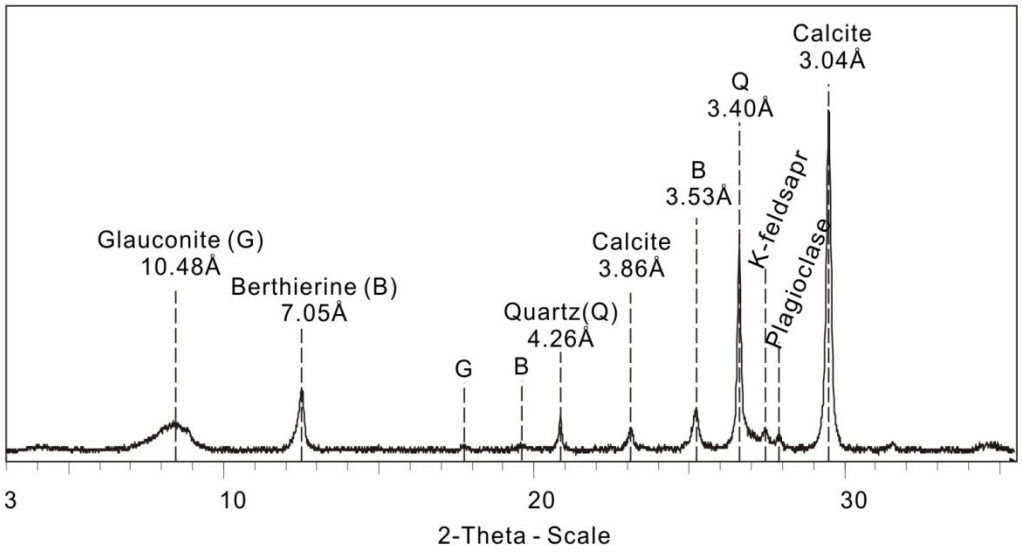

Figure 3.3 Representative XRD pattern (orientated, air-dried) of berthierine in the Heimdal sandstone, Well Siri-2, OWC. Note that only 0.7 nm peak is present and there is no 1.4 nm peak, indicating the exclusive presence of berthierine rather than chlorite in the Heimdal sandstone.

Type 2 berthierine is as pore-filling cement (Figs. 3.2d, 3.2f, 3.2g), which is absent at grain-grain contacts (Figs. 3.2d, 3.2f) and which is cemented by calcite (Fig. 3.5c). The pore-filling berthierine is also abundant at the OWC (Table 3.2).

Type 3 berthierine is characterized by 1−2 μm sized crystals forming in glauconite. This berthierine type occurs together with lath shape mica (10−20 μm long and 1−3 μm wide; Fig. 3.5b). Importantly, Type 3 berthierine was also observed in strongly dissolved glauconite grains (Figs. 3.2f, 3.5a). Detailed TEM studies show that berthierine type 3 grows into the residual oil phase (Figs. 3.6c) and close to mineralized oil-water emulsions (Figs. 3.6f, 3.6g). Type 3 berthierine is more abundant in the oil leg, especially near the current OWC (Table 3.2).

Type 4 berthierine occurs between and on individual lamellae of mica/micaceous glauconite together with siderite crystals (Figs. 3.5c, 3.5d). Mica lamellae may be covered by

berthierine crystal layers of 0.5 μm width and berthierine also prevails as blade crystals (2−3 μm) together with authigenic fine siderite crystals (1−5 μm) in pores between mica lamellae. This type 4 berthierine was observed in the gas cap, in the oil leg and at the OWC (Table 3.2).

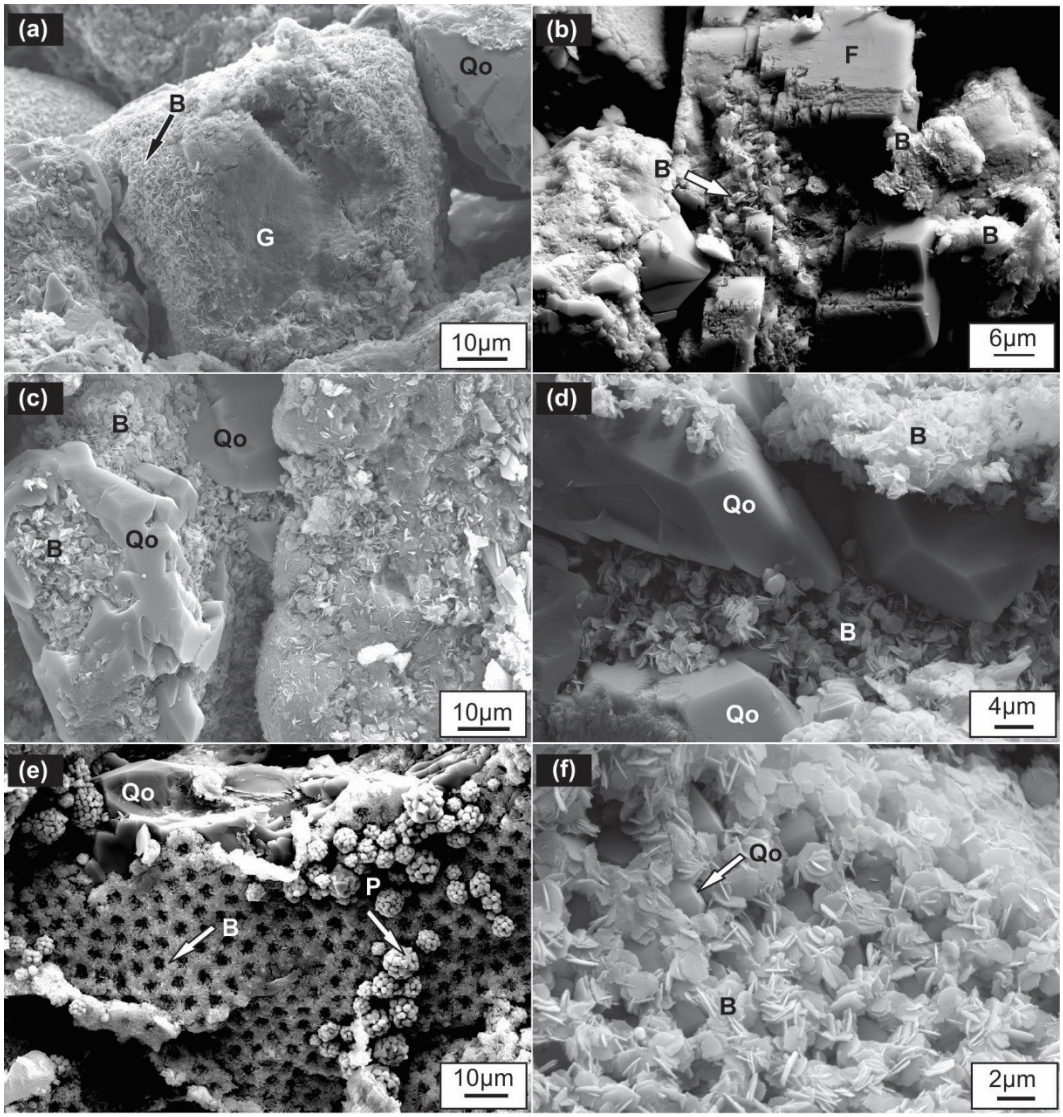

Figure 3.4 SEM micrographs of berthierine type 1. (a) Subtype I: as coating on a glauconite grain, Well Siri-2, oil leg. (b) Subtype II: berthierine coating on dissolved feldspar. (c) Subtype III: berthierine coating surrounded by quartz overgrowth, Well Siri-2, oil leg; (d) Berthierine coating on quartz overgrowth, Well Siri-2, OWC. (e) Subtype IV: berthierine net with attached pyrite framboids, Well Siri-1, oil leg (Fu, 2014); (f) Berthierine net coating microquartz, Well Siri-2, OWC. B: berthierine; G: glauconite; Q: quartz; Qo: microquartz; M: mica; S: siderite; P: pyrite; C: calcite cement.

Type 5 berthierine exclusively fills pores of siderite concretions as fine blade crystal (1−2 μm) which appear perpendicular to siderite crystals (Figs. 3.5e, 3.7a and 3.7b).

Importantly, the pores in siderite concretions contain residual immobile oil (Figs. 3.7a, 3.7b). This type 5 berthierine is closely associated with siderite concretions which only occur in several depth intervals of the oil leg (Table 3.2).

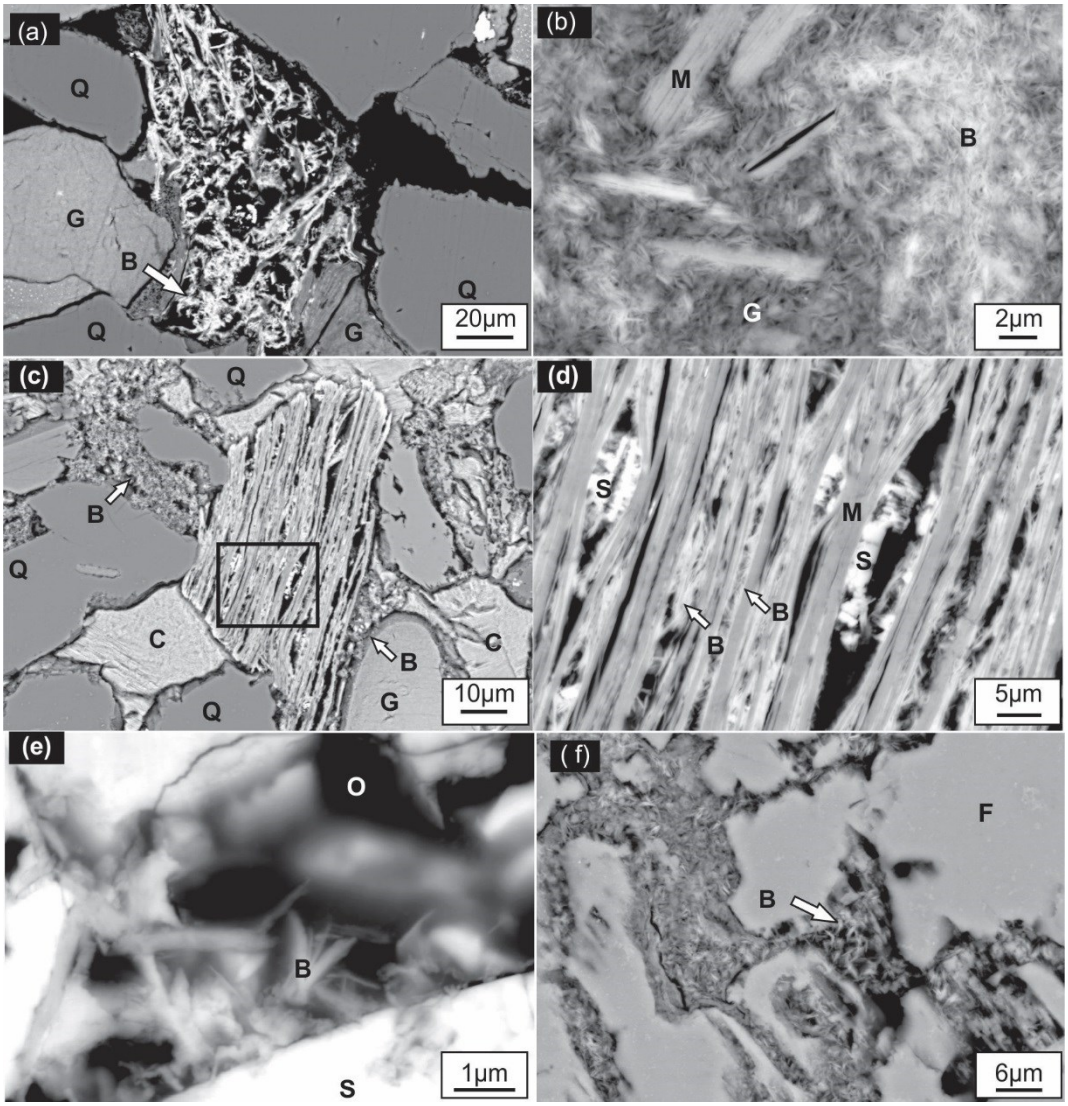

Figure 3.5 BSE images of berthierine types. (a) Type 3: berthierine (bright area) growing in strongly dissolved glauconite, Well Siri-2, oil leg; (b) Growth of berthierine crystals (bright areas) together with muscovite in transforming glauconite, Well Siri-2, OWC. (c) Type 2: pore filling berthierine (the upper left corner) cemented by calcite. The glauconite grain in the lower right corner is covered by berthierine type 1 (white arrow), Well Siri-2, OWC. (d) Type 4: as elongated crystals together with newly formed siderite between lamellae of mica transformed from glauconite. High resolution image of the rectangle area in c, Siri-2, OWC. (e) Type 5: berthierine in siderite concretions, Well Siri-2, Oil leg. (f) Type 1, Subtype II: berthierine growing in dissolved feldspar, Well Siri-2, oil leg. B: berthierine; G: glauconite; Q: quartz; M: mica; C: calcite cement; S: siderite; O: residual oil; F: feldspar.

In summary, the five berthierine types occur in all parts of the Heimdal Member but are concentrated in the oil leg and at the oil-water contact rather than in the gas cap or the water leg. However, the highest amounts of total berthierine were observed in samples from the OWC (Table 3.2).

Table 3.1 Point counted composition of samples from well Siri-2.

Depth (m)	Zone	Detrital (%)				Authigenic (%)					Porosity %	Sum %
		Quartz	Feldspar	Glauconite	Mica	Quartz overgrowth	Berthierine	Kaolinite	Siderite	Calcite		
2102.80	Gas cap	33.1	14.97	48.07	0.35	4.91	2.57	1.52	0.12	2.11	19.53	100
2104.40	Gas cap	26.32	17.19	43.51	2.11	3.68	2.63	4.39	—	0.18	13.68	100
2108.40	Oil leg	26.32	20.18	46.49	1.58	2.98	2.98	1.58	0.88	0.35	11.58	100
2110.60	Oil leg	34.74	13.68	48.42	2.28	4.56	1.93	2.11	0.18	—	16.67	100
2113.15	Oil leg	23.86	17.02	40.88	1.58	4.04	4.39	2.98	7.72	—	13.51	100
2116.30	OWC	24.56	14.56	39.12	0.18	2.98	7.72	0	0.35	36.14	—	100
2116.90	OWC	25.26	15.61	40.88	2.46	3.86	3.86	2.81	2.81	9.3	11.05	100
2136.55	Water leg	32.11	17.37	49.47	1.93	5.96	1.93	2.98	1.75	—	12.98	100

— indicates absence.

Table 3.2 Occurrence of five different berthierine types in the Heimdal sandstone of Siri field

Locations	Type 1				Type 2	Type 3	Type 4	Type 5
	Subtype I	Subtype II	Subtype III	Subtype IV				
Gas cap	x	x		x	x	x	xx	
Oil leg	xx	x	x	xxx	x	xx	xxx	xx
OWC	xx	x		xxx	xx	xxx	xxx	x
Water leg	x	x	x	x	x	x	x	

Such observed occurrence is a semi-quantitative presentation based on microscopic appearance. Occurrence: x = few; xx = mean; xxx = frequent.

3.6.3. TEM studies about berthierine formation in the presence of oil

Detailed TEM studies were carried out to further investigate the potential relationship between authigenic berthierine, specific characteristics of oil phases and associated minerals. The FIB sections were cut from characteristic interfaces observed in thin sections where residual oil was trapped in small pores or where oil-stained minerals or oil-stained mineral assemblages were present.

The TEM investigations highlight that berthierine crystals are intimately associated with glauconite, siderite, quartz, and mica, but that there is also a direct relationship with the co-occurring oil phases. Berthierine crystals were precipitated close to glauconite in nanopores which are filled with degraded oil and/or mineralized oil-water emulsions (Fig. 3.6; sample from the OWC). Berthierine crystals formed on the surface of siderite crystals and bridge them, but also precipitated in oil-filled pores (Figs. 3.7a-d; sample from the oil leg). Berthierine crystals also formed together with siderite crystals in oil-filled pores between lamellae of mica and also as thin layers in lamellas. Furthermore, they are associated with secondary quartz precipitates in oil-filled pores (Figs. 3.7e-g; sample from the gas cap).

In summary, berthierine in the Heimdal Member of the Lista Formation formed as a 0.7 nm iron-rich phyllosilicate, a berthierine-1H (a Fe-serpentine after Brindley, 1982; see insert in Figs. 3.6e, 3.7d, 3.7f, and selected area electron diffraction (SAED) pattern in Fig. 3.7g). The nanometer-sized berthierine crystals display an intimate relation to oil in pores. Such oil can occur as localized and pure single phase (e.g., in Figs. 3.6c, 3.7a, 3.7e) or structurally resemble mineralized oil-water emulsions (Fig. 3.6f).

3.6.4. Chemical composition of berthierine

The results of representative microprobe analyses of six berthierines crystals from the oil leg and three from the water leg are given in Table 3.3. Berthierine is predominantly composed of Fe with only minor variations (34.14−38.19 wt.-% FeO), which is consistent with most analyses found in the literature. However, SiO_2 (27.6−30.36 wt.-%) and Al_2O_3 contents (19.49−22.2 wt.-%) show small variations, whereas MgO contents vary from 3.08 wt.-% to 5.24 wt.-%. Other elements (given as oxides), such as MnO, CaO, Na_2O, and K_2O, occur in minor concentrations. It is important to note that all nine investigated berthierine

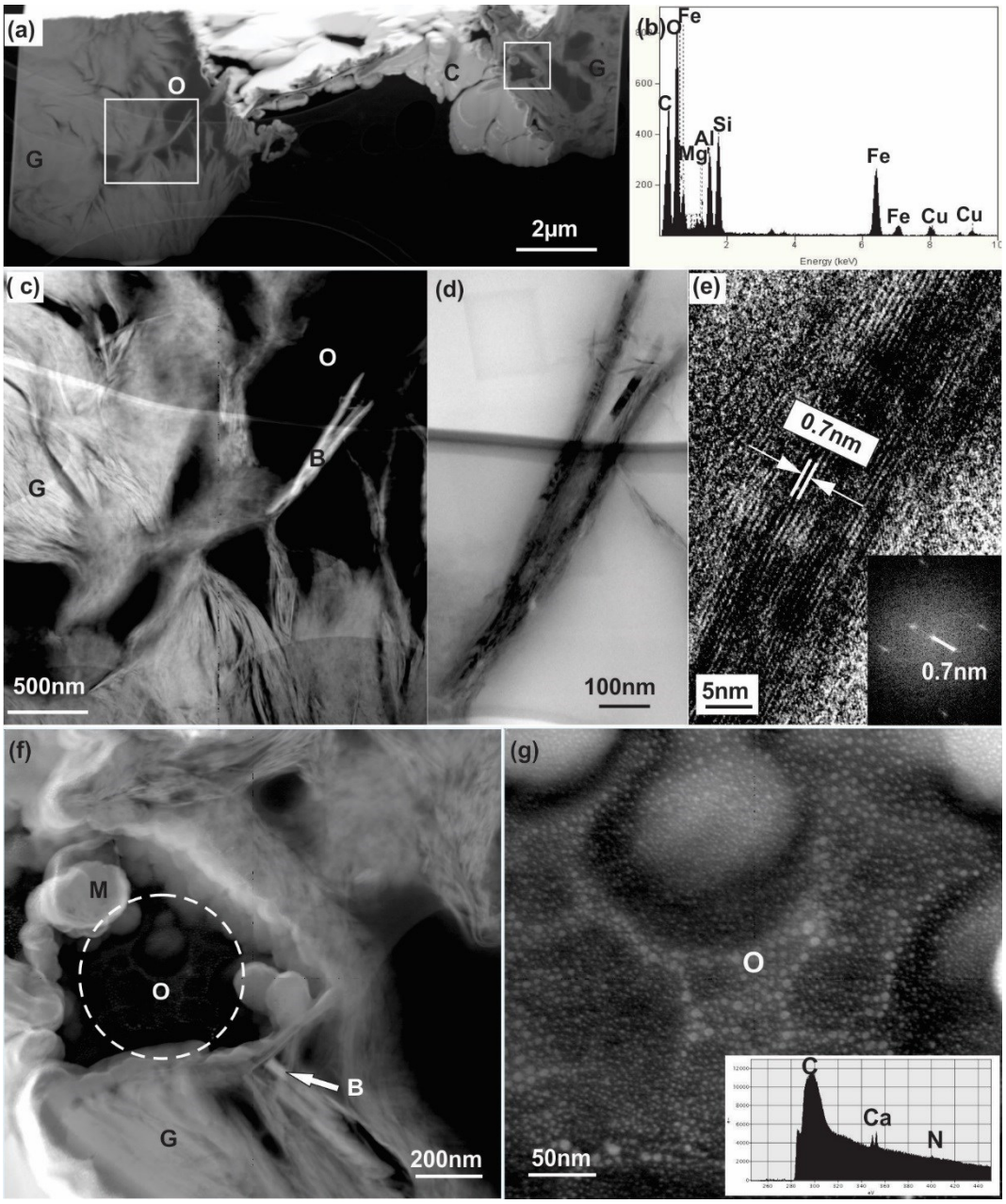

Figure 3.6 TEM investigations of berthierine type 1 and 4. Type 1 berthierine (a-e) coating glauconite grains in direct contact with residual oil. (a) High-magnification scanning transmission electron microscopy (STEM) image (high-angle annular dark-field [HAADF] mode) of a focused ion beam (FIB) foil. (b) EDS spectrum of berthierine in c. (c) High resolution image of the left white rectangle in a. (d) Bright-field image of berthierine in c. (e) High-resolution transmission electron microscopy (HRTEM) image of berthierine in d showing lattice fringes with 0.7 nm periodicity. The insert shows a selected area electron diffraction (SAED) pattern with a pronounced 0.7 nm periodicity. Type 3 berthierine (e-f) in transforming glauconite close to a mineralized oil-water emulsion. (f) High resolution image of the right rectangle in a. Berthierine co-occurs with small Mn-oxide particles close to a mineralized oil-water emulsion (white dotted circle) in a glauconite pore. (g) High resolution image of the white circle in f shows small organic matter particles with carbon, calcium and nitrogen contents

(illustrated in the inserted electron energy loss spectroscopy (EELS) spectrum). G: glauconite; B: berthierine; C: calcite; O: oil; M: Mn-Ti oxide. Well Siri-2, OWC.

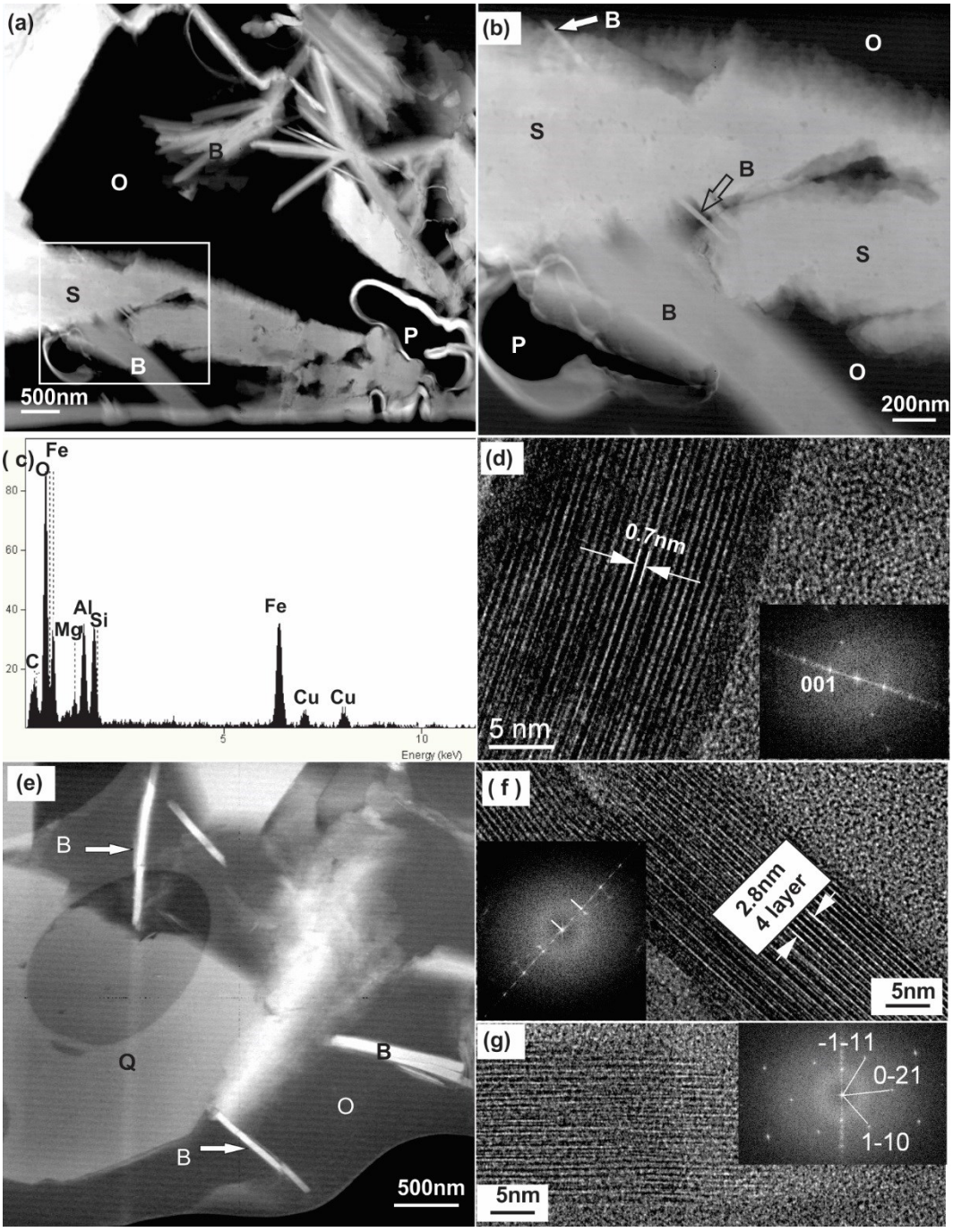

Figure 3.7 TEM investigations of berthierine type 5 (a-d) and type 2 (e-g). Type 5 berthierine (a-d) as blade-like particles in a siderite concretion. (a, b) High-magnification scanning transmission electron microscopy (STEM) images (high-angle annular dark-field [HAADF] mode) of a focused ion beam (FIB) foil extracted from the red rectangle in Figure 3.2b. (a) Growth of 1 μm large fibre-shaped berthierine in oil-filled pore. (b) High resolution image of the white rectangle area in a. Berthierine bridges siderite crystals. Additional berthierine (white arrow) is growing on a siderite surface. (c) EDS analysis of the berthierine bridge marked by the black arrow in b. (d)

High-resolution transmission electron microscopy (HRTEM) image of the berthierine bridge in b with the insert displaying its calculated diffraction (fast Fourier Transform FFT) pattern of 0.7 nm periodicity. Type 2 berthierine (e-g) in open pore space filled by residual oil. (e) Several fibrous berthierine crystals in oil near an authigenic microquartz grain. (f) High-resolution transmission electron microscopy (HRTEM) image of one fibrous berthierine crystal in e with well-defined 0.7 nm lattice fringes and selected area electron diffraction (SAED) pattern of 0.7 nm periodicity (insert). (g) High-resolution transmission electron microscopy (HRTEM) image and selected area electron diffraction (SAED pattern (insert) of the upper left berthierine in e. S: siderite; B: berthierine; O: oil; P: pore; Q: microquartz. Figure 3.7a-d: Well Siri-2, oil leg; Figure 3.7e-g: Well Siri-2, gas cap.

crystals are chemically similar. The overall chemical similarity of berthierine in this study indicates that berthierine precipitation in the oil and water leg of the Heimdal reservoir took place under similar hydrogeochemical conditions. However, they compositionally differ from berthierine crystals reported in other studies (Brindley, 1982; Hornibrook and Longstaffe, 1996; Lu et al., 1994; Stokkendal et al., 2009; Toth and Fritz, 1997; Fig. 3.8). Berthierine crystals investigated in this study are enriched in Si^{4+} compared to berthierine in the Clearwater formation (Hornibrook and Longstaffe, 1996), and are enriched in Al^{3+} and Fe^{3+} compared to berthierine in the Hermod sandstone (Stokkendal et al., 2009). However, the chemical composition of berthierine in the Heimdal sandstone (this study) closely resembles the pore-filling berthierine in the Silurian Rose Hill Formation (Lu et al., 1994; Fig. 3.8). This chemical similarity may be explained by similar mineralogical educts, which are detrital Fe-Mg silicate grains (unspecified) in the Rose Hill Fm. (Lu et al., 1994) and glauconite in the Heimdal sandstone.

The chemical structure of berthierine as shown in Table 3.3 was calculated on the basis of 7 oxygens, using the procedure described by Brindley (1982). Since berthierine belongs to the serpentine group, it can be represented by the formula $(R^{2+}_a\ R^{3+}_b\square_c)(Si_{2-x}\ Al_x)O_5(OH)_4$ where R^{2+} and R^{3+} are cations (Fe^{2+}, Mg^{2+}, Fe^{3+}, Al^{3+}) occupying octahedral positions; represents possible vacant octahedral positions, and a+b+c=3 (Brindley, 1982). To calculate the structural formula, the total valence of cations in tetrahedral and octahedral positions was normalized to +14. This procedure ideally corresponds to an oxygen + water content $O_5(OH)_4$. Cations such as Na^+, K^+, and Ca^{2+} which cannot occupy octahedral positions are listed as small oxide percentages which can often be attributed to impurities. Tetrahedral positions not filled by Si^{4+} are filled by Al^{3+} cations. The formula of berthierine was calculated as presented in Table 3.2. At the tetrahedral sites, 20−27 mole% of Si are substituted by Al, and octahedral

Al always exceeds tetrahedral Al. Compared with data summarized by Toth and Fritz (1997), berthierine in this study has a 5 mole% less Fe content averaging at 1.645 mol%, whereas it has a 5 mole% higher Si content averaging at 1.541 mol%. The Si:Al molar ratio is higher than most of the reported berthierine data. Such high silica contents require a less Al substitution in the tetrahedral layer (here: 18 mole% less Al in tetrahedral layers). The Si:Al molar ratio is higher than most of the reported berthierine data. Such high silica contents require a less Al substitution in the tetrahedral layer (here: 18 mole% less Al in tetrahedral layers).

Table 3.3 Representative microprobe analyses (wt.-%) and structural formulae of berthierine crystals in one core sample from the oil leg and one sample from the water leg.

	Oil leg						Water leg		
	1	2	3	4	5	6	7	8	9
SiO_2	30.28	30.36	28.51	26.38	27.65	27.88	29.42	29.21	27.6
FeO	35.48	37.38	37.19	38.19	36.75	37.31	35.19	34.14	36.81
Al_2O_3	21.95	22.2	21.54	21.74	21.03	21.28	19.8	19.49	20.42
MgO	3.7	3.67	3.08	3.25	3.62	3.59	4.66	5.24	4.09
MnO	0.06	0.09	0.08	0.07	0.1	0.06	0.07	0.1	0.09
CaO	0.44	0.37	0.36	0.34	0.22	0.11	0.29	0.69	0.24
Na_2O	0.14	0.26	0.1	0.16	0.35	0.32	0.35	0.26	0.32
K_2O	0.23	0.19	0.35	0.11	0.05	0.07	0.86	1.12	0.53
Total	92.28	94.52	91.2	90.24	89.77	90.62	90.63	90.26	90.1
Si^{4+}	1.587	1.566	1.538	1.455	1.517	1.516	1.588	1.582	1.516
Fe^{2+}	1.555	1.613	1.677	1.762	1.687	1.697	1.588	1.546	1.691
Al(tet)	0.41	0.43	0.458	0.541	0.478	0.481	0.409	0.413	0.48
Al(oct)	0.947	0.92	0.911	0.873	0.883	0.884	0.851	0.831	0.843
Mg^{2+}	0.289	0.282	0.247	0.267	0.296	0.291	0.375	0.423	0.335
Mn^{2+}	0.003	0.004	0.004	0.003	0.005	0.003	0.003	0.005	0.004
Ca^{2+}	0.025	0.021	0.021	0.02	0.013	0.007	0.017	0.04	0.014
Na^{+}	0.014	0.026	0.011	0.017	0.038	0.033	0.037	0.028	0.034
K^{+}	0.016	0.013	0.024	0.007	0.003	0.005	0.059	0.078	0.037
□	0.208	0.184	0.164	0.098	0.135	0.128	0.186	0.2	0.13
Fe/(Fe+Mg)	0.84	0.85	0.87	0.87	0.85	0.85	0.81	0.79	0.83
Mg/Fe	0.19	0.18	0.15	0.15	0.18	0.17	0.24	0.27	0.2
Al/Si	0.85	0.86	0.89	0.97	0.9	0.9	0.79	0.79	0.87

Total Fe as FeO. The formulae were calculated on the basis of 7 oxygens. Oxides are in weight percentage; ions are in mole percentage.

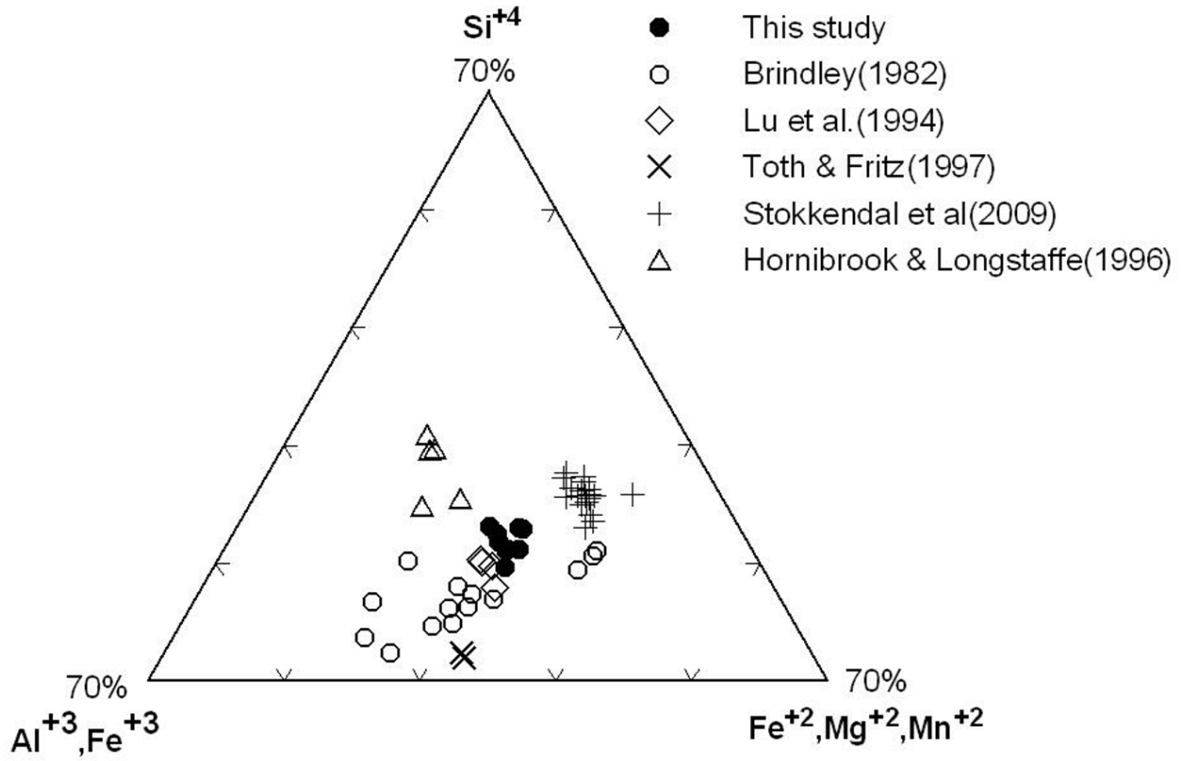

Figure 3.8 Measured cation composition of berthierine in a ternary plot in comparison with the results from other studies (Brindley, 1982; Hornibrook and Longstaffe, 1996; Lu et al., 1994; Stokkendal et al., 2009; Toth and Fritz, 1997).

3.6.5. Organic geochemistry

Oil alteration can be assessed by ratios of branched against *n*-alkanes (Welte et al., 1982), since it is assumed that straight-chained *n*-alkanes like *n*-heptadecane (*n*-C_{17}) are more susceptible to be degraded than isoprenoids such as pristane (Wenger et al., 2002). A plot of pristane/*n*-C_{17} against phytane/*n*-C_{18} is the most commonly used evaluation to describe the extent of oil alteration in low to moderately biodegraded oil. The increasing values of pristane/*n*-C_{17} and phytane/*n*-C_{18} indicate an increasing extent of oil degradation from the gas cap and the oil leg towards the oil-water contact (Fig. 3.9). Thus, it appears that the highest oil degradation took place at the OWC which is the major reactive interface for oil degradation.

3.7. Discussion

The occurrence of berthierine was reported from various depositional environments highlighting the wide variability of possible crystal morphologies. In contrast to frequently reported berthierine ooids in non-oil bearing ironstones (Madon, 1992; Taylor and Curtis, 1995), berthierine in the Heimdal sandstone of the Siri oilfield mainly occurs as grain-coatings and pore-fillings. Moreover, berthierine in the Heimdal sandstone also grew in dissolved detrital glauconite grains and mica (Figs. 3.5a-d), or in form of mineralized net-like structures (Figs. 3.4e, 3.4f). Despite these association differences, the chemical berthierine uniformity in the Heimdal sandstone in figure 3.8 indicates that berthierine was formed under similar hydrogeochemical conditions.

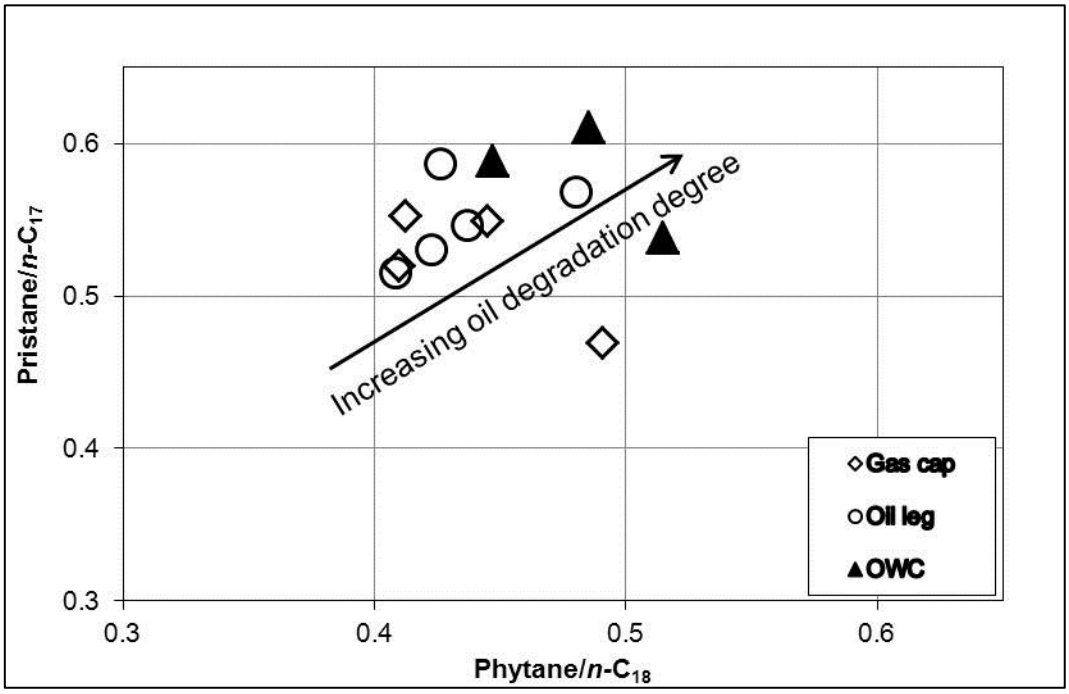

Figure 3.9 Plot of Pr/*n*-C_{17} versus Ph/*n*-C_{18} for 12 samples from the gas cap, the oil leg and OWC in well Siri-2.

3.7.1. In-situ berthierine formation

A detrital origin in form of sand deposition with berthierine as a detrital mineral can be ruled out, since berthierine coatings on detrital grains would have been completely or at least partly eroded from the grain surfaces due to sand transport over long distances (20−75 km) from the Stavanger platform area (Danielsen et al., 1995; Hamberg et al., 2005). In addition, berthierine also filled pores and is absent on grain-grain contacts (Figs. 3.2d, 3.2f, 3.2g, and

3.5c), furthermore suggesting that berthierine formation must have taken place after compaction.

The euhedral habits of berthierine in oil-filled pores clearly indicate an in-situ formation. Berthierine crystals are frequently oriented vertically on grain surfaces (Figs. 3.4a, 3.4d), which is considered to be a characteristic of authigenic crystals (Coombs et al., 2000). Moreover, the in-situ precipitation of berthierine is also supported by its characteristic relationship to other minerals in the reservoir sandstone. Berthierine crystals co-occur in or on dissolved feldspar grains, suggesting that berthierine formed after or simultaneously with feldspar dissolution (Figs. 3.4b, 3.5f). Additionally, berthierine and quartz growth co-occurred, and the formation of berthierine may even postdate quartz growth since network-like berthierine networks cover microquartz overgrowth (Fig. 3.4f) and grain-coating berthierine was observed to cover quartz overgrowth (Figs. 3.2d, 3.4d). In addition, the interfaces between quartz overgrowths on quartz detrital grains often contain oil or small oil-water containing inclusions, indicating that quartz overgrowth started parallel with oil filling and continued. Thus, it can be inferred that berthierine formed parallel with and/or postdates oil filling. Berthierine occurs in dissolving glauconite grains and lamellae of mica/micaceous glauconite (Figs. 3.2c, 3.5c and 3.5d), but also replaced glauconite grains (Fig. 3.5a). Furthermore, berthierine is most abundant at the oil-water (OWC) which corresponds to relatively low amounts of glauconite (Table 3.1). These observations point to glauconite as a precursor for berthierine in the Heimdal sandstone.

3.7.2. Berthierine formation

Precipitation of berthierine requires a depositional environment characterized by a massive supply of iron and reducing conditions (Curtis, 1985; Curtis and Spears, 1968). The influx of an external iron-rich fluid in an open system was considered to provide the iron for berthierine formation in porous sandstones (Lu et al., 1994; Stokkendal et al., 2009). However, Fu (2014) and Fu et al. (2015a) suggested that such fluid influxes are not controls for extensive berthierine formation as observed in the Siri field (5−15 vol.-% according to Stokkendal et al., 2009) due to the low concentrations of other aqueous species (e.g., Mg^{2+}, H_4SiO_4, and $Al(OH)x^{+3-x}$) in such fluids.

Alternatively, berthierine in the Heimdal sandstone may have formed in a closed system in which the dissolution of glauconite and other minerals would have provided the required

aqueous species composition needed for berthierine formation. Ferric iron dominates in glauconite compared to the dominance of ferrous iron in berthierine. Under anoxic conditions, the equilibration of glauconite with formation water may lead to the release of the following aqueous species into the formation water: K^+, Na^+, Mg^{2+}, Ca^{2+}, SiO_2(aq), Al^{3+}, Fe^{2+}, and Fe^{3+} (Fig. 3.10). These released Fe^{3+} species are incapable of being removed from the formation water under anoxic and acidic conditions, and their relatively high activity prevents further glauconite dissolution. In contrast, Fe^{3+} species are transformed to Fe^{2+} species under reducing conditions. This leads to an oversaturation with regard to berthierine and enables its precipitation. Thus, dissolution of primary glauconite and following precipitation of berthierine needs reducing conditions and a sufficient supply with reducing agents. Oxidation of organic matter due to the iron reduction pathway during early diagenesis (prior to oil charging) may also lead to berthierine formation (Taylor and Macquaker, 2011). However, the petrographic investigations showed that the sandstones of the Siri field are poor in sedimentary organic matter. Organoclasts such as lignite, alginite, etc., were not observed in the Heimdal sandstone. Thus, it can be inferred that only small amounts of berthierine formed by iron reduction during early diagenesis due to the lack of reducing agents such as sedimentary particulate organic matter.

Based on the above-presented considerations, an alternative explanation for the occurrence of berthierine in the Heimdal sandstone is presented which relates it to oil degradation in the reservoir. The oil which originally was or which today is in the reservoir can act as a reductant for Fe^{3+} in glauconite into Fe^{2+}. Due to this reduction, glauconite dissolution proceeded, causing hydrogeochemical conditions leading to the precipitation of berthierine (Fig. 3.10). Evidence for this scenario can be clearly observed in figure 3.2e.

3.7.3. Organic-inorganic interactions due to oil degradation: the control of berthierine formation

Anaerobic oil degradation is a well-known process and controlled by a maximum temperature of around 80 °C (Wilhelms et al., 2001). Oil degradation takes place near the oil-water contact (Larter et al., 2003), but also occurs throughout the hydrocarbon column in water-wet reservoirs, especially in the irreducible water film (e.g., Wenger et al., 2002). The products of anaerobic hydrocarbon degradation (oxidation of, e.g., aqueous n-alkanes) are methane, carbon dioxide, hydrogen, and acetic acid which are being released into the pore

water (Seewald, 2003; Fig. 3.10). A consequence of these processes is that reactive minerals (glauconite and feldspars) may dissolve under the changed hydrogeochemical conditions and that minerals such as berthierine may newly form (Fig. 3.10).

Oil degradation

The today´s produced oil in the Siri field has API gravities of more than 35°. However, the first oil filling might have also undergone degradation when the reservoir was buried to approximately 1,000m depth (Hamberg et al., 2005; Ohm et al., 2006). Tectonic movements led to leakage and a second filling phase later. In addition, the present-day gas in the Siri field, which is dissolved in oil, is characterized by δ^{13}C-methane values of around −50‰, by δ^{13}C-ethane values of around −33‰, and by low gas wetness values of less than 10 (Ohm et al., 2006). Such data also indicate a slight degradation level of the present-day oil and that biogenic methane gas contributions due to oil degradation are assumed for the investigated Siri fields.

A striking feature pointing to oil degradation are the berthierine net-like structures (berthierine type 1, subtype IV; Figs. 3.4e, 3.4f) which resemble mineralized oil-water emulsions (e.g., Mandal et al., 2010; Sullivan and Kilpatrick, 2002). The occurrence of oil-water emulsions is known from oil-water contacts where they are stabilized, e.g., by asphaltenes (which are enriched in degraded oils). In general, they occur in reservoirs with API gravities lower than 25° and temperatures lower than 66 °C, but also occur in tar mats in oil reservoirs (Wilhelms and Larter, 1994a, 1994b).

Evidence for a potential formation of the mineralized oil-water emulsions due to oil degradation is a higher degradation rank of the investigated oil in the Heimdal sandstone. Increased nitrogen contents of oil in an electron energy loss spectroscopy (EELS) spectrum (insert in Fig. 3.6g) may indicate oil alteration. Since crude oil contains less than 1% nitrogen, the enrichment of heterocyclic aromatic compounds containing nitrogen, sulfur, or oxygen (NSO compounds) reflects oil alteration processes (Curiale et al., 1983). Oil alteration is also assessed by plotting pristane/*n*-C_{17} versus phytane/*n*-C_{18} (Fig. 3.9). Samples from the OWC show a relatively high extent of oil degradation indicated by relatively higher values of Pr/*n*-C_{17} and Ph/*n*-C_{18} at the OWC compared with samples from the gas cap and the oil leg (Fig. 3.9). In these intervals (together with the oil leg), most of the authigenic berthierine occurs (Table. 3.1), and supports our observations about a genetic relation between oil degradation and berthierine formation in the Heimdal sandstone in the Siri field.

Organic-inorganic interactions triggered by oil degradation leading to berthierine formation

Our working hypothesis is that berthierine formation in the Siri field is due to glauconite dissolution within a close system due to gas-fluid-rock interactions driven by oil degradation at oil-water contacts but also at oil-water interfaces in the oil-filled reservoir (Fig. 3.10). The water saturation of the Heimdal sandstone is as high as 30−40% in the oil leg and the Heimdal sandstone is thus water-wet. In water-wet reservoirs, extensive oil-water interfaces may be still maintained by water-coated mineral surfaces when aqueous pore fluids are displaced by hydrocarbons (Karlsen et al., 1993; Treiber et al., 1992). At such oil-water interfaces, which thus also exist in the oil leg, the important reaction named "hydrolytic disproportionation" (Seewald, 2003) may take place during which oil degradation products (methane, carbon dioxide, hydrogen, and acetate) are being released into the pore water.

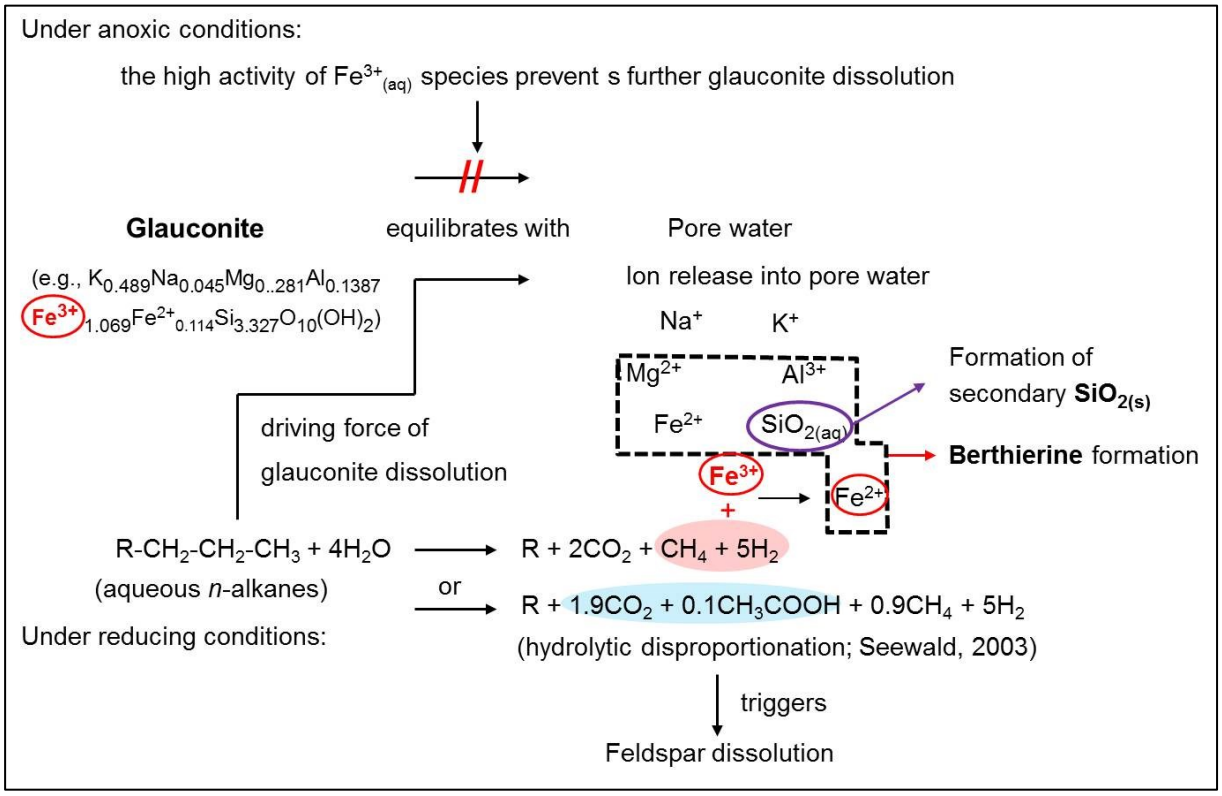

Figure 3.10 Conceptual model sketch as a result of observations showing berthierine formation and potential co-existing reactions in the Heimdal sandstone due to fluid-rock interactions triggered by oil degradation.

Consequently, minerals which are thermodynamically unstable at specific hydrogeochemical conditions, e.g., glauconite and feldspars, firstly dissolve and release K^+, Na^+, Mg^{2+}, Ca^{2+}, SiO_2(aq), Al^{3+}, Fe^{2+}, and Fe^{3+} species into the formation water. In addition,

with the supply of reducing agents from oil degradation, such as CH_4, H_2, and CH_3COOH (acetic acid) generated at oil-water interfaces, the reduction of Fe^{3+} (mainly released from glauconite) to Fe^{2+} may take place (Fig. 3.10) and leads to berthierine formation when its saturation is achieved. Berthierine formation may be favored close to iron-bearing minerals (e.g., glauconite) due to the short transportation distance of ions (Bjørlykke and Jahren, 2012). Potentially co-existing reactions may lead to quartz overgrowth (Fig. 3.10; Fu, 2014; Fu et al., 2015a).

3.7.4. Implications

Fluid-rock interactions may alter the original composition of petroleum fluids trapped in petroleum reservoirs, but consequently also the aqueous phase and the mineral matrix. A threshold of around 80°C is discussed for such "degradation" processes (Wilhelms et al., 2001), but hydrolytic disproportionation may continue at higher temperatures and can lead to further degradation of petroleum compounds (Seewald, 2003). However, quantitative approaches about the overall consequences of such complex organic-inorganic interactions are still rare, and the significance of such processes is underestimated.

The conversion of mineralizable organic components is an overall control for severe changes of the mineral matrix in sedimentary basins. Mineralizable organic matter occurs from shallow to great depth and is thus ubiquitously available for coupled organic-inorganic interactions. The actual processes take place in aqueous phase which mainly occur in residual water in pores and in the irreducible water film around mineral grains. By far the most significant interface for such processes is the OWC in oil fields. The presented data about the Siri field in the Danish North Sea highlight the possible conversion of glauconite into berthierine at such interfaces, but also point to the fact that altered petroleum residues are involved in this complex web of interconnected processes. However, the presented results raise new questions. How much of the petroleum needs to be converted to cause the observed present mineral composition of the Heimdal reservoir in the Siri field? Is the observed precipitation of berthierine an indicator of an intense oil degradation? The more observations, the more questions. Quantitative approaches are needed to answer questions about the "where", "when", and "how much" of complex rock-fluid-gas interactions. Such new conceptual approaches have strong implications for the assessment of reservoir properties and possible production measures. Moreover, quantitative hydrogeochemical modelling may help

to unravel the diagenetic histories of sedimentary sequences in basins which host organic-rich intervals (such as oil-bearing reservoirs, black shales or coal measures) which may release products like methane, carbon dioxide, etc. during diagenetic process. In consequence, mass balancing will highlight the significance of such organic compounds for the diagenetic history of sedimentary basins, and will not exclusively rely on "classical" diagenetic models.

3.8. Conclusions

1. Berthierine is the only authigenic Fe-rich clay mineral which occurs in the Heimdal sandstone revealed by applying a combination of various analytical methods. It appears as grain-coating, pore-filling and also as blade-like crystals in glauconite, mica and siderite concretions. Berthierine predominantly occurs at the oil-water contact and shows similarly chemical composition independent on type. Its relationship with other minerals indicates that it formed in-situ and after oil emplacement.

2. Berthierine frequently grows in glauconite and partly replaces glauconite grains. Its predominant abundance at the OWC, where the lowest amounts of glauconite prevail, points to glauconite as the precursor for berthierine. Since berthierine formation requires sufficient organic matter, which is not abundant in the Heimdal sandstones prior to oil charging, the oil filling and its degradation products in the Heimdal sandstones could have created suitable conditions for berthierine formation.

3. The Siri field shows a slightly higher degree of oil degradation at the oil-water contacts by higher values of Pr/*n*-C_{17} and Ph/*n*-C_{18}. The possible concept for the formation of berthierine could be that oil degradation products (CH_4, H_2, CO_2, and CH_3COOH) dissolved in formation water, lowered pH, and, consequently, led to dissolution of thermodynamically unstable minerals (such as glauconite, mica and feldspar) and to the precipitation of thermodynamically stable minerals, e.g., quartz overgrowth, siderite and berthierine.

4. Unlike previous hypotheses to explain the origin of berthierine in (Boyd et al, 2004; Hornibrook and Longstaffe, 1996; Lu et al., 1994), the presented results offer a new interpretation concept of berthierine formation: oil emplacement and following oil degradation may have caused a web of interconnected processes during which berthierine formed in oil-filled zones, especially in water-wet reservoir units.

3.9. Acknowledgements

Funding of Nana Mu was provided by the Chinese Scholarship Council (CSC). The authors would like to thank DONG Energy and the Geological Survey of Denmark and Greenland for supporting the study, and for access to core samples and data. The original manuscript was improved following reviews by Lynda Williams. Professor Carlos Rossi Nieto and an anonymous reviewer are thanked for their constructive reviews that helped to improve the manuscript.

Chapter 4 Authigenic albite formation due to fluid-rock interactions - Case study: Magnus oilfield (UK, Northern North Sea)

4.1. Abstract

It is the aim of this contribution to test whether organic-inorganic interactions could induce the formation of authigenic albite. This concept and related results are being compared with modelling scenarios which are purely based on inorganic geochemical reactions. In order to unravel the pathway of authigenic albite formation, this paper presents results of a multidisciplinary study of imaging, geochemistry, mineralogy, and hydrogeochemical modelling. The Jurassic reservoir sandstones of the Magnus oilfield (UK, North Sea) were chosen as a test site.

Albite occurs with 4-18 wt.-% in the Magnus sandstones and its contents vary with depth. However, albite contents increase with increasing K-feldspar contents and decreasing grain size. It occurs in three forms: (1) as lamellae in perthite, (2) as overgrowth on/in corroded feldspar, and, (3) as cloudy replacing albite patches in K-feldspar. The albite overgrowth has the highest chemical purity (100% albite) while albite lamellae and replacing albite patches are slightly less pure (containing 1-4% anorthite). Albite appears non-altered and has a euhedral morphology and dull cathodoluminescence. It commonly co-occurs with corroded K-feldspar grains.

The precipitation of diagenetic albite in the Magnus sandstones is attributed to deep burial 80 Ma ago and may have continued until today at temperatures between 90-120°C. The results of hydrogeochemical modelling offer two possible pathways for the authigenic albite formation: (1) Dissolution of unstable minerals (such as kaolinite and chalcedony) coupled to

This chapter has been published as: Mu, N., Fu, Y., Schulz, H.-M., van Berk, W., 2016. Authigenic albite formation due to water-rock interactions – Case study: Magnus oilfield (UK, Northern North Sea). Sedimentary Geology, 331, p. 30-41. DOI: http://doi.org/10.1016/j.sedgeo.2015.11.002

reduction of ferric iron minerals due to products generated during oil generation, migration and degradation; (2) Dissolution of non-end member feldspar, such as K-feldspar with 10% albite, coupled to illite formation can account for trace amounts of albite due to an elevated Na^+/K^+ activity ratio in the pore water.

Keywords

Albite; Jurassic; sandstone; rock-water interaction; Magnus oilfield; North Sea

4.2. Introduction and aim

In hydrocarbon-bearing systems, the driving force of organic-inorganic interactions is the conversion of thermodynamically labile organic compounds into reactive and soluble inorganic components. Water is the matrix for such complex and interrelated hydrogeochemical reactions. However, such processes are also dependent on a variety of other controls such as temperature and/or pressure. The composition of the mineral phase assemblage, the type of water (e.g., the content of total dissolved solids, pH, EH, etc.) and of co-existing gases (e.g., CO_2 partial pressure) are further important controls.

In oilfields, the hydrolytic disproportionation of low-molecular hydrocarbons across the reactive oil-water transitional zone may stimulate organic-inorganic interactions. It is argued to be the result of an irreversible production of carbonic acid. This basic assumption led Helgeson et al. (1993) in their ground-breaking article to speculate about metastable equilibria between petroleum, oilfield waters, and authigenic mineral assemblages. One topic in this respect was whether organic-inorganic interactions could lead to albite formation. In this contribution, we test whether such a hypothesis is valid for albitization of feldspar or precipitation of albite crystals, and will compare the measured/observed results with results from alternative modelling concepts which are exclusively based on inorganic geochemical reactions triggered by temperature and pressure.

In a first step, we present results about the content, petrographic characteristics and chemical composition of albite in the Jurassic sandstone reservoir of the Magnus oilfield leading to first considerations about the origin and potential hydrogeochemical conditions of albite formation. In a second step, results of hydrogeochemical models calculated by using the computer code Phreeqc are presented. The results of these conceptual model approaches aim to unravel possible pathways of authigenic albite formation in a quantitative way regarding

thermodynamic principles. Baseline data for modelling are mineral assemblages, data about formation water composition, potential slight oil degradation, and burial history.

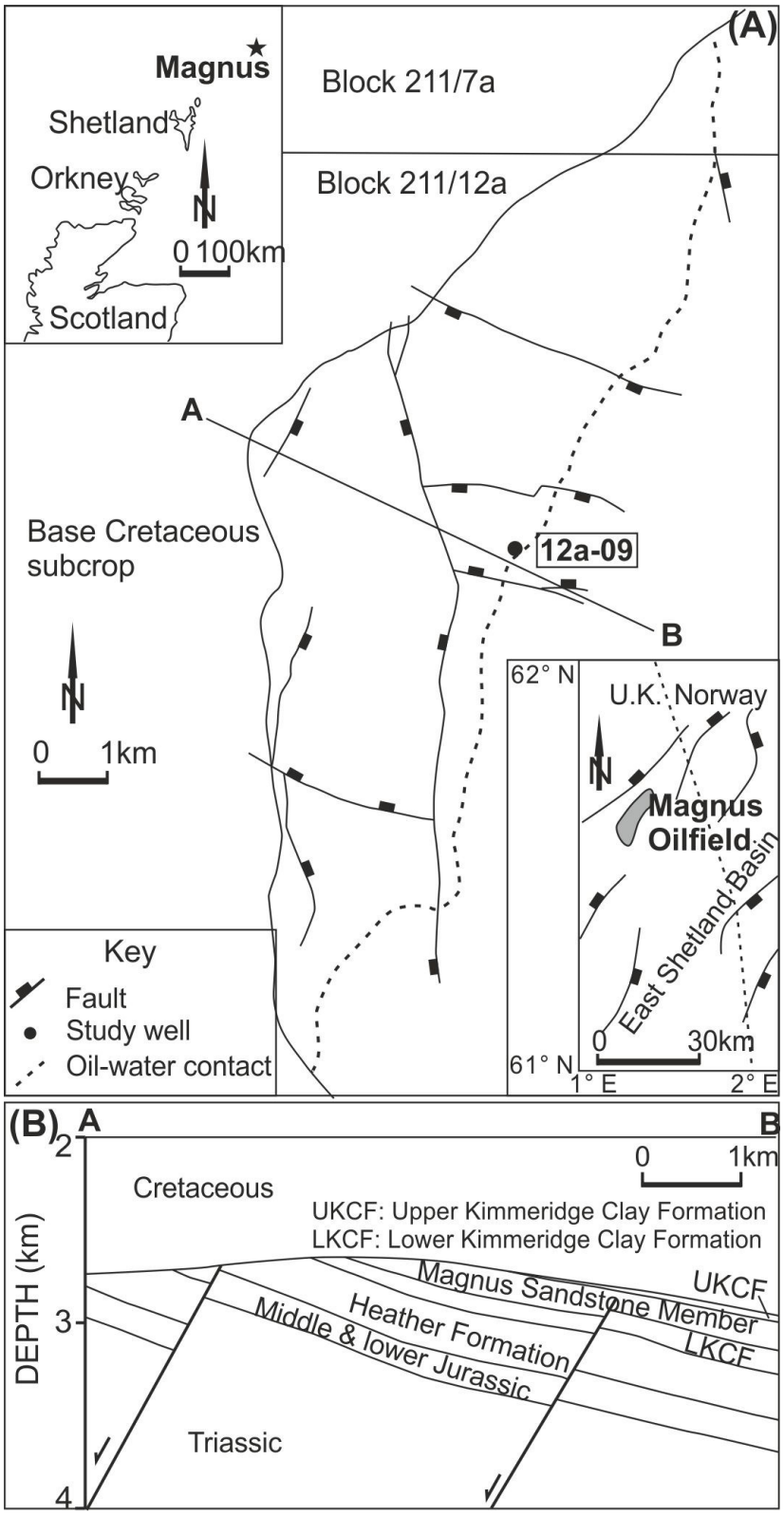

4.3. A brief review of physicochemical controls of albite formation or albitization

Authigenic albite commonly occurs in many kinds of sedimentary rocks (Kastner, 1971; Kastner and Siever, 1979), and its formation and occurrence in sandstones are widely known in numerous sedimentary basins worldwide (Walker, 1984; Gold, 1987; Saigal et al., 1988; Pittman, 1988; Milliken, 1989; Aagaard et al., 1990; Morad et al., 1990; González-Acebrón et al., 2010). Formation of authigenic albite in sandstones is reported to be coupled to high temperatures between 100-150°C (Milliken et al, 1981; Boles, 1982; Surdam et al., 1989), but it also occurs at lower temperatures in the range of 60-100°C (Saigal et al., 1988; Morad et al., 1990; Aagaard et al., 1990). However, albite formation increases with depth (Saigal et al., 1988; Aagaard et al., 1989; Milliken, 1989; Morad et al., 1990), and its precipitation at depth is reflected by distinctive textures such as the "chessboard" texture (Walker, 1984), block to tabular sector extinction patterns (Gold, 1987), or by albite overgrowths on plagioclase grains (Milliken, 1989). The growth of authigenic albite in sandstones is related to two processes: formation of overgrowth due to precipitation from saturated solutions, or replacement of K-feldspar or plagioclase by albite (Hirt et al., 1993; Bozau et al., 2015). The main cause of albite formation may be coupled to illite formation (Aagaard et al., 1990; Bjørlykke et al., 1995). Since the rate of illite formation increases at temperatures close to 100°C, precipitation of illite at the expense of smectite and kaolinite removes potassium from the pore water resulting in relatively high Na/K ratios (Aagaard et al., 1990; Bjørlykke et al., 1995). In such case the pore water becomes saturated/oversaturated with respect to albite and undersaturated with respect to K-feldspar, enabling albite formation (Aagaard et al., 1990; Bjørlykke et al., 1995). During this process, the original mineral composition can be significantly altered, whilst several diagenetic products such as calcite, kaolinite, dickite and illite can be formed modifying the pore size and geometry (Boles, 1982; Saigal et al., 1988; Morad et al., 1990).

Figure 4.1 (A) Location map of the Magnus oilfield, the sampled well (211/12a-9) and cross section A-B shown in figure B. (B) Cross section of the Magnus oilfield, which shows the intercalation of the Magnus Sandstone Member between the Upper and Lower Kimmeridge Clay Formations (UKCF, LKCF) below the mid-Cretaceous unconformity.

4.4. Geological background of the Magnus oilfield

The Magnus oilfield is located within UKCS block 211/12a and 211/7a in the North Viking Graben of the Northern North Sea (Fig. 4.1A). It situates in a south-eastward dipping, tilted fault-block structure. The areal extent of the field is defined to the east by the oil-water contact (3,150 m subsea), and to the west by a depositional pinch-out to the north and south, and by a sub-Cretaceous unconformity in the central crest region (Fig. 4.1A, Macaulay et al., 1992). The main reservoir unit of the Magnus field is the Upper Jurassic Magnus Sandstone Member (MSM) which is intercalated within the carbonaceous Kimmeridge Clay Formation (Fig. 4.1B). The MSM was deposited in the middle-fan setting of a submarine fan (De'Ath and Schuyleman, 1981; Shepherd, 1991; Macaulay et al., 1992). Oil in the Magnus sandstones was sourced from both the overlying and underlying Kimmeridge Clay Formation (De'Ath and Schuyleman, 1981; Barclay and Worden, 1998). The main source area lies to the east of the field although some oil was probably also sourced from the north (Shepherd, 1991). The main phase of oil generation is thought to have commenced approximately 75 Ma BP (Maastrichtian-Campanian) (Shepherd, 1991), and migration probably took place during the early Tertiary (De'Ath and Schuyleman, 1981).

Table 4.1 Diagenetic features of the mineral assemblage in the Magnus oilfield[a].

	Detrital particles	Diagenetic features	
		Alteration	Formation
Quartz	x		overgrowth or fine crystals
K-feldspar	x[b]	x	
Albite	x[c]		overgrowth or replacive patch
Illite			fine filamentous crystals
Kaolinite			booklets
Siderite			rhombohedral crystal
Ankerite			cement
Pyrite			framboid

Blanks indicate that the corresponding features were not observed.

[a] Compare Fig. 4.1.

[b] Including pure K-feldspar and perthite.

[c] Inherited from albitized K-feldspar from source areas cannot be excluded.

The Magnus sandstones comprise light grey, fine to medium-grained, poorly sorted sub-arkosic to arkosic sandstones, and are dominated by detrital quartz, K-feldspar, plagioclase, and minor mica (Fig.4.1; De'Ath and Schuyleman, 1981; Baines and Worden, 2004). Macaulay et al. (1993b) pointed out that the burial history of the Magnus sandstones can be divided into two stages: (1) structural uplift and tilting between 160 and 90 Ma, and (2) a continuous burial with an increase in temperature and pressure conditions after the Upper Cretaceous (ca. 90 Ma). Following the deposition of the Magnus sandstones, the sediments were shallowly buried during the late Jurassic followed by a depositional hiatus during the early Cretaceous as the reservoir was faulted and uplifted, thus exposed and eroded. A second break in deposition occurred in the mid-Cretaceous with a new uplifting of the Lower Cretaceous and Jurassic sediments. During these two uplift periods, the Magnus sandstones were exposed to subaerial erosion including a potential long-term infiltration of groundwater which led to feldspar dissolution and kaolinite precipitation. Since mid-Cretaceous, the Magnus sandstones rapidly subsided during the Tertiary and Quaternary. The main diagenetic events are thought to have occurred during this deep burial process and coincided with oil emplacement, including K-feldspar dissolution, quartz overgrowth, ankerite cementation, and formation of siderite, kaolinite and illite (Tab. 4.1; Fig. 4.2; Saigal et al., 1988; Emery et al., 1990, 1993; Macaulay et al., 1992, 1993a, 1993b; Barclay and Worden, 1998, 2000; Barclay et al., 2000; Worden and Barclay, 2000, 2003).

Numerous investigations have focussed on these main diagenetic processes of Jurassic sandstones in the Magnus oilfield (Emery et al., 1990, 1993; Macaulay et al., 1992, 1993a, 1993b; Barclay and Worden, 1998, 2000; Barclay et al., 2000; Worden and Barclay, 2000, 2003). However, authigenic albite and its potential formation pathways have not yet been studied in detail. Furthermore, hydrogeochemical modelling results presented by Barclay and Worden (2000) did not include any result about albite. Their study was out to test whether quartz and other minerals observed in the Magnus sandstones can be formed as new diagenetic phases due to the reaction between K-feldspar and source rock-derived CO_2. However, albite may make up to 18 wt.-% of the bulk reservoir rock in the Magnus oilfield (measured by XRD; this study) either as a primary or secondary mineral.

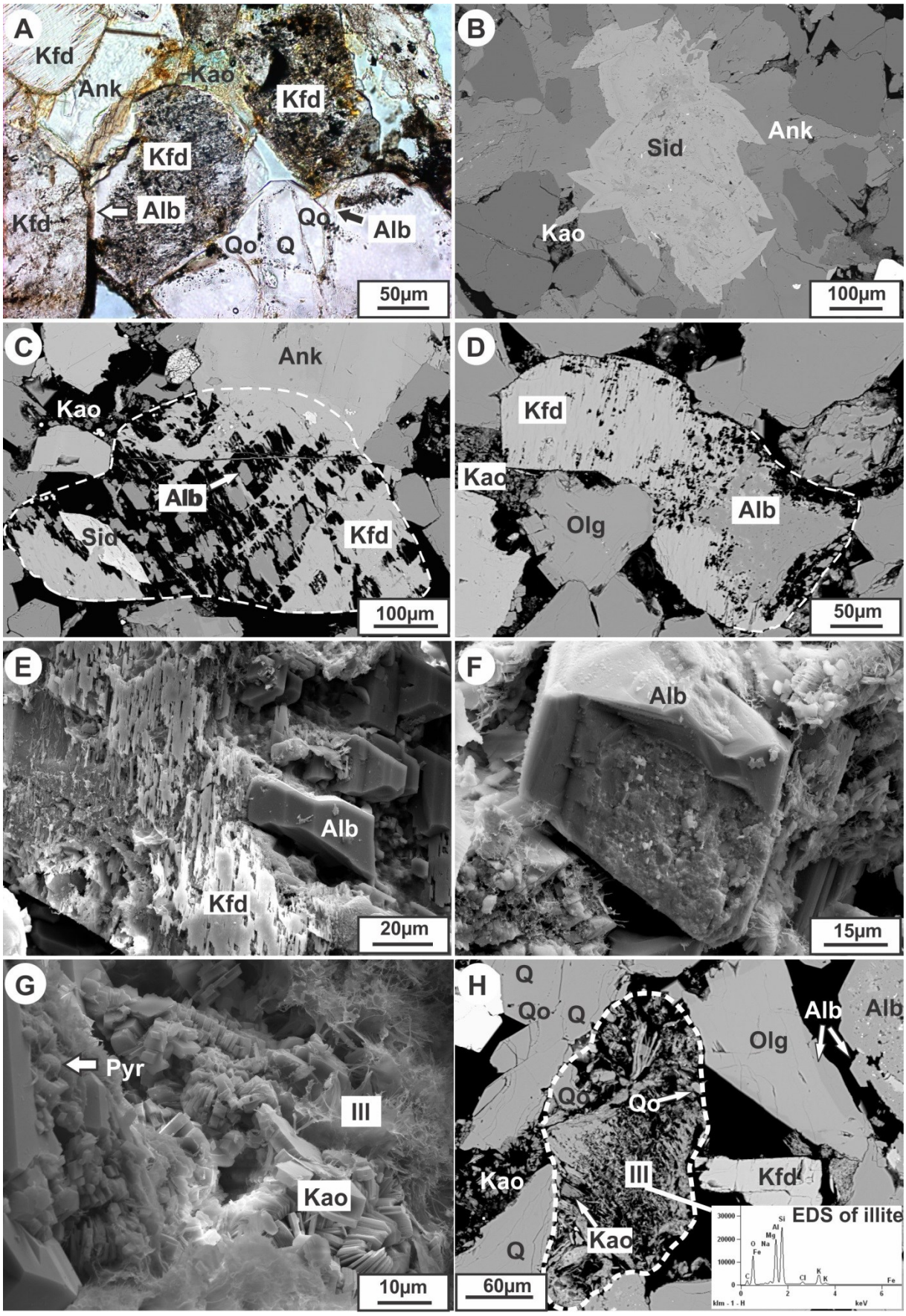
A
Kfd
Ank
Kao
Kfd
Kfd
Alb
Kfd
Qo
Alb
Qo
Q
50µm
B
Sid
Ank
Kao
100µm
C
Ank
Kao
Alb
Sid
Kfd
100µm
D
Kfd
Kao
Olg
Alb
50µm
E
Alb
Kfd
20µm
F
Alb
15µm
G
Pyr
Ill
Kao
10µm
H
Q
Qo
Q
Alb
Alb
Olg
Qo
Qo
Kao
Ill
Kfd
Kao
Q
60µm
EDS of illite

4.5. Methodology

This study is based on the investigation of 24 core samples collected from well 211/12a-9 (Fig. 4.1A) from the oil leg down to the underlying water leg crossing the present oil-water transition zone. Prior to further preparations, all core samples were extracted for 24 hours using 99 *n*-hexane: 1 dichloromethane in a Dionex ASE 200 soxhlet at 50°C in order to remove freely accessible hydrocarbons. Selected samples were impregnated with blue epoxy prior to preparation of polished thin sections and later were studied with an optical microscope. Six representative thin sections were coated with carbon for further investigations of textures, authigenic minerals, and their paragenetic relationships by using a Philips SEM-515 with an Edax PV 9100 energy-dispersive X-ray spectroscopy (EDS). Images under both scanning (SE) and backscattered scanning electron (BSE) modes were obtained. Energy-dispersive X-ray spectroscopy (EDS) analysis was conducted to study the chemical composition of feldspars. To study the cathodoluminescence of different feldspars, four thin sections were investigated by using a cold cathode luminescence device CITL 8200 MK3 coupled to a ZEISS "Amplival" microscope. Electron gun voltages and beam currents of 10 kV and 0.4 mA were used whilst the polished thin sections were held under vacuum between 0.07 and 0.01 Torr. In addition, freshly broken rock chips were investigated by SEM to study mineral morphologies and dissolution/precipitation patterns. To determine and semi-quantify mineral assemblages, all core samples were grounded to powder for X-ray diffraction analysis (XRD) by using a BRUKER-axs D5000. X-ray fluorescence analyses (XRF) were also carried out on bulk samples by using PHILIPS PW2400 to analyse the element composition of whole rock in order to identify whether albite is the exclusive

---

Figure 4.2 Main diagenetic features of the Magnus sandstones. (A) The altered K-feldspar with partly coated albite overgrowth (white arrow). The edge/boundary of albite overgrowth of the right grain following the shape of quartz overgrowth (black arrow). Both corroded and non-corroded K-feldspars occur. Ankerite and kaolinite fill pores; // nicols. (B) Siderite and ankerite cement; BSE. (C) Authigenic albite crystals in corroded K-feldspar; BSE. (D) Authigenic albite formed within a partly corroded K-feldspar grain; BSE. The white dashed line represents the original shape of the corroded K-feldspar grain. (E) Fresh, euhedral albite crystals on corroded feldspar; SEM. (F) Albite overgrowth on detrital grains; SEM. (G) Illite whiskers on kaolinite booklets; SEM. (H) A corroded and illitized detrital grain, BSE. The dashed lines indicate the outline of the original detrital grain which might have been feldspar. Within its skeleton, kaolinite, illite, and quartz were precipitated. The insert is the EDS analysis of illite. Abbreviations: Olg: oligoclase; Q: quartz; Qo: quartz overgrowth; Kfd: k-feldspar; Alb: albite; Ill: illite; Kao: kaolinite; Ank: ankerite; Sid: siderite; Pyr: pyrite.

sodium-bearing mineral (comparison with XRD data). The grain size distribution was obtained by measuring the long axis of detrital grains and 100 grains per thin section were studied. The presented grain size values are the mean diameter of 100 grains.

Based on petrographic study of the Magnus sandstones, hydrogeochemical modelling was carried out using the computer code PHREEQC Interactive version 3.2 (Parkhurst and Appelo, 2013) to simulate a closed, isothermal and isochemical system in which a state of chemical equilibrium among the mineral assemblage, pore water, and gas can be achieved based on chemical thermodynamics and mass balancing. This model does not take kinetic aspects into account. Therefore, modelling based on the thermodynamics of chemical equilibrium can be used to decipher reaction pathways because it illustrates how water-rock reactions in systems will evolve for equilibration (given sufficient time).

4.6. Results of microscopic, geochemical and mineralogical studies

The Magnus sandstones vary in grain size, sorting and mineralogical composition, and consist of 40-76 wt.-% quartz (including detrital quartz and quartz cement), 16-33 wt.-% feldspar (K-feldspar and plagioclase) and 0-5 wt.-% muscovite. Minor accessories include pyrite, siderite, and ankerite. Most of the K-feldspar and oligoclase lack indications of alteration (Figs. 4.2A, H). However, some K-feldspar grains appear strongly corroded and altered (Figs. 4.2A, 4.2C-E, and 4.5). Albite is another main component in the Magnus sandstones.

4.6.1. Bulk mineralogy and geochemistry

Both the Na_2O and the albite content of the Magnus sandstones vary with depth (Fig. 4.3), and show a linear relationship (Fig. 4.4A). This fit may indicate that Na in the Magnus sandstones is mainly incorporated in albite which could be either in the form of albite grains or even albite lamellae in perthite. The K_2O and the K-feldspar content also vary greatly with depths. However, the K_2O values above the line of stoichiometric K-feldspar indicate the presence of other K-bearing minerals (mica, illite; Fig. 4.4B). In general, there are linear relationships between the Na_2O vs. the K_2O content, and between the albite and the K-feldspar content (Figs. 4.4C-D). Importantly, more albite occurs in samples which have higher

feldspar contents (Fig. 4.4D). It is also noteworthy that the Na_2O and the albite contents show a relation with the grain size (Figs. 4.4E-F): a smaller grain size, higher Na_2O and albite contents.

Table 4.2 Characteristics of feldspars in the Magnus field.

	Oligoclase	K-feldspar		Albite		
		unalbitized K-feldspar	K-feldspar reflicts	Albite overgrowth	Albite patch	Albite lamella
Habit	detrital grains	detrital grains	irregular patches	fresh euhedral crystals on detrital feldspar grains	irregular patches in albitized feldspar	Regular/irregular lamellae in perthite
Chemical composition	25% An	0-10% Ab and minor Ba	7% Ab and minor Ba	100% Ab	1-3% An	2-4% An
Texture	undissolved, with albite overgrowth	with/without albite lamellae	with micropores and pyrite	dense, without micropores or pyrite	with micropores, pyrite and/or mica inclusions	dense, without micropores and pyrite
Cathodoluminescence	yellow	bright blue	light yellow	dull	dull	dull
Origin	detrital	detrital	detrital	precipitation from formation water	replacement of K-feldspar	exsolution

An: anorthite.
Ab: albite.

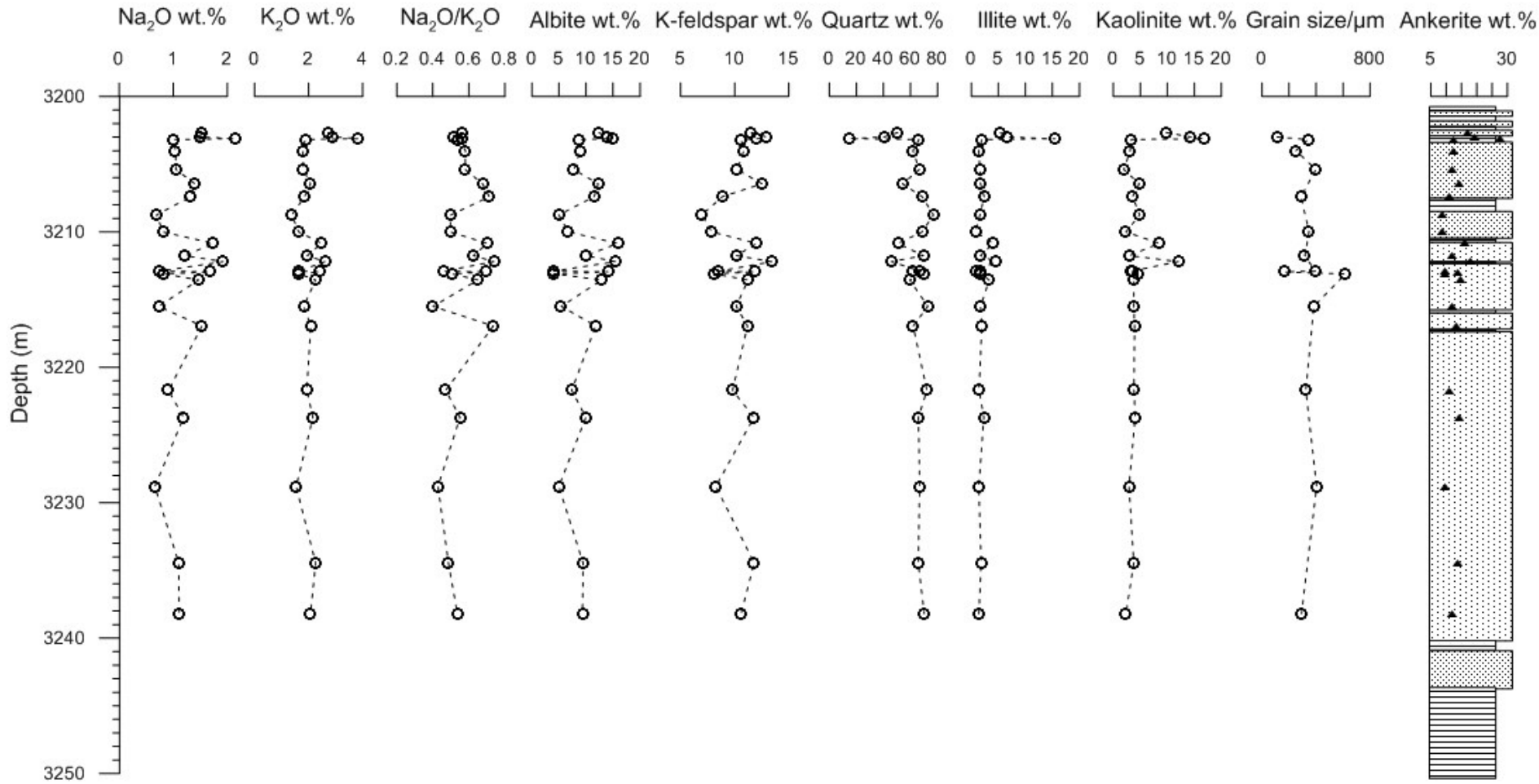

Figure 4.3 Profile of bulk rock element oxide percentages (XRF), mineral percentages (XRD) and grain size (determined by conventional light microscopy).

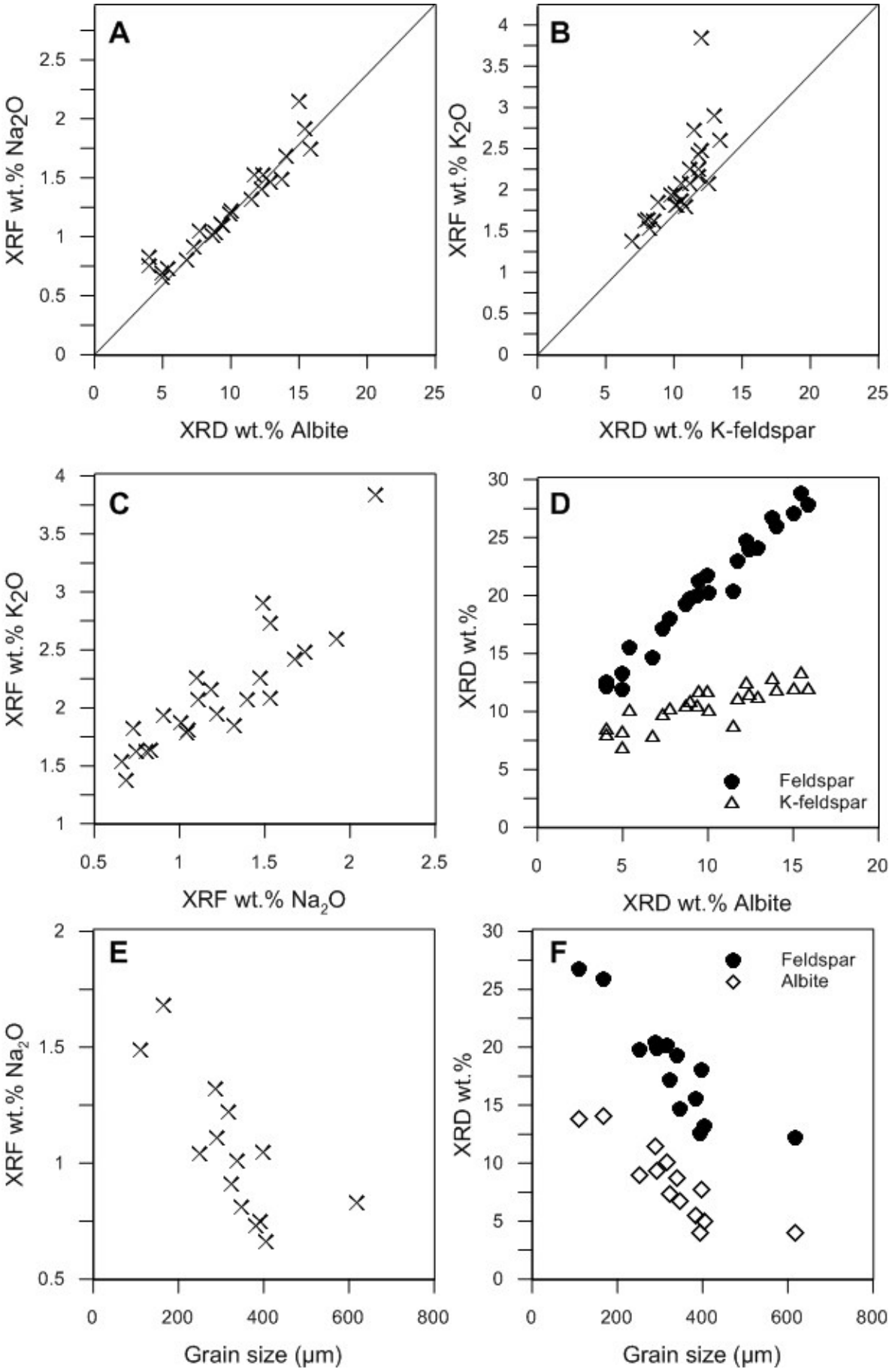
A
XRF wt.% Na2O
XRD wt.% Albite
B
XRF wt.% K2O
XRD wt.% K-feldspar
C
XRF wt.% K2O
XRF wt.% Na2O
D
XRD wt.%
Feldspar
K-feldspar
XRD wt.% Albite
E
XRF wt.% Na2O
Grain size (µm)
F
XRD wt.%
Feldspar
Albite
Grain size (µm)

4.6.2. Microscopy

Albite in the Magnus sandstones occurs in three forms (Table 4.2): (1) as regular/irregular lamellae in perthite (to a minor degree), (2) mostly as overgrowth/euhedral crystals on/in corroded feldspar (Figs. 4.2C-E, 4.5A-B), and (3) as irregular patches in albitized grains or even as albite pseudomorphs which are the products of a complete replacement of K-feldspar (Figs. 4.2D, 4.5C-D).

Albite overgrowths have a white and clear appearance under the conventional light microscope. They appear as euhedral crystals, predominately on dissolved K-feldspar, on non-altered oligoclase and albitized feldspar (Figs. 4.2A, 4.5A-B). The albite overgrowths partly cover cloudy albitized K-feldspar grains and oligoclase and show dull luminescence (Fig. 4.5A). Apart from the occurrence as overgrowth on feldspar surfaces, albite also occurs as euhedral crystals together with rhombohedral siderite in secondary pores of dissolved K-feldspar (Fig. 4.2C). These albite crystals are oriented parallel with the cleavages of dissolved K-feldspar (Fig. 4.2C). Albite overgrowth and albite euhedral crystals in dissolved K-feldspar are dense without pores or inclusions, and lack twinning.

Albite patches/pseudomorphs have a sharp edge/surface and a dark-blurred appearance under the conventional light microscope due to high porosity and the presence of fine-crystalline pyrite (Fig. 4.5C). In some cases, mica particles and fluid inclusions can even be found in replacive albite patches. In strongly altered feldspar grains/albite patches (not in full pseudomorphs), the K-feldspar relicts can be found (Figs. 4.5B, D). It is noteworthy that the replacive albite patches have dull luminescence while the K-feldspar relicts appear with a light yellow under cathodoluminescence (Fig. 4.5D).

Detailed SEM investigations reveal that the albite crystals in the Magnus sandstones

---

Figure 4.4 XRD and XRF results. (A) Bulk rock sodium content (from X-ray fluorescence) vs. albite content (from X-ray diffraction). The diagonal line represents correlation for ideal albite. The linear relation of Na_2O with albite indicates that albite is the predominant Na-bearing mineral. (B) Bulk rock potassium content vs. K-feldspar content. The diagonal line represents a correlation for an ideal K-feldspar. The points plotting above this line indicate the presence of other K-bearing minerals (mica, illite). (C) Bulk rock sodium content vs. bulk rock potassium content. The Na_2O content increases with increasing the K_2O content. (D) Albite content vs. K-feldspar and total feldspar contents. Albite is abundant in samples with abundant K-feldspar and total feldspar. (E) Bulk rock sodium content vs. grain size. (F) Albite and total feldspar content vs. grain size.

have unetched smooth surfaces, and were observed on altered K-feldspar (Fig. 4.2E). Besides, a pseudomorphous replacement of feldspar by relatively large blocky crystals of albite occurs. Albite also appears as overgrowth partly coating detrital K-feldspar/oligoclase (Fig. 4.2F).

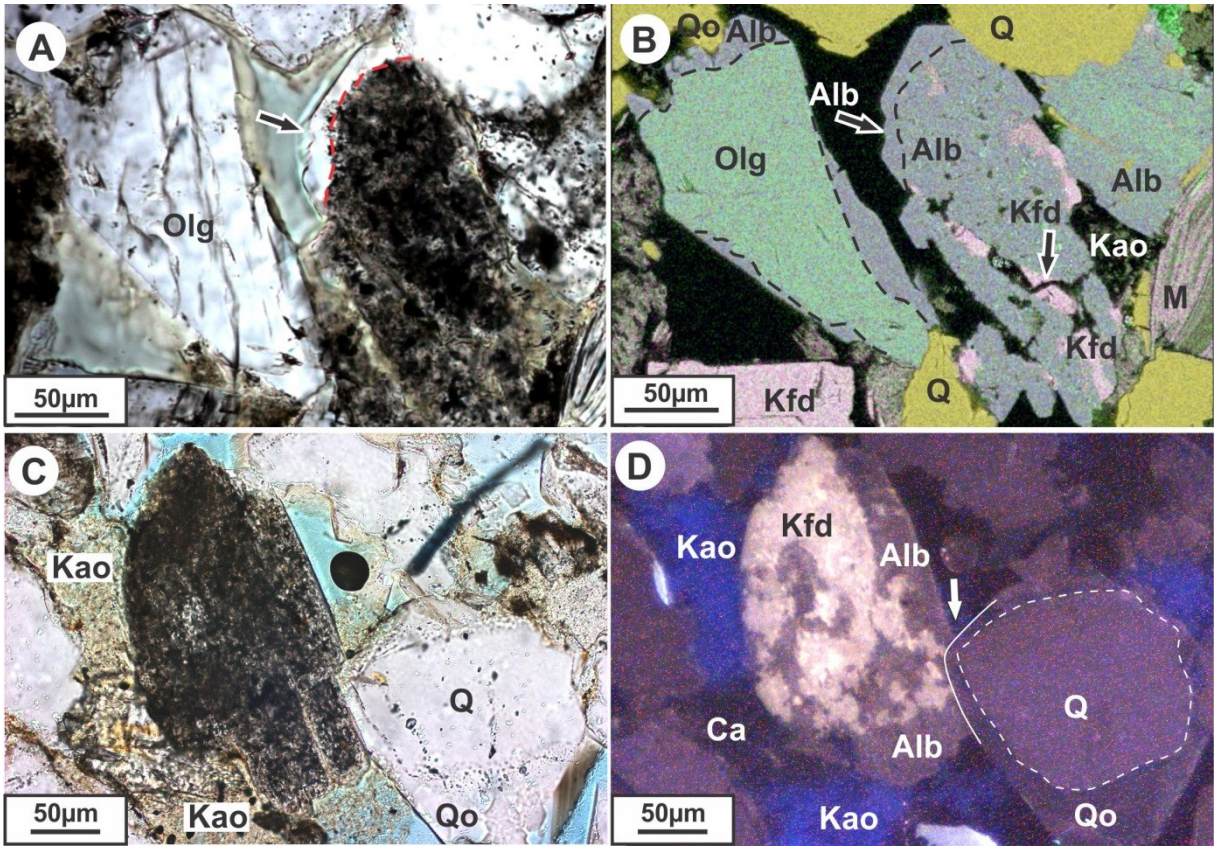

Figure 4.5 (A) An altered black albite grain with clean albite overgrowth (arrow). The unaltered oligoclase also has a semi-coated albite overgrowth rim; // nicols. (B) Element mapping under BSE; picture as for A. Note that the albitized part has abundant micropores, pyrite, and several K-feldspar relicts. (C) A black, altered K-feldspar grain under plane light. Brown kaolinite and carbonate fill part of pores; // nicols. (D) Picture as for C. The replacing albite yields dull luminescence while K-feldspar relicts show bright-yellow luminescence. Kaolinite has blue luminescence. The right quartz grain has a thick rim of quartz overgrowth with dull luminescence. Note that the right part of the replacive albite is intruded by quartz overgrowth. The dashed lines indicate the outline of detrital quartz. The solid line represents the edge of quartz overgrowth; Cathodoluminescence. Abbreviations: Olg: oligoclase; Q: quartz; Qo: quartz overgrowth; Kfd: k-feldspar; Alb: albite; M: mica; Ca: carbonate; Kao: kaolinite.

4.6.3. Chemical composition of feldspar

Based on the chemical composition, feldspar can be divided into three groups: K-feldspar, oligoclase, and albite (Fig. 4.6). Within the K-feldspar group, the K-feldspar relicts

in albitized grains have a narrow range of chemical compositions compared with the unaltered, fresh K-feldspar (Fig. 4.6A). Oligoclase commonly appears unaltered and has a 20-30% An (anorthite) content. In general, the investigated albite in the Magnus sandstones is close to pure albite. However, the three forms of albite have different chemical compositions (Fig. 4.6B). The albite overgrowth has the highest purity in view of the chemical composition, with 100% Ab (Fig. 4.6B). However, the albite lamellae and the albite patches are less pure. The albite lamellae in perthite in the Magnus sandstones are composed of 2-4% An whereas the albite patches/pseudomorphs have a chemical composition range of 1-3% An.

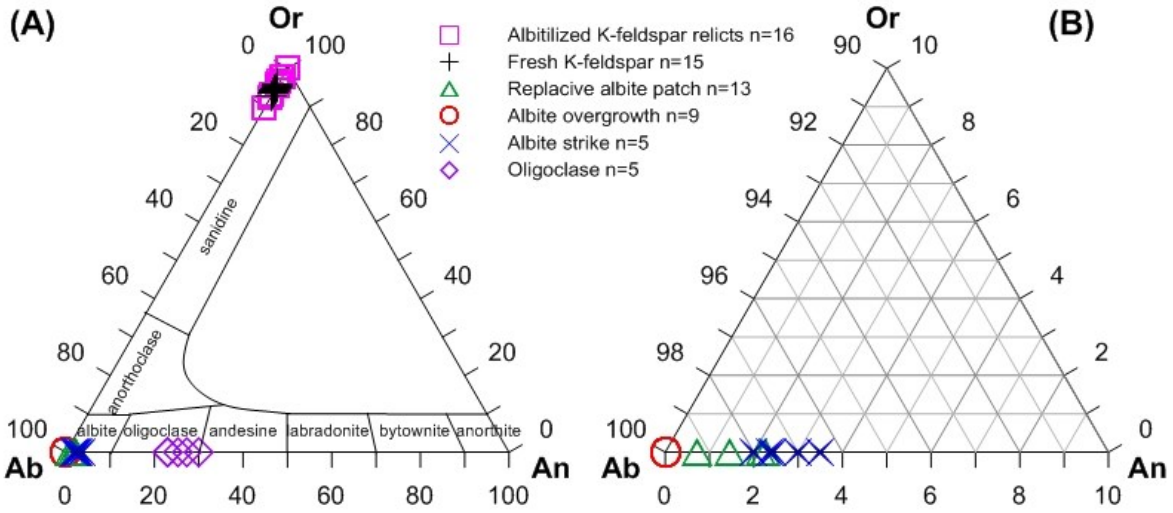

Figure 4.6 Chemical compositions of feldspars in the Magnus sandstones (measured by EDS-BSE). (A) All feldspar types. (B) Albites plotting in the albite corner of the former diagram (A). Note that albite overgrowth has 100% purity of Ab. Replacing albite patches are slightly impure with 1-3% An.

4.7. Discussion of imaging, geochemical and mineralogical results

4.7.1. Origin of albite

Diagenetic albite in siliclastic sedimentary rocks has several chemically and petrographically characteristic features: (1) compositional purity (99% Ab), (2) cloudy or vacuolised appearance in thin sections, (3) untwined crystallinity, and (4) a lack of cathodoluminescence (Smith and Stenstrom, 1965; Kanster, 1971; Kanster and Siever, 1979; Saigal et al., 1988).

Albite overgrowth in the Magnus sandstones has an undoubtedly diagenetic origin due to its fresh surface, dull luminescence, and high purity (100% Ab). However, the origin of replacing albite patches, especially as albite pseudomorphs, which are the products of a complete replacement of K-feldspar, is obscured. Besides the unaltered appearance of the albite patches (Fig. 4.5C), there are further lines of evidence that suggest that the albite patches in the studied sandstones have formed during diagenesis. First, the albite patches are observed in the dissolved part of K-feldspar and the dissolved K-feldspar still maintains its original shape (Fig. 4.2D). This suggests that the formation of albite patches postdated K-feldspar dissolution and that the dissolution of K-feldspar took place during burial after compaction. Second, the replacing albite patch is absent at the contacts of altered feldspar grains and quartz overgrowth, and its shape follows the edge of quartz overgrowth (Figs. 4.2A, 4.5D), indicating that albite patch may postdate quartz overgrowth.

However, a derivation from the source rocks which contain albitized feldspar as another origin for the albite patches type of the Magnus sandstones cannot be fully excluded. First, the chemical composition of the albite patches is 95-98% Ab, which is slightly less pure than the criteria of 99% Ab suggested by Saigal et al. (1988). Second, the cloudy albite patches also share many similarities with albite formed in granitic rocks described by Engvik et al. (2008; Fig. 4.4): cloudy appearance due to numerous pores, fine inclusions of mica, pyrite or Fe-oxide, and slight impurity (An_{2-5}). Third, the Na_2O contents of albite and the bulk albite contents in the studied well both show an increase trend with increasing feldspar amount and decreasing grain size (Figs. 4.4D, F). There are two explanations for this phenomenon: albite as allochthonous component was preferentially deposited in small grain-sized sandstones, or formed especially in small grain-sized sandstones. The first explanation is more likely for the Magnus sandstones. Odom et al. (1976) found out that the feldspar contents decrease with increasing grain size based on the investigation of sandstones of Cambrian, Ordovician, Permian, and Jurassic age. They concluded that the high concentration of feldspars in fine sandstones is a result of sorting of feldspar in contiguous high energy environments. In the Magnus sandstones, the relative abundance of feldspar in fine grain-sized sandy units is also observed (Fig. 4.4D). Coupled to the more feldspar in small grain-sized sandstone, the albite contents in these samples are also relatively abundant (Fig. 4.4D). If the albite content in small grain-sized sandstones was exclusively due to the formation of authigenic albite, then an increased Na/K ratio should be expected in albite-rich, fine grain-sized samples due to an addition of sodium during the formation of albite. However, the plots of Na_2O and K_2O

values display a linear relationship (Fig. 4.4C), which suggests an instant Na_2O/K_2O value in all studied samples. In addition, the K-feldspar contents of the Magnus sandstones do not decrease with the increased albite abundance whereas they increase with increased albite contents (Fig. 4.4D), which indicates the albite in the Magnus sandstones might not be exclusively due to the replacement of K-feldspar. It seems that albite, probably a large portion, is linked to albitized parent rocks which were albitized, eroded and transported to the present area of the Magnus field.

Based on this discussion, two origins can be argued to the albite in the Magnus sandstones: detrital albitized grains as inherited from the parent rocks and diagenetic albite during burial.

4.7.2. Timing of diagenetic albite formation

Diagenetic albite of the Magnus sandstones was formed during burial to great depths. Several petrographic observations can support this hypothesis as below: (1) fresh albite occurring in corroded K-feldspar grains which still keep their original skeleton (Figs. 4.2C, D), indicating that albite formation postdated compaction and K-feldspar-dissolution; (2) the absence of replacing albite at contacts of detrital grains and quartz overgrowth (Figs 4.2A, 4.5C-D); (3) albite overgrowth followed the shape of quartz overgrowth (Fig. 4.2A), suggesting that albite formed after quartz overgrowth. In summary, authigenic albite formation, or at least partly, postdated mechanical compaction, K-feldspar dissolution, and quartz cementation. Since the formation of the diagenetic albite is later than quartz cementation, the timing of quartz cementation can be regarded as the earliest time for diagenetic albite formation. The age of quartz cementation was assessed to be 80 Ma based on the homogenization temperature of aqueous inclusions of 90-120°C measured in the quartz cement and on the burial history of the Magnus sandstones (Emery et al., 1993; Fig 4.7). Therefore, it can be inferred that the earliest age for diagenetic albite in the Magnus sandstones could be 80 Ma when the reservoir temperature could have been around 90°C (Fig. 4.7). Albite formation seems to be still proceeding in the present Magnus sandstones since most of today's formation waters of the Magnus field fall in the stability field of albite by plotting the formation waters data from Warren and Smalley (1994) on the stability diagram of Morad et al. (1990).

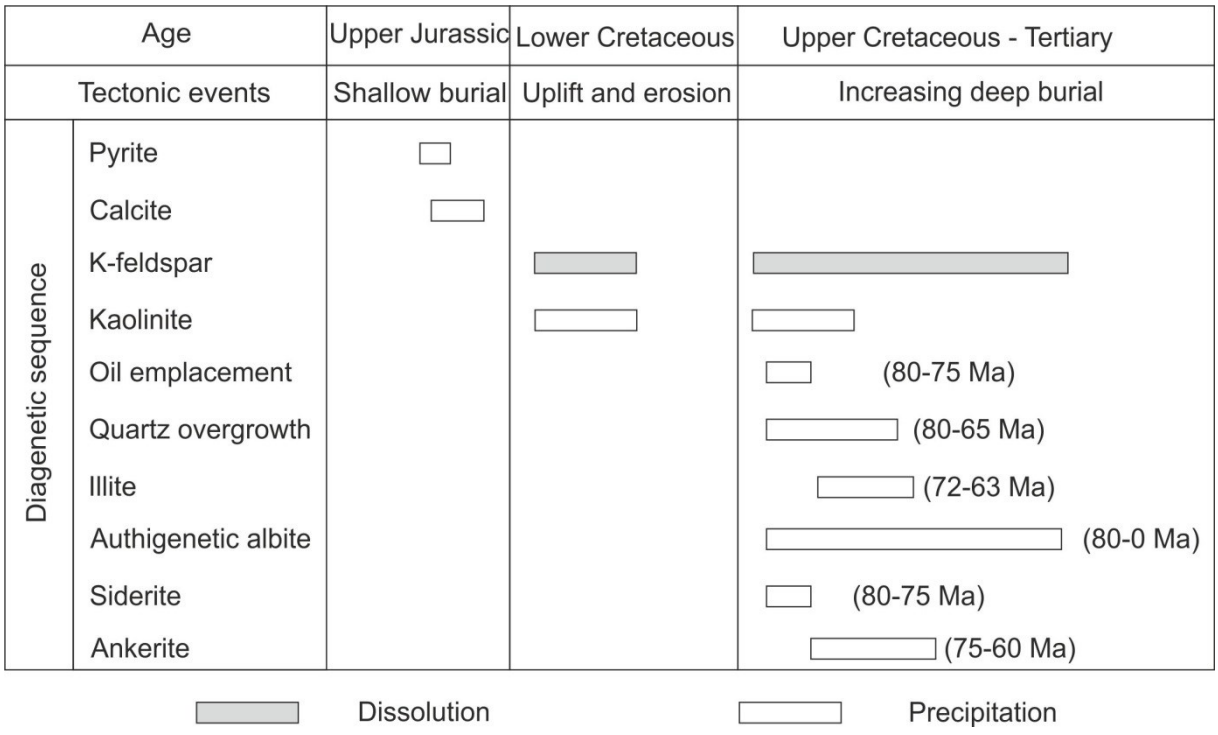

Figure 4.7 Diagenetic sequence of the Magnus sandstones (modified after Barclay et al., 2000).

4.7.3. Chemical conditions required for albitization

Source of sodium

One of the chemical conditions required for authigenic albite formation is a high activity ratio of Na^+/H^+ in combination with a high concentration of dissolved silica (H_4SiO_4) (Karster and Siever, 1979). The source of Na^+ ions may originate from the pore water. Given 2 wt.-% albite is formed in the Magnus sandstones (assuming porosity 20%, density: 2.65 mg/cm3), a pore water with a salinity of 18,630 mg/L sodium is needed for the sodium supply of albite formation. The current formation water of the Magnus field has the same order of salinity with 16,000-18,000 mg/L dissolved solids (NaCl wt.-% equivalents) (De'Ath and Schuyleman, 1981). Therefore, the formation water of the Magnus field can provide sufficient sodium source for the observed authigenic albite formation. An additional sodium source which exists -but maybe not necessary- is the Na^+ ion released from the transformation of smectite to illite in mudrocks of the surrounding Kimmeridge Clay Formation (cf. Boles and Franks, 1979). Moreover, the alkali feldspar in the Magnus sandstones contains 2-10% Ab and dissolution of such alkali feldspar can supply some additional sodium for albite formation.

Source of silica

The source of silica can either come from skeletal organisms or from the dissolution of unstable silicate grains (Karster and Siever, 1979). Silica-bearing skeletal organisms have not been observed or reported in the Magnus sandstones.

However, dissolution of unstable silicates, such as non-end-member feldspars, can also supply dissolved silica. Intermediates in either the plagioclase or alkali feldspar series are less stable than the pure end members at low temperature (Milliken, 2004). The non-end-member alkali feldspar in the Magnus sandstones accounts for 8-14 wt.-% of the whole rock and is composed with 2-10% Ab (Fig. 4.6). Dissolution of K-feldspar is common in the Magnus sandstones (Figs. 4.2C-E). Thus, dissolution of non-end member K-feldspar is the possible source for elevated dissolved H4SiO4 concentrations in the Magnus sandstones. In addition, it can also provide sodium by the following reaction:

$$K_{0.9}Na_{0.1}AlSi_3O_8 + 4H^+ + 4H_2O \rightarrow 0.9K^+ + 0.1Na^+ + Al3^+ + 3H_4SiO_4 \quad [1]$$

Potassium sink

Albitization is more sensitive to potassium removal than sodium supply (Aagaard et al., 1990). It is envisaged that the adjoining and interbedded shales within sandstone sequences provide an effective potassium sink for albitization (Saigal et al., 1988; Aagaard et al., 1990) since the change of smectite into illite can consume potassium and release sodium (Boles and Franks, 1979). In addition, the alteration of kaolinite to illite in sandstones and shales would also remove potassium (Bjørlykke et al., 1995; Bjørlykke, 1998). In the Magnus field, illite formation in the Magnus sandstones has been reported by Worden and Barclay (2003) and they interpreted that its formation is related to the dissolution of K-feldspar and kaolinite (see also Fig. 4.2G). In addition, illite is not only present in sandstones (1-2 wt.-%; Fig. 4.3) but also occurs in the interbedded shales (5-15 wt.-%; Fig. 4.3). Therefore, it can be inferred that illite in the shales of the Kimmeridge Clay Formation and in the Magnus sandstones is the likely potassium sink for diagenetic albite formation.

4.8. Hydrogeochemical modelling of albite formation

4.8.1. Geological framework and input parameters

Authigenic albite formation in the Magnus sandstones is interpreted to have occurred during burial (section 4.6.2). Correspondingly, several scenarios aim to test the possible pathways for authigenic albite formation. The sediments of the Magnus field have experienced a burial history of multiple uplifts and erosions, long-term weathering, and meteoric water flushing (sections 4.3 and 4.6.2). During uplift and shallow overburden, several diagenetic processes occurred, including dissolution of unstable feldspars and precipitation of kaolinite and chalcedony. During this period, oxidizing conditions should have prevailed in the Magnus sandstones and resulted in the formation of hydrous ferric oxides (HFO). Besides the observed detrital minerals of the Magnus sandstones (quartz, K-feldspar, and probably also albitized grains), additional minerals such as kaolinite, chalcedony, hydrous ferric oxide (HFO) are also considered to be present in the Magnus sandstones after early diagenesis (this part is excluded in our study and modelling), as the primary minerals for modelling the following continuous burial diagenetic processes.

Increasing in temperature and pressure during burial could change the solubility constant of minerals. Consequently, it should be taken into account as a possible reason for authigenic albite formation (scenario 1).

Scenario 2 considers organic-inorganic interactions during albite formation. Siderite is present together with authigenic albite (Fig. 4.2C). However, the petrographic investigations show that the Magnus sandstones lack organic matter which may serve as a reductant for ferric iron to enable siderite formation. Before and during oil generation, several reactive components could also be produced, like methane and carbon dioxide (Tissot et al., 1974, 1978; Hunt, 1995). These products could have migrated into the Magnus sandstones before oil migration or together with oil. In the presence of pore water and other mineral oxidants, oil components are unstable in view of chemical thermodynamics and can be degraded into methane, carbon dioxide, carboxylic acid and hydrogen (Seewald, 2003). These reactive products may have enabled electron transfer for siderite formation. This hypothesis is also supported by the results of former studies that found that siderite in the Magnus sandstones was formed at 90 °C coupled with oil generation and migration (Macaulay et al., 1993b; Emery et al., 1993) and that its carbon isotopic composition ($\delta^{13}C$ of -8.0 to -14.6‰ PDB;

Macaulay et al., 1993b) reflects an important influence of organic matter sourced carbon. During the transformation of ferric iron to ferrous iron minerals, the pH and redox conditions of pore water could have changed. This could have triggered a series of other diagenetic processes. The second scenario thus aims to test whether albite formation could have occurred coupled to siderite formation in the period of oil generation and migration into the Magnus sandstones during the second and major burial phase.

Illite formation at the expense of K-feldspar and kaolinite is commonly observed in North Sea oil reservoirs and is controlled by kinetics (Bjørlykke et al., 1995; Bjørlykke, 1998; Worden and Barclay, 2003). The formation waters of the North Sea oil reservoirs are undersaturated with regard to K-feldspar, and, instead, oversaturated with regard to illite and albite (Bjørlykke et al., 1995). As mentioned in section 4.6.3.3, illite formation and K-feldspar dissolution are also commonly observed in the Magnus sandstones (Fig. 4.2H). Dissolution of such non-end-member K-feldspar of the Magnus sandstones can also release sodium ions into the pore water. Consequently, this leads to an albite oversaturation and precipitation. The third scenario thus aims to test whether this process is thermodynamically admissible in the mineralogical assemblage of the Magnus sandstones. Thus, this kinetic process is not considered in the first and second scenarios that are calculated under chemical equilibrium conditions.

4.8.2. Modelling concept

To test the three possible pathways for albite formation in the Magnus sandstones, a hydrogeochemical batch modelling approach, which is based on thermodynamics of chemical equilibrium, is presented. The computer code Phreeqc Interactive 3.2 that was developed by the U.S. Geological Survey (Parkhurst and Appelo, 2013) is our modelling tool. Table 4.3 shows the potential amounts of primary and secondary minerals and the current temperature and pressure conditions in the sandstones of the Magnus oilfield. Since the primary detrital minerals have been strongly altered, their original amounts prior to burial can only be assumed according to the petrographic observations. Assuming an initial porosity of 20 % based on petrographic investigations, our modelling approach consists of a generic reactor that has a total volume of 5 L. One liter of the present-day seawater, which is documented in the Phreeqc Manual (Parkhurst and Appelo, 2013), fills the pore space of this reactor. According to an average density of 2.65 g/L, the reactor has a mineral assemblage with a total

mass of 10.6 kg. The pre-assigned mineral assemblage for modelling and their amounts are given in Table 4.3. Although quartz predominates in the mineral assemblage, it is conceptually only allowed to dissolve. Instead, chalcedony may form as secondary SiO_2(s) as it commonly occurs in form of small crystals and overgrowths. In general, less stable SiO_2(s) minerals, such as chalcedony and cristobalite, control the concentration of dissolved silica in aqueous solutions, whereas these solutions are oversaturated with respect to quartz (Appelo and Postma, 1994). K-feldspar and albite, the main sedimentary minerals besides quartz, account for 8 and 12 wt.-% of the sedimentary mineral assemblage of the sandstones, respectively (Table 4.3).

Table 4.3 Present and pre-assigned mineral assemblages of the Magnus sandstones and reservoir conditions.

	Observed[a]		**Pre-assigned for modelling**		
	wt.-%	mol/kg		wt.-%	mol/kg
			Primary minerals[b]		
Quartz	65	114.68	Quartz	65	114.68
Albite	10	4.03	Albite[c]	8	3.22
K-feldspar	10	3.81	K-feldspar	12	4.57
Kaolinite	4	1.64	$Fe(OH)_3$(a)	1	0.99
Chalcedony[c]	2	3.53	Kaolinite	5	2.05
Ankerite	7	3.60	Chalcedony[d]	3	5.29
Siderite	1	0.91	**Secondary minerals**[e]		
Illite	1	0.27	Ankerite	0	0
			Siderite	0	0
			Illite	0	0
			Pyrite	0	0
Reservoir condition					
Temperature	116°C		116°C		
Pressure	450 atm		450 atm		

Notes:
[a] Based on petrographic observations and XRD analyses.
[b] Assumed original amounts of minerals before deep burial.
[c] Detrital albite is assumed.
[d] Primary quartz can only get dissolved; instead, chalcedony forms as secondary $SiO_{2(s)}$.
[e] Minerals allowed to precipitate in the generic modelling reactor.

4.8.3. Modelling results

Scenario 1 uses an assumed temperature-pressure gradient according to the present conditions (4 to 116°C in 10 steps; 1 to 450 atm in 10 steps; Phreeqc input file as A1 in Appendix). The results (not graphically shown) suggest that the pre-assigned mineral

assemblage is stabilized with increasing temperature and pressure conditions because negligible amounts of minerals are converted in the modelling (mostly in the order of magnitude of 10−4 mol per one liter of pore water). Additionally, albite is slightly dissolved (5E−4 mole per one liter of pore water). Thus, an increase in temperature and pressure, which changes the solubility constants of minerals including K-feldspar and albite, is not the reason for albite formation under isochemical conditions.

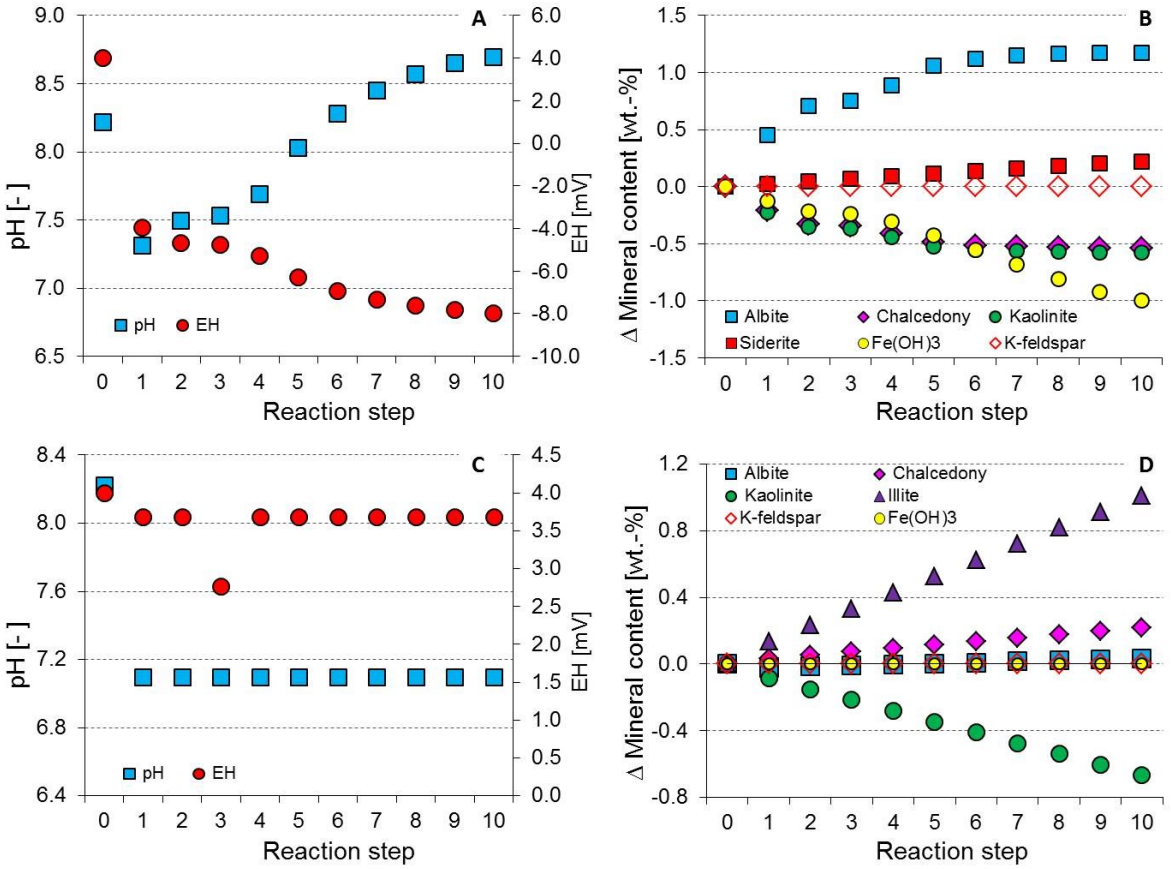

Figure 4.8 Modelling results. (A-B) Scenario 2. (A) pH and Eh of pore water change during the addition of CH_4, CO_2, and H_2 in each step. (B) The amount of dissolved and precipitated minerals is given in wt.-%. Coupled to the dissolution of kaolinite and chalcedony, albite precipitates. (C-D) Scenario 3. (C) pH and Eh of pore water change during the addition of K-feldspar into the generic reactor. (D) The amount of dissolved and precipitated minerals is given in wt.-%.

Scenario 2 considers a stepwise addition of the oil generation/degradation products methane, carbon dioxide, and hydrogen according to Seewald (2003). In total, 0.007 moles of CO_2, CH_4, and H_2 in a 2:1:5 ratio are added into the reactor in 10 steps until the assumed amount of ferric iron minerals is completely consumed (scenario 2 input file as A2 in Appendix). The modelling results show that the pH of the pore water gradually increases whereas EH decreases (Fig. 4.8A). These changes lead to a reduction of hydrous ferric oxide

and siderite formation. During this process, K-feldspar remains stable, and up to 1.5 wt.-% albite can form (Fig. 4.8B). However, the modelled K-feldspar stability does not match the common dissolution features of K-feldspar observed in the Magnus sandstones. However, K-feldspar dissolution may have occurred during uplift and erosion due to the infiltration of meteoric water. Moreover, kaolinite and chalcedony dissolve in scenario 2. In comparison, precipitation of kaolinite and quartz overgrowth are proven by SEM and optical microscopy. However, this conflict may not doubt the modelling approach, because the observed kaolinite and quartz overgrowth may have formed during uplift and erosion stages which are not included in our modelling concept.

Scenario 3 aims to test the third hypothesis: whether the kinetic transformation from non-end member K-feldspar with Ab_{10} altering to illite can lead to albite formation. This scenario considers a stepwise addition of a K-feldspar with Ab10 into the reactor in order to simulate the kinetic-controlled transformation from K-feldspar to illite (scenario 3 input file as Appendix A3). It is assumed that this K-feldspar has same thermodynamic data as the pure K-feldspar defined in the Phreeqc database. The modelling results show that dissolution of non-end member K-feldspar is coupled to a formation of albite, illite, and chalcedony (Fig. 4.8D). In parallel, kaolinite is consumed. This fits the SEM observations that illite is precipitated on the surface of kaolinite (Fig. 4.2G). Due to the low sodium content in the non-end member K-feldspar, only 0.034 wt.-% albite can be precipitated, while 1 wt.-% illite is formed (Fig. 4.8D). In comparison, the measured data show that ca. 2 wt.-% albite and 1 wt.-% illite are formed. Even though a difference exists between the modelled and measured illite/albite ratio, our modelling results suggest that the illite formation via the kinetic transformation of non-end member K-feldspar can lead to albite formation in view of chemical thermodynamics.

In summary, two alternative pathways may have led to authigenic albite formation. However, an overall valid explanation and thus exclusive pathway for the authigenic albite formation in the Magnus sandstones cannot be inferred. Thus, it is likely that selected parts of these two pathways may contribute to the complex and interacting process chain together for the albite formation in the Magnus sandstones.

4.9. Conclusions

(1) Up to 18 wt.-% albite occurs in the Magnus sandstones and its contents vary with depth and correlate with increasing K-feldspar content and increasing grain size.

(2) Albite occurs as lamellae in perthite, as overgrowth on dissolved K-feldspar and/or replacive patches in altered K-feldspar grains. All kinds of albite in the Magnus sandstones have dull cathodoluminescence and a high purity of chemical composition. Especially, the albite overgrowth is pure (100% Ab), and differs from albite lamellae with 2-4% An and replacing albite patches with 1-3% An.

(3) A part of albite can be inferred as diagenetic albite based on unaltered crystal surfaces, its high purity, and dull cathodoluminescence as well as its co-occurrence with other diagenetic minerals.

(4) Diagenetic albite was formed during burial, K-feldspar dissolution and quartz cementation. The initial start of diagenetic albite formation in the Magnus sandstones could be 80 Ma BP and it may continue to form until today. Correspondingly, the temperature range for the diagenetic albite formation in the Magnus sandstones is 90-120°C.

(5) Hydrogeochemical modelling indicates that an increase in temperature and pressure as major control is not the reason for albite formation. Two possible pathways for authigenic albite formation in the Magnus sandstones are presented and discussed: (i) dissolution of kaolinite and chalcedony coupled with reduction of ferric iron minerals by reducing agents produced during oil generation, migration and degradation, and (ii) dissolution of non-end member K-feldspar.

4.10. Acknowledgements

Funding of Nana Mu was provided by the Chinese Scholarship Council (CSC). The authors thank the British Geological Survey for access to core samples, and Laura González Acebrón and an anonymous reviewer for their constructive and helpful comments.

Chapter 5 Testing meteoric water flushing as a factor for oil degradation and mineral alteration in deep-marine sandstones - Case study: Frigg and Grane field, northern North Sea

5.1. Abstract

Two submarine fan sandstones (Eocene Frigg sandstones, Frigg field, and Palaeocene Heimdal sandstones, Grane field) both sourced from the same area were studied to unravel the controls of their mineral and oil alteration, whether both processes are coupled. Methodologically, imaging (thin section, scanning electron microscope (SEM)), mineralogical (X-ray diffraction (XRD)) and organic geochemical methods (Gas Chromatography-Flame Ionization Detection (GC-FID), Fourier Transform Ion Cyclotron Resonance Mass Spectrometry (FT-ICR-MS)) and hydrogeochemical modelling (Phreeqc) were applied.

The submarine fan sandstones of the Frigg field are mainly composed of quartz and few detrital K-feldspar grains which are extensively dissolved and altered to kaolinite. In contrast, the Heimdal submarine fan sandstones consisting of both K-feldspar and albite detrital grains show minor alteration features. The extracts of the Frigg sandstones are more intensively degraded but show an atypical signature of oxygen-bearing compounds in (-) ESI-FT-ICR-MS results hinting towards differences of the degradation pathways in the reservoir.

The Frigg sandstones in the Frigg gasfield were connected to a canyon that was cut back

This chapter has been submitted as: Mu, N., Schulz, H.-M., Fu, Y., van Berk, W., and Poetz, S., 2016. Testing meteoric water flushing as a factor for oil degradation and mineral alteration in deep-marine sandstones - Case study: Frigg and Grane field, northern North Sea. Sedimentary Geology, under review.

into a narrow shelf, facilitating flushing of meteoric water. Meteoric water intrusion may have taken place either via basinward migration of meteoric water zone during sea level fall stages and/or via hyperpycnal flows, and may have led to mineral alterations, but also to the alteration of early charged oils in the reservoirs.

Hydrogeochemical modelling results suggest that a combination of meteoric water flushing and oil degradation can have led to all observed mineral alterations in the Frigg sandstones. The depositional environment of the Heimdal sandstones in the Grane field, in contrast, was located more distant from the East Shetland shelf. Accordingly, meteoric water flushing into the Heimdal sandstones was minor or absent, preserving the original mineral matrix.

Keywords: Meteoric water; turbidite; sandstone; kaolinite; oil degradation; FT-ICR-MS

5.2. Introduction

Deep-marine turbidite sandstones which form important reservoirs in many basins (e.g. in the North Sea) increasingly become the main targets for petroleum exploration and exploitation. Besides depositional facies, diagenetic alterations of sandstones, which can significantly affect reservoir properties and distributions, are critical in predicting reservoir qualities.

In deep marine sediments, formation pyrite and/or concretionary carbonate are the main eogenetic alterations which are thought to be mediated by marine pore waters (Morad et al., 2010). Silicates dissolution and kaolinite formation, which are usually seen in continental sandstones, are less commonly found in paralic/submarine sandstones (Worden and Morad, 2003; Bjørlykke and Aagaard, 1992). This is because the deep marine sediments are less likely to be intruded by meteoric water, considering their large distance from land (Bjørlykke and Aagaard, 1992). However, an increasing number of literatures have reported that silicates dissolution and kaolinite formation due to meteoric water flushing also can occur in submarine sandstones, such as in the deep-sea turbidite sandstones of Shetland-Faroes Basin, UK (Mansurbeg et al., 2006; 2008), and in the turbidite reservoirs of Campos Basin, Brazil (Prochnow et al., 2006; Carvalho et al., 1995). Meteoric water flushing into deep-water sandstones leading to kaolinization of detrital grains is usually linked to a major sea-level fall and/or tectonic uplifts (Bjørlykke and Jahren, 2010; Morad et al., 2000; Worden and Morad,

2003). However, the parameters, which influence the likelihood and extent of meteoric water flushing and corresponding alterations of reservoir and oil quality, are still poorly understood. Moreover, the impact of oil degradation on diagenetic alterations is largely unknown.

Here, we present a multidisciplinary study of two deep marine sandstones: the Eocene Frigg sandstones in Frigg field and the Palaeocene Heimdal sandstones in Grane field, North Sea. The aim of this study is to analyze the controlling factors of meteoric water intrusion into deep marine sediments and their impacts and its associated oil degradation on minerals alterations. In order to achieve this objective, several issues regarding diagenetic alterations of submarine sandstones are discussed in this study, including: (1) eogenetic alterations of submarine sandstones; (2) the role of meteoric water leading to mineral alterations and oil degradation; and (3) the impact of oil degradation on diagenetic alterations. The analysis of potential links between diagenesis of turbidity sandstones, oil degradation, meteoric water and geological settings will shed new light on submarine sandstone properties and oil quality prediction.

5.3. Geological background

The Frigg field

The Frigg field, which is a large gas field, situates at the Norwegian-UK border in the northern North Sea (Fig. 5.1). It consists of a thick gas pool (up to 163 m) overlying an oil disc (up to 10 m thick) (Brewster, 1991). The oil disc shows features of biodegradation and has a gravity of 23-24° API (tested in well 25/1-3) (Brewster, 1991; Heritier et al., 1980). The reservoir is the Lower Eocene Frigg sandstones which were deposited as a submarine fan complex with sediments sourced from the East Shetland Platform (Heritier et al., 1980). The reservoir has a high porosity of 27-32% and a permeability of 900-4,000 mD (Brewster, 1991). It is sealed by overlying Middle Eocene marine shales. The oil of the Frigg field is thought to be derived from locally deeply buried Lower and Middle Jurassic source rocks (Brewster, 1991; Heritier et al., 1980) and have been generated and charged the reservoir from around 55-65 Ma ago (Palaeocene to Eocene) until the present day (Goff, 1983). The gas of the Frigg field is deep, thermogenic gas indicated by the $\delta^{13}C$ value of CH_4 (-43.3‰; Heritier et al., 1980). It shares the same source rocks with the Frigg oil but was generated during the late burial phase (Brewster, 1991; Heritier et al., 1980). Migration of gas into the Frigg reservoirs

probably took place during the Oligocene and Miocene via “gas chimneys” in fractured shales (Brewster, 1991).

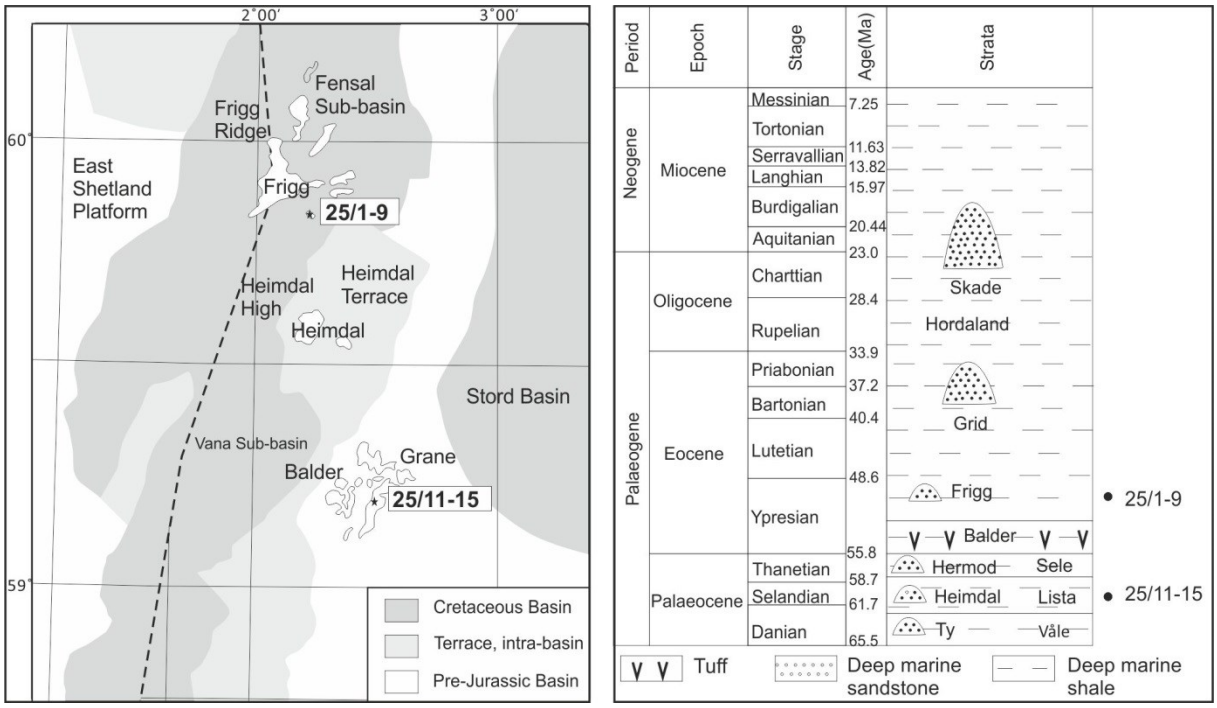

Figure 5.1 Locations of the two studied wells (left) and stratigraphy of Northern North Sea (right).

Sequence stratigraphic studies of the Frigg area have revealed that during the Tertiary the Frigg area has a strong eastward progradation feature which could be attributed to the rejuvenation of the Shetlands-Orcadian belt (Heritier et al., 1980). The Frigg area underwent an early Palaeocene marine sedimentation followed by a later Palaeocene major regression and a subsequent early Eocene marine transgression (Heritier et al., 1980). The Frigg sandstones are thought to have developed during a major base-level fall stage when the widespread incision of the earlier shelf-delta system occurred and a submarine fan system constituting the Frigg reservoir deposited in the basin (Dixon and Pearce, 1995). The sandstones of the Frigg fan were sourced by a south-west trending submarine channel, which in turn, was fed by canyons cut into the East Shetland Platform (Heritier et al., 1980).

The Grane field

The Grane oil field is located in the Norwegian North Sea, sitting on the western flank of the Utsira High. It contains degraded (19°API), highly viscous oil with no initial gas cap. The main reservoir is the Palaeocene Heimdal Formation which is made up of homogeneous unconsolidated marine turbidite sandstones sourced from the East Shetland Platform (Ross et

al., 2010). It forms the distal, east toe of the large Heimdal/Andrew deep-water system (Jones and Milton 1994; Martinsen et al., 2005). The reservoir with a high porosity of 31.5-37% and a permeability of 1,510-12,640 mD has been affected insignificantly by diagenetic processes (Ross et al., 2010). The source rock is the Upper Jurassic Draupne Formation in the South Viking Graben (Justwan et al., 2006a). Hydrocarbon generation from the source rocks in the Viking Graben is thought to proceed from the Cretaceous until today (Isaksen and Ledje, 2001) or from the early Palaeocene to the present (Justwan et al., 2006b).

5.4. Samples and Methods

Thirty representative samples were collected from porous reservoir sandstones of well 25/1-9 in the Frigg field and of well 25/11-15 in the Grane field, covering the oil legs, the oil-water contacts (OWCs) and the water legs. All core samples were extracted using a dichloromethane-methanol mixture (99:1; v: v) in a Dionex ASE 200 apparatus at 50°C for 24 hours to remove bituminous organic compounds. Extracted samples were then selected and prepared for thin sections after impregnating blue epoxy resin. Thin sections were then intensively examined under polarizing petrographic microscope. For quantifying detrital and diagenetic components, four thin sections of well 25/1-9 and one thin section of hard sandstone from well 25/11-15 were conducted on point counting (600 points per thin section). Note that most of the core samples from well 25/11-15 are very loose and XRD results indicate a quite homogeneous composition. To study the habit features and textural relationships of both detrital and authigenic minerals, six carbon-coated thin sections, and thirteen gold-coated rock chips were investigated under a Philips SEM-515 scanning electron microscope (SEM) equipped with an Edax PV 9100 energy-dispersive X-ray spectroscopy (EDS). A number of images were taken both under BSE (backscattered scanning electron) and SE (scanning electron) mode.

One mg of powdered samples was used for XRD (X-ray diffraction) analysis to characterize and semi-quantify mineral assemblages of both sandstone reservoirs. Prepared samples were measured using a Bruker-axs D8 X-ray Microdiffractometer. The spectra were recorded from 5° to 125° in 2 hours using a step interval of 0.1°.

Fifteen oil extracts of core samples from both wells were separated into three fractions of aliphatic, aromatic, and hetero-(NSO) compounds by using medium pressure liquid

chromatography (MPLC; Radke et al., 1980) after deasphalting. The aliphatic fractions were diluted in n-hexane and examined on a GC-FID system (6890A, Agilent Technologies, USA) equipped with an HP Ultra 1 capillary column (film thickness = 0.33 μm, 50 m x 0.2 mm i.d.). 5α-androstane was used as internal standards. The injector was set an initial temperature of 30°C and then was heated up to 300°C within 23 seconds, held for 3 minutes. The GC oven was heated from 40°C (2 min isothermal) to a final temperature 300°C (65 min isothermal) at a heating rate of 5°C/min. The helium gas was used as the carrier gas with a constant flow rate of 1 ml/min. The operation temperature for the FID was 310 °C.

For Fourier Transform Ion Cyclotron Resonance Mass Spectrometry (FT-ICR-MS) analysis, the extracted bitumen of ten selected samples from both wells were dissolved in dichloromethane and diluted with a methanol-toluene mixture (1:1; v: v) to produce a concentration of 100 μg/mL. Prior to the measurement, 10 μL of a concentrated aqueous NH3 solution was added to each sample solution. Mass analyses were performed in negative electrospray ionization (ESI) mode with a Bruker Solarix FT-ICR-MS. The procedure of measuring, data evaluation and sorting have been described previously in detail (Poetz et al., 2014). Besides the compound class depicting the sort and number of abundant heteroatoms in a molecule, the double bond equivalents (DBE) as a measure for unsaturation and the carbon number distributions have been evaluated. The DBE has been calculated for each assigned molecular according to the formula: DBE = C - H/2 + N/2 + 1 (C: the number of carbon; H: the number of hydrogen; N: the number of nitrogen).

5.5. Results

5.4.1. The Eocene Frigg sandstones of Frigg field

Detrital composition of sandstones

The Frigg Formation in well 25/1-9 is lithologically heterogeneous with several intercalations of shale layers. The Frigg sandstones are subarkosic sandstones (Fig. 5.2) which are fine to medium in grain size with moderate sorting. Quartz is the most abundant detrital component (54.5-62.7 vol. %, Table 5.1). Feldspar, mainly K-feldspar, comprises the second abundant detrital grains (5.12-11.5 vol. %, Table 5.1), and shows an intensive degree of dissolution (Fig. 5.3A-B). Lithic fragments, including mud clasts and altered igneous clasts, are only in a minor trace amount (0-1.2 vol. %, Table 5.1). Mica occurs in variable amounts

(0-0.7 vol. %) in which muscovite predominates (Table 5.1). Porosity, based on point-counting of thin section, ranges from 16.1 to 22.3 vol. % (Table 5.1).

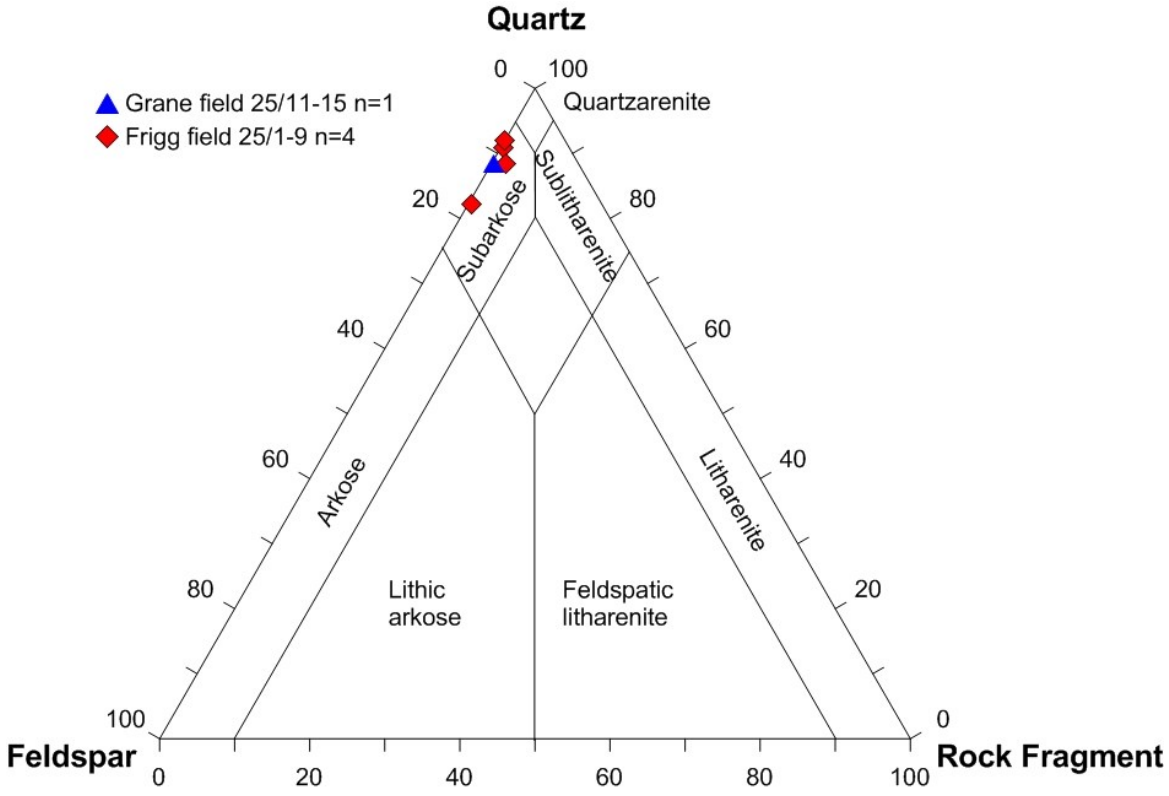

Figure 5.2 Detrital mineral compositions of the investigated Frigg and Heimdal sandstone samples. n: sample numbers.

Petrography and geochemistry of diagenetic minerals

Quartz cement

Quartz cements (4.2-6.8 vol. %) as one of the most significant diagenetic phases commonly occur as syntaxial overgrowths (5-10 μm) on detrital quartz grains (Fig. 5.3B). SEM images reveal that quartz overgrowths are engulfed by kaolinite (Fig. 5.3D). Minor amounts of quartz cement also take the form of discrete euhedral crystals, filling intergranular space adjacent to quartz and kaolinite. Quantitatively, quartz overgrowths show no obvious systematic variations in sampled intervals of the well 25/1-9 (Table 5.1).

Feldspar

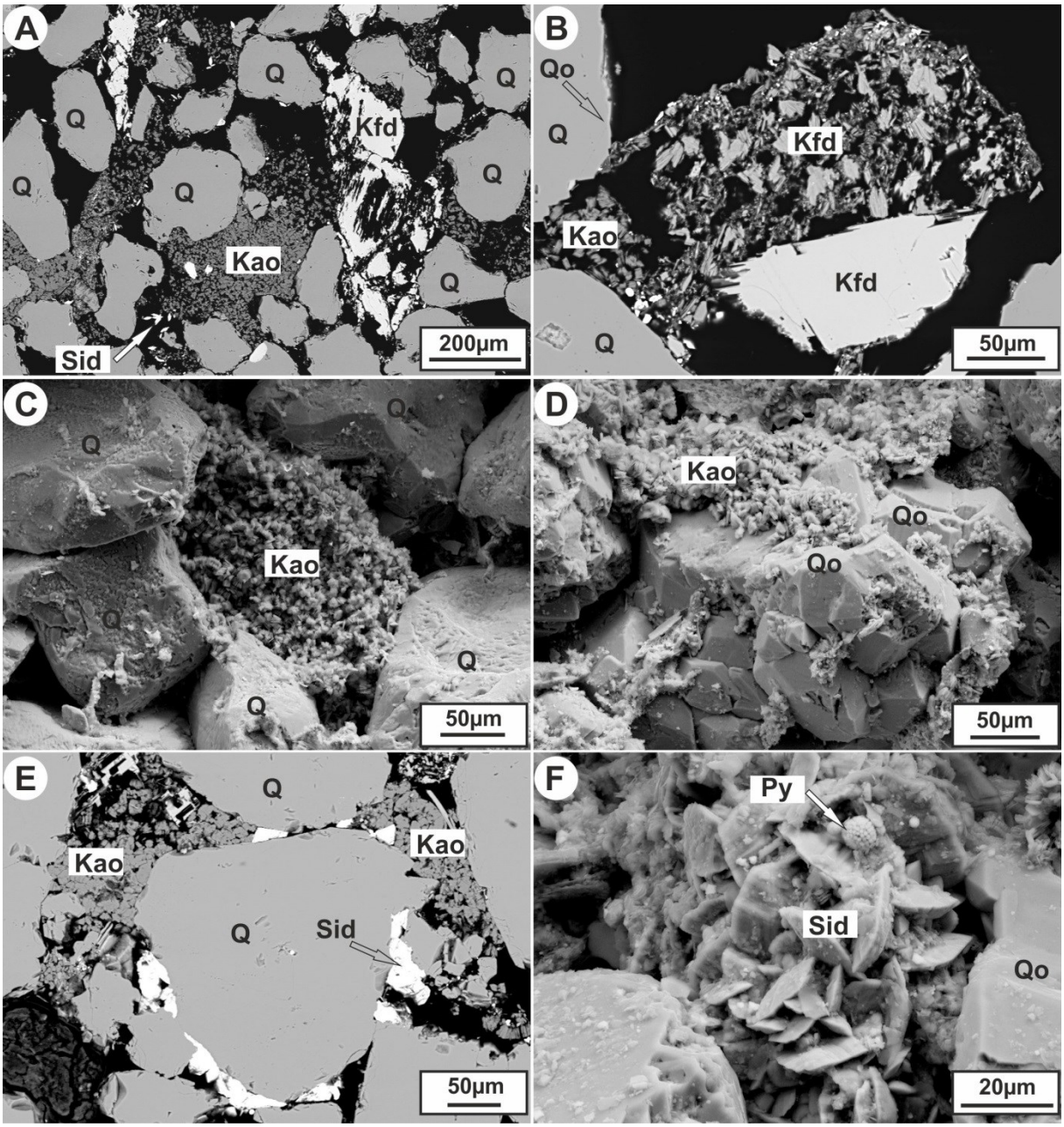

Figure 5.3 Diagenetic features in the Frigg sandstone samples in well 25/1-9, Frigg field: (a) K-feldspar dissolution and pore-filling kaolinite, BSE; (b) kaolinite growing in strongly dissolved K-feldspar, BSE; (c) grain-shape kaolinite replacing detrital grain, SEM; (d) quartz cement engulfed by kaolinite; (e) siderite coating detrital quartz, BSE; (f) framboidal pyrite coating siderite, SEM. Q: quartz; Qo: quartz overgrowth; Kfd: K-feldspar; Kao: kaolinite; Sid: siderite; Py: pyrite.

K-feldspar, the only feldspar type in the Frigg sandstones of well 25/1-9, accounts for 8 to 10 wt.-% of bulk rock (Table 5.2). Chemically, it contains a minor amount of sodium. The textures of most K-feldspars show evidence of strong dissolution and have abundant

Table 5.1 Mineral composition by point counting.

Oil field	Well	Sample ID	Location	Depth (m)	Detrital compositions vol. %					Authigenic minerals vol. %				Porosity %
					Quartz	K-feldspar	Albite	Lithic fragments	Mica	Kaolinite	Quartz cement	Siderite	Pyrite	
Frigg	25/1-9	G013619	Gas cap	2050.6	62.69	5.97	0.00	0.30	0.60	7.46	4.18	2.69	0.00	16.12
	25/1-9	G013622	Oil leg	2053.4	54.35	11.49	0.00	0.31	0.00	6.83	6.83	0.62	0.00	19.57
	25/1-9	G013627	Oil leg	2061.9	58.85	5.12	0.00	0.00	0.62	9.47	6.83	0.31	0.00	18.79
	25/1-9	G013632	Water leg	2069.6	54.48	5.89	0.00	1.21	0.73	9.36	5.41	0.61	0.00	22.30
Grane	25/11-15	G013590	Oil leg	1775.4	63.77	4.64	3.48	0.29	1.45	0.87	0.58	0.00	0.58	24.35

Table 5.2 Mineral composition by XRD analysis.

Oil field	Well	Sample ID	Location	Depth (m)	Quartz wt.-%	Albite* wt.-%	K-feldspar wt.-%	Muscovite wt.-%	Calcite wt.-%	Dolomite wt.-%	Siderite wt.-%	Kaolinite wt.-%	Pyrite wt.-%
Frigg	25/1-9	G013619	Gas cap	2050.6	86.8	3.8	9.0	0.8	0.0	0.0	0.3	3.1	0.1
		G013620	Gas cap	2051.5	84.1	3.9	9.6	1.3	0.0	0.0	0.6	4.3	0.1
		G013622	Oil leg	2053.4	89.1	2.3	7.1	0.0	0.0	0.0	0.5	3.2	0.1
		G013624	Oil leg	2055.9	88.6	2.5	8.0	0.0	0.0	0.0	0.5	2.8	0.1
		G013626	Oil leg	2058.6	80.8	2.8	7.8	2.1	0.0	0.0	1.2	7.7	0.3
		G013628	OWC	2062.8	90.6	2.1	6.8	0.0	0.0	0.0	0.2	2.4	0.0
		G013629	Water leg	2063.7	90.7	1.4	7.0	0.0	0.0	0.0	0.2	2.1	0.0
		G013632	Water leg	2069.6	87.8	2.2	8.5	0.0	0.0	0.0	0.4	3.2	0.1
Grane	25/11-15	G013588	Oil leg	1762.6	87.4	3.9	7.0	0.8	0.2	0.5	0.1	0.0	0.0
		G013590	Oil leg	1775.4	87.5	4.2	6.2	1.0	0.6	0.5	0.0	0.0	0.0
		G013591	Oil leg	1779.75	87.3	4.1	7.3	0.4	0.3	0.5	0.0	0.0	0.0
		G013593	Oil leg	1782.75	86.2	4.9	7.6	0.7	0.3	0.3	0.0	0.0	0.0
		G013594	Oil leg	1783.7	86.9	4.4	7.5	0.6	0.2	0.4	0.0	0.0	0.0
		G013595	OWC	1784.5	87.7	4.4	6.9	0.5	0.3	0.2	0.1	0.0	0.0

Continued on next page

Table 5.2 Mineral composition by XRD analysis.-continued

Oil field	Well	Sample ID	Location	Depth (m)	Quartz wt.-%	Albite* wt.-%	K-feldspar wt.-%	Muscovite wt.-%	Calcite wt.-%	Dolomite wt.-%	Siderite wt.-%	Kaolinite wt.-%	Pyrite wt.-%
		G013597	Water leg	1785.6	86.7	4.7	7.2	0.4	0.3	0.7	0.0	0.0	0.0
		G013598	Water leg	1786.7	85.8	4.1	8.0	1.5	0.1	0.4	0.0	0.0	0.0
		G013599	Water leg	1787.7	85.2	4.7	8.0	1.6	0.2	0.3	0.0	0.0	0.0
		G013601	Water leg	1792.5	85.1	4.1	8.4	1.7	0.3	0.4	0.0	0.0	0.0

*Albite determined in well 25/1-9 probably occurs as tiny albite lamellae in detrital K-feldspar grains rather than as detrital albite grains.

Table 5.3 Percentages of SARA fractions and calculated parameters of the aliphatic fractions.

Oil field	Well	Sample ID	Location	Depth (m)	SARA (wt.-%)				Aliphatic faction parameters						
					Asphaltenes	Aliphatics	Aromatics	NSO-compound	Pr/*n*-C_{17}	Ph/*n*-C_{18}	Pr/Ph	Waxiness	CPI	CPI2	LHCPI
Frigg	25/1-9	G013622	Oil leg	2053.4	4.82	58.39	11.08	25.7	8.1	7.94	0.88	n.a.	n.a.	n.a.	n.a.
		G013624	Oil leg	2055.9	1.78	59.62	20.55	18.06	12.26	9.67	1.06	n.a.	n.a.	n.a.	n.a.
		G013628	OWC	2062.8	3.6	58.99	13.44	23.97	3.22	5.38	0.59	n.a.	n.a.	n.a.	n.a.
Grane	25/11-15	G013588	Oil leg	1762.6	16.01	34.79	14.24	34.96	1.02	0.66	1.4	0.61	1.04	1.01	2.01
		G013590	Oil leg	1775.4	18.8	31.6	13.47	36.13	1.08	0.67	1.45	0.62	1.05	1.04	2.12
		G013591	Oil leg	1779.75	13.02	35.37	15.14	36.48	1.03	0.65	1.53	0.62	1.06	1.05	2.05
		G013593	Oil leg	1782.75	13.91	35.1	13.99	36.99	1.09	0.67	1.52	0.59	1.03	1.03	1.82
		G013594	Oil leg	1783.7	13.39	34.99	15.27	36.35	1.06	0.68	1.5	0.61	1.11	1.04	1.83
		G013595	OWC	1784.5	13.02	35.66	14.51	36.81	1.14	0.68	1.51	0.55	1.04	1.04	1.56
		G013597	OWC	1785.6	13.82	34.66	14.68	36.84	1.09	0.65	1.47	0.55	1.03	1.01	1.66

Notes: Pr/*n*-C_{17}: Pristane/*n*-C_{17}; Ph/*n*-C_{18}: Pytane/*n*-C_{18}; Pr/Ph: Pristane/ Pytane; Waxiness: *n*-C_{17}/(*n*-C_{17}+*n*-C_{27}); CPI (carbon preference index): 0.5*((*n*-C_{25}+ *n*-C_{27}+*n*-C_{29}+*n*-C_{31})/(*n*-C_{24}+*n*-C_{26}+*n*-C_{28}+*n*-C_{30})+(*n*-C_{25}+ *n*-C_{27}+*n*-C_{29}+*n*-C_{31})/(*n*-C_{26}+*n*-C_{28}+*n*-C_{30}+*n*-C_{32})) (Bray and Evans 1961); CPI2 (carbon preference index 2): ((*n*-C_{23}+*n*-C_{25}+*n*-C_{27})+(*n*-C_{25}+*n*-C_{27}+*n*-C_{29}))/(2*(*n*-C_{24}+*n*-C_{26}+*n*-C_{28})) (Marzi et al., 1993); LHCPI (light hydrocarbon carbon preference index): (*n*-C_{17}+*n*-C_{18}+*n*-C_{19})/(*n*-C_{27}+*n*-C_{28}+*n*-C_{29}).

secondary pores (Figs. 5.3A-B). In some strongly altered K-feldspar grains, newly formed kaolinite is present with remaining K-feldspar relicts (Fig. 5.3B). In some cases, K-feldspar seems to be completely replaced by kaolinite (Fig. 5.3C).

Clay minerals

Kaolinite is the main pore-filling clay mineral and accounts for up 7.7 wt.-% of the bulk composition of the Frigg sandstones. It commonly takes the form of booklets consisting of pseudohexagonal phase and fills primary pores (Fig. 5.3A). At some locations, kaolinite aggregations show a solid compaction feature (Fig. 5.3A). In addition, SEM images reveal that kaolinite aggregation also resembles the shape of detrital grains (might be detrital K-feldspar; Fig. 5.3C). The amount of kaolinite does not show any trend in the sampled intervals of the Frigg sandstones (Table 5.2).

Carbonate

The carbonate in the Frigg sandstones of well 25/1-9 is mainly siderite (Tables 5.1 and 5.2). It accounts for a minor amount (0.3 to 2.7 wt.-%) in the Frigg sandstone and commonly occurs as small (20 to 50 μm diameter) rhombic crystals coatings on detrital quartz and/or feldspar grains (Figs. 5.3E-F). In some cases, it also fills the pores or replaces lithic fragments and/or expanding mica. EDS analyses indicate that siderite is Ca-poor with various amounts of Mg (Fig. 5.4).

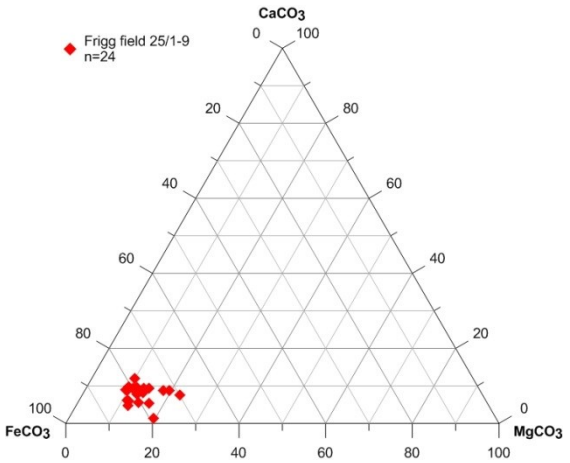

Figure 5.4. Carbonate composition of the investigated Frigg sandstone samples (well 25/1-9). n: sample numbers.

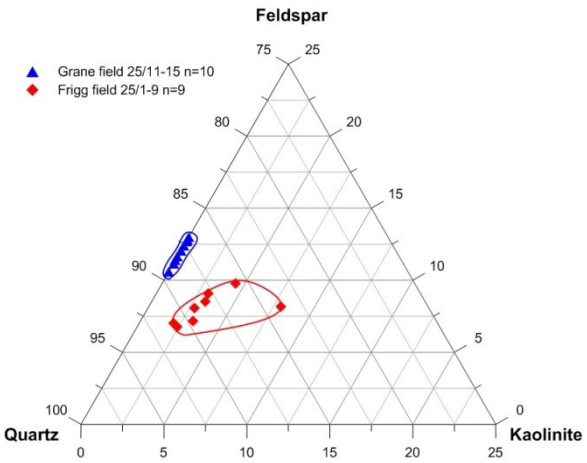

Figure 5.6. XRD results of the investigated Frigg and Heimdal sandstone samples. n: sample numbers.

The Frigg core extracts

The extracts of the Frigg sandstones display slight variations in chemical composition, with a strong predominance of aliphatic hydrocarbons (58.4 to 59.6 wt.-%), 11.1-20.6 wt.-% of aromatic hydrocarbons, 18.1-25.7 wt.-% of NSO and minor amounts of asphaltenes (Table 5.3). The gas chromatograms of the aliphatic fractions show an extensive loss of almost all *n*-alkanes and the presence of huge hump representing an unresolved complex mixture (UCM) which increases from the oil leg towards the OWC (Fig. 5.7). Pristane and phytane are the two predominant peaks (Fig. 5.7), with Pr/Ph ratios ranging from 0.59 to 1.06. The Pr/*n*-C_{17} and Ph/*n*-C_{18} ratios are extremely high, with the range of 3.22 to 12.26 and 5.38 to 9.67, respectively (Fig. 5.7, Table 5.3). Because of the extreme absence of nearly all n-alkanes, any calculation of other parameters (waxiness, CPI, and LHCPI) was not possible.

The (-) ESI-FT-ICR-MS analysis of the Frigg extracts revealed a dominance of oxygen containing compounds as expected for biodegraded petroleum samples (Hughey et al., 2002, 2007; Kim et al., 2005). The most abundant compound class O_2 covers a DBE range of 1-20 and a carbon number range of 10-45 (Fig. 5.8). The O_2 species with 1 and 2 DBE corresponding to fatty acids and monocyclic fatty acids ("one-ring-naphthenic acids") or monounsaturated fatty acids are most abundant in the Frigg extracts (Figs. 5.8 and 5.9). N_1 compounds containing carbazole and its benzolated analoga are only minor constituents. The samples from the OWC show a slightly different compositional pattern in the O_1, O_2 and O_3 compounds with a relative enrichment in 5-8 DBE compounds for the O_1 class, in 6-8 DBE for the O_2 class and in 2-3 and 5-9 DBE for the O_3 class (Fig. 5.8). The acyclic/cyclic naphthenic acids (A/C) ratios [Σ O_2 DBE=1/ Σ O_2 DBE=3, 4, 5] cover a range of 0.65 to 0.99 with an average value of 0.80.

5.4.2. The Palaeocene Heimdal sandstones of Grane field

Petrographic features of the Heimdal sandstone

The Heimdal sandstones in well 25/11-15 are fine- to medium-grained, poorly cemented sandstones. The mineralogical composition is homogeneous through the sampled interval (see XRD results in Table 5.2). The results by means of point counting of one representative sample show a more differentiated picture. Detrital components consist of 63 vol. % quartz, 4.6 vol. % K-feldspar, 3.5 vol. % albite and minor lithic fragments and mica (Table 5.1). Diagenetic phases, such as quartz and carbonate cement are poorly developed in the Heimdal sandstones (Fig. 5.5). Only a small portion of albite is characterized by slight dissolution

features (Figs. 5.5E-F). Overall, the Heimdal sandstones have experienced limited chemical alterations and were mainly affected by mechanical compaction.

The Grane core extracts

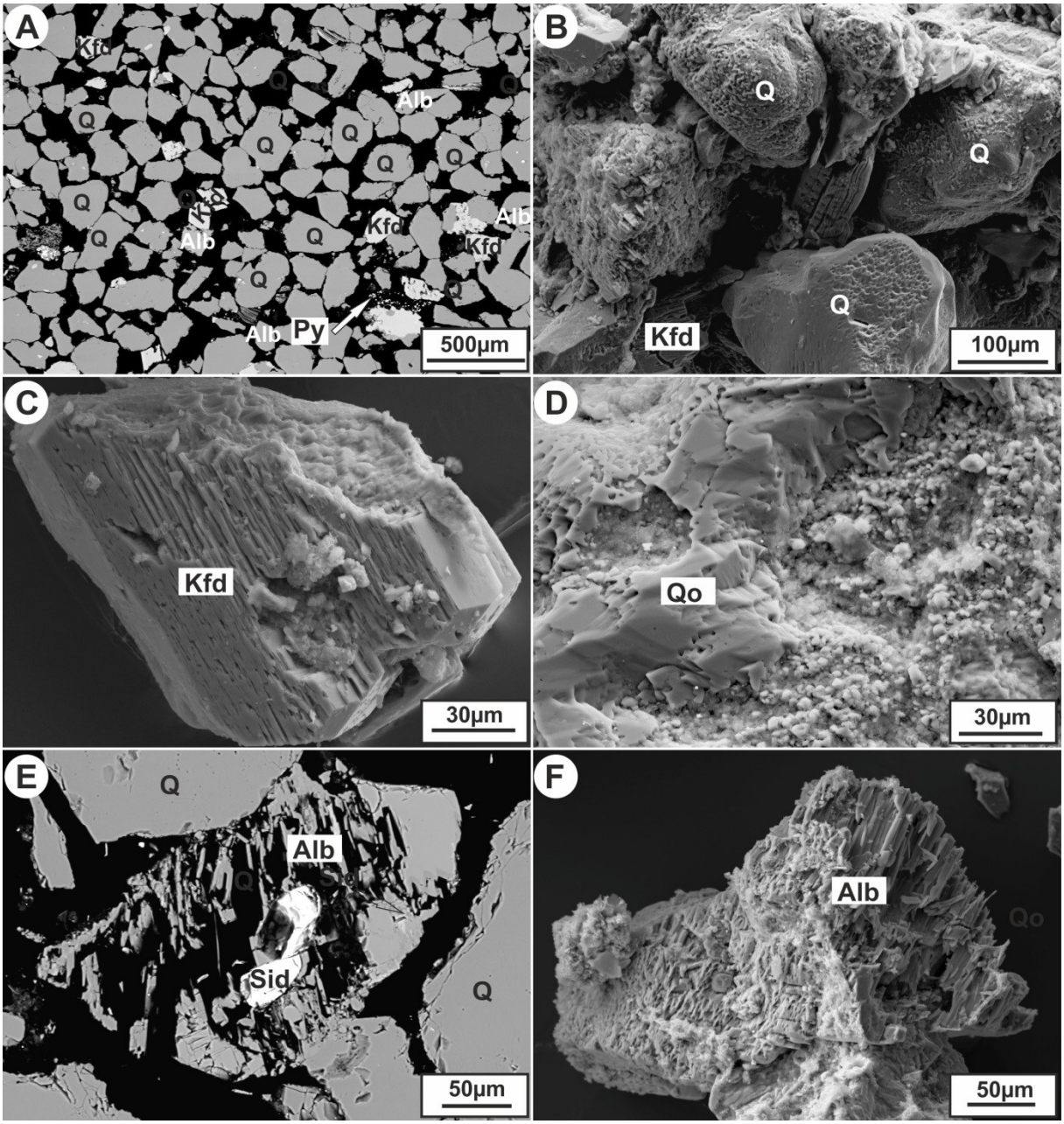

Figure 5.5 Diagenetic features of the investigated Heimdal sandstone samples in well 25/11-15, Grane field: (a) unaltered sandstones without pore-filling minerals, BSE; (b) detrital quartz grains covered by thin micro-quartz cement and dissolved albite, SEM; (c) fresh, unaltered K-feldspar, BSE; (d) quartz cement, SEM; (e) siderite growth in dissolved albite, BSE; (f) dissolved albite, SEM. Q: quartz; Qo: quartz overgrowth; Kfd: K-feldspar; Alb: albite; Sid: siderite.

The oil extracts of the Heimdal sandstones in the Grane field are predominantly composed of saturated hydrocarbons (31.6-35.7 wt.-%) and NSO compounds (35.0 to 37.0 wt.-%). Aromatic hydrocarbons and asphaltenes are in lower amounts (Table 5.3). The aliphatic fractions of the oil extracts contain n-alkanes in the range of *n*-C_{15} to *n*-C_{33} with the absence of *n*-alkanes (*n*<15) (due to evaporation loss during the preparation procedure). In addition, a distinct UCM hump is present, which does not increase from the oil legs towards the OWC (Fig. 5.7). Akin to the mineralogy, the oil extracts of the Heimdal sandstones in the Grane field also show low variations in e.g. bulk organic composition from the SARA fractionation (Table 5.3), gas chromatogram patterns of saturated compounds (Fig. 5.7), and parameters derived from those CPI, Pr/*n*-C_{17} and Ph/*n*-C_{18} values (Table 5.3, Fig. 5.10).

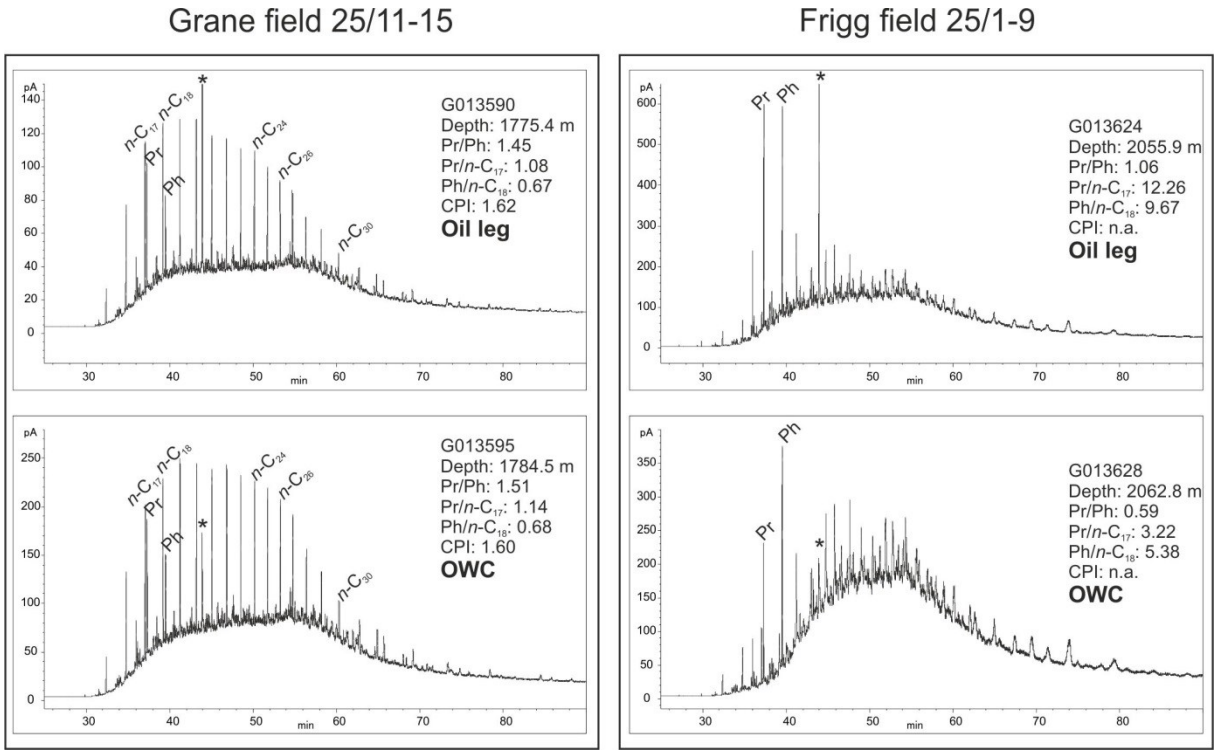

Figure 5.7 Gas chromatograms of the aliphatic fractions of samples taken from the oil-filled reservoir and from the oil-water contact (OWC) in the Grane and Frigg field. * indicates the internal standard 5α-androstane.

Like the Frigg extracts, the (-) ESI-FT-ICR-MS analysis of the Grane extracts also reveals that the O_2 species predominate. Unlike the Frigg extracts, the O_2 species in the Grane extracts cover a wider carbon number range of 11-51 (Fig. 5.8). Moreover, the O_2 species with 3-4 DBE are predominant (Figs. 5.8 and 5.9). The samples from the oil leg and OWC show a similar distribution pattern in O_2 species except for a slight decrease in the relative

abundance of DBE>5 O_2 compounds (Fig. 5.8). The O_1 species in the extracts from the oil leg and the OWC spread over a similar DBE range of 1-17 and a carbon number range of 12-35 (Fig. 5.8). O_1 compounds with 1-4 DBE are nearly absent in both extracts (Figs. 5.8 and 5.9). The O_3 species in the two Grane extracts are alike, with a relative enrichment of 5-9 DBE O_3 compounds (Fig. 5.8). The A/C ratios of the Grane extracts are much lower than those of the Frigg extracts with values of 0.12 and 0.08 in the oil leg and at the OWC, respectively.

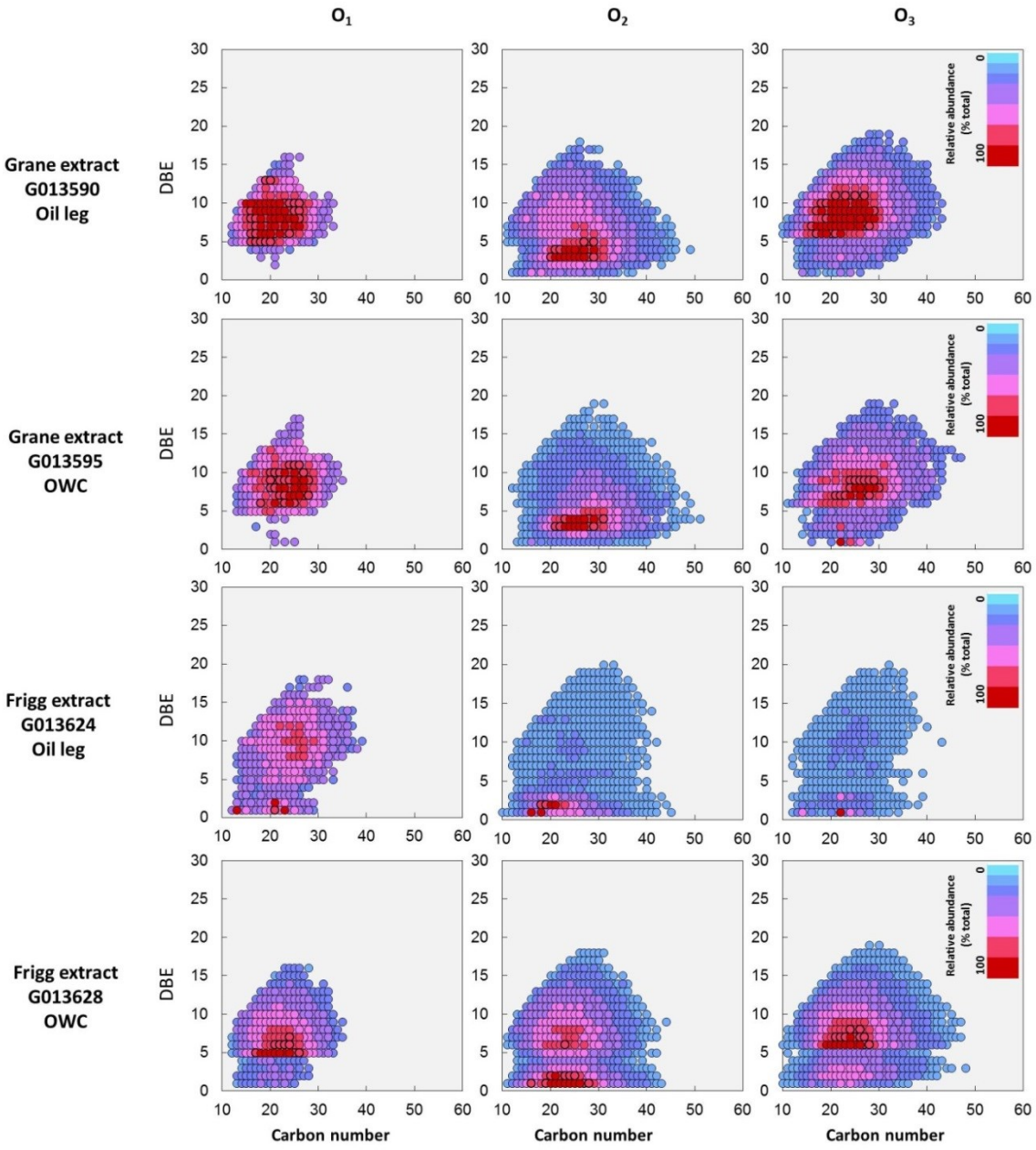

Figure 5.8 Iso-abundance plots of double bond equivalent (DBE) vs. carbon number of O_1, O_2 and O_3 classes in the extracts of well 25/11-15 (Grane field) and well 25/1-9 (Frigg field).

5.6. Discussions

5.6.1. Mineralogy and oil geochemistry of the Palaeocene

Detrital components

Both the Eocene Frigg sandstones and the Palaeocene Heimdal sandstones were deposited as deep-marine fan with sediments derived from the East Shetland (Heritier et al., 1980; Ross et al., 2010). However, they differ in detrital components (Table 5.1). Quartz and feldspar are two dominant detrital components in both sandstones. However, the Frigg sandstones appear to have less detrital feldspar and K-feldspar is the exclusive type of feldspar occurring in the Frigg sandstones (Table 5.1). Detrital albite accounts for 3.5 vol. % of the Heimdal sandstones, but is absent in the Frigg sandstones (Table 5.1, Fig. 5.3). The absence of albite and relatively few detrital K-feldspar in the Eocene Frigg sandstones may be partly attributed to their origin differing from that of the Palaeocene Heimdal sandstones. The Palaeocene reservoir sandstones were sourced from the large delta/margin system along the eastern margins of the East Shetland Platform (Jones et al., 2003), whereas the Eocene reservoir sandstones underwent extensive reworking on the shelf prior to transportation into the deep sea (Bowman, 1998).

Diagenetic processes

The Frigg sandstones in well 25/1-9 and the Heimdal sandstones in well 25/11-15 are buried at depths of 2,045-2,075 m and 1,734-1,798 m, respectively. The present reservoir temperatures of both reservoir sandstones are around 60 ˚C and 70˚C (data from Norwegian Petroleum Directorate), and can be considered as their maximum burial temperatures according to the burial history reconstructed by Justwan et al. (2006b). Although both sandstone reservoirs are still under eodiagenetic temperature conditions (<70˚C), they are markedly different in diagenetic features (Figs. 5.3 and 5.5). The Heimdal sandstones are supposed to have been affected mainly by mechanical compaction and less, if any, by chemical alterations (Fig. 5.5). In contrast, the Frigg sandstones were subjected to significant chemical alteration - in addition to mechanical compaction- which is reflected by abundant authigenic quartz cement, siderite and kaolinite precipitation, and intense K-feldspar dissolution (Fig. 5.3). Authigenic quartz cement is very few in the Heimdal sandstones (Figs. 5.5B and D), but is fairly abundant in the Frigg sandstones, in which it takes the forms of

quartz overgrowth or of euhedral quartz crystals filling in pores (Fig. 5.3B). Moreover, authigenic siderite, which is negligible in the Heimdal sandstones, occurs in a minor amount in the Frigg sandstones in forms of grain coatings (Figs. 5.3E-F), single rhombic crystals, and aggregations. Furthermore, K-feldspar grains appear free of any dissolution features in the Heimdal sandstones (Fig. 5.5C), but commonly show different degrees of dissolution in the Frigg sandstones (Figs. 5.3A-B). Most importantly, authigenic kaolinite, nearly undetectable in the Heimdal sandstones (Table 5.2; Figs. 5.5 and 5.6), comprises up to 7 wt.-% of bulk compositions of the Frigg sandstones (Table 5.2).

Oil degradation

Oil extracts of both sandstones show huge UCM humps (Fig. 5.7), indicating that oils in both sandstone reservoirs have been subjected to oil degradation. Moreover, the Frigg oils seem to be more severely degraded than the oils in the Heimdal sandstones, which can be supported by three lines of evidence revealed by GC-FID: (1) extent loss of almost all *n*-alkanes (Fig. 5.7), (2) extremely high Pr/*n*-C_{17} and Ph/*n*-C_{18} values (Fig. 5.10), and (3) huger UCM humps. However, FT-ICR-MS results indicate a less degradation for the Frigg extracts. As acyclic fatty acids decrease while cyclic fatty acids increase with increasing degradation, the acyclic/cyclic naphthenic acids (A/C) ratio can be used as a new parameter to assess the biodegradation degree (Kim et al., 2005). The Frigg extracts have an A/C ratio range of 0.64-0.99, which is much higher than that of the Grane extracts (A/C 0.08 and 0.12). These higher A/C values of the Frigg extracts may suggest a lower degree of biodegradation than the Grane extracts, contradicting the GC-FID results.

The high A/C values in the Frigg extracts due to the relative abundant aliphatic acids (1 DBE O_2 species) might account for two other reasons rather than a lower degree of biodegradation. First, the Frigg oils might have been mixed with immature organic matter from interbedded shales or cap rocks, as the relative abundance of saturated acid and monounsaturated fatty acids is also observed in immature Posidonia Shale (Ro 0.53%, Poetz et al., 2014; Fig. 5.9). The second possible reason could relate to different degradation pathways. Relatively saturated acid and monounsaturated fatty acids were also reported in the O_2 species of weathered crude oil extracted from beach sands (Rowland et al., 2014). Moreover, the O_1 species in the Frigg extracts also resemble those weathered crude oil, containing 1-4 DBE compounds (Figs. 5.8 and 5.9) that are usually absent in biodegraded oils (Liao et al., 2012; Pan et al., 2013; Hughey et al., 2002, 2007; Kim et al., 2005), in the Grane

extracts and in immature Posidonia shale extracts (Fig. 5.9). Accordingly, it can be inferred that the Frigg oils might resemble the weathered crude oils extracted from beach sands and might have undergone aerobic degradation. This assumption is also supported by the presence of highly oxygenated compounds (up to O_8) in the Frigg extracts, as Tomcsyk et al. (2001) previously identified highly oxygenated species (up to O_6 species) in a San Joaquin Valley oil and ascribed their presence to aerobic biodegradation.

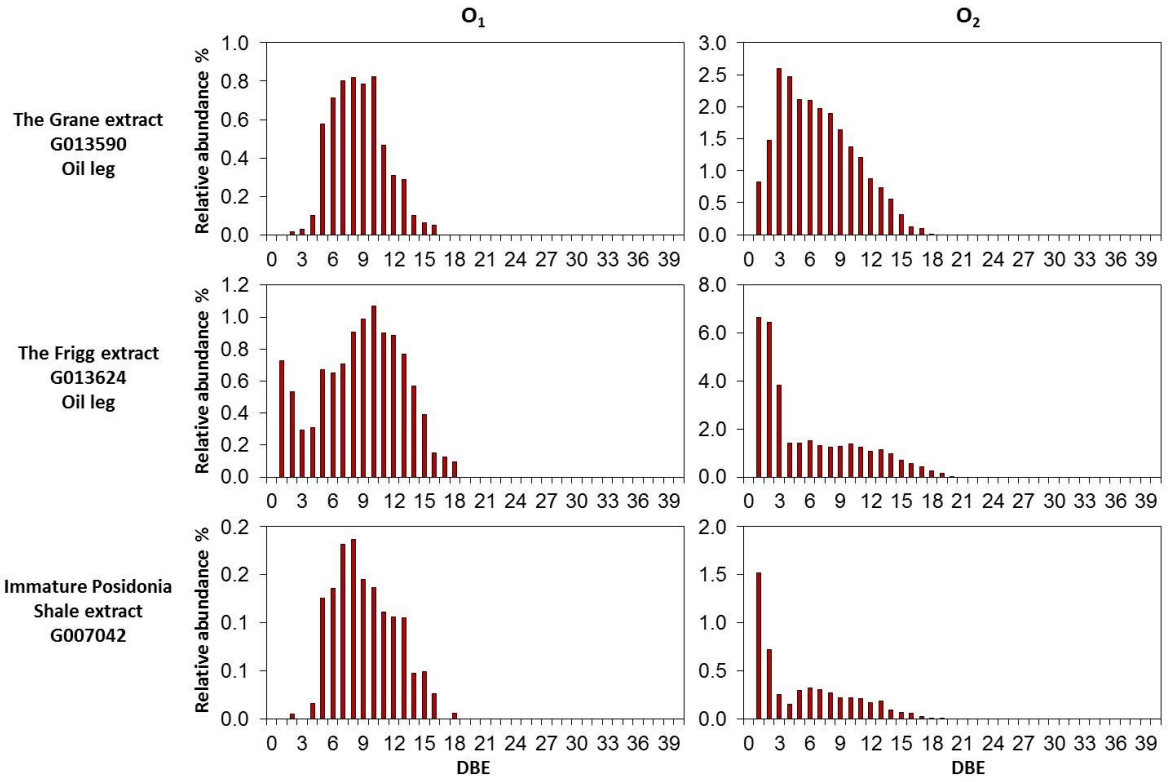

Figure 5.9 Relative abundance of double bond equivalent (DBE) of O_1 and O_2 species in the Grane extract (well 25/11-15), in the Frigg extract (well 25/1-9) and in an immature Posidonia shale (Ro 0.53%) extract (data provided by S. Poetz).

However, anaerobic degradation should have also taken place in the Frigg sandstones. The associated CO_2 in the gas cap of the Frigg field has positive stable carbon isotope values ($\delta^{13}C$ PDB: +9.5‰ and +11.9‰; well 25/1-9 well report). Such positive $\delta^{13}C$ values may be an indicator of anaerobic degradation of oil and gas, as aerobic degradation leads to negative $\delta^{13}C$ values of CO_2 (-25 to -45‰ PDB) while CO_2 with positive $\delta^{13}C$ values (0 to +20‰ PDB) accounts for anaerobic degradation (Pallasser, 2000).

Unlike the Frigg extracts, the Grane extracts share many similarities with previous ESI FT-ICR-MS studies of degraded oil (Liao et al., 2012; Pan et al., 2013; Hughey et al., 2002, 2007; Kim et al., 2005): (1) enrichment of multi-ring naphthenic acids (3-4 DBE O_2 species; Figs. 5.8 and 5.9); (2) the absence of 1-4 DBE O_1 species (Figs. 5.8 and 5.9); and (3) a low A/C ratio. Accordingly, the Grane oils resemble most degraded reservoir oils, and might have predominantly been subject to anaerobic degradation.

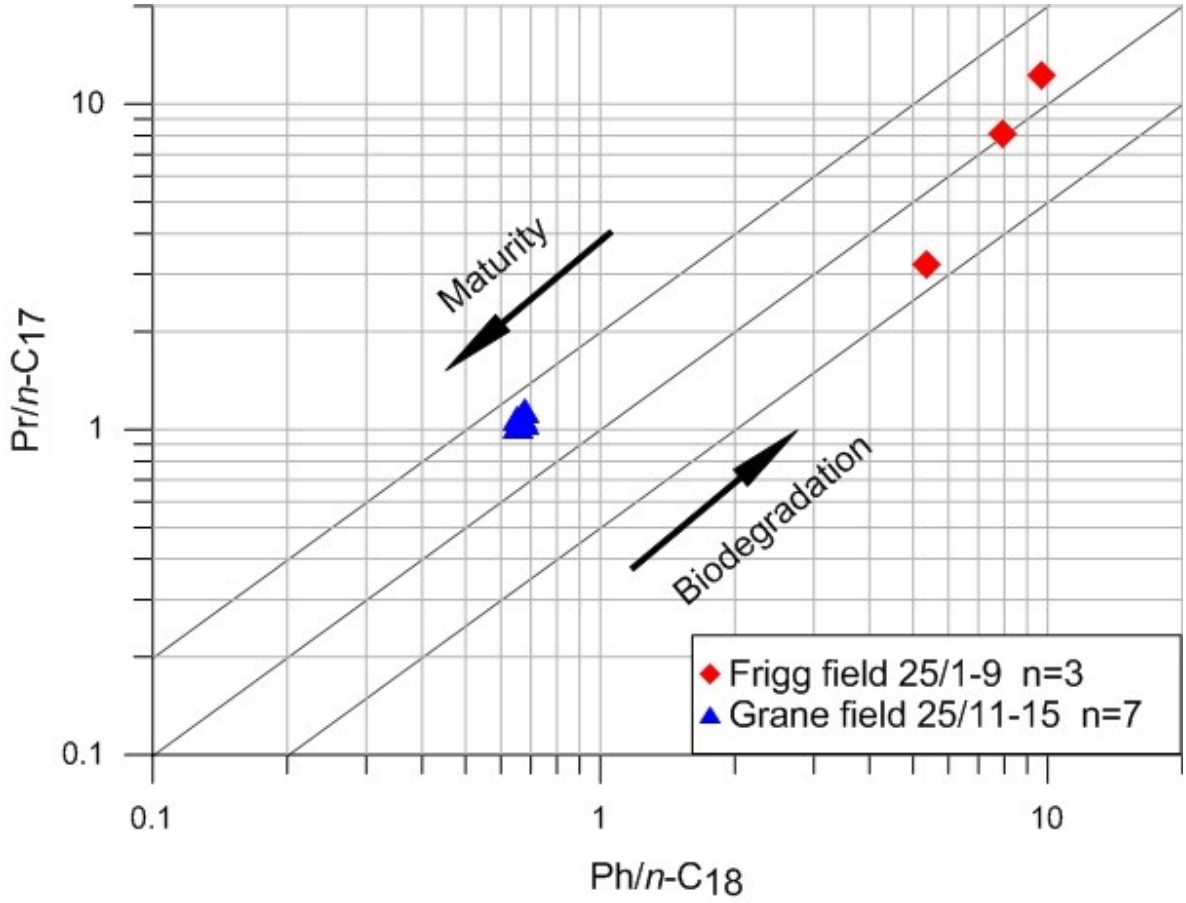

Figure 5.10 Pristane/*n*-C_{17} versus pytane/*n*-C_{18} ratios of extracts from the investigated Frigg and Heimdal sandstone samples (according to Shanmugam, 1985).

5.6.2. Process considerations

Intensive oil degradation in the Frigg sandstones

The Frigg extracts show more intensive oil degradation which partly accounts for their relative lower reservoir temperature, as reservoir temperate is one of the primary controls on oil degradation (Larter et al., 2003). The present burial depths of the Heimdal sandstones in well 25/11-15 are between 1,734 and 1,798 m with a reservoir temperature of 70˚C. The Frigg

sandstones in well 25/1-9 are buried at 2,045-2,075 m, about 300 m deeper than those in well 25/11-15, but their present reservoir temperature is around 60˚C. The relative lower reservoir temperature of the Frigg sandstones may contribute to their relative higher degree of oil degradation, as degradation rates decrease with increasing reservoir temperatures (Larter et al., 2003).

The main cause for the intensified degree of oil degradation in the Frigg sandstones could be attributed to temporally aerobic field water conditions. Unlike the anaerobic degradation of the Grane oils discussed in paragraph 5.1.3, the Frigg oils might have thus undergone both aerobic and anaerobic degradation. The oxygenated environment for aerobic degradation is likely to be created by meteoric water intrusions which can supply –at least in the short term- dissolved oxygen and nutrients for aerobic microorganisms. Since organic matter is degraded much faster under aerobic conditions compared to anaerobic conditions (Larter et al., 2003), it can be inferred that the Frigg oils could have been subject to more intensive aerobic alteration.

Hydrogeochemical mechanisms leading to K-feldspar dissolution and kaolinite formation

Meteoric water intrusion is often invoked as a driving mechanism for feldspar dissolution and accompanying kaolinite formation in sandstones (Longstaffe, 1993; Bjørlykke and Aagaard, 1992; Morad et al., 2000). This is because it can remove K^+ from the existing marine pore water system and make the pore water maintain relatively low H^+/K^+ ratios remaining in the stability field so that enables K-feldspar dissolution and accompanying kaolinite formation (Bjørlykke and Jahren, 2012).

Another geochemical condition that favours K-feldspar dissolution and kaolinite formation is the addition of CO_2 and organic acids, as they can increase the H^+/K^+ ratio in the pore water. It was commonly believed that CO_2 and organic acids, both generated from maturation of source rocks, are the main cause for secondary porosity due to feldspar dissolution in sandstones (Surdam and Crossey, 1985; Surdam et al., 1989). However, some doubts have been raised upon their efficiency as these source rock products could have been neutralized within source rocks and/or during migration before they reached potential reservoirs (Bjørlykke and Jahren, 2010). On the other hand, CO_2 and organic acids generated by oil degradation (Mackenzie et al., 1981; Watson et al., 2002) may act as effective agents

for mineral dissolution in reservoirs due to their short migration distance. This driving force for rock-water interactions in oil-bearing reservoirs has been extensively studied (Ehrenberg and Jakobsen, 2001; Prochnow et al., 2006; van Berk et al., 2009, 2013; Fu et al., 2015a; Mu et al., 2015, 2016). However, oil degradation might have played a less important role in triggering feldspar dissolution and kaolinite formation in the Frigg sandstones, as the Frigg sandstones in the East Frigg Field contain non-biodegraded oil (Heritier et al., 1980), but also have high kaolinite contents (East Frigg 25/2-1 well; Cussey, 1974).

5.6.3. Meteoric water intrusion into Frigg turbidite sandstones

Factors controlling meteoric water intrusion

The presence of feldspar dissolution and kaolinite formation in the Frigg reservoirs could indicate that meteoric water might have reached the Frigg sandstones. Reasons for meteoric water intruding into the Frigg sandstones in the Frigg field but not reaching the Heimdal sandstones in the Grane field could be ascribed to the following differences: (1) the Frigg sandstones were deposited immediately below the Shetland escarpment (Heritier et al., 1980; Fig. 5.11) while the Heimdal sandstone deposition in the Grane field lay 50-100 km distant from the East Shetland Platform; (2) the Palaeo-shelf area during deposition of the Frigg sandstones was narrow (Ahmadi et al., 2003; Jones et al., 2003; Fig. 5.11), but it was wide when the Heimdal sandstones deposited (Fig. 14.9b in Ahmadi et al., 2003; Fig. 11 in Martinsen et al., 2005; Fig. 5.11); (3) the Frigg sandstones were fed via a channel that connected with an incised valley/canyon on the earlier shelf-delta system (Dixon and Pearce, 1995; Fig. 5.11), whereas the Heimdal sandstone in the Grane field were sourced from a large delta/margin system along the eastern margins of the East Shetland Platform (Jones et al., 2003). All these dissimilarities between them could indicate that the Frigg sandstones in the Frigg field were more likely affected by meteoric water flushing.

Mechanisms for meteoric water intrusion

Previous studies have demonstrated that meteoric water could enter into deep marine sandstones (turbidities) through three mechanisms (Mansurbeg et al., 2006; 2008): (1) telodiagenesis during uplifts (Morad et al., 2000), (2) hydraulic heads generated from the land mass on the Shelf platform (Morad et al., 2000, 2012; Ketzer et al., 2003), and (3) hyperpycnal flow. However, the first mechanism –telodiagenesis is unlikely in the Frigg area,

as no evidence indicates that this area has been uplifted to cause erosion since the Frigg sandstones were deposited.

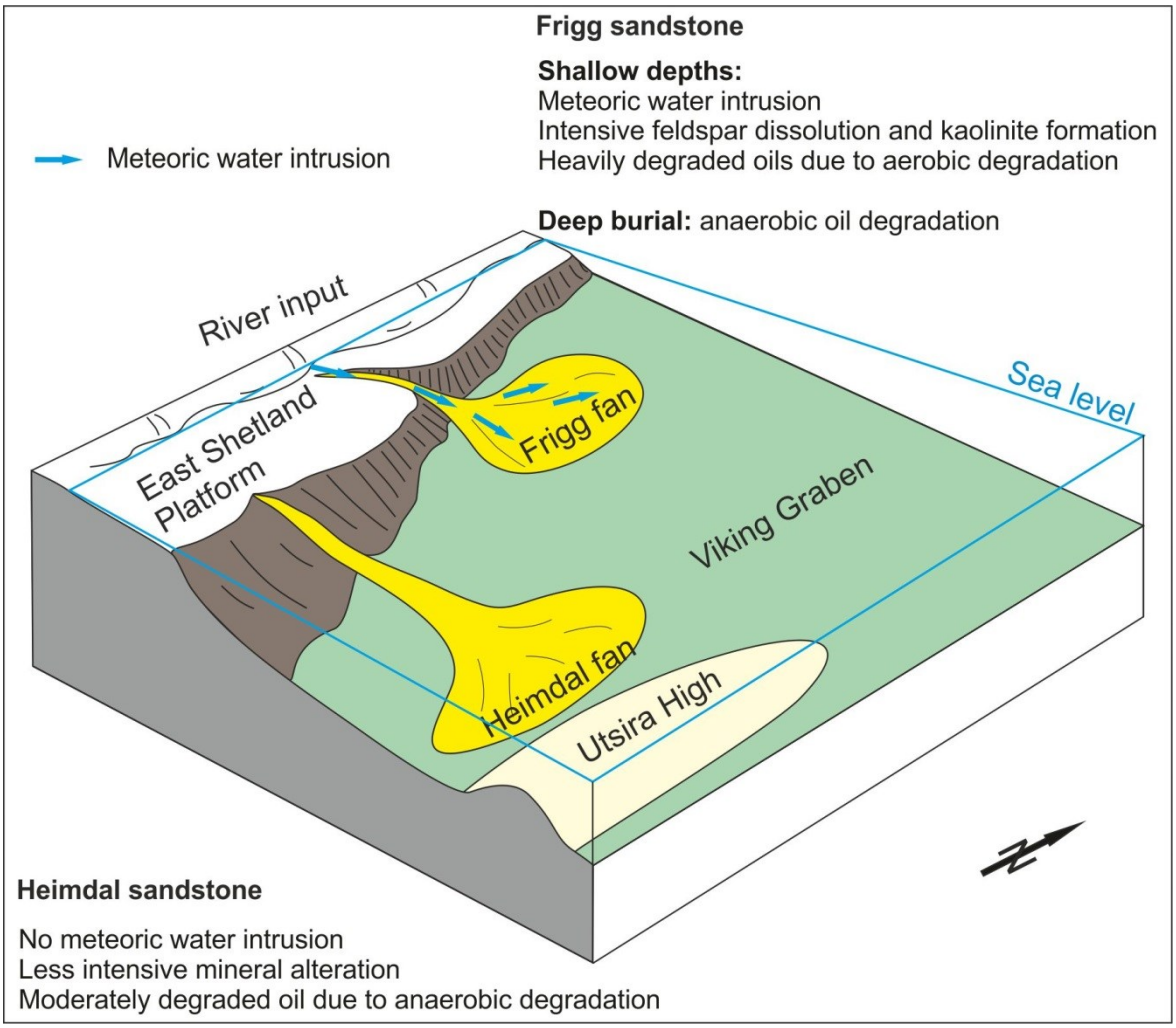

Figure 5.11 Conceptual sketch of the potential meteoric water intrusion pathways into the Frigg submarine fan sandstones and subsequent alterations in the reservoirs.

Fluxing of meteoric water into the Frigg submarine sandstone could be achieved by the hydraulic heads generated at East Shetland shelf during two periods of relative sea-level fall: during deposition (Dixon and Pearce, 1995) and at the end of the Eocene (Priabonian) (Galloway et al., 1993). This is because a major fall of relative sea-level can lead to the exposure of the East Shetland shelf and migration of shorelines toward basin, which thus, could result in basinward migration of meteoric water zone (Morad et al., 2000, 2012; Ketzer et al., 2003). This enlarged and basinward migrated meteoric water zone might have reached the Frigg sandstones via the underlying Mauser sandstones, as the Mauser sandstones have

high porosity and permeability and they extend widely from the East Shetland Platform to the Viking basin (Dixon and Pearce, 1995; Jones et al., 2003). Thus, the Mauser sandstones could well connect the meteoric water zone and the Frigg sandstones.

Hyperpycnal flow is another plausible mechanism of meteoric water intrusion into the Frigg sediments. Since the hyperpycnal flow is a dense underflow generated by river effluents (Plink-Björklund and Steel, 2004; references herein), the likelihood of hydraulic connections of river waters with turbidite sediments via hyperpycnal flows increases when there is a narrow shelf (Kneller and Buckee, 2000; Petter and Steel, 2006). During the deposition of the Frigg sandstones, a narrow palaeo-shelf was constructed (Ahmadi et al., 2003; Jones et al., 2003; Fig. 5.11), which could suggest that meteoric water intrusion into the Frigg sandstones by means of transportation of fresh river water via hyperpycnal flows could be possible.

5.6.4. Hydrogeochemical modelling of the Eocene Frigg sandstones

Working hypotheses

Meteoric water could have intruded into the Frigg submarine sandstones by two possible means: hydraulic heads generated at East Shetland shelf during relative sea-level falls or hyperpycnal flows. Due to meteoric water flushing, the Frigg sandstones could have been subject to intensive mineral alterations (Fig. 5.11). In the meantime, oils in the Frigg sandstones could have been also intensively degraded via short-term or periodic aerobic degradation as a result of meteoric water intrusion (Fig. 5.11). As the Frigg sandstones were increasingly buried to greater depths, the Frigg oil and the later charged gas underwent anaerobic degradation. Even through oil degradation might have played a less significant role in K-feldspar dissolution and kaolinite formation (sec. 5.2.2) in the Frigg sandstones, authigenic siderite (a product of iron reduction) may indicate that anaerobic degradation must have also impacted the mineral matrix in the Frigg sandstones.

Minerals can become thermodynamically unstable with increasing temperature and pressure during burial. Therefore, the impact of progressive burial on mineral alterations should also be taken into account. Accordingly, three conceptual scenarios can be developed in order to hydrogeochemically model diagenetic alterations in the Frigg sandstones:

progressive burial as scenario 1, meteoric water flushing as scenario 2, and anaerobic oil degradation as scenario 3.

Hydrogeochemical modelling

To test the aforementioned three scenarios, hydrogeochemical batch modelling was carried out based on chemical thermodynamics by using the Phreeqc Interactive 3.2 (Parkhurst and Appelo, 2013). Assuming a sandstone with a porosity of 25 %, our batch model reactor has a total volume of 4.0 litres, of which 3.0 litres are composed of primary minerals and 1.0 liter represents pores that filled with original seawater. As an average sandstone density is 2.65 kg/L, the reactor consists of an assemblage of minerals that weighs 7.95 kg. Table 5.4 summarizes the observed petrographic results and pre-assigned modelling parameters including the estimated amounts of primary minerals, the lists of potential secondary minerals and the present reservoir condition in terms of its temperature and pressure. Quartz and K-feldspar are dominant in the mineral assemblage, accounting for 70 wt.-% and 20 wt.-% of the original frameworks of Frigg sandstones, respectively (Table 5.4).

Table 5.4 Present and pre-assigned mineral assemblages of the Eocene Frigg sandstones.

	Observed[a]		Pre-assigned for modeling		
	wt.-%	mol/kgw		wt.-%	mol/kgw
			Primary minerals[b]		
Quartz	80	105.85	Quartz	70	92.62
K-feldspar	10	2.86	K-feldspar	20	5.71
Kaolinite	5	1.54	Muscovite	5	1.00
Quartz overgrowth	2	2.65	$Fe(OH)_{3(a)}$	1.5	0.99
Siderite	3	1.37	Others[c]	3.5	n.a.
Muscovite	1	0.2	Secondary minerals[d]		
			Quartz overgrowth	0	0
			Siderite	0	0
			Kaolinite	0	0
			Pyrite	0	0
		Reservoir conditions[e]			
Temperature	61°C		Pressure	195 atm	
Depth	2050-2070 m		Porosity	27-32%	

Notes:
a Based on the petrographic observations and XRD analysis.
b Original amounts of minerals after deposition are assumed.
c Other detrital grains, such as mud clasts. Not considering as reactive primary minerals for modelling.
d Minerals allowed to precipitate in the modelling reactor.
e Brewster, 1991

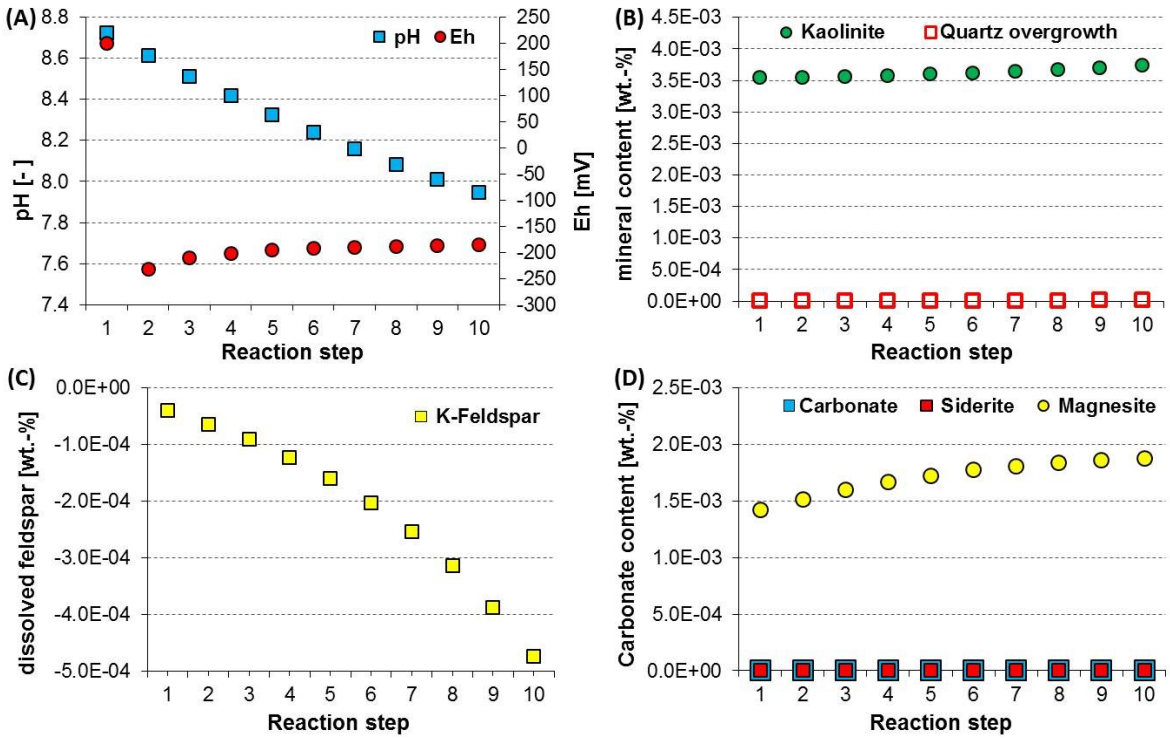

Figure 5.12 Modelling results of scenario 1: increasing temperature and pressure during progressive burial. (A) pH and Eh of the pore water. (B) The amounts of precipitated quartz overgrowth and kaolinite precipitation. (C) The amount of K-feldspar dissolution. (D) The amounts of different carbonates precipitation. The amounts of minerals in (B, C, D) are given in wt.-%.

As the Frigg sandstones were deposited in deep marine environments, seawater is assumed as the initial pore fluid that the framework minerals firstly contacted with. Scenario 1 (input file as A4 in Appendix) is set up to test how the primary mineral assemblage reacts with seawater under an assumed T-P (temperature-pressure) gradient (T: 10 to 60°C in 10 steps; P: 1 to 200 atm in 10 steps). The present-day seawater provided by Parkhurst and Appelo (2013) is used in scenario 1. The results reveal that the pre-assigned minerals are destabilized during the increase of temperature and pressure. However, only insignificant amounts of these pre-assigned minerals get dissolved in the modelling scenario 1 (mostly in the order of 10−4 mole). For example, K-feldspar slightly dissolves (1.35E−4 moles) and a minor amount of kaolinite (1.15E−3 mole) precipitates (Fig. 5.12). These modelling results indicate that this diagenetic pathway can lead to K-feldspar dissolution and kaolinite formation. However, the amounts of dissolved K-feldspar and formed kaolinite are minor compared with the observed intensive K-feldspar dissolution and kaolinite formation. The reason for these could be that pore water rapidly gets saturated with respect to K-feldspar due

to a close modelling system. Therefore, a system in which the ratio of activities of H^+, K^+, Al^{3+}, and silica changes are needed for significant K-feldspar dissolution and kaolinite formation (up to 7.7 wt.-%).

The scenario 2 (input file as Appendix A5) simulates the intrusion of meteoric water by designing a stepwise addition of meteoric water into the pores that filled with seawater. Since meteoric water in nature is highly variable in chemical compositions, pure water is used for modelling. In scenario 2, 1,450 liters of pure water were added into the generic reactor each step in a total of 10 steps. With the stepwise addition of meteoric water, the pH and Eh of pore water change insignificantly (Fig. 5.13). However, the pre-assigned mineral assemblages become unstable. By flushing 1 liter of pure water into the modelling reactor, only a limited amount of K-feldspar dissolve and a minor amount of kaolinite precipitate (2.17E−3 mole and 1.09E−3 mole, respectively). To gain 5 wt.-% of newly formed kaolinite, large volumes (14,500 liters in total; Fig. 5.13) of meteoric water are needed to flush the Frigg sandstones. Such large volumes of meteoric water could be transported by frequent repetitions of or long-lasting meteoric water flushing.

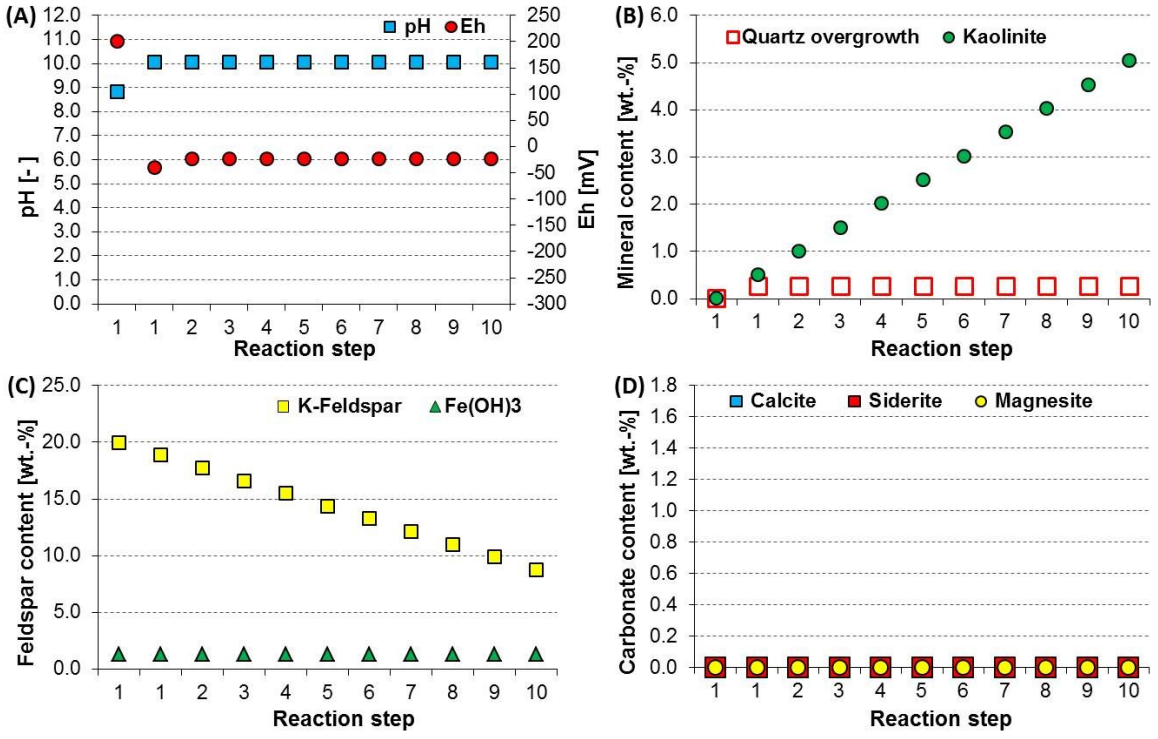

Figure 5.13 Modelling results of scenario 2: meteoric water flushing. (A) pH and Eh of the pore water. (B) The amounts of precipitated quartz overgrowth and kaolinite precipitation. (C) The amount of K-feldspar dissolution. (D) The amounts of different carbonates precipitation. The amounts of minerals in (B, C, D) are given in wt.-%.

Scenario 3 models a system that takes the products of anaerobic oil degradation into account. The products of oil generation/degradation, including CH_4, CO_2, and H_2 (according to Seewald (2003)), were added into the generic reactor in order to simulate oil degradation processes in the Frigg sandstones. In this scenario, 2.2 moles of CO_2, CH_4, and H_2 in a ratio of 2:1:5 were added into the reactor in each step until the observed amounts of kaolinite are formed (see Appendix A6 for the input file of scenario 3). Modelling results show that the Eh of pore water increases while the pH gradually decreases with stepwise adding CH_4, CO_2, and H_2 (Fig. 5.14). Such changes of pore water result in the reduction of hydrous ferric oxides/iron oxides and the formation of siderite. In addition, during this process, up to 10.9 wt.-% K-feldspar dissolves, and up to 5.0 wt.-% kaolinite are formed (Fig. 5.14).

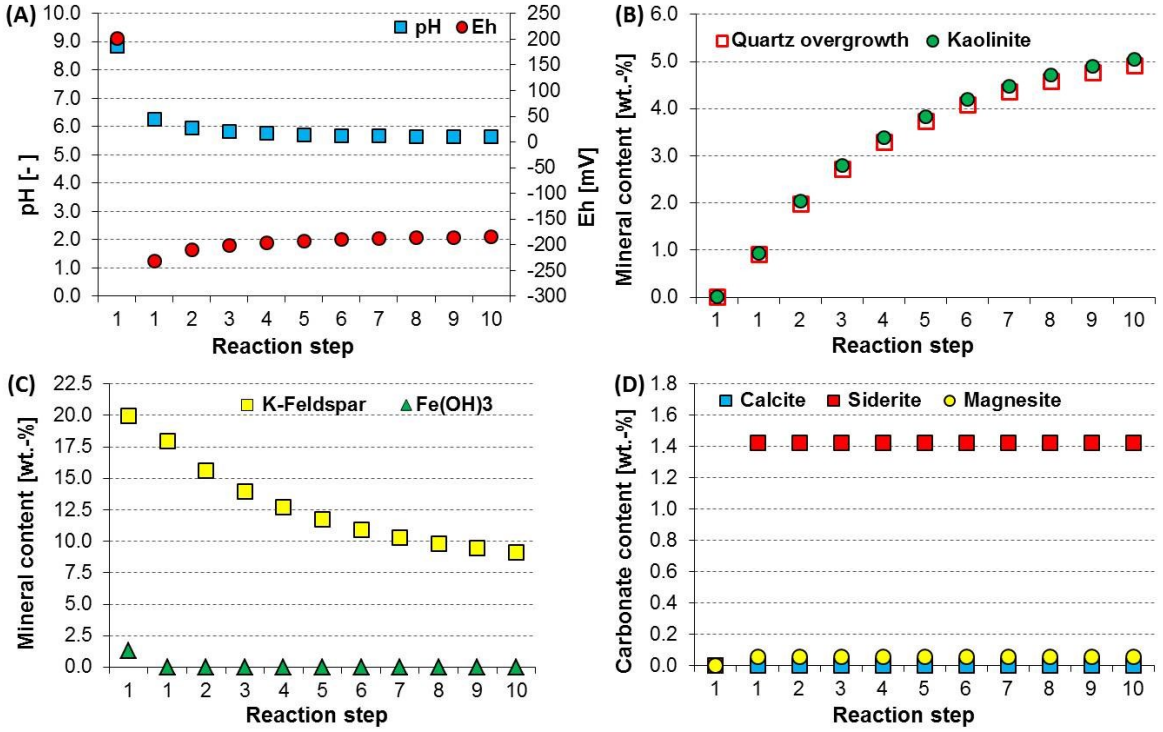

Figure 5.14 Modelling results of scenario 3: oil degradation. (A) pH and Eh of the pore water. (B) Thes amount of precipitated quartz overgrowth and Kaolinite precipitation. (C) The amount of K-feldspar dissolution. (D) The amounts of different carbonates precipitation. The amounts of minerals in (B, C, D) are given in wt.-%.

In summary, all three hypotheses can result in feldspar dissolution and kaolinite formation. However, the scenario 1 results suggest that the increasing temperature and pressure conditions during progressive burial can only account for a minor amount of altered minerals. The results of scenario 2 modelling match well with petrographic observations of intensive K-feldspar dissolution and kaolinite formation in the Frigg sandstones except for

siderite formation and quartz overgrowth. However, this shortcoming can be improved by combining the following scenario 3 with scenario 2, which is the case in the Frigg sandstone (sec. 5.4.1, Fig. 5.11). Therefore, meteoric water flushing and following oil degradation led to all minerals and oil alterations in the Frigg sandstones.

5.7. Conclusions

1. In contrast to the Palaeocene Heimdal sandstones, the Eocene Frigg sandstones are composed of a strongly altered mineral assemblage, e.g. dissolved feldspar and kaolinite growth.

2. Unlike the moderately degraded oils in Heimdal sandstones in Grane field, the Eocene Frigg sandstones host heavily altered oils mainly due to aerobic and anaerobic degradation. A contribution of immature organic matter from interbedded rocks cannot be ruled out.

3. The aerobic alteration of oil and the intensive K-feldspar dissolution and kaolinite formation in the Frigg sandstones can be ascribed to the intrusion of meteoric water.

4. Flushing meteoric water into the Frigg sandstones could have been achieved either via basinward migration of meteoric water zone during sea level fall stages or connections with river water via hyperpycnal flows during/after its deposition.

5. The Frigg submarine sandstones were deposited close to a narrow palaeo-shelf, were fed directly via canyons, and were, therefore, more likely intruded by meteoric water. Flushing of meteoric water led to minerals alteration and also oil quality deterioration.

6. The Heimdal sandstones in the Grane field, deposited far away from the East Shetland Platform, were less likely fluxed by meteoric water. Therefore, both minerals and oils have not been significantly altered.

7. Hydrogeochemical modelling results indicate that a combination of meteoric water intrusion and both short-term-aerobic and later anaerobic oil degradation could have led to the observed diagenetic features in the Frigg sandstones.

5.8. Acknowledgements

The Chinese Scholarship Council (CSC) is acknowledged for funding Nana Mu to conduct this study. The authors would like to thank the Norwegian Petroleum Directorate for providing core samples and for permitting to publish this study. We also would like to express our gratitude to Mr. Pan Li from the University of Aberdeen for his effort in improving the language of the first draft.

Chapter 6 Summary and Outlook

6.1. Summary

The objective of this dissertation is to evaluate the influence of inorganic-organic interactions on reservoir properties. The main question is how and to what extent inorganic-organic interactions influence mineral alterations of sandstones at different depths and lithologic facies. Three case studies were undertaken and integrated, in which core samples from four oil fields in the North Sea (Siri field, Magnus field, Frigg field, and Grane field) were analyzed. An interdisciplinary approach involving both inorganic and organic techniques was applied for sample analysis. The main results are summarized as below:

(1) The Siri filed

In the Siri field, the reservoir examined is the Heimdal sandstone which is a glauconite-bearing sandstone transported by turbidite currents from the Stavanger Platform. The Heimdal sandstone in Well Siri-2 is today mediately buried at depths of 2,096-2,137 m with reservoir temperature at around 78°C. In this glauconite-bearing Heimdal sandstone, authigenic berthierine, a Fe^{2+}-rich clay mineral with a basal spacing of 0.7 nm, is one of the most significant diagenetic phases. Berthierine is revealed and identified by applying a combination of various analytical methods including XRD, light microscope, and also TEM. Berthierine takes various forms, such as grain-coating, pore-filling and also as blade-like crystals in glauconite, mica and siderite concretions. EMPA analysis indicates that berthierine has similar chemical composition independent of types. Point counting and petrographic observations reveal that berthierine occurs in the whole interval from the oil leg to the water leg but it concentrates at the oil-water contact, where glauconite has lowest amounts and core extracts show a slightly higher degree of oil degradation. The relationships of berthierine and other minerals suggest that berthierine might form in-situ and after oil emplacement. Importantly, it frequently grows in glauconite and partly replaces glauconite grains, suggesting that glauconite could be the precursor for berthierine formation.

As berthierine is a Fe^{2+}-rich clay mineral, its formation requires reducing environment. However, in the Heimdal sandstones, the deposited organic matter is probably insufficient to create a reducing environment. Given that berthierine formed after oil emplacement, suitable

conditions for berthierine formation in the Heimdal sandstones could be attributed to oil charging and its secondary products during degradation.

Unlike the hypotheses invoked in previous studies, a new potential formative mechanism of berthierine formation could be that oil degradation products (CH_4, H_2, CO_2, and CH_3COOH) dissolved in formation water, lowered pH, and, consequently, led to dissolution of thermodynamically unstable minerals (such as glauconite, mica and feldspar) and also to the precipitation of thermodynamically stable minerals, e.g., quartz overgrowth, siderite and berthierine.

(2) The Magnus field

In the Magnus field, the Jurassic Magnus sandstone is the main reservoir which is at present deeply buried at depths of 3,200-3,240 m with reservoir temperature of 116°C. The Magnus sandstone is an arkose sandstone which has experienced various intensive post-deposited alterations, including quartz overgrowth, ankerite, siderite, and kaolinite formation, K-feldspar dissolution, and albite formation. Among them, K-feldspar dissolution and albite formation were poorly studied in previous studies.

Petrographic and geochemical analyses show that in the Magnus sandstones albite comprises up to 18 wt.-% and its contents vary greatly with depth but correlate well with K-feldspar content: the more K-feldspar, the more albite. Moreover, albite content increases with decreasing grain size. In detail, albite occurs as different forms: as lamellae in perthite, as overgrowth on dissolved K-feldspar and/or replacive patches in altered K-feldspar grains. All kinds of albite in the Magnus sandstones have dull cathodoluminescence and a high purity of chemical composition. Significantly, the albite overgrowth is highly pure (100% Ab), which differs from albite lamellae (with 2-4% An) and replacing albite patches (with 1-3% An).

A part of albite can be inferred as diagenetic albite based on unaltered crystal surfaces, high purity of chemical composition, and dull cathodoluminescence as well as its co-occurrence with other diagenetic minerals. Petrographic observation indicates that diagenetic albite was probably formed during burial, coinciding with K-feldspar dissolution and quartz cementation. The initial start of diagenetic albite formation in the Magnus sandstones could be 80 Ma BP and it may continue to form until today. Correspondingly, the temperature range for the diagenetic albite formation in the Magnus sandstones could be 90-120°C. Three mechanisms for albite formation were proposed and tested by hydrogeochemical modelling to

draw conclusions as below: (1) an increase in temperature and pressure is not the main reason for albite formation, whereas (2) dissolution of unstable minerals (such as kaolinite and chalcedony) coupled to reduction of ferric iron minerals due to products generated during oil generation, migration and degradation and (3) dissolution of non-end member feldspar (K-feldspar with 10% albite) coupled to illite formation can account for trace amounts of authigenic albite.

(3) The Frigg and Grane field

In the Frigg field, the main reservoir is the Eocene Frigg sandstone while in the Grane field the Palaeocene Heimdal sandstone is the main reservoir. Both sandstones are sub-arkose sandstones which deposited as submarine fans. They are both buried at a shallow to mediate depth: the Eocene Frigg sandstone and the Palaeocene Heimdal sandstone are buried at 2,045-2,075 m and 1,734-1,798 m, respectively. In comparison with the Palaeocene Heimdal sandstone, albite is absent in the Frigg sandstone in the Frigg field, which is attributed to two reasons: (1) the different parent areas that the Frigg sandstone was sourced from and (2) the more intensive dissolution of feldspar occurred in the Frigg sandstone. Coupling to feldspar dissolution, kaolinite formation is also better developed in the Frigg sandstone. Moreover, core extracts from both reservoirs also show differences: the Grane extracts are moderately degraded while the Frigg extracts are heavily altered. In addition, unlike the Grane extracts, the O_1 species with 1-4 DBE are present in the Frigg extracts, which resemble weathered crude oil from beach sands even though a contribution of immature organic matter cannot be ruled out. Therefore, the heavily altered Frigg extracts are probably attributed to both aerobic and anaerobic degradation in the Frigg sandstone.

Both aerobic alteration of oil and intensive kaolinization of K-feldspar in the Frigg sandstones can be ascribed to intrusion of meteoric water. Flushing meteoric water into the Frigg sandstone could have been achieved either via basinward migration of a meteoric water zone during two stages of sea level fall (during deposition and at the end of the Eocene) or via connections with river water by hyperpycnal flows during/after its deposition. The controls for meteoric water intrusion into the Frigg sandstone of the Frigg field could be: (1) the Frigg sandstones were deposited immediately below the Shetland escarpment; (2) the Palaeo-shelf area during deposition of the Frigg sandstones was narrow; (3) the Frigg sandstones were fed via a channel that connected with an incised valley/canyon on the earlier shelf-delta system. In contrast, the Heimdal sandstone of the Grane field was deposited far away from the East

Shetland Platform and therefore seems to be less likely fluxed by meteoric water. As a result, both minerals and oils in the Grane field have not been significantly altered.

Hydrogeochemical modelling results indicate that a combination of meteoric water intrusion and organic-inorganic interaction triggered by oil degradation could have led to the observed diagenetic features in the Frigg sandstones.

6.2. Outlook

The present dissertation shows that organic-inorganic interactions could influence sandstone alterations. The degree of alteration, however, is also influenced by different burial depth and lithofacies. For example, in the intermediately buried glauconite-bearing sandstone of the Siri field, organic-inorganic interactions result in the possible conversion of glauconite into berthierine while in deeply buried Magnus sandstone in the Magnus field, it might play a role in albite formation. In contrast, in the Frigg sandstone, meteoric water apart from organic-inorganic interactions plays a more important role in kaolinization of K-feldspar. It seems that organic-inorganic interaction influences mineral alterations depending on burial depth and lithofacies. Therefore, the impact of depth and lithofacies on organic-inorganic interactions leading to sandstone alterations should be another step to unravel a systematic alteration system. A sample set with the same lithofacies at different burial depths should be considered in order to eliminate the original differences caused by deposition and “classic diagenesis”.

In addition, organic-inorganic interactions take place at OWCs but also in “micro OWCs” created by maintaining a thin water film on the surface of grains in oil filling zones. Such common occurrences of organic-inorganic interactions in subsurface reservoirs could lead to spatial alterations of minerals. For the assessment of reservoir properties and possible production measures, quantitative approaches in 2D and 3D are needed to answer questions about “where”, “when”, and “how much” of complex rock-fluid-gas interactions.

References

Aagaard, P., Egeberg, P.K., Saigal, G.C., Morad, S., and Bjørlykke, K., 1990. Diagenetic albitization of detrital K-feldspars in Jurassic, Lower Cretaceous, and Tertiary clastic reservoir rocks from offshore Norway, II: Formation water chemistry and kinetic considerations. Journal of Sedimentary Petrology, 60, 575–581.

Ahmadi, Z.M., Sawyers, M., Kenyon-Roberts, S., Stanworth, C.W., Kugler, K.A., Kristensen, J., and Fugelli, E.M.G., 2003. Palaeocene. In: Evans, D., Graham, C., Armour, A., and Bathurst, P. (eds.) The Millennium Atlas: petroleum geology of the central and northern North Sea. Geological Society, London, 235-259.

Aitken, C.M, Jones, D.M., and Larter, S.R., 2002. Isolation and Identification of Biomarkers Indicative of Anaerobic Biodegradation in Petroleum Reservoirs. Geological Society of London, London.

Appelo, C.A.J., and Postma, D., 1994. Geochemistry, Groundwater and Pollution. A.A. Balkema, Rotterdam, pp. 213–214.

Bailey, S.W., 1988. Odinite, a new dioctahedral-trioctahedral Fe^{3+}-rich l: l clay mineral. Clay Minerals, 23, 237–247.

Baines, S.J., and Worden R.H., 2004. The long-term fate of CO_2 in the subsurface: natural analogues for CO_2 storage. In: Baines, S.J., Worden, R.H. (Eds.), Geological storage of carbon dioxide, Special Publications, 233. The Geological Society of London, London, pp. 59–86.

Barclay, S.A., and Worden, R.H., 1998. Quartz cement volumes across oil-water contacts in oil fields from petrography and wireline logs: preliminary results from the Magnus Field, Northern North Sea. In: Harvey, P.K., Lovell, M.A. (Eds.), Core-log integration, Special Publications 136. The Geological Society of London, London, pp. 327–339.

Barclay, S.A., and Worden, R.H., 2000. Geochemical modelling of diagenetic reactions in a sub-arkosic sandstone. Clay Minerals, 35, 57–57.

Barclay, S.A., Worden, R.H., Parnell, J., Hall, D.L., and Sterner, S.M., 2000. Assessment of Fluid Contacts and Compartmentalization in Sandstone Reservoirs Using Fluid Inclusions : An Example from the Magnus Oil Field, North Sea. AAPG Bulletin, 84, 489–504.

Barth, T., and Bjørlykke, K., 1993. Organic acids from source rock maturation: Generation potentials, transport mechanisms and relevance for mineral diagenesis. Applied Geochemistry, 8, 325-337.

Bernard, F.P., and Connan, J., 1992. Indigenous microorganisms in connate waters of many oilfields: a new tool in exploration and production techniques. SPE 24811. In: 67th Annual Technical Conference and exhibition of the Society of Petroleum Engineers, Washington D.C., October 1992, 467-476.

Bevan, J., and Savage, D., 1989. The effect of organic acids on the dissolution of K-feldspar under conditions relevant to burial diagenesis. Mineralogy Magazine, 53, 415-425.

Bhattacharyya, D.P., 1983. Origin of berthierine in ironstones. Clays and Clay Minerals, 31, 173–182.

Bjørlykke, K. and Jahren J., 2012. Open or closed geochemical systems during diagenesis in sedimentary basins: Constraints on mass transfer during diagenesis and the prediction of porosity in sandstone and carbonate reservoirs. AAPG Bulletin, 96, 2193-2214.

Bjørlykke, K., 1984. Formation of secondary porosity: How important is it? In: D. A. MacDonald and R. C. Surdam (eds.), Clastic diagenesis. AAPG Memoir, 37, 277-286.

Bjørlykke, K., 1998. Clay mineral diagenesis in sedimentary basins: a key to the prediction of rock properties, examples from the North Sea Basin. Clay Minerals, 33, 15–34.

Bjørlykke, K., Aagaard, P., Egeberg, P.K., and Simmons, S.P., 1995. Geochemical constraints from formation water analyses from the North Sea and Gulf Coast Basin on quartz, feldspar and illite precipitation in reservoir rocks. In: Cubitt, J.M., England, W.A. (Eds.), The Geochemistry of Reservoirs, Geochemical Society Special Publication, 86, pp. 33–50.

Bjørlykke, K., and Aagaard, P., 1992. Clay minerals in North Sea sandstones. In: Houseknecht, D.W., Pitman, E.D. (Eds.), Origin, Diagenesis and Petrophysics of Clay Minerals in Sandstones. SEPM Special Publication, 47, 65-80.

Bjørlykke, K., and Jahren, J., 2010. Sandstones and sandstone reservoirs. In: Bjørlykke, K. (eds.), Petroleum Geoscience: from Sedimentary Environments to Rock Physics. Springer-Verlag, Berlin, 139-141.

Bjørlykke, K., and Jahren, J., 2012. Open or closed geochemical systems during diagenesis in sedimentary basins: Constraints on mass transfer during diagenesis and the prediction of porosity in sandstone and carbonate reservoirs. AAPG Bulletin, 96, 2193–2214.

Bjørlykke, K., Ramm, M., and Saigal, G.C., 1989. Sandstone diagenesis and porosity modification during basins evolution. Geologische Rundschau, 78, 243-268.

Boles, J.R., 1982. Active albitization of plagioclase. Gulf Coast Tertiary. American Journal of Science, 282, 165–180.

Boles, J.R., and Franks, S.G., 1979. Clay diagenesis in Wilcox sandstones of southwestern Texas: implications of smectite diagenesis on sandstone cementation. Journal of Sedimentary Petrology, 49, 55–70.

Bowman, M.B.J., 1998. Cenozoic. In: Glennie, K.W. (eds.) Petroleum geology of the North Sea, basic concepts and recent advances (fourth edition). Oxford Blackwell Scientific Publication, 350-375.

Boyd, G.A., Wallace, M.W., Holdgate, G.R., and Gallagher, S.J., 2004. Marine clays and porosity evolution in Nullawarre Greenland, Otway Basin, southeastern Australia, in: PESA Eastern Australasian Basins Symposium II held in Adelaide, 20–22 September, 2004.

Bozau, E., Sattler, C-D., and van Berk, W., 2015. Hydrogeochemical classification of deep formation waters. Applied Geochemistry, 52, 23–30.

Bray, E.E., and Evans, E.D., 1961. Distribution of n-paraffins as a clue to recognition of source beds. Geochimica et Cosmochimica Acta, 22, 2-15.

Brewster, J., 1991. The Frigg field, Block 10/1 UK North Sea and 25/1, Norwegian North Sea. In: Abbotrs, I. L. (eds.) United Kingdom Oil and Gas Fields, 25 Years Commemorative Volume. Geological Society, London, Memoirs, 14, 117-126.

Brindley, G.W., 1982. Chemical compositions of berthierines−A review. Clays and Clay Minerals, 30, 153–155.

Brzozowska, J., Eriksen, S., Holm, L., and Olsen, S., 2003. Exploration history. In: Evans, D., Graham, C., Armour, A., and Bathurst, P. (eds.), The Millennium Atlas: petroleum geology of the central and northern North Sea. Geological Society, London, 331-343.

Burley, S.D, Kantorwicz, J.D, and Waugh, B, 1985. Clastic diagenesis. In: P.J Brenchley, and B.P.J Williams (Eds.), Sedimentology: Recent developments and applied aspects. Geological Society Special

Publication, 18, pp. 198–226.

Burley, S.D., Kantorowicz, J.D., and Waugh, B., 1985. Clastic diagenesis. Geological Society London, Special Publications, 18, 189-226.

Carvalho, M.V.F., De Ros, L.F., and Gomes, N.S., 1995. Carbonate cementation patterns and diagenetic reservoir facies in the Campos Basin Cretaceous turbidites, offshore eastern Brazil. Marine and Petroleum Geology, 12, 741-758.

Connan, J., 1984. Biodegradation of crude oils in reservoirs. In: Brooks J, and Welte, D.H. (eds.), Advances in Petroleum Geochemistry. Academic Press, London, pp. 299-330.

Coombs, D.S., Zhao, G., and Peacor, D.R, 2000. Manganoan berthierine, Meyers Pass, New Zealand: occurrence in the prehnite-pumpellyite facies. Mineralogical Magazine, 64, 1037–1046.

Corver, M.P., Doust, H., van Wees, J.-D., and Cloetingh, S., 2011. Source-rock maturation characteristics of symmetric and asymmetric grabens inferred from integrated analogue and numerical modeling: The southern Viking Graben (North Sea). Marine and petroleum geology, 28, 921-935.

Coward, M.P., Dewey, J.F., Hempton, M., and Holroyd, J., 2003. Tectonic evolution. In: Evans, D., Graham, C., Armour, A., and Bathurst, P. (eds.) The Millennium Atlas: petroleum geology of the central and northern North Sea. Geological Society, London, 17-33.

Curiale, J.A., Harrison, W.E., and Smith, G., 1983. Sterane distribution of solid bitumen pyrolyzates. Changes with biodegradation of crude oil in the Ouachita Mountains, Oklahoma. Geochimica et Cosmochimica Acta, 47, 517–523.

Curtis, C.D., 1978. Possible links between sandstone diagenesis and depth-related geochemical reactions occurring in enclosing mudstones. Journal of the Geological Society, 135, 107-117.

Curtis, C.D., 1985. Clay mineral precipitation and transformation during burial diagenesis. Philosophical Transactions of the Royal Society of London. Series A, Mathematical and Physical Sciences, A315, 91–105.

Curtis, C.D., and Spears, D.A., 1968. The formation of sedimentary iron minerals. Economic Geology, 24, 257–270.

Cussey, R., 1974. East Frigg 25/ 2-1 well - Sedimentological study of the base of the Tertiary series. http://factpages.npd.no/

Damyanov, Z., and Vassileva, M., 2001. Authigenic phyllosilicates in the Middle Triassic Kremikovtsi sedimentary exhalative siderite iron formation, Western Balkan, Bulgaria. Clays and Clay Minerals, 49, 559–585.

Danielsen, M., Clausen, O.R., and Michelsen, O., 1995. Stratigraphic correlation of late Palaeocene sand deposits in the Søgne Basin area of the Danish and Norwegian central North Sea. Terra Nova, 7, 516–527.

De'Ath, N.G., and Schuyleman, S.F., 1981. The geology of Magnus oilfield. In: Illing, L.V., Hobson, G.D. (Eds.), Petroleum geology of the continental shelf of the north-west Europe, Heyden, London, pp. 342–351.

Deer, W.A., Howie, R.A., and Zussman, J., 1992. An introduction to the rock forming minerals, 2nd ed., Longman, London, pp. 696.

Dixon, R.J., and Pearce, J., 1995. Tertiary sequence stratigraphy and play fairway definition, Bruce-Beryl

Embayment, Quadrant 9, UKCS. In: by Steel, R.J. et al. (eds.) Sequence Stratigraphy on the Northwest European Margin. Norwegian Petroleum Society (NPF), Special Publication, 5, 443-469.

Ehrenberg, S.N., and Jacobsen, K.G., 2001. Plagioclase dissolution related to biodegradation of oil in Brent Group sandstones (Middle Jurassic) of Gullfaks Field, northern North Sea. Sedimentology, 48, 703-722.

Emery, D., Myers, K., and Young, R., 1990. Ancient subaerial exposure and freshwater leaching in sandstones. Geology, 18, 1178-1181.

Emery, D., Smalley, P.C., Oxtoby, N.H., Ragnarsdottir, K.V., Aagaard, P., Halliday, A., Coleman, M.L., and Petrovich, R., 1993. Synchronous Oil Migration and Cementation in Sandstone Reservoirs Demonstrated by Quantitative Description of Diagenesis [and Discussion]. Philosophical Transactions of the Royal Society A: Mathematical, Physical and Engineering Sciences, 344, 115-125.

Engvik, A.L., Putnis, A., Fitz Gerald, J.D., and Austrheim, H., 2008. Albitization of granitic rocks: the mechanism of replacement of oligoclase by albite. Canadian Mineralogist, 46, 1401-1415.

Franks, S.G., and Forester, R.W., 1984. Relationships among secondary porosity, pore-fluid chemistry and carbon dioxide, Texas Gulf Coast. In: D. A. MacDonald and R. C. Surdam (eds.), Clastic diagenesis. AAPG Memoir, 37, 63-79.

Fritz, S.J, and Toth, T.A, 1997. An Fe-berthierine from a Cretaceous laterite: Part II. Estimation of Eh, pH and pCO_2 conditions of formation. Clays and Clay Minerals, 45, 580–586.

Fu, Y., 2014. Development and application of numerical modeling for evaluating and predicting hydrogeochemical processes temporally and spatially evolving in petroleum reservoirs: Case studies: Miller oilfield (UK North Sea) and Siri oilfield (Danish North Sea). Ph.D. thesis, Clausthal University of Technology, 76–83.

Fu, Y., van Berk, W., Schulz, H.-M., and Mu, N., 2015a. Berthierine formation in reservoir rocks from the Siri oilfield (Danish North Sea) as result of fluid-rock interactions: Part II. Deciphering organic-inorganic processes by hydrogeochemical modeling. Marine and Petroleum Geology, 65, 317-326.

Fu, Y., van Berk, W., Schulz, H.-M., and Mu, N., 2015b. Berthierine formation in reservoir rocks from the Siri oilfield (Danish North Sea) as result of fluid-rock interactions: Part III. Deciphering mineral stability and CO_2-sequestering capacity of glauconitic sandstones. Marine and Petroleum Geology, 65, 327-333. http://dx.doi.org/10.1016/j.marpetgeo.2015.01.008

Furmann, A., Mastalerz, M., Schimmelmann, A., Pedersen, P. K., and Bish, D., 2014. Relationships between porosity, organic matter, and mineral matter in mature organic-rich marine mudstones of the Belle Fourche and Second White Specks formations in Alberta, Canada. Marine and petroleum geology, 54, 65-81.

Galloway, W. E., Garber, J. L., Liu, X., and Sloan, B. J., 1993. Sequence stratigraphic and depositional framework of the Cenozoic fill, central and northern North Sea, Petroleum Geology of Northwestern Europe: Proceedings of 4th Conference (eds. by J. R. Parker), Geological Society of London, 299-315.

Giles, M.R., and Marshall, J.D., 1986. Constraints on the development of secondary porosity in the subsurface: Re-evaluation of processes. Marine and Petroleum Geology, 3, 243-255.

Glennie, K.W., and Underhill, J.R., 1998. Origin, development and evolution structural styles. In: Glennie, K.W. (ed.), Petroleum geology of the North Sea: Basic concepts and recent advances (4th ed.). Oxford: Blackwell Science, pp. 42-84.

Goff, J.C., 1983. Hydrocarbon generation and migration from Jurassic source rocks in the E Shetland Basin and Viking Graben of the northern North Sea. Geological Society, London, 140, 445-474.

Gold, P.B., 1987. Textures and geochemistry of authigenic albite from Miocene sands, Louisiana Gulf Coast. Journal of Sedimentary Petrology, 57, 353-362.

González-Acebrón, L., Arribas, J., and Mas, R., 2010. The role of sandstone provenance in diagenetic albitization of feldspars. A case study in the Jurassic Tera Group sandstones (Cameros Basin, NE Spain). Sedimentary Geology, 229, 53–63.

Habermehl, M.A., 1980. The Great Artesian Basin, Australia. BMR Journal of Australian Geology & Geophysics, 5, 9-38.

Hamberg, L., Dam, G., Wilhelmson, C., and Ottesen, T., 2005. Palaeocene deep-marine sandstone plays in the Siri Canyon, offshore Denmark-southern Norway, in Doré, A.G., Vining, B.A. (Eds.), Petroleum Geology: North-West Europe and Global Perspectives, Proceedings of the 6th Petroleum Geology Conference. Geological Society of London, pp. 1185–1198.

Harder, H., 1978. Synthesis of iron layer silicate minerals under natural conditions. Clays and Clay Minerals, 26, 65–72.

Harder, H., 1989. Mineral genesis in ironstones: a model based upon laboratory experiments and petrographic observations, in: Yong, T.P., Taylor, W.E.G. (Eds.), Phanerozoic Ironstones 46, Geological Society, London, Special Publication, pp. 9–18.

Head, I.M., Jones, D.M., and Larter, S.R., 2003. Biological activity in the deep subsurface and the origin of heavy oil. Nature, 426, 344–352.

Helgeson, H.C., Knox, A.M., Owens, D.H., and Shock, E.L., 1993. Petroleum, oil-field waters, and authigenic mineral assemblages – are they in metastable equilibrium in hydrocarbon reservoirs. Geochimica et Cosmochimica Acta, 57, 3295–3339.

Heritier, F.E., Lossee, P., and Wathne, E., 1980. Frigg Field—large submarine-fan trap in Lower Eocene Rocks of the Viking Graben, North Sea. AAPG Memoir, 30, 59-79.

Hirt, W.G., Wenk, H-R., and Boles, J.R., 1993. Albitization of plagioclase crystals in the Stevens sandstone (Miocene), San Joaquin Basin, California, and the Frio Formation (Oligocene), Gulf Coast, Texas: a TEM/AEM study. Geological Society of America Bulletin 105, 708–714.

Hornibrook, E.R.C, and Longstaffe, F.J., 1996. Berthierine from the lower cretaceous clearwater formation, Alberta, Canada. Clays and Clay Minerals, 44, 1–21.

Huggett, J.M., and Gale, A.S., 2002. Petrology and environmental significance of iron-rich clays in the Middle Eocene of NE Texas, in: Bolder Clays: Clay Minerals Society 39th Annual Meeting Program and Abstracts.

Huggett, J.M., and Hesselbo, S.P., 2003. Low oxygen levels in earliest Triassic soils: Comment and Reply: COMMENT. Geology, 31, e20–e20.

Hughey, C. A., Galasso, S. A., and Zumberge, J. E., 2007. Detailed compositional comparison of acidic NSO compounds in biodegraded reservoir and surface crude oils by negative ion electrospray Fourier transform ion cyclotron resonance mass spectrometry. Fuel, 86, 758–768.

Hughey, C. A., Rodgers, R. P., Marshall, A. G., Qian, K., and Robbins, W. K., 2002. Identification of acidic NSO compounds in crude oils of different geochemical origins by negative ion electrospray Fourier

transform ion cyclotron resonance mass spectrometry. Organic Geochemistry, 33, 743–759.

Hunt, J.M., 1995. Petroleum Geochemistry and Geology, Second edition. W.H. Freeman and Company, New York.

Huuse, M., 1999. Detailed morphology of the top Chalk surface in the eastern Danish North Sea. Petroleum Geoscience, 5, 303–314.

Iijima, A., and Matsumoto, R., 1982. Berthierine and chamosite in coal measures of Japan. Clays and Clay Minerals, 30, 264–274.

Isaksen, G.H., and Ledje, K.H.I., 2001. Source rock quality and hydrocarbon migration pathways within the greater Utsira High area, Viking Graben, Norwegian North Sea. AAPG Bulletin, 85, 861-883.

Johnson, H., Richards, P.C., Long, D., and Graham, C.C., 1993. United Kingdom offshore regional report: the geology of the northern North Sea. (London: HMSO for the British Geological Survey.), pp. 4–21.

Jones, D.M., Head, I.M., Gray, N.D., Adams, J.J., Rowan, A.K., Aitken, C.M., Bennett, B., Huang, H., Brown, A., Bowler, B.F.J. Oldenburg, T., Erdmann, M., and Larter, S.R., 2008. Crude-oil biodegradation via methanogenesis in subsurface petroleum reservoirs. Nature, 451, 176-181.

Jones, E., Jones, R., Ebdon, C., Ewen, D., Milner, P., Plunkett, J., Hudson, G., and Slater, P., 2003. Eocene. In: Evans, D., Graham, C., Armour, A., and Bathurst, P. (eds.) The Millennium Atlas: petroleum geology of the central and northern North Sea. Geological Society, London, 261-277.

Jones, R. W., and Milton, N. J., 1994. Sequence development during uplift: Palaeogene stratigraphy and relative sea-level history of the Outer Moray Firth, UK North Sea. Marine and Petroleum Geology, 2, 157-165.

Justwan, H., Dahl, B., and Isaksen, G.H., 2006a. Geochemical characterisation and genetic origin of oils and condensates in the South Viking Graben, Norway. Marine and Petroleum Geology, 23, 213-239.

Justwan, H., Meisingset, I., Dahl, B., and Isaksen, G.H., 2006b. Geothermal history and petroleum generation in the Norwegian South Viking Graben revealed by pseudo-3D basin modelling. Marine and Petroleum Geology, 23, 791-819.

Karlsen, D.A., Nedkvitne, T., Larter, S.R., and Bjørlykke, K., 1993. Hydrocarbon composition of authigenic inclusions: Application to elucidation of petroleum reservoir filling history. Geochimica et Cosmochimica Acta, 57, 3641–3659.

Kastner, M., 1971. Authigenic feldspars in carbonate rocks. American Mineralogist, 56, 1403-1442.

Kastner, M., and Siever, R., 1979. Low temperature feldspars in sedimentary rocks. American Journal of Science, 279, 435–479.

Ketzer, J.M., Morad, S., and Amorosi, A., 2003. Predictive clay cementation in a sequence stratigraphy framework. In: Worden, R., Morad, S. (eds.), Clay Cementation in Sandstones, International Association of Sedimentologists. Special Publication, 34, 42-59.

Killops, S.D., and Killops, V.J., 2005. Introduction to organic geochemistry, John Wiley & Sons, pp. 232-245, 145-165.

Kim, S., Stanford, L. A., Rodgers, R. P., Marshall, A. G., Walters, C. C., Qian, K., Wenger, L. M., and Mankiewicz, P., 2005. Microbial alteration of the acidic and neutral polar NSO compounds revealed by Fourier transform ion cyclotron resonance mass spectrometry. Organic Geochemistry, 36, 1117–1134.

Kneller, B.C., and Buckee, C.M., 2000. The structure and fluid mechanics of turbidity currents; a review of some recent studies and their geological implications. Sedimentology, 47, 62-94.

Kodama, H., and Foscolos, A., 1981. Occurrence of berthierine in Canadian Arctic desert soil. Canadian Mineralogist, 19, 279–283.

Larter, S., Hockey, A., Aplin, A., Telnaes, N., Wilhelms, A., Horstad, I., Di Primio, R., and Sylta O., 1999. When biodegradation preserves petroleum! Petroleum geochemistry of N. Sea Oil Rimmed Gas Accumulations (ORGA's). In: Proceedings AAPG Hedberg Research Conference on "Natural Gas Formation and Occurence", Durango, CO.

Larter, S., Huang, H., Adams, J., Bennett, B., and Snowdon, L.R., 2012. A practical biodegradation scale for use in reservoir geochemical studies of biodegraded oils. Organic Geochemistry, 45, 66-76.

Larter, S., Wilhelms, A., Head, I., Koopmans, M., Aplin, A., Di Primio, R., Zwach, C., Erdmann, M., and Telnaes, N., 2003. The controls on the composition of biodegraded oils in the deep subsurface—part 1: biodegradation rates in petroleum reservoirs. Organic Geochemistry, 34, 601–613.

Larter, S.R., Head, I. M., Huang, H., Bennett, B., Jones, M., Aplin, A.C., Murray, A., Erdmann, M., Wilhelms, A., and di Primio, R., 2005. Biodegradation, gas destruction and methane generation in deep subsurface petroleum reservoirs: an overview. Petroleum geology: North-West Europe and Global Perspectives, in Proceedings of 6th Geology Conference, Geological Society (London), 6, 633–639.

Liao, Y.H., Shi, Q., Hsu, C.S., Pan, Y.H., and Zhang, Y.H., 2012. Distribution of acids and nitrogen-containing compounds in biodegraded oils of the Liaohe Basin by negative ion ESI FT-ICR MS. Organic Geochemistry, 47, 51–65.

Longstaffe, F.J., 1993. Meteoric water and sandstone diagenesis in the western Canada sedimentary basin. In: Diagenesis and Basin Development. In Hornbury, A.D. and Robinson, A.G. (eds) AAPG Studies in Geology, 36, 49-68. American Association of Petroleum Geologists, Tulsa, OK.

Lu, G., .McCabe, C., Henry, D.J., and Schedl, S., 1994. Origin of hematite carrying a Late Paleozoic remagnetization in a quartz sandstone bed from the Silurian Rose Hill Formation, Virginia, USA. Earth and Planetary Science Letters, 126, 235–246.

Lundegard, P. D., Land, L.S., and Galloway, W.E., 1984. Problem of secondary porosity: Frio Formation, Texas Gulf Coast. Geology, 12, 399-402.

Lundegard, P.D., and Kharaka,Y.K., 1994. Distribution and occurrence of organic acids in subsurface waters. In: E. D. Pittman and M. D. Lewan (eds.), Organic acids in geological processes. New York, Springer-Verlag, 38-69.

Macaulay, C., Fallick, A., and Haszeldine, R., 1993a. Textural and isotopic variations in diagenetic kaolinite from the Magnus Oilfield Sandstones. Clay minerals, 28, 625–639.

Macaulay, C., Haszeldine, R., and Fallick, A., 1992. Diagenetic pore waters stratified for at least 35 Million Years: Magnus oil field, North Sea. AAPG Bulletin, 76, 1625–1634.

Macaulay, C., Haszeldine, R., and Fallick, A., 1993b. Distribution, chemistry, isotopic composition and origin of diagenetic carbonates: Magnus Sandstone, North Sea. Journal of Sedimentary Research, 63, 33–43.

Mackenzie, A.S., Wolff, G.A., and Maxwell, J.R., 1981. Fatty acids in some biodegraded petroleums. Possible origins and significance. In: Bjorøy, M. et al. (eds.) Advances in Organic Geochemistry. Wiley, Chichester, 637-649.

Mackenzie, A.S., Wolff, G.A., and Maxwell, J.R., 1983. In: Bjoroy, M. et al. (eds.), Advances in Organic Geochemistry 1981.Wiley Heyden, London, pp. 637–649.

Madon, M.B.H., 1992. Depositional setting and origin of berthierine oolitic ironstones in the lower Miocene Terengganu Shale, Tenggol Arch, offshore peninsular Malaysia. Journal of Sedimentary Research, 62, 899–916.

Mandal, A., Samanta, A., Bera, A., and Ojha, K., 2010. Characterization of oil-water emulsion and its use in enhanced oil recovery. Industrial & Engineering Chemistry Research, 49, 12756–12761.

Manheim, F.T., 1967. Evidence for submarine discharge of water on the Atlantic continental slope of southern United States and suggestions for further research. New York Academy of Sciences Transactions, 29, 839-853.

Manning, D. A. C., E. I. C. Rae, and J. S. Small, 1991. An exploratory study of acetate decomposition and dissolution of quartz and Pb-rich potassiumfeldspar at 150°C, 50MPa (500 bars). Mineralogy Magazine, 88, 183-195.

Mansurbeg, H., El-ghali, M.A.K., Morad, S. and Plink-Björklund, P., 2006. The impact of meteoric water on the diagenetic alterations in deep-water, marine siliciclastic turbidites. Journal of Geochemical Exploration, 89, 254-258.

Mansurbeg, H., Morad, S., Salem, A., Marfil, R., El-ghali, M.A.K., Nystuen, J.P., Caja, M.A., Amorosi, A., Garcia, D. and La Iglesia, A., 2008. Diagenesis and reservoir quality evolution of palaeocene deep-water, marine sandstones, the Shetland-Faroes Basin, British continental shelf. Marine and Petroleum Geology, 25, 514-543.

Martinsen, O.J., Lien, T., and Jackson, C., 2005. Cretaceous and Paleogene turbidite systems in the North Sea and Norweigan Sea Basins: source, staging area and basin physiography controls on reservoir development. In: Dore, A.G., Vining, B.A., (eds.), Petroleum Geology: Northwest Europe and Global Perspectives Proceedings of the 6th Petroleum Geology Conference, 1147-1164.

Marzi, R., Torkelson, B.E., and Olson, R.K., 1993. A revised carbon preference index, Organic Geochemistry, 20, 1303-1306.

Maynard, J.B., 1986. Geochemistry of oolitic iron ores, an electron microprobe study. Economic Geology, 81, 1473–1483.

Meredith, W., Kelland, S.-J., and Jones, D.M., 2000. Influence of biodegradation on crude oil acidity and carboxylic acid composition. Organic Geochemistry, 31, 1059-1073.

Milliken, K.L., 1989. Petrography and composition of authigenic feldspars, Oligocene Frio Formation, South Texas. Journal of Sedimentary Petrology, 59, 361–374.

Milliken, K.L., 2004. Late diagenesis and mass transfer in sandstones-shale sequences. In: Mackenzie, F.T. (Eds.), Sediments, Diagenesis, and Sedimentary Rocks: Treatise on Geochemistry. Elservier-Pergamon, Oxford, UK, 7, pp.159–190.

Milliken, K.L., Land, L.S., and Loucks, R.G., 1981. History of burial diagenesis determined from isotopic geochemistry, Frio Formation, Brazoria County, Texas. AAPG Bulletin, 65, 1397–1413.

Morad, S., Al-Ramadan, K., Ketzer, J.M. and De Ros, L.F., 2010. The impact of diagenesis on the heterogeneity of sandstone reservoirs: A review of the role of depositional facies and sequence stratigraphy. AAPG Bulletin, 94, 1267-1309.

Morad, S., Bergan, M., Knarud, R., and Nystuen, J.P., 1990. Albitization of detrital plagioclase in Triassic reservoir sandstones from the Snorre Field, Norwegian North Sea. Journal of Sedimentary Petrology, 60,

411–425.

Morad, S., Ketzer, J.M., and De Ros, F., 2000. Spatial and temporal distribution of diagenetic alterations in siliciclastic rocks: implications for mass transfer in sedimentary basins. Sedimentology, 47, 95-120.

Morad, S., Ketzer, J.M., and De Ros, F., 2012. Linking diagenesis to sequence stratigraphy: an integrated tool for understanding and predicting reservoir quality and distribution. In: Morad, S., Ketzer, J.M., and De Ros, F., (eds.), Liking diagenesis to sequence stratigraphy, Special publication Number 45 of the International Association of Sedimentologist, 1-36.

Mu, N., Fu, Y., Schulz, H.-M., and van Berk, W., 2016. Authigenic albite formation due to water-rock interactions – Case study: Magnus oilfield (UK, Northern North Sea). Sedimentary Geology, 331, 30-41.

Mu, N., Schulz, H.-M., Fu, Y., Schovsbo, N. H., Wirth, R., Rhede, D., and van Berk, W., 2015. Berthierine formation in reservoir rocks from the Siri oilfield (Danish North Sea) as result of fluid-rock interactions: Part I. Characterization. Marine and Petroleum Geology, 65, 302-316.

Odin, G.S., 1990. Clay mineral formation at the continent-ocean boundary: the Verdine facies. Clay Minerals, 25, 477–483.

Odom, I.E., Doe, T.W., Dott, R.H., 1976. Nature of feldspar-grain size relations in some quartz-rich sandstones. Journal of Sedimentary Petrology, 46, 862–870.

Ohm, S.E., Karlsen, D.A., Roberts, A., Johannessen, E., and Høiland, O., 2006. The Palaeocene sandy Siri Fairway: An efficient “pipeline” draining the prolific Central Graben? Journal of Petroleum Geology, 29, 53–82.

Onstott, T.C., Hinton, S.M., Silver, B.J., and King, H.E. Jr., 2010. Coupling hydrocarbon degradation to anaerobic respiration and mineral diagenesis: theoretical constraints. Geobiology, 8, 69–88.

Pallaser, R.J., 2000. Recognising biodegradation in gas/oil accumulations through the $\delta^{13}C$ composition of gas components. Organic Geochemistry, 31, 1363–1373.

Pallasser, R.J., 2000. Recognising biodegradation in gas/oil accumulations through the $\delta^{13}C$ compositions of gas components. Organic Geochemistry, 31, 1363-1373.

Palmer, E.S.,1993. Effect of biodegradation and water washing on crude oil composition. In Engel M., and Macko S. A. (eds.), Organic Geochemistry Principles and Applications. New York, Plenum Press, pp. 511–534

Pan, Y.H., Liao, Y.H., Shi, Q., and Hsu, C.S., 2013. Acidic and neutral polar NSO compounds in heavily biodegraded oils characterized by negative-ion ESI FT-ICR MS. Energy & Fuels, 27, 2960 -2973.

Parkhurst, D.L., and Appelo, C.A.J., 2013. Description of input and examples for PHREEQC Version 3–A computer program for speciation, batch-reaction, one-dimensional transport, and inverse geochemical calculations. U.S. Geological Survey Techniques and Methods, book 6, chapter A43, available only at http://pubs.usgs.gov/tm/06/a43/.

Parkhurst, D.L., and Appelo, C.A.J., 2013. Description of input and examples for PHREEQC Version 3–A computer program for speciation, batch-reaction, one-dimensional transport, and inverse geochemical calculations. U.S. Geological Survey Techniques and Methods, book 6, chapter A43, available only at http://pubs.usgs.gov/tm/06/a43/.

Peters, K.E., Walters, C.C., and Moldowan, J. M., 2005, The biomarker guide, Cambridge, UK; New York, Cambridge University Press, pp. 72-118, 227-310,604-705.

Petrovich, R., 2001. Mechanisms of fossilization of the soft-bodied and lightly armored faunas of the Burgess Shale and of some other classical localities. American Journal of Science, 301, 683–726.

Petter, A., and Steel, R.J., 2006. Hyperpycnal flow variability and slope organization on an Eocene shelf margin, Central Basin, Spitsbergen. AAPG Bulletin, 90, 1451-1472.

Pittman, E.D., 1988. Diagenesis of Terry sandstone (Upper Cretaceous), Spindle Field, Colorado. Journal of Sedimentary Petrology, 58, 785–800.

Plink-Björklund, P., and Steel, R., 2004. Initiation of turbidity currents: evidence for hyperpycnal flow turbidites in Eocene Central Basin of Spitsbergen. Sedimentary Geology, 165, 29-52.

Poetz, S., Horsfield, B., and Wilkes, H., 2014. Maturity-driven generation and transformation of acidic compounds in the organic-rich posidonia shale as revealed by electrospray ionization fourier transform ion cyclotron resonance mass spectrometry. Energy & Fuels, 28, 4877- 4888.

Poulsen, M.L.K., Friis, H., Svendsen, J.B., Jensen, C.B., and Bruhn, R., 2007. The application of bulk geochemistry to reveal heavy mineral sorting and flow units in thick massive gravity flow deposits, Siri Canyon Palaeocene Sandstones, Danish North Sea, in: Heavy Minerals in Use 58, Developments in Sedimentology, Elsevier, Amsterdam, pp. 1099–1121.

Price, L.C., 1989. Hydrocarbon generation and migration from Type III kerogen as related to the oil window. USGS, Open-File Report, 89-194.

Price, L.C., and DeWitt, E., 2001. Evidence and characteristics of hydrolytic disproportionation of organic matter during metasomatic processes. Geochimica et Cosmochimica. Acta, 65, 3791-3826.

Price, L.C., and Wenger, L.M., 1992. The influence of pressure on petroleum generation and maturation as suggested by aqueous pyrolysis. Organic Geochemistry, 19, 141-159.

Prochnow, E.A., Remus, M.V.D., Ketzer, J.M., Gouvea Jr., J.C.R., Schiffer de Souza, R. and De Ros, L.F., 2006. Organic-inorganic interactions in oilfield sandstones: Examples from turbidite reservoirs in the Campos Basin, Offshore eastern Brazil. Journal of Petroleum Geology, 29, 361-380.

Radke, M., Willsch, H., and Welte, D.H., 1980. Preparative hydrocarbon group type determination by automated medium pressure liquid chromatography. Analytical Chemistry, 52, 406–411.

Rivard, C., Pelletier, M., Michau, N., Razafitianamaharavo, A., Bihannic I., Abelmoula, M., Ghanbaja, J., and Villieras, F., 2013. Berthierine-like mineral formation and stability during the interaction of kaolinite with metallic iron at 90 °C under anoxic and oxic conditions. American Mineralogist, 98, 163–180.

Rivas-Sanchez, M.L., Alva-Valdivia, L.M. Arenas-Alatorre, J., Urrutia-Fucugauchi, M., Ruiz-Sandoval, M., and Ramos-Molina, M.A., 2006. Berthierine and chamosite hydrothermal: genetic guides in the Pena Colorada magnetite-bearing ore deposit, Mexico. Earth Planets Space 58, 1389–1400.

Robertson, J., 2013. Overpressure and lateral drainage in the Palaeogene Strate of the Central North Sea. Ph.D. thesis, Durham University, p.14.

Rohrlich, V., Price, N.B., and Calvert, S.E., 1969. Chamosite in recent sediments of Loch Etive, Scotland. Journal of Sedimentary Research, 39, 624–631.

Ross, A.S., Farrimond, P., Erdmann, M., and Larter, S.R., 2010. Geochemical compositional gradients in a mixed oil reservoir indicative of ongoing biodegradation. Organic Geochemistry, 41, 307-20.

Rowland, S. M., Robbins, W. K., Marshall, A. G. and Rodgers, R. P., 2014. Characterization of Highly Oxygenated and Environmentally Weathered Crude Oils by Liquid Chromatography Fourier Transform

Ion Cyclotron Mass Spectrometry (FT-ICR MS). International Oil Spill Conference, Savannah GA, May 5th-8th 2014. Poster. DOI: 10.7901/2169-3358-2014-1-300205.1

Ruotsala, A. P., Pfluger, C. E., and Garnett, M., 1964. Iron-rich serpentine and chamosite from Ely, Minnesota. American Mineralogist, 49, 993–1001.

Saigal, G.C., Bjørlykke, K., Larter, S., 1992. The effects of oil emplacement on diagenetic processes--examples from the Fulmar reservoir sandstones, Central North Sea. AAPG Bulletin, 76, 1024-1033.

Saigal, G.C., Morad, S., Bjørlykke, K., Egeberg, P.K., and Aagaard, P., 1988. Diagenetic albitization of detrital K-feldspar in Jurassic, Lower Cretaceous, and Tertiary clastic reservoir rocks from offshore Norway, I. Textures and origin. Journal of Sedimentary Petrology, 58, 1003–1013.

Sánchez-Navas, A., Martín-Algarra, A., Eder, V, Reddy, B.J., Nieto, F, Z, and Zanin, Y.N., 2008. Color, mineralogy and composition of Upper Jurassic West Siberian glauconite: useful indicators of paleoenvironment. Canadian Mineralogist, 46, 1249–1268.

Schmidt, V., and D.A. McDonald, 1979. The role of secondary porosity in the course of sandstone diagenesis. In: P.Scholle and P. Schluger (eds.), Aspects of diagenesis: SEPM Special Publication, 26, 175-207.

Schulz, H.-M., Biermann,S., van Berk, W., Krüger, M., Straaten, N., Bechtel, A., Wirth, R., Lüders, V., Schovsbo, N.H., and Crabtree, S., 2015. From shale oil to biogenic shale gas: retracing organic–inorganic interactions in the Alum Shale (Furongian–Lower Ordovician) in southern Sweden. AAPG Bulletin, 99, 927-956.

Seewald, J.S., 2003. Organic-inorganic interactions in petroleum-producing sedimentary basins. Nature, 426, 327-333.

Shanmugam, G., 1985. Significance of coniferous rain forests and related organic matter in generating commercial quantities of oil, Gippsland Basin. AAPG Bulletin, 69, 1241-1254.

Sheldon, N.D., and Retallack, G.J., 2002. Low oxygen levels in earliest Triassic soils. Geology, 30, 919.

Shepherd, M., 1991. The Magnus Field, Block 211/7a, 12a, UK North Sea. Geological Society, London, Memoirs, 14, 153–157.

Slack, J.F., Jiang, W.T., Peacor, D.R., and Okita, P.M., 1992. Hydrothermal and metamorphic berthierine from the Kidd Creek volcanogenic massive sulfide deposit, Timmins, Ontario. Canadian Mineralogist, 30, 1127–1142.

Smith, J.V., and Stenstrom, R.C., 1965. Electron-excited luminescence as a petrologic tool. Geology, 73, 627-63.

Steinmann, Y., 2015. Organic-inorganic interactions across oil-water contacts in a siliciclastic oil reservoir: A comparison of a Tertiary reservoir unit with different oil degradation in two wells from the Norwegian continental margin, Central Viking Graben. Master thesis, Freie Universität Berlin, p. 21.

Stoessell, R.K., and Pittman, E.D., 1990. Secondary porosity revisited: The chemistry of feldspar dissolution by carboxylic acids and anions. AAPG Bulletin, 74, 1795-1805.

Stokkendal, J., Friis, H., Svendsen, J.B., Poulsen, M.L.K., and Hamberg, L., 2009. Predictive permeability variations in a Hermod sand reservoir, Stine Segments, Siri Field, Danish North Sea. Marine and Petroleum Geology, 26, 397–415.

Sullivan, A.P., and Kilpatrick, P.K., 2002. The effects of inorganic solid particles on water and crude oil emulsion stability. Industrial & Engineering Chemistry Research, 41, 3389–3404.

Surdam, R.C, Crossey, L.J., Hagen, E.S., and Heasler, H.P., 1989. Organic-inorganic interactions and sandstone

diagenesis. AAPG Bulletin, 73, 1–23.

Surdam, R.C., and Crossey, L.J., 1985. Organic-inorganic reactions during progressive burial: key to porosity/permeability enhancement and/or preservation. Philosophical Transactions of the Royal Society of London, Series A, 315, 135-156.

Surdam, R.C., Jiao, Z.S., and MacGowan, D.B., 1993. Redox reactions involving hydrocarbons and mineral oxidants: a mechanism for significant porosity enhancement in sandstones. AAPG Bulletin, 77, 1509-1518.

Surdham, R.C., Boese, S.W., and Crossey, L.J., 1984. The chemistry of secondary porosity. In: D. A. McDonald and R. C. Surdham (eds.), Clastic Diagenesis. AAPG Memoir, 37, 127-149.

Taylor, B.J., 1978. Westphalian. In : Moseley, F. (eds.), The geology of the Lake District. Yorkshire Geological Society Occasional Publication, 3, 9-180.

Taylor, K., 1990. Berthierine from the non-marine Wealden (Early Cretaceous) sediments of south-east England. Clay Minerals, 25, 391–399.

Taylor, K.G., and Curtis, C.D., 1995. Stability and facies association of early diagnetic mineral assemblages: an example from a Jurassic ironstone-mudstone succession, U.K. Journal of Sedimentary Research, A65, 358–368.

Taylor, K.G., and Macquaker, J.H.S., 2011. Iron minerals in marine sediments record chemical environments. Elements, 7, 113–118.

Taylor, P.N., Bennett, B., Jones, D.M., and Larter, S., 2001. The effect of biodegradation and water washing on the occurrence of alkylphenols in crude oils. Organic Geochemistry, 32, 341–358.

Taylor, T.R., and Land, L.S., 1996. Association of allochthonous waters and reservoir enhancement in deeply buried Miocene sandstones: Picaroon field, Corsair trend, offshore Texas. In: L. J. Crossey, R. Loucks, and M.Totten (eds.), Siliciclastic diagenesis and fluid flow: Concepts and applications. SEPM Special Publication, 55, 37–48.

Tissot, B. P., Welte, D. H., 1984. Petroleum formation and occurrence. Berlin; New York, Springer-Verlag, pp. 69-266.

Tissot, B., Durand, B., Espitalie, J., and Combaz, A., 1974. Influence of nature and diagenesis of organic matter in formation of petroleum. AAPG Bulletin, 58, 499–506.

Tissot, B.P., and Welte, D.H., 1978. Petroleum Formation and Occurrence: A New Approach to Oil and Gas Exploration. Springer-Verlag, Berlin, pp. 538.

Tomczyk, N.A., Winans, R.E., Shinn, J.H., and Robinson, R.C., 2001. On the nature and origin of acidic species in petroleum. 1. Detailed acid type distribution in a California crude oil. Energy and Fuels, 15, 1498–1504.

Toth, T., and Fritz, S., 1997. An Fe-berthierine from a cretaceous laterite: Part I. Characterization. Clays and Clay Minerals, 45, 564–579.

Treiber, L.E., Archer, D. L., and Owens, W.W., 1992. Laboratory evaluation of the wettability of 55 oil producing reservoirs. Society of Petroleum Engineers Journal, 12, 531–540.

van Berk, W., Schulz, H.-.M., and Fu, Y., 2013. Controls on CO_2 fate and behavior in the Gullfaks oilfield (Norway): how hydrogeochemical modeling can help decipher organic-inorganic interactions. AAPG Bulletin, 97, 2233-2255.

van Berk, W., Schulz, H.-M., and Fu, Y., 2009. Hydrogeochemical modelling of CO_2 equilibria and mass transfer induced by organic-inorganic interactions in siliciclastic petroleum reservoirs. Geofluids, 9, 253-262.

Van Houten, F.B., and Purucker, M.E., 1984. Glauconitic peloids and chamositic ooids-favorable factors, constraints, and problems. Earth-Science Reviews, 20, 211–243.

Walker, T.R., 1984. Diagenetic albitization of potassium feldspar in arkosic sandstones. Journal of Sedimentary Petrology, 54 (1), 3–16.

Warren, E.A., and Smalley, P.C., 1994. The Magnus field. In: Warren, E.A., Smalley, P.C. (Eds.), North Sea formation waters atlas. Memoir No. 15. The Geological Society, London, pp.51.

Watson, J.S., Jones, D.M., Swannell, R.P.J., and van Duin, A.C.T., 2002. Formation of carboxylic acids during aerobic biodegradation of crude oil and evidence of microbial oxidation of hopanes. Organic Geochemistry, 33, 1153-1169.

Watson, R.S., Trewin, N.H., and Fallick, A.E., 1995. The formation of carbonate cements in the Forth and Balmoral Fields, northern North Sea: a case for biodegradation, carbonate cementation and oil leakage during early burial. In: A.J. Hartley & D.J. Prosser (eds.), Characterisation of Deep Marine Clastic Systems. Geological Society London, Special Publications, 94, 177-200.

Welte, D.H., Kratochvil, H., Rullkötter, J., Ladwein, H., and Schaefer, R.G., 1982. Organic geochemistry of crude oils from the Vienna Basin and an assessment of their origin. Chemical Geology, 35, 33-68.

Wenger, L.M., and Price, L.C., 1991. Differential petroleum generation and maturation paths of the different organic matter types as determined by hydrous pyrolysis studies over a wide range of experimental temperatures. In European Association of Organic Geochemists 15th International Meeting, Advances and Applications in the Natural Environment: Organic Geochemistry, pp. 335-339. Manchester Press.

Wenger, L.M., Davis, C.L., Isaksen, G.H., and Upstream, E., 2002. Multiple controls on petroleum biodegradation and impact on oil quality, in: 2002 SPE Reservoir Evaluation & Engineering. pp. 375–383.

Wilhelms, A., and Larter, S.R., 1994a. Origin of tar mats in petroleum reservoirs. Part I: introduction and case studies. Marine and Petroleum Geology, 11, 418–441.

Wilhelms, A., and Larter, S.R., 1994b. Origin of tar mats in petroleum reservoirs. Part II: formation mechanisms for tar mats. Marine and Petroleum Geology, 11, 442–456.

Wilhelms, A., Larter, S. R., Head, I., Farrimond, P., Di-Primio, R., and Zwach, C., 2001. Biodegradation of oil in uplifted basins prevented by deep-burial sterilization. Nature, 411, 1034–1037.

Wilkes, H., Boreham, C., Harms, G., Zengler, K. and Rabus, R., 2000. Anaerobic degradation and carbon isotopic fractionation of alkylbenzenes in crude oil by sulphate-reducing bacteria. Organic Geochemistry, 31, 101-115.

Wirth, R., 2004. Focused ion beam (FIB): a novel technology for advanced application of micro- and nanoanalysis in geosciences and applied mineralogy. European Journal of Mineralogy, 16, 863–876.

Wirth, R., 2009. Focused Ion Beam (FIB) combined with SEM and TEM: Advanced analytical tools for studies of chemical composition, microstructure and crystal structure in geomaterials on a nanometre scale. Chemical Geology, 261, 217–229.

Wise, M.A., 2007. Crystallization of “pocket” berthierine from the pulsifer granitic pegmatite, Poland, Maine,

USA. Clays and Clay Minerals, 55, 583–592.

Wolicka, D., and Borkowski, A., 2012. Micro-organisms and crude oil. In: L Romero-Zeron (eds.), Introduction to enhanced oil recovery (EOR) processes and bioremediation of oil-contaminated sites. Croatia: Intech, Rijeka. 2012, 113-142.

Worden, R.H., and Barclay, S.A., 2000. Internally-sourced quartz cement due to externally-derived CO_2 in sub-arkosic sandstones, North Sea. Journal of Geochemical Exploration, 69-70, 645–649.

Worden, R.H., and Barclay, S.A., 2003. The effect of oil emplacement on diagenetic clay minerology: the Upper Jurassic Magnus Sandstone Member, North Sea. In: Worden, R.H., Morad, S. (Eds.), Clay minerals in sandstones. Blackwells, Oxford, UK, pp. 453–469.

Worden, R.H., and Burley, S.D., 2003. Sandstone Diagenesis: The Evolution of Sand to Stone. In Burley, S.D. and Worden, R.H. (eds.): Sandstone Diagenesis: Recent and Ancient. Malden, Massachusetts, USA: Wiley-Blackwell Publishing, International Association of Sedimentologists Reprint Series, 4, 3-44.

Worden, R.H., and Morad, S., 2003. Clay minerals in sandstones: controls on formation, distribution and evolution, In: Worden, R.H., and Morad, S. (eds.), Clay Mineral Cements in Sandstones. IAS Special Publication, 34, 1-41.

Zengler, K., Richnow, H.H., Rossello-Mora, R., Michaelis, W., and Widdel, F., 1999. Methane formation from long-chain alkanes by anaerobic microorganisms. Nature, 401, 266–269.

Ziegler, P.A., and Haag, D., 1977. Geology and hydrocarbon provinces of the North Sea. GeoJournal, 1, 7-32.

Ziegler, P.A.,1975. Geologic evolution of North Sea and its tectonic framework. AAPG Bulletin, 59, 1073-1097.

Quantockgoblin. Digital image. Soxhlet_extractor. Wikipedia. Oct 27. 2006 <https://en.wikipedia.org/wiki/Soxhlet_extractor>

Blogreu. Digital image. Gas Chromatography for fatty acid analysis. Ft. Johnson Summer REU Program @ College of Charleston. June 30.2015. <https://blogreu.files.wordpress.com/2015/06/11.gif>

Appendix

A1. PHREEQC input file for the scenario 1 in section 4.8.3

```
TITLE 1


PHASES


Magnesite
        MgCO3 = Mg+2 + CO3-2
        log_k           -8.029
        delta_h -6.169 kcal

Illite-Al  #phreeqc3
     K0.85Al2.85Si3.15O10(OH)2  +  9.400H+  +  0.600H2O  =  0.850K+  +  2.850Al+3
+3.150H4SiO4
     log_k     11.62        #
     delta_h  -62.313 kcal  #-260.722      kJ/mol
     # Enthalpy of formation:            -5919.3       kJ/mol        10BLA/VIE

KNa-feldspar
       K0.9Na0.1AlSi3O8 + 8 H2O = 0.9K+ + 0.1 Na+ + Al(OH)4- + 3 H4SiO4
       -log_k -20.573
       -delta_h 30.820     kcal

Selected_output
-file   1.xls
-equilibrium_phases Albite Chalcedony K-feldspar Kaolinite Pyrite Quartz Fe(OH)3(a)
-solid_solutions Calcite Magnesite Siderite

Solution 1
pH           8.22
density      1.023
units        ppm
temp         4
#redox       O(0)/O(-2)
Ca          412.3
Mg          1291.8
Na          10768
K           339.1
Fe          0.002
Mn          0.0002
Si          7.5
Cl          19353.0
Alkalinity  141.682 as HCO3
S(6)        2712.0

Equilibrium_phases 1
Albite            0.0 3.22
Calcite           0.0 0.0
Chalcedony        0.0 5.29
Dolomite          0.0 0.0
K-feldspar        0.0 4.57 dissolve_only
Kaolinite         0.0 2.05
Pyrite            0.0 0.0
Quartz            0.0 114.68 dissolve_only  #65 wt%
Fe(OH)3(a)        0.0 0.99 dissolve_only
Siderite          0.0 0.0

SAVE SOLUTION 2
END
```

```
USE SOLUTION 2
Equilibrium_phases 2
Albite            0.0 3.22
Calcite           0.0 0.0
Chalcedony        0.0 5.29
Dolomite          0.0 0.0
K-feldspar        0.0 4.57 dissolve_only
Kaolinite         0.0 2.05
Pyrite            0.0 0.0
Quartz            0.0 105.86 dissolve_only  #65 wt%
Fe(OH)3(a)        0.0 0.99 dissolve_only
Siderite          0.0 0.0

Reaction_pressure 2
1 450 in 10 steps

Reaction_temperature 2
4 116 in 10 steps
END
```

A2. PHREEQC input file for the scenario 2 in section 4.8.3

```
TITLE 1

PHASES
Magnesite
        MgCO3 = Mg+2 + CO3-2
        log_k           -8.029
        delta_h -6.169 kcal

Illite-Al  #phreeqc3 database of phreeqc interactive 3.0
     K0.85Al2.85Si3.15O10(OH)2  +  9.400H+  +  0.600H2O  =  0.850K+  +  2.850Al+3
+3.150H4SiO4
     log_k     11.62        #
     delta_h  -62.313 kcal  #-260.722      kJ/mol
     # Enthalpy of formation:             -5919.3       kJ/mol        10BLA/VIE

KNa-feldspar
       K0.9Na0.1AlSi3O8 + 8 H2O = 0.9K+ + 0.1 Na+ + Al(OH)4- + 3 H4SiO4
       -log_k -20.573
       -delta_h 30.820     kcal

Selected_output
-file   2.xls
-equilibrium_phases Albite Chalcedony K-feldspar Kaolinite Pyrite Quartz Fe(OH)3(a)
Illite-Al
-solid_solutions Calcite Magnesite Siderite

Solution 1
pH           8.22
density      1.023
units        ppm
temp         4
#redox       O(0)/O(-2)
Ca          412.3
Mg          1291.8
Na          10768
K           339.1
Fe          0.002
Mn          0.0002
Si          7.5
Cl          19353.0
Alkalinity  141.682 as HCO3
```

```
S(6)        2712.0

Equilibrium_phases 1
Albite              0.0 3.22
Calcite             0.0 0.0
Chalcedony          0.0 5.29
Dolomite            0.0 0.0
K-feldspar          0.0 4.57 dissolve_only
Kaolinite           0.0 2.05
Pyrite              0.0 0.0
Quartz              0.0 114.68 dissolve_only  #65 wt%
Fe(OH)3(a)          0.0 0.99 dissolve_only
Siderite            0.0 0.0

Reaction_pressure 1
450

Reaction_temperature 1
116

Reaction 1
CO2         2
CH4         1
H2          5
0.07 moles in 10 steps

Solid_solutions 1
Ankerite
-comp  Calcite 0.0
-comp  Magnesite 0.0
-comp  Siderite   0.0

END
```

A3. PHREEQC input file for the scenario 3 in section 4.8.3

```
TITLE 1

PHASES
Magnesite
        MgCO3 = Mg+2 + CO3-2
        log_k           -8.029
        delta_h -6.169 kcal

Illite-Al  #phreeqc3
     K0.85Al2.85Si3.15O10(OH)2  +  9.400H+  +  0.600H2O  =  0.850K+  +  2.850Al+3
+3.150H4SiO4
     log_k     11.62        #
     delta_h  -62.313 kcal  #-260.722      kJ/mol
     # Enthalpy of formation:             -5919.3       kJ/mol        10BLA/VIE
K0.9Na0.1-feldspar
       K0.9Na0.1AlSi3O8 + 8 H2O = 0.9K+ + 0.1 Na+ + Al(OH)4- + 3 H4SiO4
       -log_k -20.573
       -delta_h 30.820     kcal


Selected_output
-file   3.xls
-equilibrium_phases Albite Chalcedony K-feldspar Kaolinite Pyrite Quartz Fe(OH)3(a)
Illite-Al
-solid_solutions Calcite Magnesite Siderite

Solution 1
```

```
pH           8.22
density      1.023
units        ppm
temp         4
#redox       O(0)/O(-2)
Ca          412.3
Mg          1291.8
Na          10768
K           339.1
Fe          0.002
Mn          0.0002
Si          7.5
Cl          19353.0
Alkalinity  141.682 as HCO3
S(6)        2712.0

Equilibrium_phases 1
Albite            0.0 3.22
Calcite           0.0 0.0
Chalcedony        0.0 5.29
Dolomite          0.0 0.0
Kaolinite         0.0 2.05
Pyrite            0.0 0.0
Quartz            0.0 105.86 dissolve_only  #65 wt%
Fe(OH)3(a)        0.0 0.99 dissolve_only
Siderite          0.0 0.0
Illite-Al        0 0.0

Reaction_pressure 1
450

Reaction_temperature 1
116

Reaction 2
K0.9Na0.1-feldspar  1.0
0.25 moles in 10 steps
END
```

A4. PHREEQC input file for the scenario 1 in section 5.6.4

```
TITLE 1 Frigg field- progressive burial

Phases
Magnesite           10 #taken from the database minteq.dat from the computer code
phreeqc (Parkhurst and Appelo, 2013)
        MgCO3 = Mg+2 + CO3-2
        log_k           -8.029
        delta_h -6.169 kcal

SELECTED_OUTPUT
-file progressive buiral.xls
-equilibrium_phases  Quartz K-feldspar K-mica Kaolinite Pyrite Fe(OH)3(a)
-solid_solutions Calcite Magnesite Siderite

Solution 1 #seawater from Parkhurst and Appelo (2013)
pH           8.22
density      1.023
units        ppm
temp         4
#redox       O(0)/O(-2)
Ca          412.3
```

```
Mg          1291.8
Na          10768
K           339.1
Fe          0.002
Mn          0.0002
Si          7.5
Cl          19353.0
Alkalinity  141.682 as HCO3
S(6)        2712.0

EQUILIBRIUM_PHASES 1
Quartz           0.0 92.62                # Wt.70%
K-feldspar       0.0 5.71   dissolve_only # Wt.20%
K-mica           0.0 1.0    dissolve_only # Wt.5%
Kaolinite        0.0 0.0
Pyrite           0.0 0.0
Fe(OH)3(a)       0.0 0.99   dissolve_only

SOLID_SOLUTIONS 1
Ternary Solid Solution
-comp Calcite    0
-comp Siderite   0
-comp Magnesite  0

Save solution 2
SAVE EQUILIBRIUM_PHASES 2
SAVE SOLID_SOLUTIONS 2
End
#---------------------------------------Seawater equilibrates with primary phase
assemblage

Use solution 2
USE EQUILIBRIUM_PHASES 2
USE SOLID_SOLUTIONS 2

Reaction_pressure 2
1 200 in 10 steps

Reaction_temperature 2
10 60 in 10 steps

END
```

A5. PHREEQC input file for the scenario 2 in section 5.6.4

```
TITLE 2 Frigg field-Mix seawater with meteoric water 1-15000

Phases
Magnesite           10 #taken from the database minteq.dat from the computer code
phreeqc (Parkhurst and Appelo, 2013)

        MgCO3 = Mg+2 + CO3-2
        log_k           -8.029
        delta_h -6.169 kcal

SELECTED_OUTPUT
-file meteoric water flushing.xls
-equilibrium_phases  Quartz K-feldspar K-mica Kaolinite Pyrite Fe(OH)3(a)
-solid_solutions Calcite Magnesite Siderite

Solution 1 #seawater from Parkhurst and Appelo (2013)
pH          8.22
density     1.023
units       ppm
```

```
temp         4
#redox       O(0)/O(-2)
Ca          412.3
Mg          1291.8
Na          10768
K           339.1
Fe          0.002
Mn          0.0002
Si          7.5
Cl          19353.0
Alkalinity  141.682 as HCO3
S(6)        2712.0

EQUILIBRIUM_PHASES 1
Quartz           0.0 92.62               # Wt.70%
K-feldspar       0.0 5.71   dissolve_only # Wt.20%
K-mica           0.0 1.0    dissolve_only # Wt.5%
Kaolinite        0.0 0.0
Pyrite           0.0 0.0
Fe(OH)3(a)       0.0 0.99   dissolve_only

SOLID_SOLUTIONS 1
Ternary Solid Solution
-comp Calcite   0
-comp Siderite  0
-comp Magnesite 0

Save solution 2
SAVE EQUILIBRIUM_PHASES 2
SAVE SOLID_SOLUTIONS 2
End

#----------------------------------------Seawater equilibrates with primary phase
assemblage
#----------------------------------------Prior to the influx of meteoric water
#----------------------------------------leading to the formation of generic pore
water at starting conditions
Solution 2 #pure water
pH 7.0
temp 20.0

Mix 1
1  1
2  1450
#----------------------------------------Mixing seawater and meteoric water in the
ratio of 1:1450 for the first time

Use EQUILIBRIUM_PHASES 2
Use SOLID_SOLUTIONS 2

SAVE EQUILIBRIUM_PHASES 3
SAVE SOLID_SOLUTIONS 3
End

Mix 2
1  1
2  1450
#----------------------------------------Mixing seawater and meteoric water in the
ratio of 1:1450 for the second time

Use EQUILIBRIUM_PHASES 3
Use SOLID_SOLUTIONS 3

SAVE EQUILIBRIUM_PHASES 4
SAVE SOLID_SOLUTIONS 4
End
```

```
Mix 3
1  1
2  1450
#---------------------------------------Mixing seawater and meteoric water in the
ratio of 1:1450 for the third time

Use EQUILIBRIUM_PHASES 4
Use SOLID_SOLUTIONS 4

SAVE EQUILIBRIUM_PHASES 5
SAVE SOLID_SOLUTIONS 5
End

Mix 4
1  1
2  1450
#---------------------------------------Mixing seawater and meteoric water in the
ratio of 1:1450 for the fourth time

Use EQUILIBRIUM_PHASES 5
Use SOLID_SOLUTIONS 5

SAVE EQUILIBRIUM_PHASES 6
SAVE SOLID_SOLUTIONS 6
End

Mix 5
1  1
2  1450
#---------------------------------------Mixing seawater and meteoric water in the
ratio of 1:1450 for the fifth time

Use EQUILIBRIUM_PHASES 6
Use SOLID_SOLUTIONS 6

SAVE EQUILIBRIUM_PHASES 7
SAVE SOLID_SOLUTIONS 7
End

Mix 6
1  1
2  1450
#---------------------------------------Mixing seawater and meteoric water in the
ratio of 1:1450 for the sixth time

Use EQUILIBRIUM_PHASES 7
Use SOLID_SOLUTIONS 7

SAVE EQUILIBRIUM_PHASES 8
SAVE SOLID_SOLUTIONS 8
End

Mix 7
1  1
2  1450
#---------------------------------------Mixing seawater and meteoric water in the
ratio of 1:1450 for the seventh time

Use EQUILIBRIUM_PHASES 8
Use SOLID_SOLUTIONS 8

SAVE EQUILIBRIUM_PHASES 9
SAVE SOLID_SOLUTIONS 9
End

Mix 8
1  1
```

```
2  1450
#----------------------------------------Mixing seawater and meteoric water in the
ratio of 1:1450 for the eighth time

Use EQUILIBRIUM_PHASES 9
Use SOLID_SOLUTIONS 9

SAVE EQUILIBRIUM_PHASES 10
SAVE SOLID_SOLUTIONS 10
End

Mix 9
1  1
2  1450
#----------------------------------------Mixing seawater and meteoric water in the
ratio of 1:1450 for the ninth time

Use EQUILIBRIUM_PHASES 10
Use SOLID_SOLUTIONS 10

SAVE EQUILIBRIUM_PHASES 11
SAVE SOLID_SOLUTIONS 11
End

Mix 10
1  1
2  1450
#----------------------------------------Mixing seawater and meteoric water in the
ratio of 1:1450 fort the tenth time

Use EQUILIBRIUM_PHASES 11
Use SOLID_SOLUTIONS 11

SAVE EQUILIBRIUM_PHASES 12
SAVE SOLID_SOLUTIONS 12
End
```

A6. PHREEQC input file for the scenario 3 in section 5.6.4

```
TITLE 3 Frigg field-Sea water + oil degradation products

Phases
Magnesite           10 #taken from the database minteq.dat from the computer code
phreeqc (Parkhurst and Appelo, 2013)
        MgCO3 = Mg+2 + CO3-2
        log_k           -8.029
        delta_h -6.169 kcal

SELECTED_OUTPUT
-file oil degradation.xls
-equilibrium_phases  Quartz K-feldspar K-mica Kaolinite Pyrite Fe(OH)3(a)
-solid_solutions Calcite Magnesite Siderite

Solution 1 #seawater from Parkhurst and Appelo (2013)
pH           8.22
density      1.023
units        ppm
temp         4
#redox       O(0)/O(-2)
Ca          412.3
Mg          1291.8
Na          10768
K           339.1
```

```
Fe          0.002
Mn          0.0002
Si          7.5
Cl          19353.0
Alkalinity  141.682 as HCO3
S(6)        2712.0

EQUILIBRIUM_PHASES 1
Quartz           0.0 92.62               # Wt.70%
K-feldspar       0.0 5.71   dissolve_only # Wt.20%
K-mica           0.0 1.0    dissolve_only # Wt.5%
Kaolinite        0.0 0.0
Pyrite           0.0 0.0
Fe(OH)3(a)       0.0 0.99   dissolve_only

Solid_solutions 1
Ternary Solid Solution
-comp  Calcite    0.0
-comp  Magnesite  0.0
-comp  Siderite   0.0

Save solution 2
save EQUILIBRIUM_PHASES 2
Save Solid_solutions 2
End
#----------------------------------------Seawater equilibrates with primary phase
assemblage
#----------------------------------------Prior to the addition of hydrocarbon
degradation products(HDP)
#----------------------------------------leading to the formation of generic pore
water at starting conditions

Use solution 2
Use Equilibrium_phases 2
Use Solid_solutions 2

REACTION 2 #HDP formation summarized by the overall reaction: R-CH2-CH2-CH3+4H20=
R+ 2CO2+CH4+5H2 (Seewald, 2003)
CO2 2
CH4 1
H2  5
22 mole in 10 steps #increasing addition of HDP

Reaction_temperature 2
60


Reaction_pressure 2
195


Save solution 3
SAVE Equilibrium_phases 3
Save Solid_solutions 3
#----------------------------------------Re-equilibration driven by HDP addition
End
```

Table A1 Sample set from Siri 2 well (Denmark)

Oil field	Well	GFZ-No.	Depth (m)	Age	Formation /Member	Lithology	Location
Siri	Siri 2	G012202	2096.55	Palaeoce	Lista/Heimdal	sh	Seal
Siri	Siri 2	G012203	2097.60	Palaeoce	Lista/Heimdal	sh	Seal
Siri	Siri 2	G012204	2098.80	Palaeoce	Lista/Heimdal	sst	Seal
Siri	Siri 2	G012205	2099.80	Palaeoce	Lista/Heimdal	sst	Seal
Siri	Siri 2	G012206	2100.50	Palaeoce	Lista/Heimdal	sst	Oil leg
Siri	Siri 2	G012207	2101.10	Palaeoce	Lista/Heimdal	sst	Gas cap
Siri	Siri 2	G012208	2102.80	Palaeoce	Lista/Heimdal	sst	Gas cap
Siri	Siri 2	G012209	2103.10	Palaeoce	Lista/Heimdal	sst	Gas cap
Siri	Siri 2	G012210	2104.40	Palaeoce	Lista/Heimdal	sst	Gas cap
Siri	Siri 2	G012211	2106.40	Palaeoce	Lista/Heimdal	sst	Oil leg
Siri	Siri 2	G012212	2108.40	Palaeoce	Lista/Heimdal	sst	Oil leg
Siri	Siri 2	G012213	2109.20	Palaeoce	Lista/Heimdal	sst	Oil leg
Siri	Siri 2	G012214	2109.50	Palaeoce	Lista/Heimdal	sst	Oil leg
Siri	Siri 2	G012215	2109.60	Palaeoce	Lista/Heimdal	sst	Oil leg
Siri	Siri 2	G012216	2110.40	Palaeoce	Lista/Heimdal	sst	Oil leg
Siri	Siri 2	G012217	2110.50	Palaeoce	Lista/Heimdal	sst	Oil leg
Siri	Siri 2	G012218	2110.60	Palaeoce	Lista/Heimdal	sst	Oil leg
Siri	Siri 2	G012219	2112.40	Palaeoce	Lista/Heimdal	sst	Oil leg
Siri	Siri 2	G012220	2113.15	Palaeoce	Lista/Heimdal	sst	Oil leg
Siri	Siri 2	G012221	2115.50	Palaeoce	Lista/Heimdal	sst	Oil leg
Siri	Siri 2	G012222	2116.30	Palaeoce	Lista/Heimdal	sst	OWC
Siri	Siri 2	G012223	2116.40	Palaeoce	Lista/Heimdal	sst	OWC
Siri	Siri 2	G012224	2116.90	Palaeoce	Lista/Heimdal	sst	OWC
Siri	Siri 2	G012225	2117.50	Palaeoce	Lista/Heimdal	sst	Water leg
Siri	Siri 2	G012226	2117.70	Palaeoce	Lista/Heimdal	sh	Water leg
Siri	Siri 2	G012227	2118.70	Palaeoce	Lista/Heimdal	sst	Water leg
Siri	Siri 2	G012228	2119.70	Palaeoce	Lista/Heimdal	sst	Water leg
Siri	Siri 2	G012229	2120.50	Palaeoce	Lista/Heimdal	sst	Water leg
Siri	Siri 2	G012230	2120.55	Palaeoce	Lista/Heimdal	sst	Water leg
Siri	Siri 2	G012231	2121.50	Palaeoce	Lista/Heimdal	sst	Water leg
Siri	Siri 2	G012232	2121.60	Palaeoce	Lista/Heimdal	sst	Water leg
Siri	Siri 2	G012233	2126.10	Palaeoce	Lista/Heimdal	sst	Water leg
Siri	Siri 2	G012234	2127.60	Palaeoce	Lista/Heimdal	sst	Water leg
Siri	Siri 2	G012235	2128.15	Palaeoce	Lista/Heimdal	sst	Paleao OWC
Siri	Siri 2	G012236	2129.40	Palaeoce	Lista/Heimdal	sst	Paleao OWC
Siri	Siri 2	G012237	2130.60	Palaeoce	Lista/Heimdal	sst	Paleao OWC
Siri	Siri 2	G012238	2131.70	Palaeoce	Lista/Heimdal	sst	Paleao OWC
Siri	Siri 2	G012239	2133.80	Palaeoce	Lista/Heimdal	sst	Water leg
Siri	Siri 2	G012240	2134.40	Palaeoce	Lista/Heimdal	sst	Water leg
Siri	Siri 2	G012241	2136.50	Palaeoce	Lista/Heimdal	sst	Water leg
Siri	Siri 2	G012242	2136.55	Palaeoce	Lista/Heimdal	sst	Water leg
Siri	Siri 2	G012243	2136.65	Palaeoce	Lista/Heimdal	sst	Water leg

Table A2 Sample set from well 211/1-9, Magnus field (UK)

Oil field	Well	GFZ-No.	Depth (m)	Age	Formation /Member	Lithology	Location
Magnus	211/12a-9	G012856	3202.66	Jurassic	Kimmeridge Clay/Magnus	sst	Seal
Magnus	211/12a-9	G012857	3202.99	Jurassic	Kimmeridge Clay/Magnus	sst	Seal
Magnus	211/12a-9	G012858	3203.12	Jurassic	Kimmeridge Clay/Magnus	sst	Seal
Magnus	211/12a-9	G012859	3203.18	Jurassic	Kimmeridge Clay/Magnus	sst	Oil leg
Magnus	211/12a-9	G012860	3204.00	Jurassic	Kimmeridge Clay/Magnus	sst	Oil leg
Magnus	211/12a-9	G012861	3205.40	Jurassic	Kimmeridge Clay/Magnus	sst	Oil leg
Magnus	211/12a-9	G012862	3206.45	Jurassic	Kimmeridge Clay/Magnus	sst	Oil leg
Magnus	211/12a-9	G012863	3207.40	Jurassic	Kimmeridge Clay/Magnus	sst	Oil leg
Magnus	211/12a-9	G012864	3208.75	Jurassic	Kimmeridge Clay/Magnus	sst	Oil leg
Magnus	211/12a-9	G012865	3210.00	Jurassic	Kimmeridge Clay/Magnus	sst	Oil leg
Magnus	211/12a-9	G012866	3210.85	Jurassic	Kimmeridge Clay/Magnus	sst	Oil leg
Magnus	211/12a-9	G012867	3211.75	Jurassic	Kimmeridge Clay/Magnus	sst	Oil leg
Magnus	211/12a-9	G012868	3212.20	Jurassic	Kimmeridge Clay/Magnus	sst	Oil leg
Magnus	211/12a-9	G012869	3212.90	Jurassic	Kimmeridge Clay/Magnus	sst	OWC
Magnus	211/12a-9	G012870	3212.95	Jurassic	Kimmeridge Clay/Magnus	sst	OWC
Magnus	211/12a-9	G012871	3213.10	Jurassic	Kimmeridge Clay/Magnus	sst	OWC
Magnus	211/12a-9	G012872	3213.55	Jurassic	Kimmeridge Clay/Magnus	sst	Water leg
Magnus	211/12a-9	G012873	3215.50	Jurassic	Kimmeridge Clay/Magnus	sst	Water leg
Magnus	211/12a-9	G012874	3216.95	Jurassic	Kimmeridge Clay/Magnus	sst	Water leg
Magnus	211/12a-9	G012875	3221.70	Jurassic	Kimmeridge Clay/Magnus	sst	Water leg
Magnus	211/12a-9	G012876	3223.70	Jurassic	Kimmeridge Clay/Magnus	sst	Water leg
Magnus	211/12a-9	G012877	3228.80	Jurassic	Kimmeridge Clay/Magnus	sst	Water leg
Magnus	211/12a-9	G012878	3234.45	Jurassic	Kimmeridge Clay/Magnus	sst	Water leg
Magnus	211/12a-9	G012879	3238.20	Jurassic	Kimmeridge Clay/Magnus	sst	Water leg

Table A3 Sample set from well 25/1-9, Frigg field (Norway)

Oil field	Well	GFZ-No.	Depth (m)	Age	Formation	Lithology	Location
Frigg	25/1-9	G013618	2048.30	Eocene	Frigg	clay	Seal
Frigg	25/1-9	G013619	2050.60	Eocene	Frigg	sst	Gas cap
Frigg	25/1-9	G013620	2051.50	Eocene	Frigg	sst	Gas cap
Frigg	25/1-9	G013621	2052.50	Eocene	Frigg	clay	Gas cap
Frigg	25/1-9	G013622	2053.40	Eocene	Frigg	sst	Oil leg
Frigg	25/1-9	G013623	2054.50	Eocene	Frigg	sst	Oil leg
Frigg	25/1-9	G013624	2055.90	Eocene	Frigg	sst	Oil leg
Frigg	25/1-9	G013625	2056.70	Eocene	Frigg	sst	Oil leg
Frigg	25/1-9	G013626	2058.60	Eocene	Frigg	sst	Oil leg

Continued on next page

Table A3 Sample set from well 25/1-9, Frigg field (Norway)-continued

Oil field	Well	GFZ-No.	Depth (m)	Age	Formation	Lithology	Location
Frigg	25/1-9	G013627	2061.90	Eocene	Frigg	sst	Oil leg
Frigg	25/1-9	G013628	2062.80	Eocene	Frigg	sst	OWC
Frigg	25/1-9	G013629	2063.70	Eocene	Frigg	sst	Water leg
Frigg	25/1-9	G013630	2065.70	Eocene	Frigg	sst	Water leg
Frigg	25/1-9	G013631	2067.80	Eocene	Frigg	sst	Water leg
Frigg	25/1-9	G013632	2069.60	Eocene	Frigg	sst	Water leg

Table A4 Sample set from well 25/11-15, Grane field (Norway)

Oil field	Well	GFZ-No.	Depth (m)	Age	Formation /Member	Lithology	Location
Grane	25/11-15	G013588	1762.6	Palaeoce	Lista/Heimdal	sst	Oil leg
Grane	25/11-15	G013589	1768.7	Palaeoce	Lista/Heimdal	sst	Oil leg
Grane	25/11-15	G013590	1775.4	Palaeoce	Lista/Heimdal	sst	Oil leg
Grane	25/11-15	G013591	1779.75	Palaeoce	Lista/Heimdal	sst	Oil leg
Grane	25/11-15	G013592	1781.8	Palaeoce	Lista/Heimdal	sst	Oil leg
Grane	25/11-15	G013593	1782.75	Palaeoce	Lista/Heimdal	sst	Oil leg
Grane	25/11-15	G013594	1783.7	Palaeoce	Lista/Heimdal	sst	Oil leg
Grane	25/11-15	G013595	1784.5	Palaeoce	Lista/Heimdal	sst	OWC
Grane	25/11-15	G013596	1784.9	Palaeoce	Lista/Heimdal	clay	OWC
Grane	25/11-15	G013597	1785.6	Palaeoce	Lista/Heimdal	sst	OWC
Grane	25/11-15	G013598	1786.7	Palaeoce	Lista/Heimdal	sst	Water leg
Grane	25/11-15	G013599	1787.7	Palaeoce	Lista/Heimdal	sst	Water leg
Grane	25/11-15	G013600	1788.7	Palaeoce	Lista/Heimdal	sst	Water leg
Grane	25/11-15	G013601	1792.5	Palaeoce	Lista/Heimdal	sst	Water leg
Grane	25/11-15	G013602	1795.75	Palaeoce	Lista/Heimdal	sst	Water leg